

*Characterisation Protocol for Liquid-
Phase-Synthesised Graphene*

Lin Li-Shang

*Submitted in accordance with the requirements for
the degree of Doctor of Philosophy*

University of Leeds

School of Chemical and Process Engineering

August 2018

Acknowledgement

I would like to thank my girlfriend Paula Perez Romero. Paula who always provide supporting and taking care of throughout my study. Without Paula's companion, patience and her selflessness understanding, I would not have been able to complete the thesis. I would also like to thank my family and my parents. They have always encouraged me to develop my interest and think independently. Without their selfless supports, I will not have the chance to achieve this stage.

I would like to thanks to my dearest friends in Leeds: Michel, Ohm, Arron and Steven, who is always willing to spend their time with me for great dinner and wonderful discussions. I would also like thanks to Mischa and the kick about community for regular football events, bringing me happinesses, relaxations and also inspirations. With their companion, life in Leeds is no longer dark and cold.

Thanks to Yu-Ju Lee in Academic Sinica, who not only let me use their equipment but also bring up many interesting ideas. Thanks to Wei-bin Tay, who has partially contributed his idea and data analysis to Chapter 6.1. Robbie Britain, who has partially contributed his idea and data to Chapter 7.1. I would also like to thanks to Haoran Qiao and Mathew Best for their interesting projects , which helped me to think deeper and wider in the relative topic. I would also like to thank Dr. Zabeada Aslam for her help in TEM experiment; Dr. Rolf Crook for his encouragement and suggestions on my project. Also, I am appreciated the help and discussion brought from Prof. Rik Brydson and Dr. Aidan Westwood. Without their introduction to microscopic and carbon science, I would not realise how fruitful the research field is.

Abstract

Graphene, a two-dimensional honeycomb sp^2 carbon lattice has received enormous attention because of the potential for various applications such as the electrodes of photovoltaic devices and batteries, next generation flexible electronics and even antibacterial coatings. Interest in the application of graphene is mainly due to its unique physical and chemical properties, flexibility, and tuneability of the properties in graphene-based materials. However, while promising applications of graphene are being discussed, the term 'graphene' is often misused, and the difficulties in large-scale production of true two-dimensional graphene have further limited its applications. Methods such as top-down solution-processed exfoliation was developed to overcome the obstacles for large-scale graphene production, but these approaches do not yet produce completely delaminated and homogeneous graphene. To monitor and optimise the graphene production process, the development of a fast, standardised and reliable characterisation protocol for large-scale solution-processed graphene is therefore desirable.

Among the many characteristics of graphene flakes, the nano-structural features including the lateral dimension, crystal imperfections and the thicknesses of graphene are the most important factors that affect the various properties of graphene. However, though many of the analytical techniques have continuously been improved, methods to obtain and quantify these graphene nano-structural features are still limited. This is owing to the difficulties of visualising the ultra-thin nano-flakes and the fact that many of the properties of graphene are still unknown to be used to identify the material.

In this study, a characterisation protocol was proposed to quantify the fundamental nano-structural features of graphene. In all cases, the nano-structural feature was initially characterised by using the most precise technique based on direct imaging from transmission electron microscopy (TEM), the results were being used as benchmarks for the other fast but less direct methods that based on photon-probe techniques. To integrate and assess different characterisation techniques, quantification and statistical analysis of results have been used.

By utilising the method proposed, it was found that the lateral dimension distribution of graphene can be rapidly obtained by Dynamic Light Scattering (DLS), especially for flakes smaller than 1000 nm. The crystalline imperfections within graphene can be obtained and quantified by conventional Raman spectroscopy, in which a simple method based on linear correlation and random sampling was proposed to indicate the source of disorder in graphene samples. The result was compared to the TEM study, and the differences were assigned to the uneven distribution of the defects in graphene flakes. The thickness of graphene was characterised via various techniques. Several empirical equations were derived in order to can be rapidly obtained the thickness of graphene. However, it may not be feasible at this stage to develop a method to accurately determine graphene thickness for large-scale characterisation. It was found that the level of graphitic character could be obtained utilising the variation of Raman 2D (G') band, which is rather more important , and can be used to improve the graphene synthesis process.

In summary, the proposed graphene characterisation protocol offers a practical method to integrate and evaluate different characterisation techniques. Also, the protocol development method can be used as a reference point, which can be applied to other materials for developing material-specific characterisation protocols. Nevertheless, it has been shown that such a graphene characterisation protocol has the ability to quantify and differentiate between inhomogeneous solution-processed graphene samples and can be used for optimising the graphene synthesis processes.

List of content

Acknowledgement

Abstract

List of content

Chapter 1 Introduction

1.1 Motivation for studying graphene ... [16]

1.2 The challenge for scalable Graphene production ... [17]

1.3 Objective: Requirements of the graphene characterisation protocol ... [20]

Chapter 2 Literature Review on Graphene and its Characterisation

2.1 Pristine graphene ... [23]

2.2 Common disorder in real graphene ... [27]

2.3 Characterising graphene using transmitted electron microscopy ... [35]

2.4 Characterising graphene using photons ... [45]

2.5 The knowledge gap ... [56]

Chapter 3 Experimental Methodology and Data Analysis

3.1 Synthesis of graphene ... [59]

3.2 Characterisation techniques ... [68]

3.3 Data quantification and interpretation ... [80]

Chapter 4 Determination of Graphene Lateral Dimension

4.1 Lateral dimension obtained from TEM image analysis ... [98]

4.2 Graphene lateral size distribution from Optical Microscopy ... [105]

4.3 Light scattering techniques ... [119]

4.4 Conclusion ... [132]

Chapter 5 Determination of Graphene Crystal Imperfections

5.1 Characterise graphene crystal imperfection by TEM ... [137]

5.2 Characterise graphene crystal imperfection by Raman spectroscopy ... [152]

5.3 Comparison of Raman spectroscopy to the TEM ... [159]

5.4 Conclusion ... [163]

Chapter 6 The Thickness of Graphene

6.1 Determination of graphene thickness using TEM ... [167]

6.2 The 2D (G') band dispersion in Raman spectroscopy ... [183]

6.3 Obtaining flake thickness distribution for the SAEG graphene ... [189]

6.4 Comparison between different characterisation techniques ... [193]

6.5 Conclusion ... [198]

Chapter 7 Synthesis of graphene via electrochemical exfoliation and comparison with other methods

7.1 The starting material ... [203]

7.2 Electrochemical Exfoliation ... [205]

7.3 Comparison to other exfoliation methods ... [214]

7.4 The possible mechanism of electrochemical exfoliation ... [218]

7.5 Conclusion ... [229]

Chapter 8 Summary and Outlook

8.1 Summary of results and conclusions ... [235]

8.2 Outlook and future perspectives ... [240]

References ... [244]

Nomenclature & Abbreviations

| | |
|--|--|
| <i>Absolute sample thickness</i> : t | <i>Frequency- dependent electrical conductivity</i> : σ (ω) |
| <i>Absorption coefficient</i> : σ | <i>Full Width Half Maximum</i> : FWHM |
| <i>Absorption constant for the material</i> : δ | <i>Gibbs free energy change</i> : ΔG |
| <i>Adaptive local thresholding algorithm</i> : ALTA | <i>Global thresholding algorithm</i> : GTA |
| <i>Atomic Force Microscopy</i> : AFM | <i>Graphene oxide</i> : GO |
| <i>Average distance between defects</i> : L_D | <i>Graphite nanoplatelets</i> : GNP |
| <i>Bilayer graphene</i> :BLG | <i>Highly orientated pyrotytic graphite</i> :HOPG |
| <i>Bright field</i> : BF | <i>Image contrast</i> : $C(\lambda)$ |
| <i>Centre Limit Theorem</i> : CLT | <i>Imaginary part of refractive index</i> : κ |
| <i>Chemical Vapour Deposition</i> :CVD | <i>Incident beam intensity</i> : I_{in} |
| <i>Collection semi-angle</i> : β | <i>Inelastic mean free path</i> :IMFP |
| <i>Concentration of point defect</i> : n_D | <i>Inverse Fast Fourier Transformation</i> : IFFT |
| <i>Cumulative distribution function</i> : CDF | <i>Isopropanol alcohol</i> : IPA |
| <i>Current density per unit cross section area</i> : J | <i>Level of noise</i> : σ_1 |
| <i>Dark field</i> : DF | <i>Liquid viscosity</i> : η |
| <i>Dynamic light scattering</i> : DLS | <i>Liquid-phase Exfoliation</i> : LPE |
| <i>Effective atomic number</i> : Z_{eff} | <i>Magnetic field in the medium</i> : H |
| <i>Electric displacement fields</i> : D : | <i>Mean absorption distance</i> : ξ_0' |
| <i>Electrochemical exfoliation</i> : ECE) | <i>Mean energy loss</i> : E_m |
| <i>Electron energy loss</i> : ΔE | <i>Mean Greyscale Value Ratio</i> : MGVR |
| <i>Electron energy loss spectroscopy</i> :EELS | <i>Mean lateral dimension</i> : $\langle L \rangle$ |
| <i>Electrostatic potential of atom</i> : V_r | <i>Milled graphene</i> : MG |
| <i>Enthalpy</i> : ΔH | <i>Momentum</i> : k |
| <i>Entropy</i> : ΔS | <i>Momentum transfer</i> : q |
| <i>Extinction distance of the reflected beam</i> : ξ_g | <i>N-Methyl-2- pyrrolidone</i> : NMP |
| <i>Fast Fourier Transformation</i> : FFT | <i>N, N- dimethylformamide</i> :DMF |
| <i>few-layer graphene</i> :FLG | <i>Normalised transmitted beam intensity</i> : T |

Number of graphene layers : N
 Operation voltage : E_0
 Optical absorption : α
 Particle size distribution : PSD
 Peak centre : X_c
 Phonon frequency shift : ω_q
 Photon angular frequency : ω
 Probability density : $I = \psi(r, \theta)^2 = \psi \psi^*$
 Raman scattered intensity : I_q
 Reflection spectrum : $R(\lambda)$
 Refractive index \mathcal{N}
 Region of interest : ROI
 Relative factor : F
 Relative thickness of the specimen : t_r
 Scattered amplitude : $f(\theta) = f(\theta) e^{i\eta(\theta)}$
 Selected area electron diffraction : SAED
 Single-layer graphene : SLG
 Solution-assisted exfoliated graphene : SAEG
 Surface energy of graphene nano flakes : r_G
 Surface energy of solvent : r_s
 Thermal energy : $k_B T$
 Thickness of sample : t
 Translational diffusion coefficient : D
 Transmission electron microscopy : TEM
 Transmitted beam intensity: I_{tr}
 Universal conductance of a monolayer graphene near the K point : G_0
 X-ray Diffraction: XRD
 Zero-loss peak : ZLP

Part one

Background

1.

Introduction

1.1. Motivation for studying graphene

There is increasing interest in the scientific community in devices and materials that are low-dimensional. Three-dimensional materials have been researched extensively, as well as “zero-dimensional” (e.g., quantum dots/atoms) and “one-dimensional” (e.g., nanotubes / nanowire) materials. Research on “two-dimensional” materials has been limited due to a lack of stable materials that can easily form a single atomic layer crystal.

Graphene, a two-dimensional honeycomb sp^2 -carbon lattice, can be grown by chemical vapour deposition, or exfoliated from the three-dimensional graphite. Theories about graphene have been mentioned since the 1940s, but the existence of the material was thought impossible in free space ¹. In 2004, Novoselov and Geim showed practically the isolation of graphene from graphite under ambient conditions ^{2,3}, which subsequently demonstrated the unique electrical properties of graphene. This result has attracted many researchers to the field; in particular : the quantum Hall effects have been measured at room temperature; the carrier mobility of suspended graphene has been measured to be up to 230,000 cm^2/V , both of which suggest its potential for various applications ⁴⁻⁸.

However, the name ‘graphene’ is often misused in many research fields. Strictly speaking, the term “graphene” denotes: “a quasi-two-dimensional isolated monolayer of carbon atoms that are arranged in a hexagonal lattice ³”. As will be discussed in the next chapter, the properties of graphene depend strongly on the number of graphene layers ⁹. Only single-layer graphene (SLG) and bilayer graphene (BLG) have the unique zero-bandgap electronic configuration. For few-layer graphene (FLG, 3 to <10 layers), the conduction

and valence bands start to overlap. Thus, thicker graphene structures should be considered as thin film graphite ^{10,11}.

Difficulties in producing large-scale two-dimensional graphene have limited its further application ^{6,7,12-14}, which could also be the reason the term “graphene” is often misused in both industry and academia. Therefore, methods to distinguish graphene from graphite is an important task. This is possible by directly examining graphene/graphite using modern high-resolution electron microscopy techniques. However, this approach is time-consuming and costly. Another way to characterise the material within a shorter time frame is by identifying graphene by its unique properties ¹⁵⁻²¹. However, many of the properties of graphene, if they are to be used to identify the material, are still unknown. Thus, this approach must rely semi-empirically on measuring a series of graphene/graphite samples, in which the precision and accuracy are still unknown, accurate assessments are therefore needed for a more universal application.

1.2. The challenge for scalable Graphene production

Owing to the unique properties of graphene, promising potential applications of graphene have been discussed in various literatures ⁴⁻⁸, ranging from utilising graphene as the electrodes of photovoltaic devices and batteries, next-generation flexible electronics and even antibacterial coatings ^{4,5}. However, the main obstacle is developing a practical large-scale production process. Today, methods used to produce graphene can be categorised into top-down and bottom-up synthesis. The top-down method for graphene synthesis exfoliates the three-dimensional graphite into two-dimensional graphene, while the bottom-up method of synthesis involves the growth of graphene on a supporting substrate ²².

i. Bottom-up graphene synthesis:

1) Chemical Vapour Deposition (CVD)

The technique is the most popular bottom-up graphene synthesis method, here epitaxial growth exploits catalytic metal substrates such as Ni or Cu ^{23,24}. This method can produce large area and high-quality graphene directly on the substrate. However, the requirements of high temperature and the multi-step transferral process to isolate the graphene from the catalytic substrate pose significant challenges for cheap and industrial-scale production ^{7,25}.

ii. Top-down synthesis:

1) Micro-mechanical cleavage

It was the earliest technique used to isolate monolayer graphene. Although such a method can produce good quality graphene flakes, the yields are limited to lab-scale uses ^{2,26}.

2) Mechanical milling

It was first performed by dispersing graphite powder in distilled water following continuous wet ball milling for days. The distilled water was deemed to decrease the slip of graphene sheets and also prevent back agglomeration of the graphene sheets ^{13,27,28}. The gentle but lengthy process ensures that the shear stress is dominant and avoids damage to the graphite along the in-plane crystal direction. By replacing the water with N, N-dimethylformamide (DMF) solvent, it was reported that some of the monolayer and few-layer graphene flakes could be synthesised ²⁷⁻²⁹.

3) Hummers' method

It is an attractive chemical method for producing solution-processed graphene oxide (GO). However, subsequent chemical or thermal treatments to reduce GO to graphene can only

partially remove its oxygen content and regenerate its structure so that electrical properties cannot be fully restored ^{25,30}.

4) *Ultrasonication exfoliation*

Also known as Liquid-phase Exfoliation (LPE). It is considered a more straightforward method, whereby graphite powder is dispersed in a polar solvent such as N-Methyl-2-pyrrolidone (NMP), in which the solvent molecule intercalates between the graphite layer due to the chemical potential. The van-der-Waals forces that stick the graphene sheets together can then be overcome using the assistance of sonication ^{13,14}.

5) *Electrochemical exfoliation (ECE)*

The method has been developed relatively recently and utilises a biased potential to drift and intercalate electrolyte anions into a graphite electrode. The subsequent electrochemical reaction and gas evolution peels graphene flakes from the graphite electrode ^{6,7,12}.

Although many synthesis techniques have been developed for scalable graphene synthesis, an inexpensive, high-quality graphene production method is not achieved yet, in which it is owing to the overall quality and homogeneity of graphene samples inversely proportional to its process time, and this is the reason why making high-quality graphene is expensive ³¹. However, it seems that the method based on solution-assisted graphite exfoliation (i.e. mechanical milling, LPE and ECE) has the potential to produce fair-quality graphene rapidly. Also, the equipment for synthesising such graphene sample is widely accessible, making the graphene less expensive. Moreover, the solution-assisted graphite exfoliation method directly produces graphene suspension in a solution, beneficial for future application on ink-jet printing electronics. Therefore, graphene synthesised by the solution-assisted graphite exfoliation method will be the focus of this thesis.

1.3. Objective: Requirements of the graphene characterisation protocol

Even though methods like solution-assisted graphite exfoliation have the potential to achieve large-scale graphene production, these approaches do not yet produce completely delaminated and stabilised graphene. Multiple sonication or purification processes are therefore required^{4,7,32–34}. Considerable challenges need to be overcome for the development of an industrially scalable process. One of the most critical tasks is to have a fast and reliable characterisation method that can be used to monitor the degree of exfoliation as well as the crystal quality, the sheet thickness and the lateral dimension achieved during the synthesis process^{35,36}.

Although spectroscopic and microscopic techniques have been continuously improved to characterise ultra-thin nanomaterial, a rapid and accurate method remains elusive challenge. Today, graphene characterisation mainly relies on the transfer of the sample to a substrate, where flake damage or re-aggregation cannot be totally avoided. Most approaches proposed in previous literature have mainly focused on characterising the laboratory-scale homogeneous graphene, where CVD or mechanical exfoliation synthesis methods were employed. Thus, an improved characterisation protocol that can be used to monitor the effectiveness of a general graphene synthesis method is desirable.

Ideally, the characterisation protocol should be able to rapidly differentiate the thin graphene flakes from thick graphite chunks. Also, it is crucial to quantify the lateral dimension of graphene flakes and the crystal imperfections within the graphene flakes are important parameters in terms of application. The protocol development is schematically shown in figure 1.1. In order to develop this protocol, the theories of graphene and its characterisation techniques are reviewed in Chapter 2. The experimental methods and data

analysis techniques used in this project are introduced in Chapter 3. Based on the theories and techniques introduced, the project aims to develop a rapid protocol to characterise solution-assisted exfoliated graphene (SAEG), which focuses on three main fundamental graphene nano-structural features: the graphene lateral dimension (Chapter 4), crystal imperfections (Chapter 5) and the thicknesses of graphene (Chapter 6). Direct imaging methods based on transmission electron microscopy (TEM) are initially used to study the properties of graphene before other measurements are made. Quantification and statistical analysis of results have been used to evaluate the limitations and errors in the different characterisation methods. After the characterisation protocol is finally developed, it is then applied to various SAEG graphene samples exfoliated via electrochemical exfoliation (ECE) under different conditions, and the results and proposed exfoliation mechanism are discussed in chapter 7.

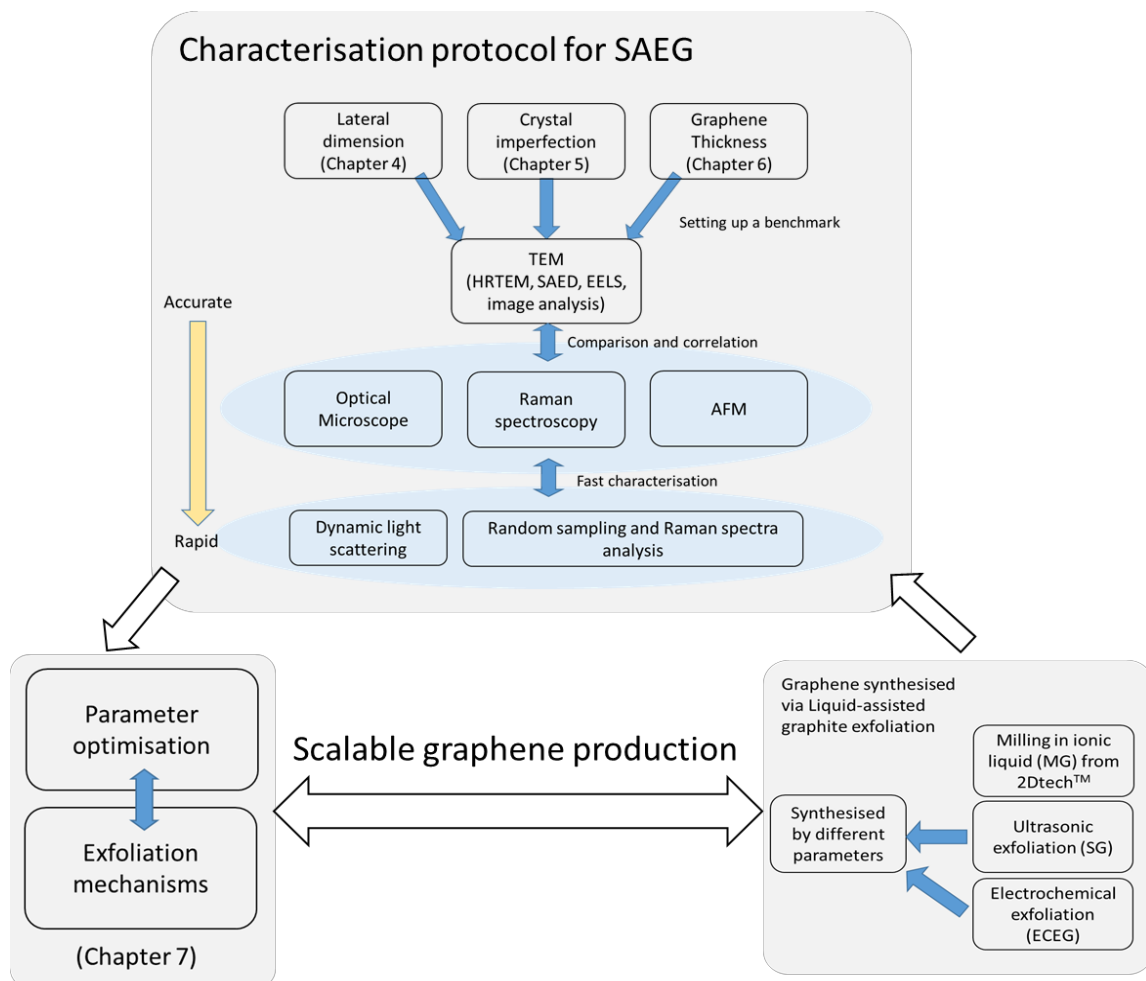


Figure 1.1: The need for a graphene characterisation protocol to assess scalable graphene production

2.

Literature Review on Graphene and its Characterisation

In this chapter, the general background regarding graphene and its characterisation are introduced. Although many techniques have been developed to characterise graphene from different perspectives (i.e. mechanical, electrical, or optical properties), this chapter will only review theories and experimental findings that are relevant in helping to interpret the experimental results in the following chapters.

2.1. Pristine graphene

I. Crystal structure

The ideal structure of graphene is a two-dimensional (2D) crystal consisting of carbon atoms arranged in a hexagonal honeycomb lattice. All atoms are sp^2 hybridised in pristine graphene: the sp^2 orbital being formed (and filled) from the $2s$, $2p_x$ and $2p_y$ orbitals (and electrons) whereas the $2p_z$ orbital and its electron remains relatively unaffected²². As seen in figure 2.1 (a), the $2p_z$ -orbital is oriented perpendicular to the remaining in-plane sp^2 -orbitals, with the in-plane sp^2 -orbitals lying symmetrically in the X–Y plane at an angle of 120° to each other. The distance between nearest-neighbour atoms (carbon-carbon bond length, known as a) is $a = 1.420\text{\AA}$. Figure 2.1 (b) and (c) shows the unit cell in real space and the Brillouin zone in the reciprocal lattice respectively. The real space basis vectors of the unit cell \mathbf{a}_1 and \mathbf{a}_2 in Cartesian coordinates are expressed as:

$$\mathbf{a}_1 = \frac{a}{2}(3, \sqrt{3}), \quad \mathbf{a}_2 = \frac{a}{2}(3, -\sqrt{3}) \dots (\text{equation 2.1})$$

, where the lattice constant $|\mathbf{a}_1| = |\mathbf{a}_2| = \sqrt{3}a = 2.46 \text{ \AA}$. In the reciprocal lattice, the unit vectors (primitive lattice vector) are:

$$\mathbf{b}_1 = \frac{2\pi}{3a}(1, \sqrt{3}), \quad \mathbf{b}_2 = \frac{2\pi}{3a}(1, -\sqrt{3}) \dots (\text{equation 2.2})$$

, corresponding to a lattice constant of length of $b = |\mathbf{b}_1| = |\mathbf{b}_2| = \frac{4\pi}{\sqrt{3}a}$. The

symmetry points Γ, M, K are shown in figure 2.1(c), which correspond to the centre, corner and centre of the edge in the Brillouin zone³⁷.

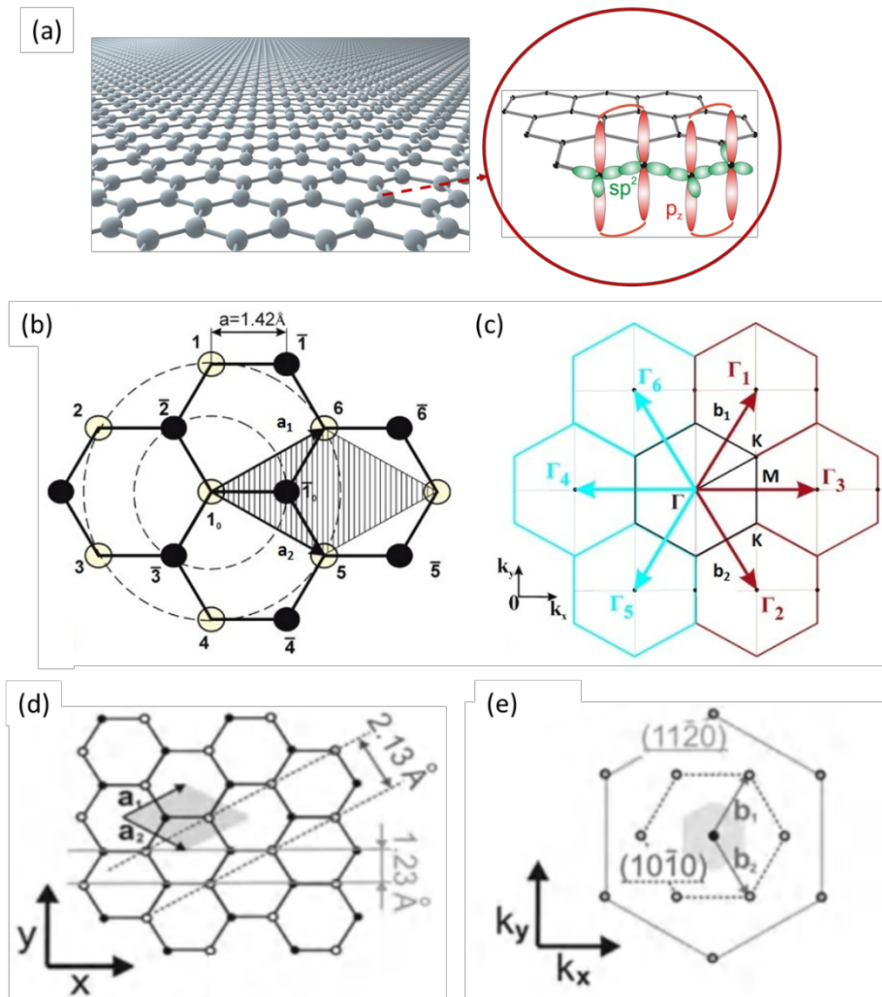


Figure 2.1: shows the lattice structure of pristine graphene: (a) illustration of atoms forming a two-dimensional hexagonal lattice with sp^2 bonding; (b) lattice of graphene in real space; (c) the reciprocal lattice of graphene. (d) two set of planes with and in real space can be seen using electron diffraction, which corresponds to the reciprocal lattice as shown in (e); picture adopted from reference^{38, 22}.

The reciprocal lattice is often used to describe the diffraction data: each constructive diffraction point corresponds to a specific set of lattice planes of the crystal in real space as shown in Figure 2.1 (d) and (e) ^{22,38–40}. The diffraction pattern of graphene is schematically shown in Figure 2.1 (e); the diffraction spot in the corners of the dotted hexagon are the $\{10\bar{1}0\}$ planes, corresponding to the real lattice spacing of $d = 2.13 \text{ \AA}$, as shown in Figure 2.1 (d). Similarly, the $\{11\bar{2}0\}$ planes have a shorter lattice spacing of $d = 1.23 \text{ \AA}$, resulting in the six diffraction spots of the larger hexagon in reciprocal space ^{22,38–40}.

II. *The band structure and massless electron*

Using the primitive lattice vectors (\mathbf{b}_1 and \mathbf{b}_2), the energy band diagram for $\pi - \pi^*$ band (arising from p_z -orbitals) can be constructed using a tight-binding model. The tight-binding model calculates the electronic band structure by considering the nearest-neighbour atom configuration ^{39–41}. The $\pi - \pi^*$ ($E_{\pi-\pi^*}$) band energy diagram of graphene is calculated as ⁴⁰:

$$E_{\pi-\pi^*}(\mathbf{k}) = \frac{\epsilon_{2p} \pm b \cdot u_{\mathbf{g}}(\mathbf{k})}{1 \pm s \cdot u_{\mathbf{g}}(\mathbf{k})} \dots (\text{equation 2.3})$$

$$u_{\mathbf{g}}(\mathbf{k}) = \left\{ 1 + 4\cos\left(\frac{3k_x a}{2}\right)\cos\left(\frac{k_y a}{2}\right) + 4\cos^2\left(\frac{k_y a}{2}\right) \right\}^{\frac{1}{2}} \dots (\text{equation 2.4})$$

, where ϵ_{2p} is the atomic $2p$ level energy of an isolated carbon atom, b is the nearest neighbour transfer integral and s is the nearest neighbour overlap integral, in which the value can differ by lattice configuration, and can be approached by fitting these parameters to experimental results ⁴¹. The value of $\epsilon_{2p} = 0$, $b = -3.033 \text{ eV}$ and $s = 0.129$ were used for calculation of the graphene energy band shown in figure 2.2 ⁴¹. The k_x , k_y are the coordinates in reciprocal space. The sign \pm is related to the bonding and

anti-bonding of π energy bands ⁴⁰. The $E_{\pi-\pi^*}$ energy band diagram in \mathbf{k} -space is shown in Figure 2.2. An important feature in the graphene band diagram is that the conduction band and valence band meet each other at the K point in the Brillouin zone (see Figure 2.2). Thus, graphene is not classified as a metal, insulator or semiconductor, but rather as a semi-metal or zero-gap semiconductor. The linear energy dispersion relation around the K point (Dirac cone) is another important feature, which can be expressed as ⁴⁰ :

$$u_{linear}^{\pm}(\mathbf{k}) = \pm \hbar c_g |\mathbf{k}| \dots (\text{equation 2.5})$$

, where \hbar is the reduced Planck's constant ($\frac{h}{2\pi}$) and c_g is the electron Fermi velocity. The effective mass of an electron (m_e^*) in ideal pristine graphene near the K point can be expressed as:

$$m_e^*(\mathbf{k}) = \hbar^2 \mathbf{k} \left(\frac{du(\mathbf{k})}{d\mathbf{k}} \right)^{-1} = \hbar^2 \mathbf{k} \left(\frac{du_{linear}^{\pm}(\mathbf{k})}{d\mathbf{k}} \right)^{-1} = \hbar \mathbf{k} c_g^{-1} \dots (\text{equation 2.6})$$

, where an alternative definition of effective mass is used from the relativistic consideration of electrons in graphene near the K point ⁴². The effective mass of electron vanishes when $k \rightarrow 0$, all external excitation energy being transferred into the kinetic energy for the electron and holes ^{3,42}, thereby showing a unique charge carrier transportation behaviour in graphene, known as the “massless electron” ⁴².

Figure 2.2 (c) shows $\sigma - \sigma^*$ energy band diagram in comparison with the $\pi - \pi^*$ energy band. The $\sigma - \sigma^*$ band originates from the sp^2 orbitals, and graphene was estimated to have a 6.0 eV $\sigma - \sigma^*$ bandgap at the Γ point. Since the $\pi - \pi^*$ and $\sigma - \sigma^*$ band are evident for the sp^2 electronic configuration, it gives information about the crystallinity of a sp^2 carbon material and can be used for characterising the crystallinity of graphene. Nevertheless, since the Fermi level in a charge neutral graphene lies at the intersection of the $\pi - \pi^*$ bands, various optical and electrical properties of graphene will be significantly affected by the unique band structure. Thus, the $\pi - \pi^*$ band structure is more widely discussed and being used to differentiate from graphite.

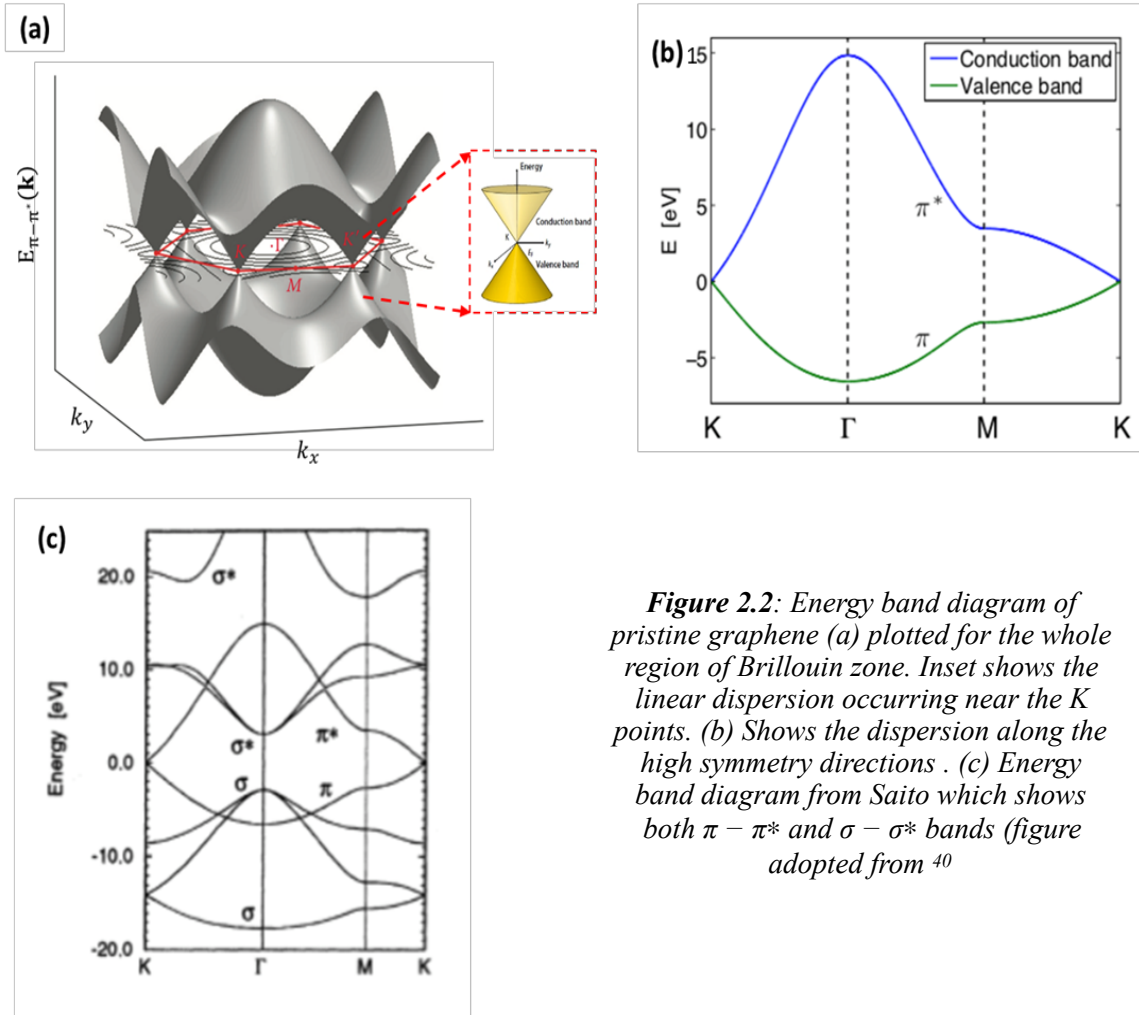


Figure 2.2: Energy band diagram of pristine graphene (a) plotted for the whole region of Brillouin zone. Inset shows the linear dispersion occurring near the K points. (b) Shows the dispersion along the high symmetry directions. (c) Energy band diagram from Saito which shows both $\pi - \pi^*$ and $\sigma - \sigma^*$ bands (figure adopted from ⁴⁰)

2.2. Common disorders in real graphene

I. In-plane disorder

i. Zero-dimensional point defects

Zero-dimensional point defects are the most general and simplest disorder in graphene. Point defects are caused by missing atoms in the lattice such as single vacancy (SV) and double vacancy (DV) defects, as shown in figure 2.3 (a) and (b) respectively. In the absence of adatoms, the missing atoms in lattice could cause the formation of dangling bonds in the lattice, leading to C-C bond rotation to obtain a more energetically stable atomic configuration ⁴³. This could result in the construction of polygonal rings within the

hexagonal lattice structure distorting the lattice locally. Commonly seen cases are: the formation of an octagon in between two side pentagons from the DV defect (5–8–5 configuration as seen in figure 2.3 (c))⁴⁴; the Stone-Wales (SW) defect commonly observed due to its stable topological nature (see Figure 1.3 (d))⁴⁴; the (555–777) defect is a case that merges a Stone–Wales and a double 5–8–5 vacancy, which forms a three pentagons and three heptagons configuration as seen in figure 2.3(e)⁴⁴. These defects can be experimentally visualised using transmission electron microscope (TEM)⁴⁵, which will be introduced later in this chapter.

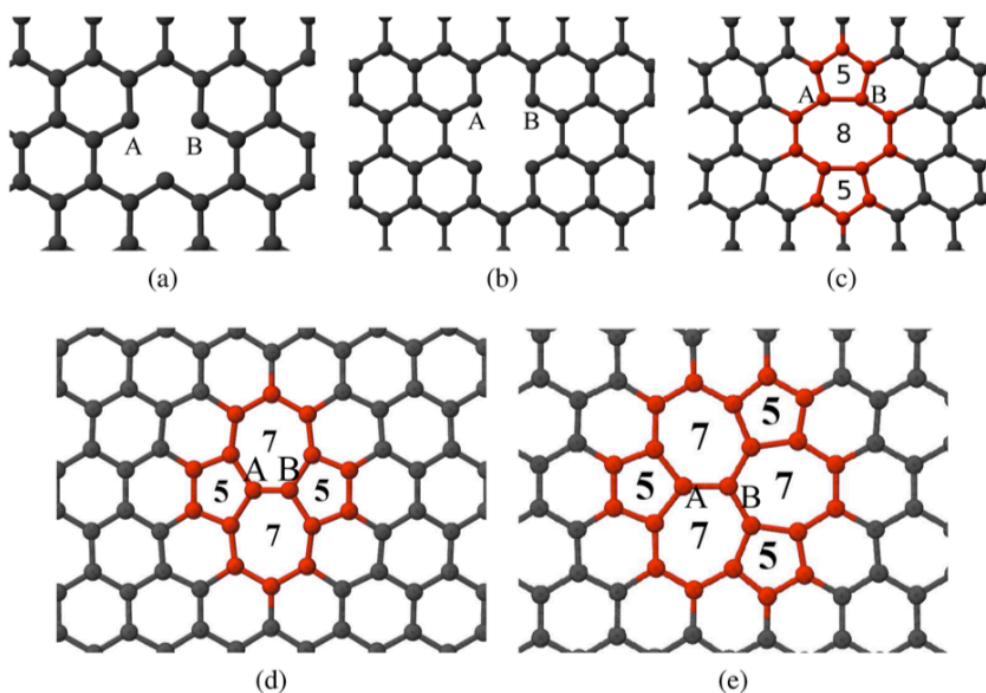


Figure 2.3: Illustrate commonly seen structural defects in graphene. (a) Single vacancy; (b) double vacancy ;(c) 5–8–5 configuration due to double vacancy; (d) Stone–Wales defect; (e) 555–777 defect. The n -fold rings due to lattice reconstruction are shown in colour. Picture adopted from Reference⁴⁴

ii. Dislocation and grain boundaries

The presence of dislocations in graphene could cause the two-dimensional lattice to orient differently. As seen in figure 2.4, the existence of a pentagon–heptagon dislocation induces strain in the nearby crystal planes, the two nearby coherent crystal regions therefore misoriented slightly (see figure 2.4 (b)-(d)). However, the dislocations could migrate

toward each other in order to release the internal lattice strain ⁴⁵⁻⁴⁷. A series of dislocations aligned into a one-dimensional chain form grain boundary in monolayer graphene. The grain boundary separates two-dimensional domain into different lattice orientations, which have been experimentally observed by high-resolution TEM ⁴⁸⁻⁵⁰. Figure 2.5 shows a tilt grain boundary in monolayer graphene visualised by electron microscopy technique, in which the tilt grain boundary is formed by a series of connected polygons. This separates the graphene into two domains with a relative misorientation of 27°. Nevertheless, it has been reported that for a copper supported CVD graphene, low-angle grain boundaries with a ~7° tilt and high angle grain boundaries a ~30° tilt are preferable ⁴⁸⁻⁵⁰.

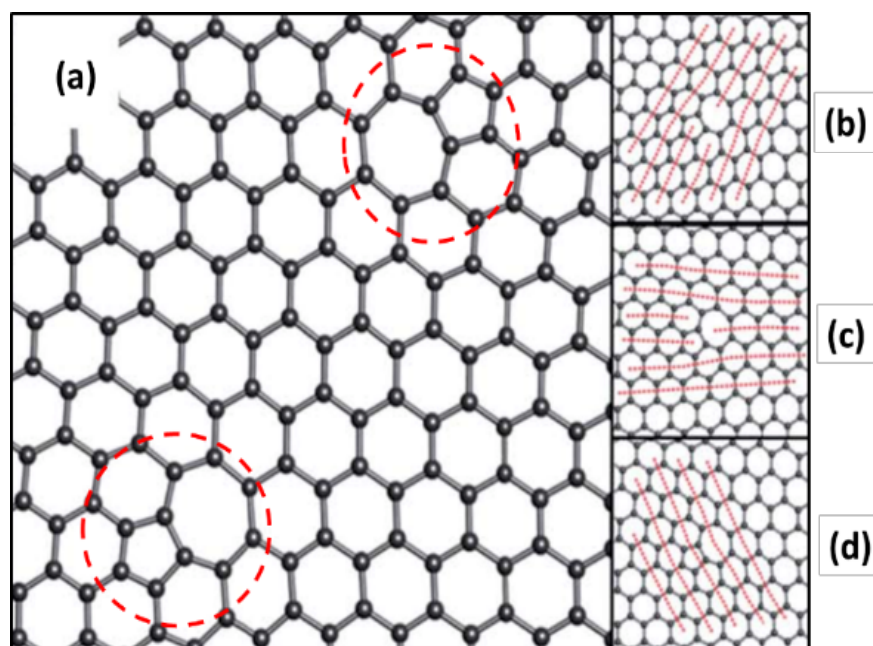


Figure 2.4: shows dislocation in graphene (a) a model of dislocation pair with two pentagon-heptagon (5-7) cores, highlighted by red dash circles. (b)-(d) shows a pentagon-heptagon (5-7) dislocation core induces strains and misorientation to the nearby lattices, Graph adopted from ⁴⁵⁻⁴⁷.

Besides grain boundaries in monolayer graphene, the grain boundaries in multilayer graphene appear in two distinct configurations, as schematically shown in figure 2.6. The grain boundary can exhibit an atomically bonded arrangement as introduced for the monolayer graphene (Figure 2.6 (b)) or formed by an interlayer overlap (figure 2.6(c)) ⁵¹. Both boundary configurations could cause multiple misoriented lattice regions that shorten the lattice coherence length (L_a), which further affects the carrier transportation properties within a graphene film ^{46,48}. Thus, the study of grain boundaries as well as lattice coherence length in graphene is critical. Experimentally, such lattice imperfections can be

characterised by high-resolution TEM and electron diffraction techniques (SAED). Further detail will be introduced later in this section and experimental results are discussed in Chapter 5.

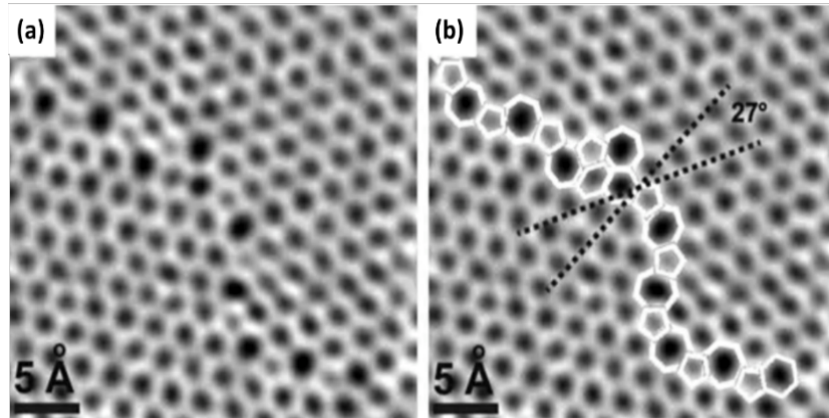


Figure 2.5: STEM image of a curved tilt boundary with a 27° relative misorientation between the domains. The grain boundary is mainly composed of alternating pentagon–heptagon pairs. This type boundary has been repeatedly reported in graphene film is synthesised by CVD. Figure adopted from ^{48–50}

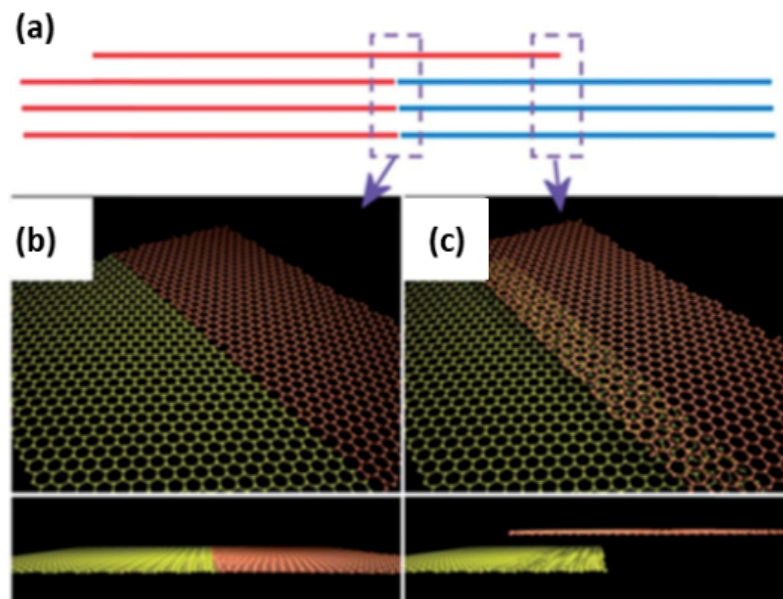


Figure 2.6: (a) Line illustrating the two types of grain boundaries in few-layer graphene: (b) atomically bonded and (c) overlapping grain boundaries. Figure adopted from ⁵¹

iii. Graphene edge structure

The edge is a common translational-symmetry breaking structure in graphene. The armchair and zigzag edges are two of the most general edge structures, due to such configurations minimising the number of dangling bonds along the edge site, as shown in figure 2.7⁵². However, theoretical calculations have indicated that a perfect zigzag edge could be metastable, and transformation to a pentagon–heptagon (5-7) or a pentagon–octagon (5-8-5) arrangement could occur spontaneously at room temperature. Therefore, topological defects often appear nearby zigzag edges (see figure 1.7 (b) and (c))^{49,52,53}.

The edge structure of graphene and its atomic arrangement has been experimentally studied by (S)TEM and Raman spectroscopy. Recently, electron energy loss spectroscopy (EELS) has also been used to study the chemical bonding near the edge structure. The results indicated that graphene edges can be pristine but are likely to be passivated by hydrogen and oxygen heteroatom, which could possibly alter the electronic band structure and the charge carrier transport behaviour^{54–57}.

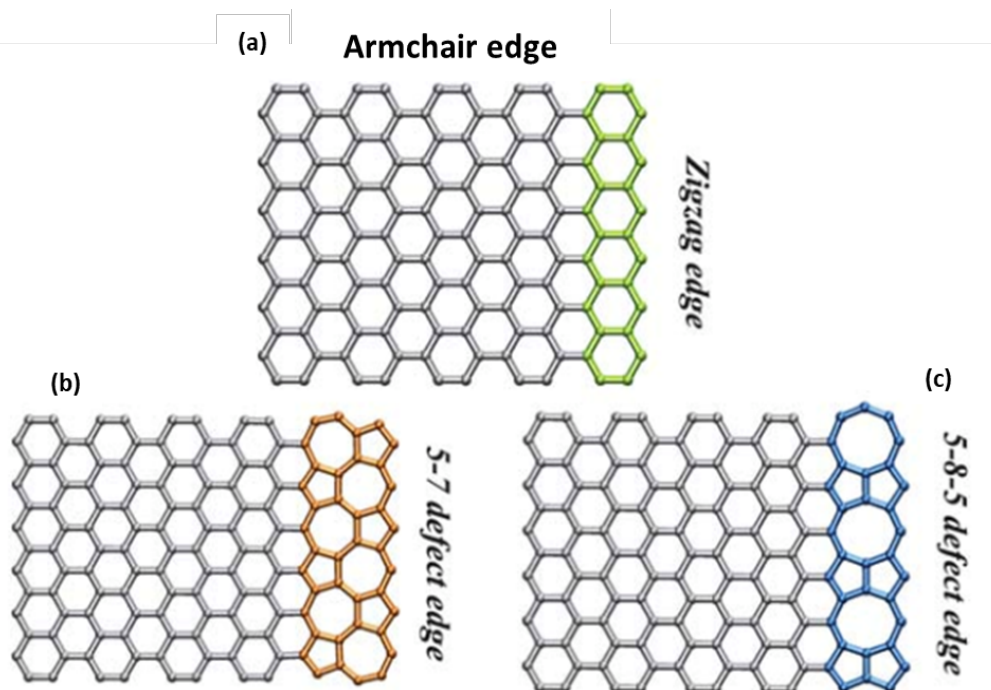


Figure 2.7: Shows different edge configurations in graphene: (a) a zigzag edge and an armchair edge. (b) and (c) shows the reconstructed zigzag edge, which consists of alternating 5-7 or 5-8-5 defects.⁵²

II. Out-of-plane disorder

i. Multilayer graphene

Incompletely delaminated multilayer graphene regions are often observed in experiments. The presence of incomplete delaminated graphene regions is critical and could significantly affect the various opto-electrical properties of graphene. Multilayer graphene exhibits several variations in terms of stacking configuration. AB Bernal stacking is the most stable configuration, where each of the graphene layers is slightly shifted, so that the carbon atoms above are at the centre of the underlying hexagons. This configuration is schematically shown in figure 2.8(a) and has an interlayer spacing of 0.335 nm. The energy landscape in comparison to other stacking structures is shown in figure 2.8 (c) ⁵⁸. AA stacking is a less stable configuration, where the graphene layers are directly stacked above each other and all carbon atoms are on top of each other giving an interlayer spacing of 0.353 nm (figure 2.8(a) and (c)). As seen in figure 2.8(c) ⁵⁸, the AA' stacking is slightly less stable than the AB stacking configuration, where each graphene plane is shifted by 1/2 hexagon from zigzag AA stacking or by 1/4 hexagon from armchair AB stacking⁵⁸ and having an interlayer spacing of 0.344 nm ⁵⁸. The stacking configuration has been interpreted as having a turbostratic structure in previous literature due to its unique diffraction pattern ^{58,59}. Turbostratic graphene / graphite structures are where the graphene layers are weakly bonded and could have a rotation with respect to each other. The relative rotation gives rise to unique Moiré patterns as schematically shown in 2.8 (b) ⁶⁰, which can be observed using atomic-resolution transmission electron microscopy (TEM) technique discussed in Chapter 5 ⁵⁸⁻⁶².

Both the stacking configuration and the number of graphene layers can affect the electron band structure in graphene. By introducing additional coefficients that describe interlayer coupling between each of the adjacent graphene layers, the band structure of multilayer graphene can be calculated via the tight-binding model ^{18,63}. As seen in figure 2.9 (a), the characteristic linear band structure in monolayer graphene is replaced by pairs of split hyperbolic bands in an AB stacked bilayer graphene. For a trilayer graphene, the conduction and valence bands start to overlap, as seen in figure 2.9 (b) ^{18,63}. As for thicker

graphene layers, the band overlap phenomena fluctuate but continuously increase. In figure 2.9 (c) ⁶³, the band overlap becomes severed and approximates to the bulk graphite limit for a ~40 layer thick graphene. At this point, the properties of graphene and graphite are indistinguishable and should be categorised as graphite instead of graphene ⁶³.

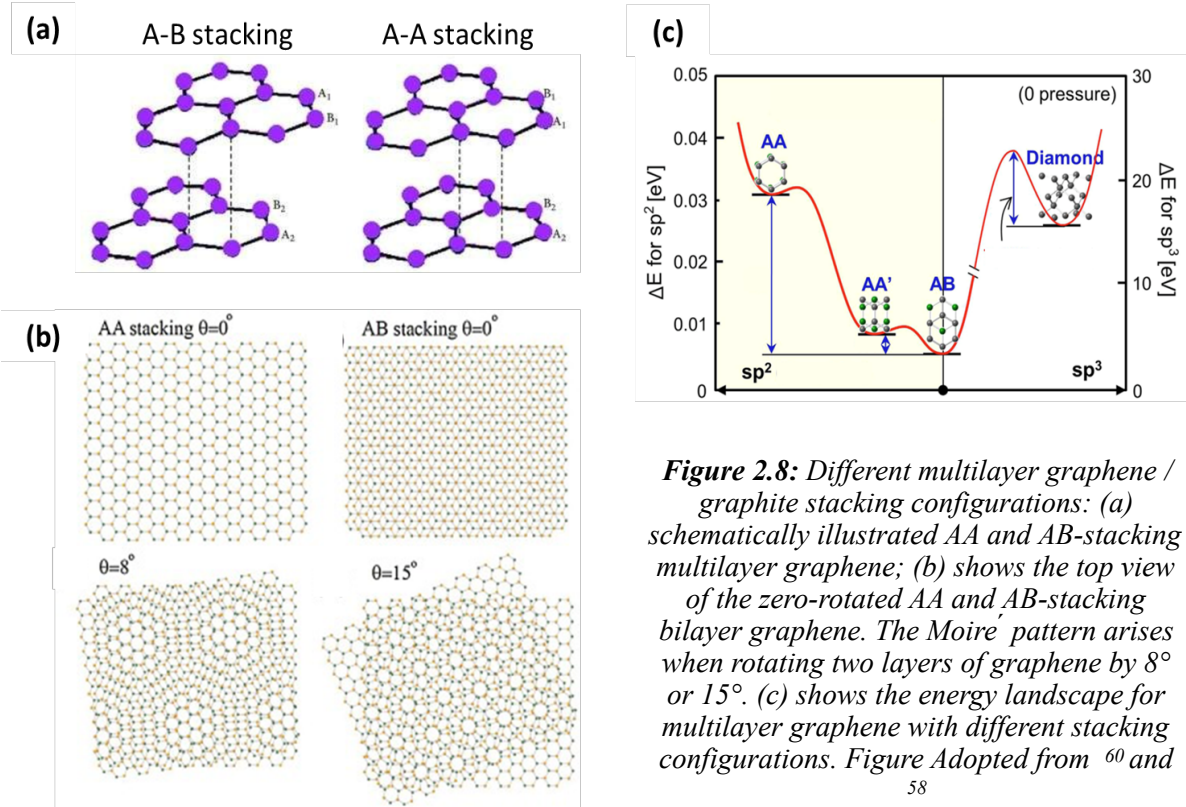


Figure 2.8: Different multilayer graphene / graphite stacking configurations: (a) schematically illustrated AA and AB-stacking multilayer graphene; (b) shows the top view of the zero-rotated AA and AB-stacking bilayer graphene. The Moiré pattern arises when rotating two layers of graphene by 8° or 15°. (c) shows the energy landscape for multilayer graphene with different stacking configurations. Figure Adopted from ⁶⁰ and ⁵⁸

Nevertheless, an alteration in the stacking configuration could also result in a different electronic band structure. This is owing to the stacking configuration and the interlayer spacing significantly affecting the electron cloud distribution near the adjacent plane, modifying the interlayer coupling states and thereby the band structure ⁵⁸. Figure 2.10 compares the band structure of bilayer AA and AB stacking graphene. Figure 2.10 below, the degeneracy of the Dirac cone is symmetrically shifted along the momentum axis for AA stacking of graphene. Whilst, in AB stacking bilayer graphene, the linear band structure is transformed to a parabolic band, as introduced previously. The electric band structure of various stacking configurations has been extensively studied by Lee et al., Zhong et al. and Bistritzer et al., where the interlayer coupling through the 2p_z orbitals is deemed to be the major reason for the band alteration near the K point ^{58,64,65}.

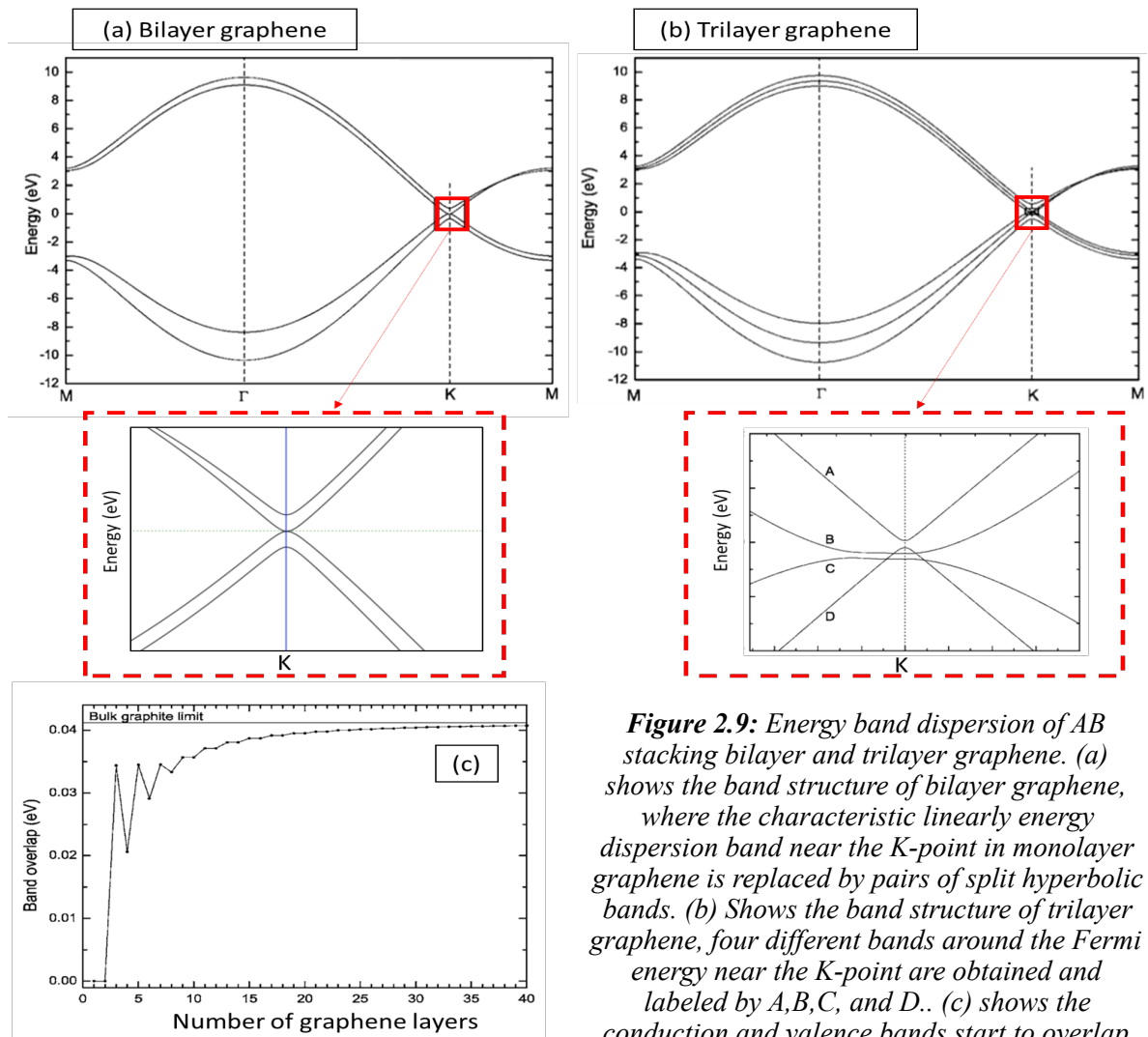


Figure 2.9: Energy band dispersion of AB stacking bilayer and trilayer graphene. (a) shows the band structure of bilayer graphene, where the characteristic linearly energy dispersion band near the K-point in monolayer graphene is replaced by pairs of split hyperbolic bands. (b) Shows the band structure of trilayer graphene, four different bands around the Fermi energy near the K-point are obtained and labeled by A, B, C, and D. (c) shows the conduction and valence bands start to overlap for a trilayer graphene, and the band overlap increase as number of graphene layer increases. Figure adopted from reference ^{18,63}.

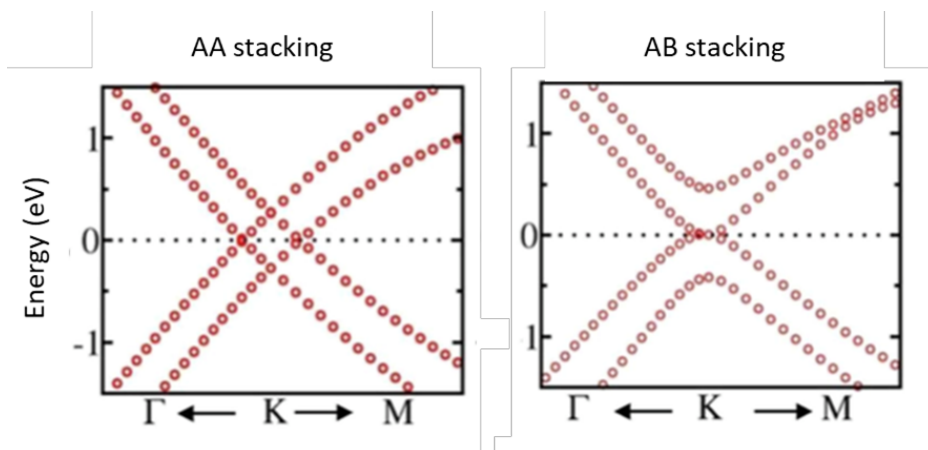


Figure 2.10: shows electronic band structure of AA and AB bilayer graphene. Figure adopted from reference ⁵⁸.

2.3. Characterising graphene using transmitted electrons

Due to the short de Broglie wavelength of accelerated electrons, the interaction between electron and graphene is very sensitive, thereby providing a platform to characterise the thin material. Transmission Electron Microscopy (TEM) is one of the most used electron-probe based technique to visualise and characterise a thin specimen. The formation of a TEM image involves three steps: (1) Electrons interact with the specimen; (2) formation of a diffraction pattern in the back focal plane of an objective lens; (3) formation of an image in the image plane. To describe the general case (of arbitrary specimens), each of the above steps requires a sophisticated mathematical and computational treatment that is outside the scope of this thesis, so the sections below will only introduce the basic concepts that are used in this project.

I. The interaction between electrons and the specimen

It is convenient to categorise electron scattering events into elastic and inelastic scattering components.

i. Elastic scattering

Elastic scattering means that the electron energy loss is minimal and negligible in the experimental system. Elastic scattering arises due to the interaction between the incident electron and the electrostatic field of atomic nuclei. Since the difference in rest mass (m_0) of a nucleus is thousands of times larger than the incident electron, the energy transfer is

usually negligible. In the classical point of view, the attractive Coulomb force between the electron and the nucleus can cause the electrons to travel with a hyperbolic trajectory; the electron would travel straight past the nucleus if there were no interaction between them.

1) *Electron scattered by a single atom*

A general approach to describe the scattering is to consider the incident electron beam as an undisturbed plane wave with amplitude $\psi_{in} = \psi_0 e^{ik_0 \cdot z}$. When the plane wave travels through a single atom with electrostatic potential V_r , the scattered wave can be approximated as a spherical wave $\psi_{sc} = \psi_0 f(\theta) \frac{e^{ikr}}{r}$. The transmitted wave ψ_{Tr} , is described by the superposition of the incident plane wave and the scattered spherical wave, as ⁶⁶:

$$\psi_{Tr}(r, \theta) = \psi_{in} + \psi_{sc} = \psi_0 [e^{ikz} + f(\theta) \frac{e^{ikr}}{r}] \dots (\text{equation .2.6})$$

, where z and r are the distance from the origin, the wavenumber k is related to the energy of incident electron (E_{in}), expressed as $k \equiv \frac{\sqrt{2m_e E_{in}}}{\hbar}$, where m_e is the effective mass of electron. For elastic scattering, the incident and scattered electron have the same energy ($\Delta E = E_{in} - E_{scr} = 0$). In the stationary state, the intensity of each beam can be obtained by the probability density: $I = |\psi(r, \theta)|^2 = \psi \psi^* = |\psi|^2$. The scattered amplitude $f(\theta) = |f(\theta)| e^{i\eta(\theta)}$ is complex, the probability of scattering in a given direction θ . $\eta(\theta)$ is the phase shift index induced by the presence of electrostatic potential of atom (V_r) as a function of θ .

2) *Electron scattered by crystal*

Here we consider the incident plane wave $\psi_{in} = \psi_0 e^{ik_0 \cdot z}$ scattered by a crystal, where the electrostatic potential is V_r is arranged periodically. ψ_{in} is either transmitted or scattered (reflected) into spherical waves by this periodic potential. The scattered waves interfere with each other and give rise to a standing wave causing a periodic charge density

vibration within the crystal. Bloch's theorem in solid state physics is used describe the wavefunction of electrons in the periodic potential environment, known as a Bloch wave^{39,66}. The Bloch waves interfere when they exit the crystal and form an electron diffraction pattern at the back focal plane where constructive interference occurs for the Bragg condition ($2d_{hkl}\sin(\theta_B) = n\lambda_{electron}$). Therefore, the diffraction pattern carries important information about the geometry of the crystal structure and is equivalent to the reciprocal lattice of the crystal as mentioned in section 2.1^{39,66}.

However, since most of crystals have more than one diffracted beam, direct formulation of the transmitted beam intensity can be complicated and requires solving an eigenvalue problem with the help of computer simulation (many-beam problems)⁶⁶. The two-beam case is often introduced to clarify the discussion. The two-beam case considers only the direct (transmitted) and one diffracted beam (reflection g). The transmitted beam intensity (T) can thereby be derived from dynamical theory using the two-beam case approximation. The normalised transmitted beam intensity (T) in the Bragg condition can then be expressed as⁶⁶:

$$T = \frac{I_{tr}}{I_{in}} = 1 - R = 1 - \psi_g \psi_g^* = 1 - \sin^2\left(\frac{\pi t}{\xi_g}\right) \dots (\text{equation .2.7})$$

, where I_{in} and I_{tr} are the incident and transmitted beam intensity respectively, thus T was mentioned as the normalised transmitted beam intensity; R is the normalised reflected beam intensity; ξ_g is extinction distance of the reflected beam; t is the thickness of sample where the absorption of Bloch wave is neglected⁶⁶. As seen in equation 2.7, the intensity oscillates between the transmitted and Bragg-reflected beam as the sample thickness increases, known as "Pendellösung oscillations" in dynamical theory⁶⁶. The extinction distance (ξ_g) is defined as the distance of one periodicity of the Pendellösung oscillation⁶⁶.

ii. Inelastic scattering

Unlike elastic scattering where the electron kinetic energy and momentum are conserved, in an inelastic scattering event, part of the electron kinetic energy is converted into atom-electron excitation (the energy loss of the incident electron is referred to as ΔE). Different atom-electron excitation mechanisms can be distinguished as:

1) Excitation of oscillations in molecules / phonon excitations in solids

These excitation mechanisms cause electron energy loss in the range of $\Delta E = 20 \text{ meV}$ to 1 eV . The excitation can also be observed in the infrared part of the electromagnetic spectrum, which is of considerable interest for molecular and solid-state physics but can only be observed after monochromating the primary electron beam, which is difficult to achieve using conventional electron microscopy ⁶⁶⁻⁶⁸.

2) Collective oscillations

The energy loss caused by the excitation of outer atomic electrons give rise to collective oscillations (plasmons) of the valence and conduction electrons and often referred as plasmon losses. Most of plasmon losses are in the range of $\Delta E = 3 \text{ eV}$ to 25 eV , depending on the concentration of valence and conduction electrons and are analogous to optical excitations from visible to ultraviolet region ⁶⁶⁻⁶⁸.

3) The ionisation of core electrons in inner atomic shells.

Atomic electrons can be excited from an inner shell to an unoccupied energy state above the Fermi level with a material-dependent ionisation energy E_I . The incident electron suffers a loss of kinetic energy by energy $\Delta E \geq E_I$ due to the energy transfer. Spectroscopic features are observed in the spectral range that is a few eVs higher than the E_I , which are caused by excitation of inner atomic electrons to the higher energy bonding states. Thus, the energy-loss spectrum in this region provides information about the bonding states of a material, which are an indicator of the structure and composition ⁶⁶⁻⁶⁸.

II. Application of TEM in graphene characterisation

i. Electron diffraction

As mentioned in section 2.1, the reciprocal lattice of graphene is hexagonal. A single crystal graphene region is expected to have a six-fold symmetry for its diffraction pattern. This is experimentally demonstrated via the normal incidence selected area electron diffraction (SAED) ⁶⁹ (see figure 2.11(a)). In comparison, the diffraction pattern will exhibit a series of relatively oriented six-fold symmetry diffraction spots for a polycrystalline or misoriented region (see figure 2.11(b)).

Hernandez et al. and Meyer et al. have proposed a method to identify monolayer or bilayer graphene using the normal incidence SAED patterns ^{14,70}. Their experimental work showed that in the monolayer graphene, the inner $\{10\bar{1}0\}$ diffraction spots are more

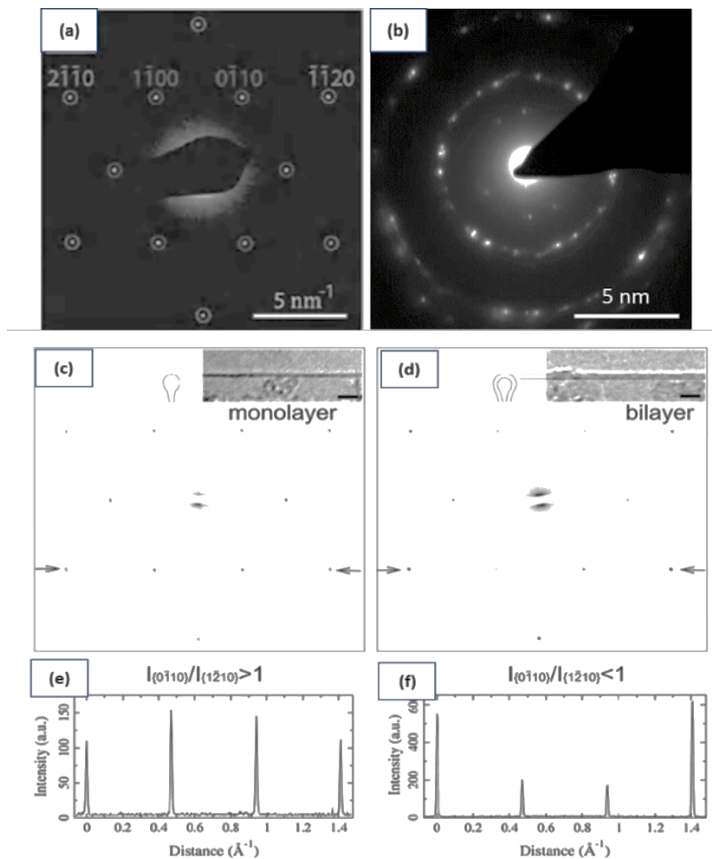


Figure 2.11: Shows electron diffraction of graphene. (a) SAED pattern of single crystal graphene. (b) SAED pattern of polycrystalline graphene. (c) and (e) SAED pattern of monolayer graphene showing a $I_{(1100)}/I_{(2110)} > 1$. (d) and (f) SAED pattern of bilayer graphene, which showing a $I_{(1100)}/I_{(2110)} < 1$ ^{14,70}.

intense than the outer $\{11\bar{2}0\}$ spots (see Figure 2.11 (c) and (e)) and the relative intensity is reversed for the bilayer graphene (see Figure 2.11 (d) and (f)). These findings are consistent with the computational studies of AB (Bernal)-stacked multilayer graphene, suggesting that the intensity ratio $\frac{I_{\{10\bar{1}0\}}}{I_{\{11\bar{2}0\}}} < 1$ is a multilayer region, but the ratio becomes

larger than 1 for monolayer graphene⁷¹. Thus, assuming graphene samples retain the AB stacking from the graphitic precursor, one can identify a graphene monolayer from the intensity ratios of the diffraction peaks. Nevertheless, this thickness identification method can be ambiguous when the graphene is multilayered or polycrystalline or does not have AB stacking configuration. Therefore, an unambiguous identification method for the number graphene layers is still needed^{14,70}.

ii. Image contrast

Rubino et al.³⁴ proposed utilising TEM (bright-field) image contrast to estimate the thickness of a graphene flake. By quantifying the intensity difference between the direct and transmitted beam, information about graphene thickness can be obtained³⁴. The method takes the absorption of Bloch waves into account, so that the relation $T + R = 1$ shown in equation 2.7 will no longer be valid. This means the amplitude of the Pendellösung oscillations will decrease with an increase in specimen thickness^{34,72,73}. According to the two-beam approximation, it was suggested that the transmitted intensity decreases linearly as a thin sample thickness increases, expressed as³⁴:

$$T(t) = \frac{I_{tr}}{I_{in}} = \frac{1}{4} \left[4 - 4 \left(\frac{2\pi t}{\xi'_0} \right) \right] = \left(1 - \frac{2\pi t}{\xi'_0} \right) \dots (\text{equation .2.8})$$

,where ξ'_0 is the mean absorption distance and the term $\frac{\xi'_0}{2\pi}$ was defined as the material dependent absorption constant for electrons. Since equation 2.8 is derived from the two-beam approximation, it may not be applicable for a graphene sample oriented in such a

way that it exhibits six diffracted beams. Rubino et al. therefore tilted the graphene sample away from the zone axis and used a small objective aperture to approximate the two-beam case, and experimentally tested the analytical equation 2.8.

Figure 2.12 (a)-(d) shows the experimental work presented by Rubino et al.³⁴. The six-fold electron diffraction pattern of graphene at zone axis was minimised to the two-beam case with a 7-degree sample tilt. With the graphene thickness obtained by the folded edge method (see chapter 3), Rubino et al. experimentally demonstrated the intensity of transmitted beam decayed linearly as sample thickness increased (for thickness <30nm). The experimental result was further compared to the simulation work, showing that the experimental data obtained at the 7-degree tilt agreed well with the JEMS computer simulation and the analytical equations. However, the JEMS simulation suggested that the transmitted beam intensity decays faster under zone-axis orientation due to the additional diffraction intensity losses from the (100) reflections.

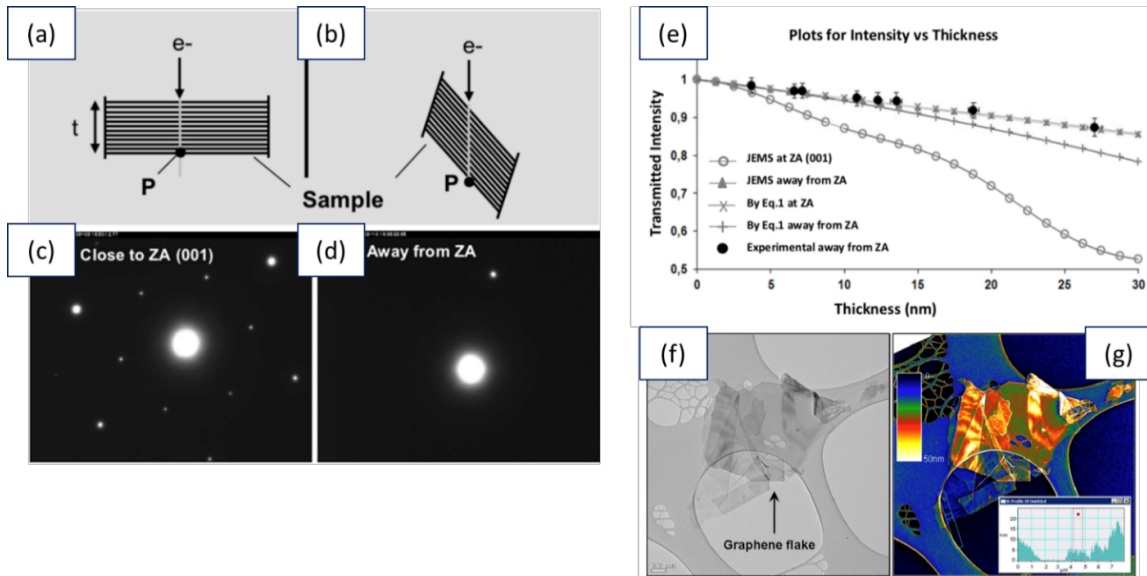


Figure 2.12: Schematic of multilayer graphene crystal orientation with high (a) and low(b) symmetry orientation. P is the exit point of the electron beam and t is the thickness of the sample. (c) and (d) show the experimental SAED patterns close to the high and low symmetry orientations respectively. (e) compares the experimental data and simulation results. The experimental data (black solid circles) obtained by measuring transmitted intensity with known graphite thickness from the bright-field TEM image. The simulation results were obtained by JEMS software in a high/low symmetry orientation. The analytical equations for transmitted intensity derived were derived from the two-beam case approximation, where both the non-sample tilt and sample tilt condition were calculated, denoted as “” and “” respectively. (f) shows a bright-field TEM image of a graphene flake. (g) shows the corresponding thickness map obtained using the method proposed. The figure adopted from³⁴.

Finally, the mean absorption distance (ξ'_0) for graphene was experimentally obtained from the slope of the graph of transmitted beam intensity versus graphene thickness. This was used to generate a thickness map of a graphene flake from the Bright-field TEM image, as seen in figure 2.12 (f) and (g).

iii. High-resolution imaging

As mentioned in equation 2.6, the phase of incident electron beam will be shifted by the electrostatic potential of specimen atoms. The information about the phase difference can be extracted by high-resolution TEM (HRTEM), so producing atomic resolution images of the presented structure ^{66,74}.

In 2008, Meyer et al. studied the formation and dynamics of topological defects in graphene ^{45,75}. They experimentally showed the involvement of the in-plane C-C bond rotation that formed and healed the Stone–Wales (SW) defect in graphene ⁴⁵. Chuvilin et al. further used HRTEM to visualise the edge configuration of graphene, where they experimentally observed a zig-zag edge can be spontaneously reconstructed to an alternative pentagon-heptagon (5-7) edge configuration ⁵³, shown in figure 2.13.

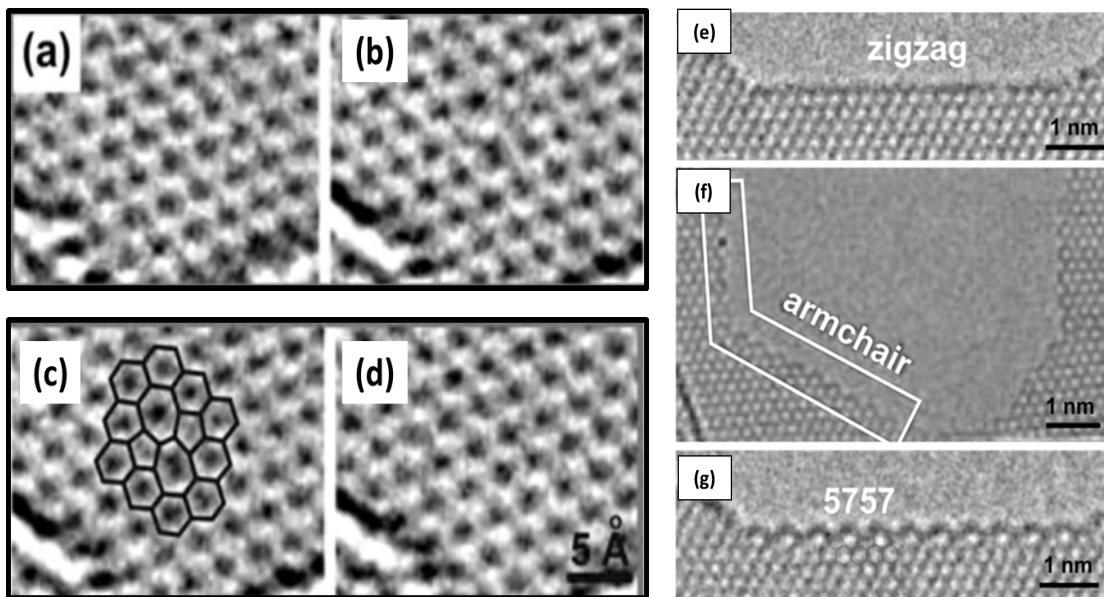


Figure 2.13: Example HRTEM Images of graphene atomic configuration around defects and edges. (a) unperturbed graphene lattice. (b) Stone–Wales defect with the atomic configuration highlighted in ; (c) (d) graphene lattice after relaxation ⁴⁵; image of a zigzag (e) and armchair edge (f); (g) shows an image of a reconstructed zigzag edge, showing pentagons and heptagons ⁵³.

iv. Dark-field imaging

A TEM dark-field image is formed by solely diffracted beams selected by the objective aperture. The diffracted beams carry information about crystal structure, and can be used to identify crystalline regions with a specific crystal orientation as well as structural imperfections such as planar defects, misoriented grains which appear bright in a dark-field image ⁶⁶.

Na et al. and Kim et al. utilised the Dark-field (DF) imaging technique to acquire the grain structure of graphene from the SAED diffraction spots ^{76,77}. Huang et al. further utilised the technique to collect complete maps of the grain orientation ⁴⁸, which showed that CVD grown graphene had a mean grain size of ~250 nm with complex shapes. The reconstructed orientation map also demonstrated a preference of low-angle grain boundaries with a tilt angle of ~7°, and high angle grain boundaries with ~30° tilt angles ⁴⁸.

Not only the grain structure of graphene, but the topological defect distribution can be studied by DFTEM technique. It has been shown that the topological defects in graphene can cause deformation of the basal plane ⁷⁸, where deformation appears as bright spots in a dark-field TEM image ⁷⁹⁻⁸². This provides the possibility to study the spatial distribution and concentration of graphene defects.

v. Electron energy loss spectroscopy (EELS)

EELS measure the transmitted electron energy loss due to inelastic scattering between the incident electrons and the atoms of the specimen. An EELS spectrum plots the relationship of transmitted electron intensity vs energy loss (ΔE). Since the transmitted electrons have the possibility to travel through the specimen without losing energy, a zero-loss peak (ZLP) is apparent in an EELS spectrum. As for electrons that have interacted with the specimen, energy loss can be caused by the collective plasmon oscillations of outer

electron clouds or single electron excitation, corresponding to the plasmon and inner-shell excitation features in the low-loss and core-loss regions respectively. The intensity of these features is dependent on the probability of the corresponding events occurring in a specimen ^{66,67}.

The low-loss EELS spectrum is in the region below 50eV, containing the ZLP and the plasmon peaks. The plasmon loss originates by the formation of a backward attraction force (correlation holes): the oscillation of weakly bound electron clouds, resulting in alternating positive space charge void along the electron trajectory that drags the moving electrons. Since the outer electron clouds play an important role in a material's dielectric property, such information can be extracted by analysing the plasmon loss peaks ^{66,67}.

The plasmon loss of graphene is dominated by two distinctive peaks at 4.9 eV and 15.3 eV, corresponding to the collective oscillation of the π and $\pi + \sigma$ electrons clouds and is lower than the corresponding features observed for a three-dimensional graphite structure (i.e. at 7eV and 27eV) ⁸³. Lu et al. utilised a momentum resolved technique to obtain the band structure of monolayer / few layer graphene. It was found that the π plasmon peak dispersed linearly near the K point for monolayer graphene, while a parabolic dispersion was obtained in graphite ^{84,85}. Wachsmuth et al. studied the plasmon structure evolution from three-dimensional graphite to two-dimensional graphene, suggesting the extra out-of-plane oscillation mode in graphite could be the reason for variation in peak shape and peak position ⁸³.

The core-loss region of the EELS spectrum ranges from 50eV to several thousand electron volts depending on the specimen material. Compared to the plasmon excitation, the probability of the core electron excitation event occurs much lower, resulting in much lower intensity compared to the plasmon peaks in the low-loss region. Since the core-loss region corresponds to be the electrons of atomic electrons in inner shells to the conduction band, the spectrum can be used to identify the element and the chemical bonding present in the specimen ^{66,67}.

The carbon K-edge spectrum of sp^2 carbon materials has been extensively discussed. As shown in Figure 2.2, the transition from carbon inner shell electrons to the unoccupied π^*

anti-bonding electron states gives rise to the π^* peak around 285eV in carbon K-edge spectrum, whilst excitation to the unoccupied σ^* (p) anti-bonding electron state produces a σ^* peak around 290eV. The π^* and σ^* features are less defined in an amorphous or defective graphene/graphite due to its poorer sp^2 bonding structure^{86,87}. Zhang et al. proposed a comparison method based on analysing the σ^* and π^* peaks to quantify the sp^2 bonding content in a specimen^{86,87}. Mironov et al. further suggested that the residual peak intensity between the σ^* and π^* peak originates from non-planar sp^2 bonding⁸⁸. Both methods were used to characterise graphene in this thesis and are introduced in the next chapter.

2.4. Characterising graphene using photons

The concept “photon” can be seen as a quantised electromagnetic wave. Similar to the electron-specimen interaction introduced earlier, the scattered photon can be divided into elastic and inelastic scattering components when interacted with material. For elastic scattering, the energy is conserved between incident and scattered photon. For inelastic scattering, the incident and scattered photons carry different photon energy. Since the incident photons interact with the outer shell electron cloud of a material in the visible energy region (1.7eV ~3.18eV), the scattered photon could provide information about part of the electron band structure of the material. Thus, it is a useful tool for material characterisation.

As introduced in section 2.1, the pristine graphene has a unique band structure and electrical properties. It is possible to extract the information from the photon that has interacted with graphene and use it for graphene identification. The reflection spectroscopy and Raman spectroscopy are two of the most commonly used techniques that collect information from elastically and inelastically scattered photons respectively. The photon-based techniques provided a comparably convenient and efficient way to identify/

characterise graphene and the basic theories and application will be introduced in this section.

I. Elastic scattering: electromagnetic wave in conductive material

Assuming the electric field of an incident photon is oscillating with angular frequency ω , the electric field vector can be expressed as:

$$\mathbf{E} = E_0 e^{i\omega\tau} \dots (\text{equation 2.9})$$

Since graphene is a conductive material, it is reasonable to consider \mathbf{E} incident to a conductive medium, the current density per unit cross section area (\mathbf{J}) is:

$$\mathbf{J} = \frac{\sigma(\omega)}{t} \mathbf{E} \dots (\text{equation 2.10})$$

, where t is the thickness of the thin conductive medium and $\sigma(\omega)$ is the material conductance. Maxwell's equation states that ⁸⁹:

$$\nabla \times \mathbf{H} = \mathbf{J} + \frac{\partial \mathbf{D}_0}{\partial \tau} = \frac{\partial \mathbf{D}}{\partial \tau} \dots (\text{equation 2.11})$$

, where \mathbf{H} is the magnetic field in the medium, \mathbf{J} is the current density in equation 2.10, $\mathbf{D}_0 = \epsilon_0 \mathbf{E}$ and $\mathbf{D} = \epsilon_0 \epsilon_r \mathbf{E}$ are the electric displacement fields for vacuum and medium respectively. Substituting equation 2.10 in equation 2.11 yields:

$$\frac{\sigma(\omega)}{t} \mathbf{E} + i\omega \epsilon_0 \mathbf{E} = i\omega \epsilon_0 \epsilon_r \mathbf{E} \dots (\text{equation 2.12})$$

In which the relative dielectric constant (ϵ_r) can be expressed as:

$$\epsilon_r = 1 - i \frac{\sigma(\omega)}{\omega \epsilon_0 t} \dots (\text{equation 2.13})$$

The refractive index \mathcal{N} is defined as ^{89,90}:

$$\mathcal{N} = \sqrt{\epsilon_r} = \sqrt{1 - i \frac{\sigma(\omega)}{\omega \epsilon_0 t}} = n + i\kappa \dots (\text{equation 2.14})$$

, where n represents the real part of refractive index and κ is the imaginary part of refractive index. Equation 2.14 shows a relationship between electrical conductance $\sigma(\omega)$ and the refractive index \mathcal{N} as a function of incident electromagnetic wave frequency ω . Using such a relationship, the refractive index of graphene can be obtained from its electrical conductance.

i. The refractive index of monolayer graphene from optical conductance

As seen in equation 2.13 and 2.14, the conductivity of a material is closely related to its optical properties. For convenience, the optical conductivity is defined as the frequency-dependent electrical conductivity $\sigma(\omega)$ present in the visible light region (ω_{vis} , between ~ 400 to ~ 800 THz). In monolayer graphene, only the $\pi - \pi^*$ band can contribute to the real part of optical conductance, due to the energy bandgap of the $\sigma - \sigma^*$ band at the Γ point being estimated to be ~ 6 eV, which is larger than visible photon energies (for $\lambda = 550$ nm, the photon energy is estimated to be 2.6 eV). Thus, the effect of $\sigma - \sigma^*$ band transition is not considered and only the $\pi - \pi^*$ transitions are considered to contribute to the optical response of graphene ^{91,92}.

For the $\pi - \pi^*$ transition, the optical conductance can be expressed as:

$$\sigma_{\pi-\pi^*}(\omega) = G_{r1}(\omega) + iG_{i1}(\omega) \dots (\text{equation . 2.15})$$

,where the real part $G_{r1}(\omega)$ arises from the $\pi - \pi^*$ transition near the K point, while the imaginary part $iG_{i1}(\omega)$ is formed by the $\pi - \pi^*$ transition near the M point ⁹⁰. The real and imaginary part of the optical conductance of graphene monolayer was reported by A. B. Kuzmenko et al., to be ⁹³:

$$G_{r1}(\omega) = G_0 \left[\frac{1}{2} + \frac{1}{72} \frac{(\hbar\omega)^2}{\xi^2} \right] \times \left(\tanh \frac{\hbar\omega + 2\mu}{4k_B T} + \tanh \frac{\hbar\omega - 2\mu}{4k_B T} \right) \dots (\text{equation 2.16})$$

$$G_{i1}(\omega) = G_0 \left[\left(\frac{\mu}{\hbar\omega} \frac{4}{\pi} \left(1 - \frac{2}{9} \frac{\mu^2}{\xi^2} \right) - \log \frac{|\hbar\omega + 2\mu|}{|\hbar\omega - 2\mu|} \left(\frac{1}{\pi} + \frac{1}{36\pi} \frac{(\hbar\omega)^2}{\xi^2} \right) \right) \right] \dots (\text{equation 2.17})$$

, where $\xi = -b$ is the nearest-neighbor hopping parameter ($\sim 3eV$) for the p_z orbital in the tight-binding model, μ is the chemical potential with respect to the Dirac point, $k_B T$ is the thermal energy and $\hbar\omega$ is the incident photon energy. G_0 is the universal conductance of a monolayer graphene near the K point, which has been calculated to be ⁹⁴⁻⁹⁶:

$$G_0 = \frac{\pi}{2} \cdot \frac{e^2}{h} = \frac{e^2}{4\hbar} \sim 6.08 \cdot 10^{-5} (\Omega^{-1}) \dots (\text{equation 2.18})$$

,where e is the electron charge and h is the Planck constant. Considering a pristine monolayer graphene (chemical potential $\mu \approx 0$) at room temperature ($T = 300K$), perturbed by an incident photon with 550 nm wavelength, the optical conductance of graphene can be calculated to be: $G_{r1}(\omega) = 1.016G_0$ and $G_{i1}(\omega) \sim 0$, which is nearly identical to the universal conductance (G_0), expressed as:

$$\sigma_{\pi-\pi^*}(550nm) \approx 1.016G_0 \approx G_0 \dots (\text{equation 2.19})$$

, the result has been experimentally tested by A. B. Kuzmenko et al. which shown a fairly accurate value in visible wavelength region ⁹⁷.

By knowing the optical conductance of graphene ($\sigma_{\pi-\pi^*}(550nm)$), the refractive index of monolayer graphene ($\mathcal{N}_{graphene}$) can be obtained by applying G_0 to equation 2.14. Using

$\sigma_{\pi-\pi^*}(550nm) \approx G_0$ and $\omega = 2\pi c/\lambda$, with $c = 3 \times 10^8$ (m/s) is speed of light, $\lambda = 550nm$ is the incident photon wavelength and assuming the thickness of monolayer graphene is $t = 0.3$ nm, equation 2.14 becomes:

$$\mathcal{N}_{monolayer\ graphene}(550nm) = \sqrt{\epsilon_r} = \sqrt{1 - i \frac{\sigma(\omega)}{\omega \epsilon_0 t}} = \sqrt{1 - i \frac{G_0 \lambda}{2\pi c \epsilon_0 t}} = 1.97 - 1.69i \dots (eq. 2.20)$$

As one can see from equation 2.19, the optical conductance per atomic graphene layer remains constant, while in equation 2.20, the refractive index of graphene depends on the thickness of graphene, which can be interpreted as an increased optical response as atomic density increases ^{89,90}.

ii. Previous studies of the refractive index of graphene

Although the optical properties of graphene have been studied and discussed since its discovery, the refractive index of graphene has not yet been well understood ^{17,98,99}. The reason for this might be due to the fact that theoretical calculations consider graphene as a perfect pristine 2D material, while the effect of edges, defects or multiple layers may be present in experiment work. Indeed, the derived optical conductance in equation 2.19 and the refractive index discussed above are all based on the linear dispersion of the $\pi - \pi^*$ band structure near the K point, which could be no longer valid for multilayer graphene or thin graphite materials ^{100,101}.

Several groups have experimentally obtained the refractive index of graphene using different techniques. Ni et al. utilised reflection spectroscopy and determined that a monolayer micro-mechanical cleavage graphene sample has a refractive index of $\mathcal{N}_{monog} = 2.0 - 1.1i$ ⁹⁸. M. Bruna et al. obtained a different wavelength-dependent refractive index of $\mathcal{N}_{monog} = 3.0 - iC\lambda$ using both reflection and transmission ¹⁷. Nelson et al. directly obtained the real and imaginary part of the refractive index using spectroscopic ellipsometry, showing a wavelength dependent refractive index on a large-

area polycrystalline CVD graphene ($\mathcal{N}_{monog} \sim 2.7 - 1.3i$ at 633nm) ⁹⁹. Therefore, it appears difficult to determine the genuine value of the refractive index of graphene at this stage. It can only be concluded that the real part of \mathcal{N}_{monog} can range from ~ 2 to 3 and is not currently a good method to use when trying to precisely determination of the thickness of graphene.

iii. Application: identify graphene by reflection spectroscopy

By knowing the refractive index of graphene, the reflection or transmission intensity of a graphene sheet can be estimated and has been used to identify graphene under the optical microscope ^{20,90,98}. In fact, an interferometer substrate was designed to enhance image contrast of graphene based on the calculated refractive index. The method is widely used for manufacturing graphene nano-devices ¹⁰².

To further improve the usability of the reflection spectroscopy, Ni et al. tried to quantify the variation in the reflection spectrum for different graphene layer thicknesses. As shown

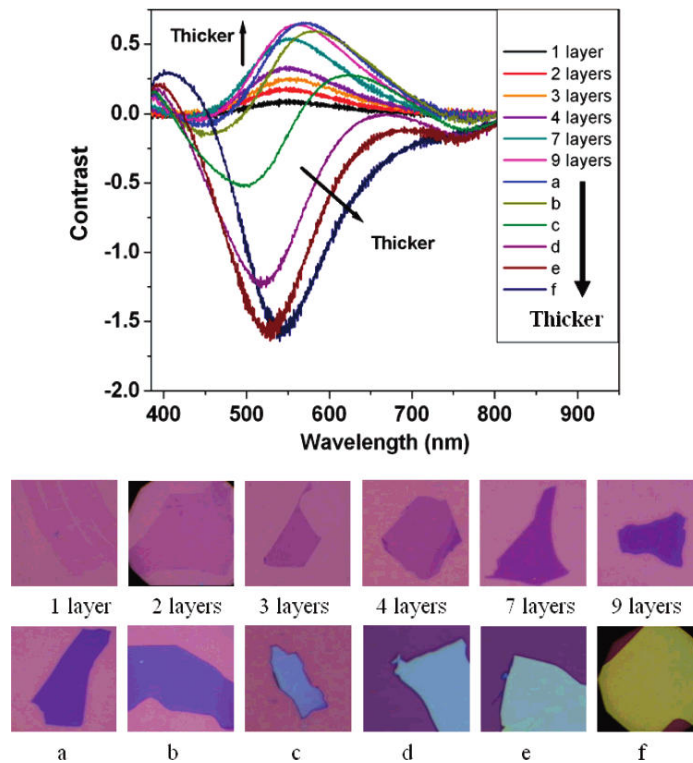


Figure 2.14: shows the contrast spectra of graphene sheets with different thickness, together with the optical images of all samples. a-f are samples > 10 layers and the thickness increase from a to f. The arrow shows the trend of curve in terms of the thickness of graphene sheets. (graph from reference ⁹⁸)

in figure 2.14, thin graphene sheets exhibited transparent purple-blue images, while thick graphene sheets started to reflect more light and appear bright-blue or yellow image. However, a quantitative method based on the graphene reflection spectrum has not been fully appreciated by the community. This is due to a lack of a standardised quantitative protocol to measure the thickness of graphene by the reflection spectrum, the colour/contrast of a graphene image thus often varies from one laboratory to another ⁹⁸.

II. Inelastic scattering of photons: the Raman effect

Raman scattering is where incident photons are inelastically scattered by phonon (i.e., quantised lattice vibrations). For small momentum transfer ($\mathbf{q} \rightarrow 0$), the scattering is known as a first-order Raman process and the selection rules is expressed as ^{39,103}:

$$\omega' = \omega \pm \omega_q ; \mathbf{k}' = \mathbf{k} \pm \mathbf{q} \dots (\text{equation .2.26})$$

, where ω and \mathbf{k} are the photon frequency and momentum respectively, the label ' denotes the scattered photon. The vector \mathbf{q} is the momentum of the phonon and ω_q is the phonon frequency. Due to the participation of phonons in the inelastic scattering process, the frequency of scattered photons is shifted in comparison to the incident photon. Thus, the \pm indicates the frequency of scattered photon is up-shifted or down-shifted by the effect of phonon, which are referred to as anti-Stokes and Stokes scattering respectively.

The Raman spectrum is a plot of the scattered intensity I_q as a function of phonon frequency shift ω_q in units of (cm^{-1}). Thereby, the centre of a Raman peak gives the natural phonon frequency (ω_q) for a specific vibrational or rotational mode in the lattice. The width of the Raman peak provides information about phonon lifetime; inharmonic vibrational modes in the lattice, which could be due to the presence of lattice disorder, cause a shorter phonon lifetime and wider peak. Therefore, combining information collected from the Raman peaks, the spectroscopy technique is a useful tool to characterise the chemical or structural properties of a material in detail ¹⁰³.

i. Vibration modes of monolayer graphene

The phonon dispersion is the key to explain the Raman spectra of graphene. Figure 2.15 shows the theoretical in-plane phonon dispersion relation of monolayer graphene. The out-of-plane vibration ZA (acoustic) and ZO (optical) are not plotted in the graph due to the fact that they are not active in the commonly observed region ($1000\sim 3200\text{ cm}^{-1}$). The remaining four in-plane vibrations modes are as shown in figure 2.15, which correspond to: TA (transverse acoustic), TO (transverse optical), LA (longitudinal acoustic), and LO (longitudinal optical) modes. A schematic plot for different phonon vibration modes is given in figure 2.15(b) ⁴⁰.

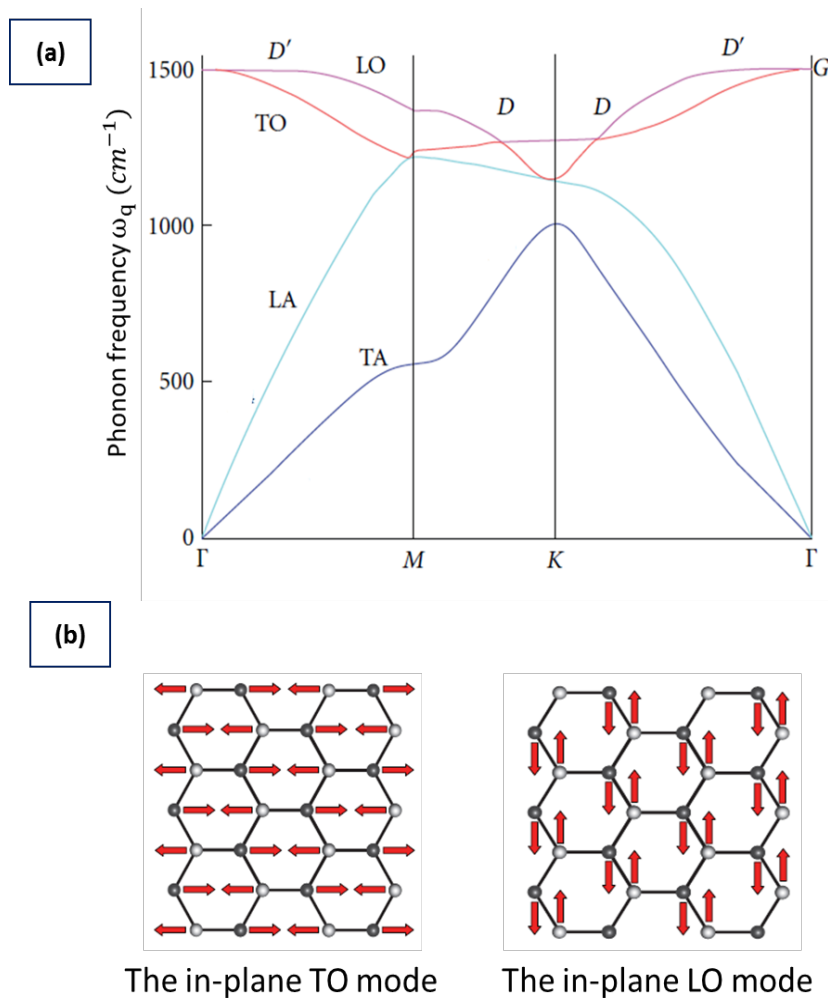


Figure 2.15: Shows the different phonon modes in graphene : (a) the theoretical phonon dispersion of pristine monolayer graphene, the labels (G,D,etc) corresponds the peaks in the Raman spectrum ⁴⁰; (b) shows the predominate phonon vibrations modes in graphene ⁴¹.

The G band

The main first-order Raman feature in graphene is the G band at 1590 cm^{-1} . It originates from the doubly degenerated in-plane TO and LO phonon at the Γ point of the Brillouin zone ($\mathbf{q} \rightarrow 0$)⁴¹, as shown in figure 2.15(a). Although the peak centre of the G band is independent of the number of graphene layers and the excitation laser energy (E_{laser}), the shape of G band can be affected by the presence of strain in graphene lattice. The presence of strain could distort the C-C bond length and its relative angle, breaking the hexagonal symmetry of the graphene lattice which splits the TO and LO phonon frequencies at the Γ point. Therefore, not only the presence of strain but also topological defects such as Stone-Wales defects or dislocations could result in a widening of the G band (FWHM(G))^{104–106}.

The D band

The D band ($\sim 1350\text{ cm}^{-1}$) gives rise to the near-K TO phonons and is activated by the translational-symmetry breaking mode in the crystal^{107–109}. Common reasons for translational-symmetry breaking are sp^3 defects, interstitial atoms, vacancy or edge sites... etc in the sp^2 carbon system^{107–109}. Since the intensity of the D band is sensitive to lattice disorder, the ratio between the D band and G band intensities ($I(D)/I(G)$) is often used to quantify the disorder in a sp^2 carbon material, as discussed in reference^{107–109}.

The 2D band

The 2D band exhibits the highest intensity in the Raman spectrum of pristine monolayer graphene. It originated from the inter-valley double resonance (DR) Raman process and gives rise to an intense peak at $\sim 2690\text{ cm}^{-1}$ ^{21,110–112}. The theory of the DR Raman process in graphene has been extensively studied by A. C. Ferrari et al. and L. M. Malard et al., who suggested that the effect of DR Raman process is enhanced by the unique cone-like electronic band structure in monolayer graphene, and the variation of the 2D peak can therefore provide information about graphene's band structure^{21,110–112}. This effect has been tested experimentally: a single Lorentzian 2D peak is obtained in monolayer graphene, whereas the 2D peak splits into four in bilayer graphene, reflecting the evolution of the band structure^{21,113}. Since the fact that the electronic band structure of

monolayer graphene evolves from the gapless Dirac-cone to a parabolic band as number of graphene layers increases ¹⁸, identifying the number of graphene layers by the variation of 2D peak seems to be possible ^{21,100,110}.

ii. Application of Raman spectroscopy in graphene characterisation

The intensity ratio between the D band and G band (I(D)/I(G)) is usually used to characterise the in-plane structural disorder of sp² carbon. Today, there are two well established models to correlate the I(D)/I(G) to the quantity of disorder in the graphene basal plane, known as: (1) The Tuinstra–Koenig relationship; and (2) The local activation model. The Tuinstra–Koenig relationship was built up as a result of empirical observation between the I(D)/I(G) ratio and XRD data using a series of graphite reference samples. As seen in figure 2.16(a), the model suggests the value of I(D)/I(G) is inversely proportional to the basal-plane crystallite size (coherence length L_a) ¹¹⁴. On the other hand, the local activation model developed by Lucchese et al., where they consider the major contribution of D band is from the zero-dimensional point defects. By studying the I(D)/I(G) ratio variation of a series of Ar+ dosed graphene films (see figure 2.16(b)), they proposed a mathematical relationship between I(D)/I(G) and the concentration of point-defects within a graphene film (i.e., the concentration of point defect (n_D) is depend on the average distance between defects (L_D) with: $n_D \propto \frac{1}{L_D^2}$) ^{115,116}. This model works very well for

quantifying zero-dimensional point defects in monolayer graphene, however, the effect of graphene edges was neglected ^{109,117}. Both Casiraghi et al. ¹⁰⁹ and Cong et al. ¹¹⁷ have shown that the D band intensity can be also affected by the existence of graphene edges. This contradiction implies that a general method that can be used to identify the origin of the D peak enhancement still remains unclear ^{109,118–120}. Difficulty in experimental study is one of the main reasons that a general model remains unavailable. Conventional Raman spectroscopy outputs an averaged spectrum over a probe size of around 1 μm^2 due to the optical diffraction limit ¹²¹. Thus, to study the relationship between D band enhancement and the degree of structural disorder of the material, any experimental study must rely on

empirically measuring a series of graphene/graphite samples ^{114–116}. The recently developed technique of Tip-Enhanced Raman Spectroscopy (TERS) can acquire a spectrum via an improved probe size and can reach ~ 50 nm spatial resolution, which gives the ability to spatially resolve the origin of D band enhancement, but a systematic study on graphene/graphite material is still lacking ¹²¹.

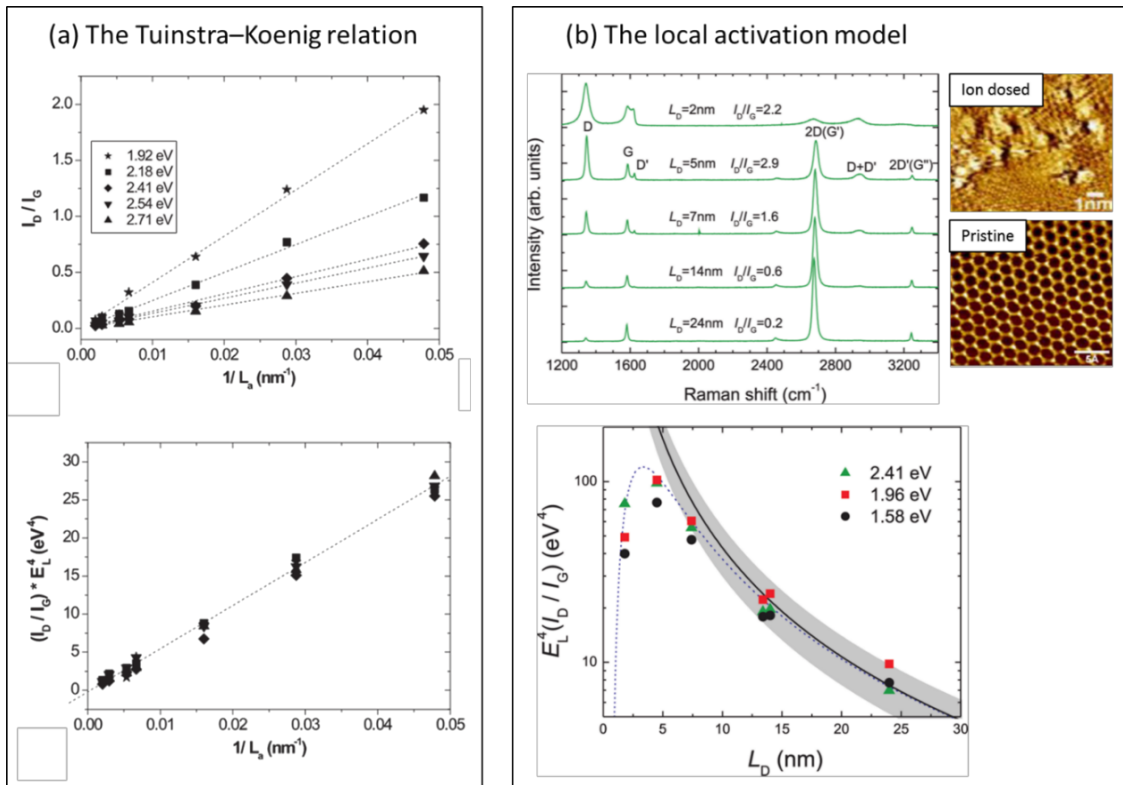


Figure 2.16: shows two well-established models that was used to estimate structure disorder in graphene/graphite. (a) The Tuinstra–Koenig relation developed by correlate the $I(D)/I(G)$ to XRD data from a series of graphite samples ¹¹⁴. (b) The local activation model built up by a series of Ar⁺ dosed monolayer graphene films (see the STM image at inset), the averaged distance between defects (L_D) was controlled by the dose concentration. ^{115,116}

Besides the D band, the 2D band is an important feature to be used to characterise graphene. The shape of 2D peak changes with the number of graphene layers and seen in figure 2.17, A. C. Ferrari et al. L. M. Malard et al. have experimentally shown the evolution of 2D band from monolayer graphene to graphite ^{21,110}, from which numerous literatures have utilised the intensity or the width of 2D peak to identify the number of graphene layers ^{12,13,98,122,123}. Nevertheless, the precision of identifying the graphene thickness is still unknown. Moreover, it has been claimed that the 2D band evolution is based upon a series of AB Bernal stacking graphite/graphene samples ^{21,110}. Thus, it will

only be applicable on samples synthesised by top-down exfoliation, where the AB Bernal stacking configuration may remain, but not necessarily applicable for samples synthesised from the bottom-up methods ^{112,124–126}.

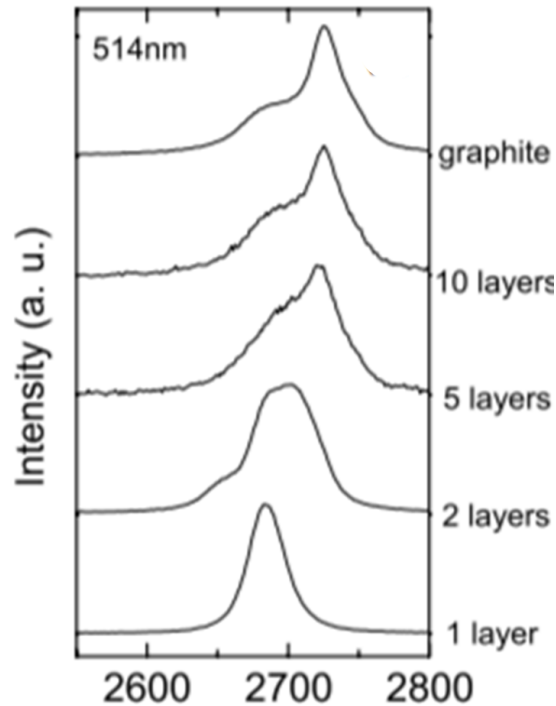


Figure 2.17: Shows Raman 2D peak at $\sim 2700\text{ cm}^{-1}$ from bulk graphite to graphene with intensity scaled to similar height. The 2D peak evolved from single Lorentzian in monolayer graphene to multi-peak composed band in graphite. Spectra were measured with 514 nm laser excitation ^{21,110}.

2.5. The knowledge gaps

As introduced in this chapter, electron probe-based techniques can provide a precise and direct imaging platform to characterise graphene in detail. However, this sensitive technique is limited by its output, which can be challenging for making statistically relevant quantitative data interpretation over large sample areas. On the other hand, photon probe-based techniques provide a less direct method but are a relatively efficient way to characterise graphene. However, the precision and accuracy is yet to be evaluated.

This is because the nanostructural features of graphene are often smaller than the wavelength of incident photon, making the photon scattering event less localised compared to the electron probe-based technique. Therefore, a methodology that can link the observation obtained from the electron probe-based technique to the photon probe-based techniques is critical if a property of graphene are to be determined.

3.

Experimental Methodology and Data Analysis

Based on the fundamental theories of graphene and the characterisation techniques that were reviewed in Chapter 2. The experimental methods and data analysis techniques used in this project are introduced in this chapter. In general, the sample synthesis conditions are introduced in the first section of this chapter. The characterisation techniques used in the project are introduced in the second section, where the data interpretation and the quantification method will be discussed.

3.1. Graphene samples

The top-down cleavage methods involved this project can be categorised into three kinds: (1) Milling in ionic liquid (Milled graphene (MG)), (2) ultrasonic cleavage (Sonicated graphene (SG)) and (3) electrochemical exfoliation (Electrochemically exfoliated graphene (ECEG)). Graphene produced by milling in ionic liquids was provided by 2Dtech™, which was used to develop the characterisation protocol and as a benchmark for the other two samples.

I. The 2Dtech aquagraph graphene sample used as the benchmark for protocol development

Graphene produced by milling in ionic liquids was provided by 2Dtech™. The sample was used to develop the graphene characterisation protocol, also used as a benchmark for the other samples.

The graphene sample was synthesised via exfoliation through milling in ionic liquid. The wet ball-milling exfoliation is based on generating shear forces on raw graphite, initiated by the relative rotation between the milling balls¹²⁷. As seen in figure 3.1, the friction forces between the graphite surface and milling balls induce shear forces when the balls rotate. The shear force breaks the weak van-der-Waals force between the graphite layers.

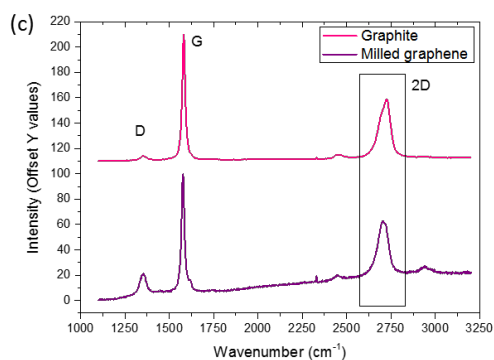
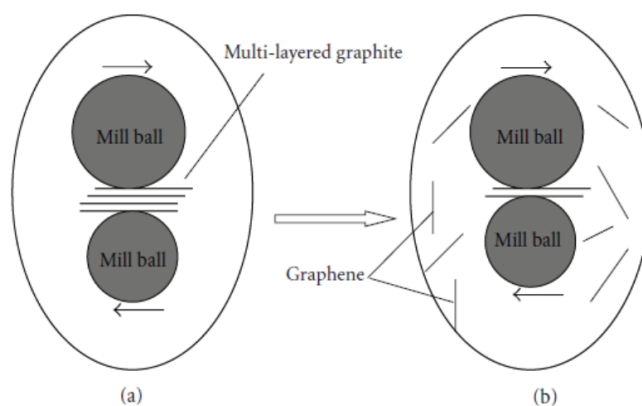


Figure 3.1: schematic illustration of ionic liquid milling for graphene preparation. (a) Illustrates the initial state that graphite powder is dispersed in the solvent. The relative rotation mill balls generate shear forces between the graphite layers^{13,27-29}. (b) Shows the end state in the system that the milling process delaminate graphite into graphene layers with optimised milling energy and time period^{13,27-29}. (c) Shows the Raman spectra of graphite and milled graphene, the blue shift of 2D peak indicates that graphite has been delaminated into multi-layer graphene via the milling process.

Thus, the original graphite can be separated into graphene sheets after milling in such a system for an optimised time ²⁸.

An important factor that effect the direct exfoliation efficiency of graphite in solvents is the suitability between the surface energy of graphite and the surface tensions of solvent ^{14,128,129}. Since the surface tensions of ionic liquids closely matches the surface energy of graphite ^{130–133}, the milling process can be enhanced by using an ionic liquid as the medium, as in the case of the graphene sample from 2Dtech which was synthesised via such milling exfoliation process. The product was sequentially centrifuged to refine graphene suspension from un-exfoliated graphite. Then the graphene was then re-dispersed in Isopropanol alcohol (IPA) for storage and usage.

In this project, the same commercialised 2DtechTM sample is used to develop the graphene characterisation protocol, which will be presented in Chapter 4, Chapter 5 and Chapter 6.

II. Ultrasonic exfoliation (SG)

Ultrasonic sound waves has frequency higher than 20 kHz, which generate cavitation bubbles in liquids. These short-lived bubbles collapsing into high-energy jets and can delaminate the layered material apart ²³⁶. This process can be initiated with a suitable solvent. The mixing process in thermodynamics was often used to interpret the mechanism of ultrasonic exfoliation. The Gibbs free energy change ($\Delta G_{mix} = \Delta H_{mix} - T \Delta S_{mix}$) determines whether the mixing process is initiated spontaneously at temperature T ^{237,238}. A dispersion can be considered to be a mixture between exfoliated graphene flakes and a solvent, the ΔG_{mix} is the Gibbs free energy difference between the unmixed and mixed state. ΔH_{mix} and ΔS_{mix} are the enthalpy and entropy of mixing respectively. A spontaneous mixing requires a negative ΔG_{mix} , which can be achieved by minimising ΔH_{mix} . This is especially critical when the mixture contains large portion of nano flakes (solute), which causes ΔS_{mix} to be small ²³⁸. The enthalpy of mixing has relationship with surface energy as¹⁴: $\Delta H_{mix} \propto (\sqrt{r_s} - \sqrt{r_G})^2$, where r_s and r_G are surface energy of

solvent and graphene nano flakes respectively. Thus, for mono-elemental layered materials like graphene, one of the key factor is choosing a solvent has surface energy close to the material, so there is very little energy difference between the ordered and a dispersed state. The Hansen parameter is related to surface energy, which is often used as the major indicator for selecting a suitable solvent. The Hansen parameter of graphene is 18 Mpa, while the acceptable values for a solvent to exfoliate graphene is between 15 to 21 Mpa^{14,23,131,237-242}. An N-methyl-pyrrolidone (NMP) has Hansen parameter value of 18, thus it was often chosen for exfoliate graphite via sonication in the earlier literatures^{14,237-242}.

In this project, graphite nanoplatelets (GNP) (provided by Cheaptubes™, chemically exfoliated from natural graphite) were used as the starting material. The GNP was then dispersed in Isopropyl alcohol (IPA) (laboratory grade $\geq 99.7\%$ pure). Unlike NMP, IPA is widely available, having a low boiling point and high volatility, and is also a chemically

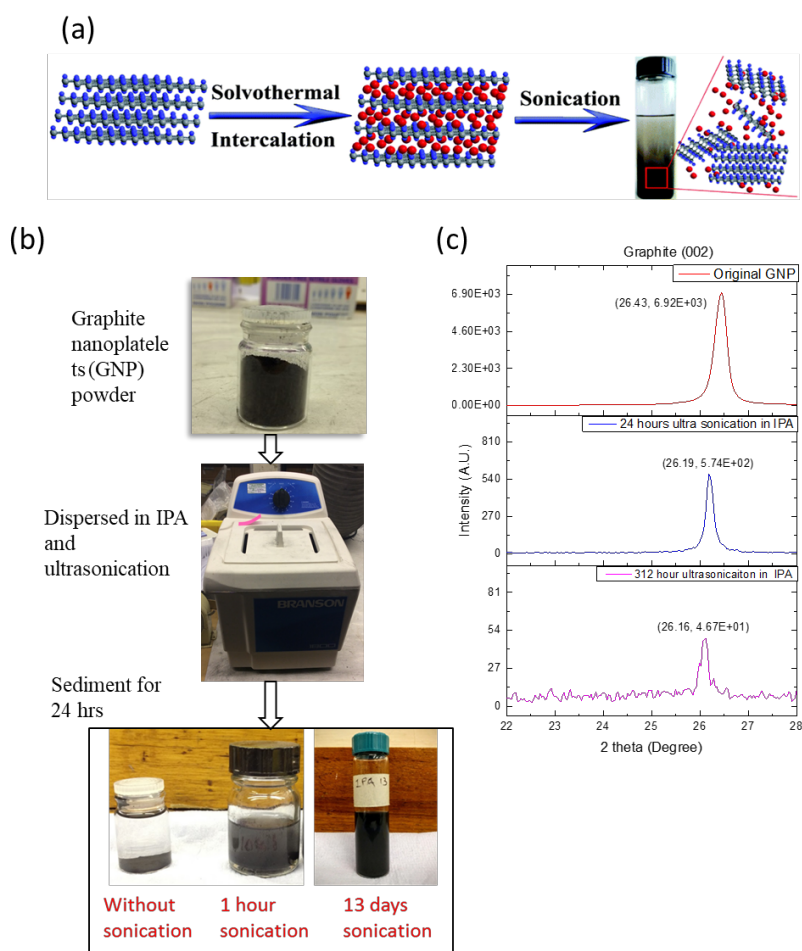


Figure 3.2 : (a) schematic illustration of graphene synthesis via ultrasonication^{131,23}. (b) Picture shows the difference in sedimentation behaviour as a result of sonication (c) XRD shows the effectiveness of ultrasonication, via the shift of the (002) peak.

stable solvent, an advantage for sample preparation and film deposition. Besides, IPA has Hansen parameters of 15.8 Mpa, suggesting the possibility to exfoliate and disperse graphene²³⁷⁻²⁴². After the graphite was dispersed into IPA, an external ultrasonication process was used to overcome the van-der-Waals forces between graphite layers and exfoliate the material into graphene flakes¹²². (Shown schematically in figure 3.2 (a)). The sonication process was performed in a sonication bath (Bransonic 1510), with 40 kHz ultrasound and 80W input power, sonication time was 312 hrs. Figure 3.2 (b) shows a picture of the original GNP powder and sonication bath used in the project.

The sonicated material shown an enhanced dispersion relative to the un-sonicated sample. Figure 3.2 (c) also shows the effectiveness of ultrasonication whereby samples were characterised by X-ray Diffraction (XRD) which revealed that the graphite (002) peak's 2θ position decreased with increasing sonication time, indicating an increase interlayer spacing. The peak Full Width Half Maximum (FWHM) was not used for crystalline size characterisation due to the limitation for characterisation of SAEG discussed in section 3.2, and the detailed discussion is presented in chapter 7.

III. Electrochemical exfoliation (ECEG)

The electrochemical exfoliation utilises a biased potential to drift and intercalate electrolyte anions into a target graphite electrode. The subsequent electrochemical reaction and gas evolution exfoliate graphene sheets from the target graphite electrode.^{6,7,12} Therefore, selecting a suitable graphite electrode and electrolyte are critical. Typically, the target electrode is a graphite rod or highly orientated pyrotytic graphite (HOPG)²⁴⁶. Common electrolytes are aqueous acids (e.g., H_2SO_4 or H_3PO_4) or ionic liquid²⁴³⁻²⁴⁵. However, the exfoliation performed in acidic electrolytes often induced significant amount of unavoidable oxygen-containing functional groups due to the over-oxidation of graphite by the acid. Exfoliation in ionic liquids results a low yield of graphene and the graphene sheets often functionalise with the ionic liquids^{25,243-245}.

In 2014, Parvez et al. performed the electrochemically exfoliated in inorganic salts aqueous solutions, suggesting a 0.1 M (NH₄)₂SO₄ electrolyte can effectively exfoliate natural graphite. In this work, a simple two-electrode electrochemical system was used to synthesis graphene, produced graphene sheets with high carbon to oxygen ratio and low defect density²⁵. Based on this observation, Parvez et al. also proposed a exfoliation mechanism as the following steps : (1) external electric field between the two electrodes drifts the electrolyte anions towards the target graphite electrode; (2) the electric field further intercalate ions into the interlayer spaces in the graphite platelets; (3) the continuously applied static potential overcomes the chemical potential barrier and triggers electrochemical reaction ($\text{SO}_4^{2-}(\text{aq}) + 4\text{H}^+ + 2\text{e}^- \rightarrow \text{SO}_2(\text{g}) + 2\text{H}_2\text{O}$). This gas evolution causes graphene flakes to peel off from the graphite electrode ²⁵.

The electrochemical approach demonstrated by Parvez et al. have shown considerable advantages. With such a simple setup, milligram scale quantities of graphene can be synthesised in the order of minutes, contrary to the chemical/sonication routes which typically need run over periods of several days ^{240,242,246}. Also, the simple method can synthesis few-layer graphene with little structural damage as opposite to the chemically or thermally reduced graphene oxide typically produce graphene sheets with high defect density ^{25,243-246}. Thus, even though the detail exfoliation mechanism is still unclear, the electrochemical exfoliation route has attracted interest from both industrial and academic researchers ²⁴⁶.

Because of the advantages mentioned above, we adopt Parvez et al.'s work for graphene synthesis. A two-electrode electrochemical cell was installed, which consists of a platinum (Pt) cathode and a target graphite anode. The distance between the platinum (Pt) cathode and the target graphite anode was fixed to be 6 cm. The graphite target electrode is made by pressing the nanoplatelets (GNP) material in a 2.54 cm diameter die, with a pressing load of 0.5 ton and hold for 5 minute (shown in figure 3.3 (a)). The GNP material is the same as used in ultrasonication exfoliation, so the effectiveness of exfoliation from both methods can be compared. Similar to Parvez et al.'s work, a 0.1M aqueous ammonium sulphate was used as electrolyte in the electrochemical cell due to its accessibility, low hazard and the effectiveness for graphene synthesis ²⁵. A control circuit

behind the electrochemical cell was designed to monitor the electrical current during the exfoliation process as shown in figure 3.3(b).

With the electrochemical cell setup, a constant electric potential of 10 V was applied to initiate the exfoliation. As the static potential is continuously applied, electrochemical reaction was triggered, generating visible gas bubbles at the interface between electrolyte and the graphite electrode. The graphite electrode was then started to dissociate and disperse into the electrolyte solution, causes a clear change in the electrolyte from colourless to dark after only within a few minutes (~300 seconds) of exfoliation time (See Figure 3.3(c)). The effectiveness of exfoliation can be observed from XRD afterwards. A clear (002) peak change is shown in Figure 3.3(d), indicating a change in crystal size / interlayer spacing after the electrochemical exfoliation.

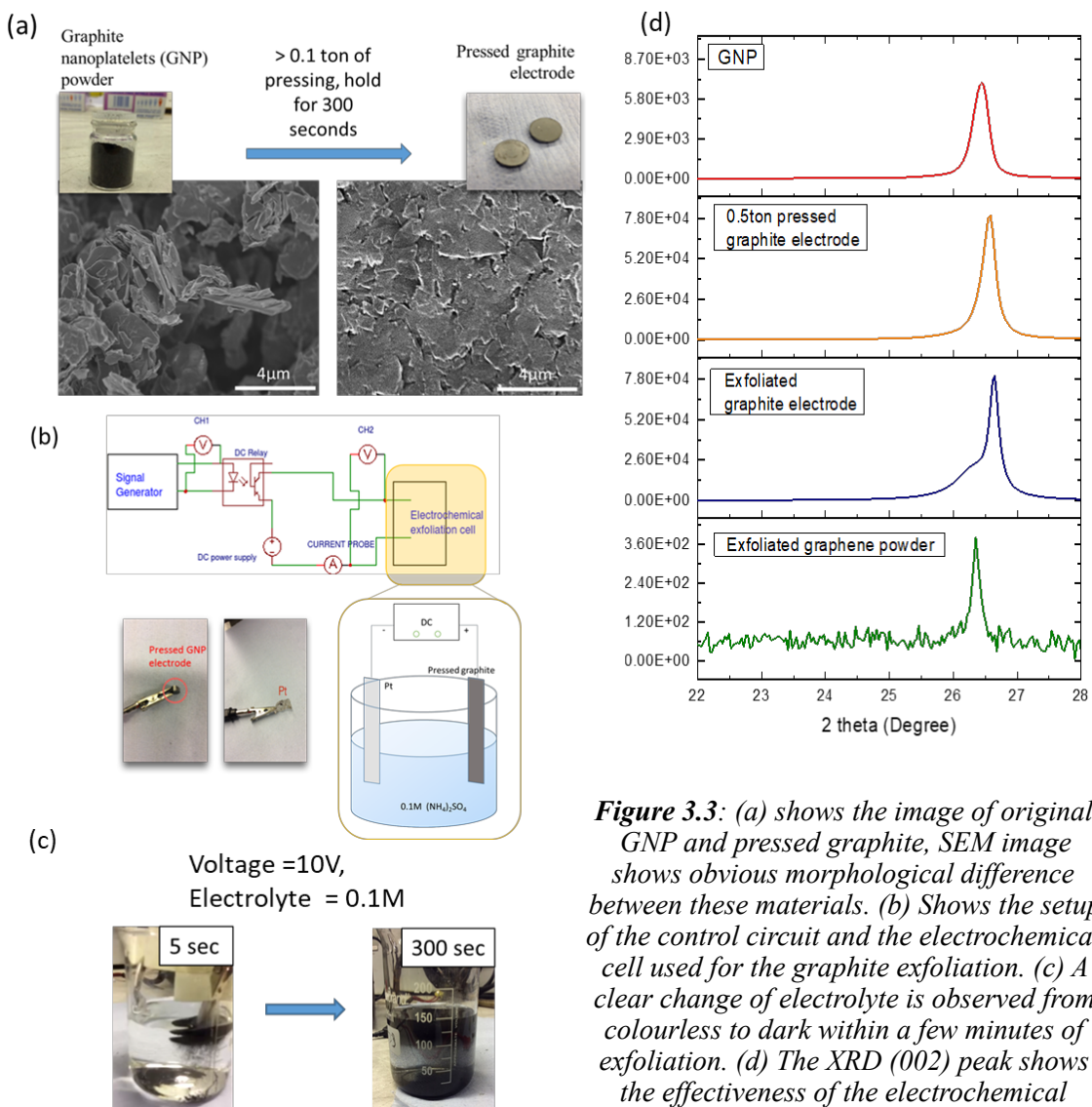


Figure 3.3: (a) shows the image of original GNP and pressed graphite, SEM image shows obvious morphological difference between these materials. (b) Shows the setup of the control circuit and the electrochemical cell used for the graphite exfoliation. (c) A clear change of electrolyte is observed from colourless to dark within a few minutes of exfoliation. (d) The XRD (002) peak shows the effectiveness of the electrochemical exfoliation.

However, a detail electrochemical exfoliation mechanism will not be provided in the thesis. Because the main purpose of this project is developing a practical protocol for graphene characterisation. A detail discussion on the exfoliation mechanism will be out of the scope. Nevertheless, to demonstrate the capability of the graphene characterisation protocol, graphene sample synthesised via electrochemical exfoliation will be compared to other synthesis methods and the detail discussion will be presented in Chapter 7.

Possible improvements for the electrochemical exfoliation experiment

Even though the two-electrode system is widely used to synthesis graphene, the simple system may not be sufficient for studying the mechanism of electrochemical exfoliation. A further in-depth research on the mechanism requires utilise a modern three-electrode system, where the extra electrode is used as reference, so the potential of working electrode can be measured accurately. Also, a detailed pulse response experiment can provide information about the ion-intercalate process. Nevertheless, a full optimisation of the electrochemical exfoliation process is required (i.e. variation in temperature, applied potential, types and concentrations of electrolyte, types of graphite electrode...etc). This process relies on the graphene characterisation protocol to provide a quantitative feedbacks from the exfoliated products. Moreover, in-situ techniques such as Raman spectroscopy can also be used for the real-time determination of crystal disorder of the graphite electrode, identification of gaseous or side-products as a function of various exfoliation condition. However, the application of these techniques to study the electrochemical exfoliation the very early stage²⁴⁶

Sample preparation

After the graphene flakes were exfoliated from graphite, the exfoliated product (a mixture of graphene/graphite and the electrolyte) was collected by vacuum filtration with a membrane filter (110 nm pore size) and repeatedly washed with de-ionised (DI) water to remove any residual salts (Shown in figure 3.4). The collected graphene / graphite was then re-dispersed in 300 ml IPA by a 10min, 40 kHz ultrasonication.

The re-dispersed graphene/graphite suspension was then sedimented for 48 hours, a clear gradient in colour was observable after the sedimentation process. The bottom part of suspensions was discarded due to it was reported to consist of a high concentration of incompletely delaminated graphite chunks ^{23,122,131}. The remaining upper part of suspension was taken for characterisation.

The graphene suspension was then drop-cast onto various substrates such as SiO₂/Silicon wafers or holey carbon coated TEM grid to allow various characterisation techniques to be used (see figure 3.4 (c) and (d)).

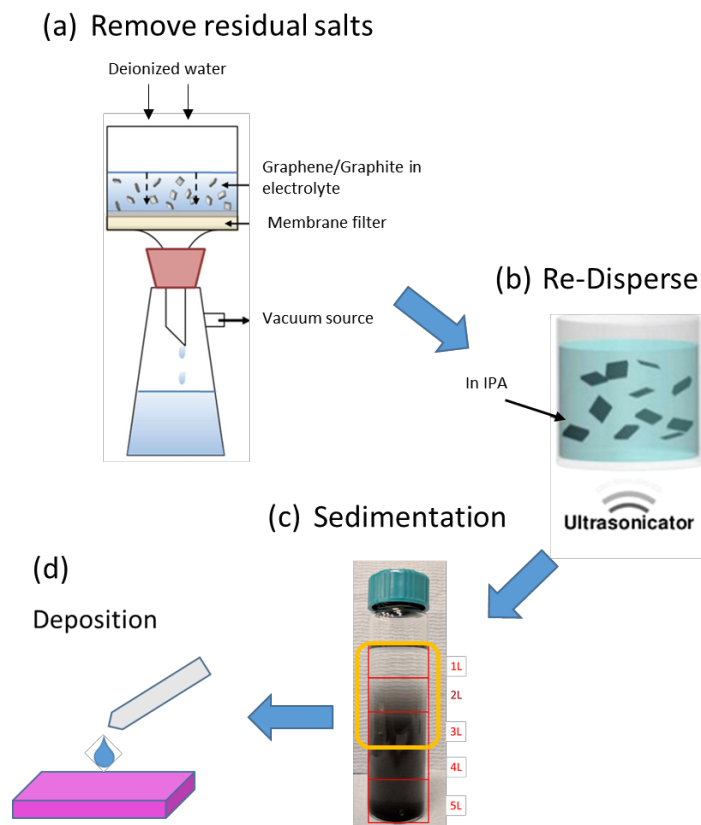


Figure 3.4 shows main process for the fabrication of graphene suspensions. (a) The exfoliated graphene/graphite mixture was washed in D.I water to remove the residual salts via vacuum filtration. (b) The collected products were re-dispersed into IPA by 10min of sonication. (c) The sedimentation process used to remove the unwanted graphite chunks. (d) Deposit the refined graphene suspension for further characterisation.

3.2. Characterisation techniques

The characterisation methods are required to determine the quality of the graphene produced and suitability for the further applications. As mentioned earlier, the focus lies on developing a characterisation protocol that can monitor various properties of graphene, and this section will cover common characterisation techniques that have been used for developing the characterisation protocol for the liquid-assisted exfoliated graphene.

I. X-Ray Diffraction (XRD)

X-ray diffraction is a widely used characterisation method to determine the crystal structure of a material. Owing to the wavelength of X-ray covering the range of lattice spacings of most materials, the incident beam can be reflected by the atoms forming constructive/deconstructive signals at specific angles of incidence. Therefore, the diffraction signal provides a fingerprint of the crystal structure.

In general, a mathematical relationship based on optical path difference is used to describe the relation between diffraction signal and material lattice spacing, known as the Bragg condition:

$$2d\sin(\theta) = n\lambda \dots (\text{equation 3.1})$$

, where d the separation between atomic planes is, θ is the angle between the incident beam and the reflecting plane, λ is the wavelength of the incident beam (Fig.3.5). n is an integer number, which depends on the order of diffraction. Since the combination of different separation of atomic planes are unique to a material, the diffraction technique allows the determination of atomic arrangement and the identification of a particular material.

An ideal perfect infinite crystal should have an extremely sharp diffraction peak without broadening (long coherence length and less variation in lattice spacing). While an amorphous, polycrystalline or a sample that possesses internal strain/stress will display a relatively broad diffraction peak (short coherence length and high variation in lattice spacing). In general, there are two main factors that can result in diffraction peak broadening: instrumental broadening and broadening due to the material itself.

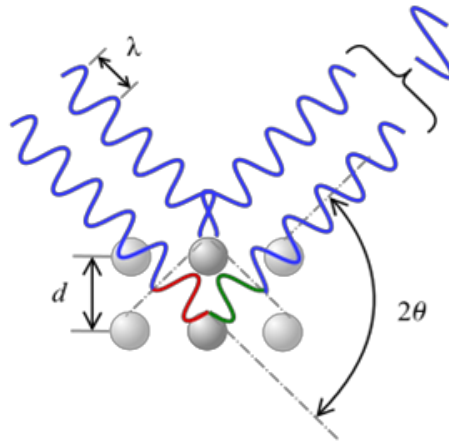


Figure 3.5: a schematic diagram showing the Bragg's diffraction condition. The difference in optical path of reflected x-ray beams will result to constructive or destructive interference

The instrumental broadening can be estimated experimentally using NIST standard reference material 660 LaB₆, since it has no strain and a known crystal grain size larger than 1 μm¹³⁴. Consequently, any diffraction peak broadening can be identified to be instrumental. For a Lorentz shaped peak, the actual broadening (β_{actual}) can be calculated by:

$$\beta_{\text{actual}} = \beta_{\text{measured}} - \beta_{\text{instrumental}} \dots \text{(Equation 3.2)}$$

, where β_{measured} and $\beta_{\text{instrumental}}$ are the FWHM of measured peak and the instrumental peak broadening respectively¹³⁵. However, when the standard NIST method is unavailable, an alternative affordable method was conducted, by measuring an Al₂O₃ standard reference material. The wavelength of X-ray is 0.154nm (CuK_α) operating in 40eV and 40mA, the step size was set to be 0.0333°. The diffraction peaks were refined by Rietveld method¹³⁶, and approached by Lorentz shape. The standard reference material exhibits

FWHM values of 0.09° at 26.2° (002), 0.09° at 57.9° (004) and 0.10° at 67.5° (110), which were considered to be the instrumental broadening.

Once the peak broadening factors were identified, XRD was used to characterise the samples. The position and FWHM of the peak at ~26.5° corresponding to the graphite (002) plane provides information about the graphene interlayer spacing. The peaks at ~42.5° and 45° correspond to the (100) and (110) planes respectively. Broadening of these peaks was interpreted as the shortening of the lateral coherence length (L_a)^{114,137}. However, since the technique relies on a sufficient amount of periodic structure to produce an observable diffraction signal, a low concentration of zero-dimensional point defects will be hardly detected.

Though XRD has been widely used to study the crystal structure of graphite, the application of conventional XRD to an ideal mono / few layer graphene is impractical. This is owing to the thinness of graphene leading to insufficiently observable diffraction peak signal intensity from each crystal plane. The full width half maximum (FWHM) of a diffraction peak will increase as the crystalline grain size decreases, as reflected by Scherrer's equation:

$$\tau = \frac{k\lambda}{\beta \cdot \cos(\theta)} \dots \text{(Equation 3.3)}$$

, where λ is the X-ray wavelength; θ is the Bragg angle; τ is the mean size of the ordered (crystalline) domains, which may be smaller or equal to the grain size; K is a dimensionless shape factor, which varies with the actual shape of the crystallite. $K = 0.89$ was used for the crystal size estimation in [002] direction (L_c) and $K = 1.84$ for the estimation of L_a ¹³⁸; β is the line broadening in radians at half the maximum intensity (FWHM), after subtracting the instrumental line broadening.

Figure 3.6 shows a simulation of the FWHM of (002) diffraction peaks as a function of number of graphene layers. It is clear to see that even for 50 layers of graphite, the FWHM can be as wide as 0.515 degrees, whilst for multilayer graphene (<10 layers), the FWHM

can be wider than 2.805 degrees, making such diffraction signals hard to be identified above the background.

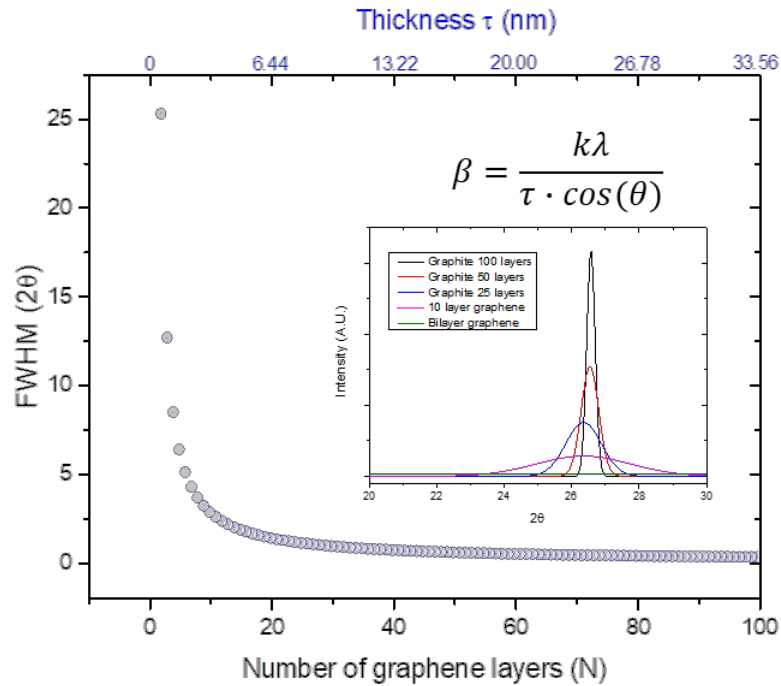


Figure 3.6: shows a simulated curve about the FWHM of the (002) diffraction peak as a function of number of graphene layers. The inset shows the simulated (002) diffraction peak with different graphite/graphene thicknesses

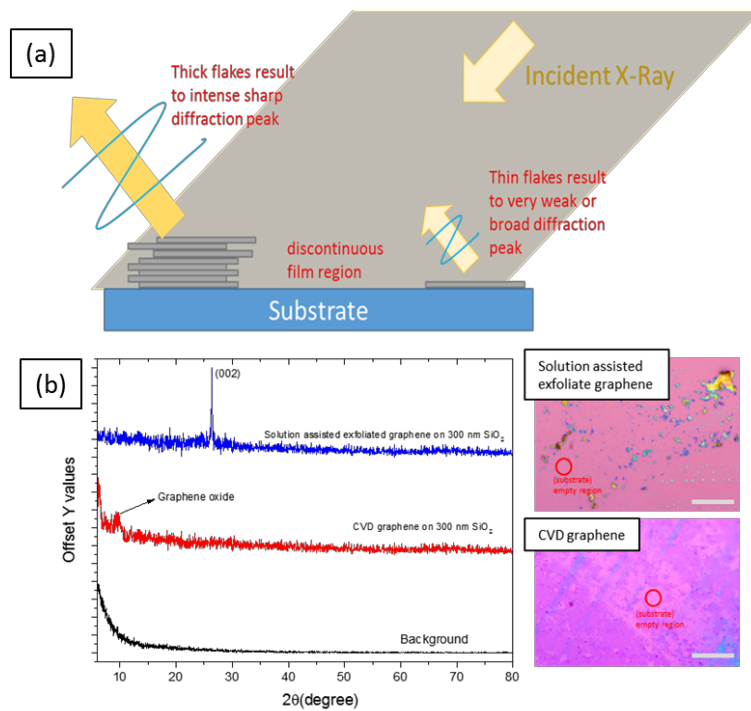


Figure 3.7: shows the limitation of applying XRD to graphene. (a) Schematically showing the cross section of graphene sample on substrate. (b) The experiment XRD results of CVD and solution assisted exfoliate graphene. The OM image shown inhomogeneity of the film surface (blue/purple spots are thin graphene, yellow patches are thick graphite on the pink background, the scale bar is 5μm)

In addition, since the thicker graphite will always have a stronger diffraction peak, estimating the thickness of graphene using XRD will always be biased to a higher number of graphene layers. As schematically shown in figure 3.7, empty / discontinuous regions will always occur when depositing graphene on a substrate for XRD observation and this will weaken the overall diffraction intensity. Although collecting graphene suspensions into graphene powders can strengthen the diffraction signal, where flake re-aggregation cannot be avoided.

In this work, XRD was not used as a major technique to study the thickness of graphene due to the limitations mentioned above. However, XRD played an important role in study of the structure of graphite electrodes used for electrochemical exfoliation.

II. Atomic Force Microscopy (AFM)

AFM is a scanning probe microscopy technique that uses a cantilever and tip to image a sample surface. Seen in figure 3.8 (a), information of sample surface is gathered via the displacement of tip that generates oscillation of the cantilever when the tip interacts with the sample surface. With a highly accurate piezoelectric element and a sensitive beam-deflection detection mechanism, the resolution of this technique can be a thousand times better than the optical diffraction limit.

According to the motion of the tip, AFM can image in one of three modes (see figure 3.8 (b)). The contact mode, also called static mode, in which the tip is "dragged" across the surface of the sample and the contours of the surface are measured using the deflection of the cantilever directly. In the tapping mode, the cantilever is driven to oscillate near its resonance frequency, thus also called intermittent contact or AC mode. The frequency and amplitude of the driving signal of the cantilever oscillation remain unchanged when the tip is uncoupled with sample surface. While an interaction tip and sample causes changes in oscillation of cantilever. Such an information is reconstructed to form the sample image. In non-contact mode, the tip of the cantilever does not contact the sample surface. However, the interaction between tip and sample from long-range force decreases the

oscillation frequency of cantilever, allows softwares to construct a topographic image of the sample surface.

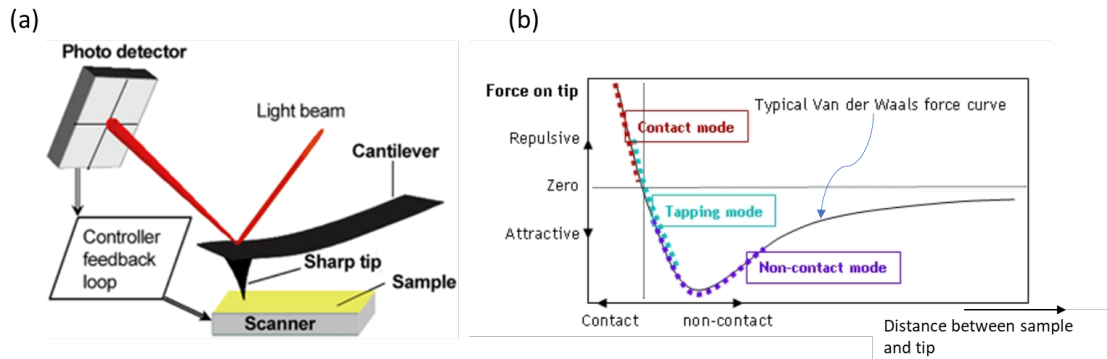


Figure 3.8 : (a) schematic diagram of atomic force microscope. Using beam deflection detection, the displacement of cantilever from the interaction with the sample surface is amplified and detected by the photodiode. (b) shows the intensity of force between sample surface and tip in different imaging modes. (Ref: <https://goo.gl/vRBW8z>)

In this work, the AFM experiment was performed in the Research centre for Applied Sciences, Academia Sinica, Taiwan. The Atomic force microscopy (AFM) imaging was carried out using a JPK NanoWizard III (JPK Instruments AG) operating in the tapping mode under dry conditions. The graphene samples were drop cast onto a 285nm thick SiO₂/Si wafer substrate (the same as in the optical microscope), with a thick glass slide bonded under the substrate to avoid unwanted vibration when interacting with the tip. The tip was manufactured from highly doped silicon (Nano-sensors, Switzerland), having the radius of curvature < 10nm. The spring constant of the cantilever was 42 N/m with a resonant frequency at 330 kHz. A standard dissipation procedure was performed prior to each measurement to avoid unwanted static charge on the tip.

Due to the thinness of graphene, it was very difficult to locate the flake of interest by direct imaging of its morphology. Therefore to locate flakes of interest, a few fast scans operating in tapping mode were used. Also, because of the difference in stiffness between graphene flakes and the substrate, there will be a ~ 20° phase shift when the tip touches the graphene sample (shown in figure 3.9(a) inset). Thin graphene flakes will therefore be more obvious in phase imaging than using height contrast (see the difference in figure 3.9(a)). The AFM was thereafter operated in phase contrast mode to rapidly locate the

region/flake of interest prior to each high resolution measurement. Figure 3.9(b) shows an example image operating at higher resolution using height contrast. The morphology and detail wrinkles of the graphene flakes can clearly be seen. Owing to the accuracy of the piezoelectric stage on the AFM, it allows us to locate the position of graphene flakes on the substrate and therefore the located flakes can also be observed via the optical microscopy technique for comparison (shown as inset in figure 3.9(b)). The detailed comparison between the observation from AFM and optical microscopy will be presented in Chapter 6.

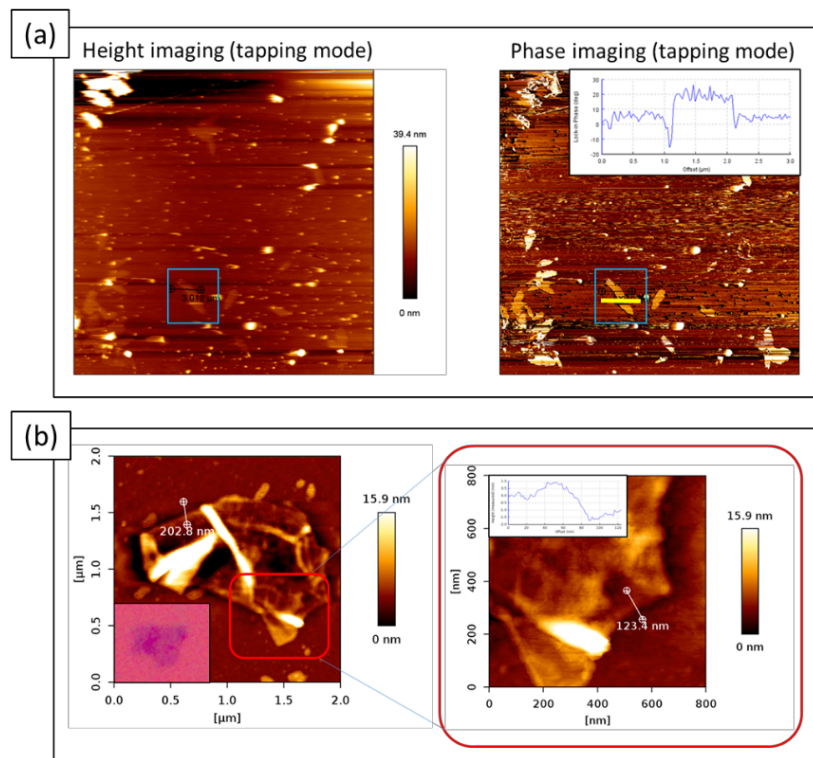


Figure 3.9: AFM image of graphene flakes (a) shows the procedure used to find the flake of interest. The same flake will appear less obvious when operating in height imaging mode (left), while the same flake appears obviously on phase imaging mode (right). (b) The shape of the flake the detail wrinkles can be resolved (inset image shows the same flake under optical microscope).

III. Raman spectroscopy

Raman spectroscopy is a spectroscopic technique widely used to characterise the quality of sp² carbon materials. A typical Raman system mainly consists of Excitation laser,

grating (beam splitter) , Rayleigh filters and Focusing mirror, as schematically shown in figure 3.10. The excitation source is usually provided by laser, produce an intense monochromatic photon beam. The incident photons interacts with the sample, resulting in the energy of the laser photons being shifted, which gives information about the vibrational modes in the system. The scattered photons are collected by a series of lens and refined by a monochromator. Elastic scattered photons with the wavelength corresponding to the excitation laser is filtered out by a filter, while the inelastic scattered photons are dispersed by the grating mechanism, and then collected by focusing mirror onto a detector for analysing (see figure 3.10).

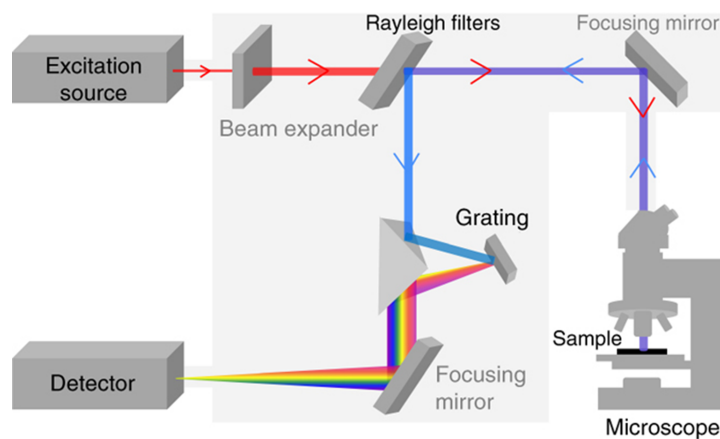


Figure 3.10: Schematically show a Raman system, which typically consists of Excitation laser, Grating , Rayleigh filters and Focusing mirror. (Ref: <https://goo.gl/gDNFc5>)

A Renishaw InVia series Raman spectrometer was used in this project. The excitation laser is 514nm, 20mW, focused by a 50X (N.A = 0.75) objective lens. Figure 3.11 shows the Raman spectrum of a CVD graphene transferred onto a SbO₂/Si wafer substrate. The excitation energy (E_L) independent G band can be observed at $\sim 1590\text{ cm}^{-1}$, related to first-order phonon scattering as expected in sp² carbon, the relative intensity of which reflects the degree of graphitisation ^{41,107}. The D band at $\sim 1350\text{ cm}^{-1}$ is activated by the translational-symmetry breaking mode, which the presence of defects, grain boundaries, functional groups or structural disorder could be the main reason to rise the D band ^{41,107}. Additional features such as D' and D+D' peaks at $\sim 1620\text{ cm}^{-1}$ and $\sim 2940\text{ cm}^{-1}$ are common in highly damaged graphene, which are induced by the presence of a high concentration of point defects or atom vacancies. As introduced in chapter 2, the 2D band

at around 2700 cm^{-1} originates from second-order double resonance Raman process. It exhibited a single Lorentzian peak with highest intensity in pristine monolayer graphene region, contrary to the multimodal broad peak observed in a three-dimensional graphite (see figure 3.11 (b)). Therefore, the 2D band is a signature for monolayer graphene, and has been used to estimate the number of graphene layers up to 10 layers^{21,41,107}. A small peak at $\sim 1450\text{ cm}^{-1}$ was also found in the spectra, this feature did not originate from graphene sample, but from the third order Raman peak of the silicon substrate^{109,141,142}.

As mentioned in Chapter 2, the intensity ratio between D band and G band ($I(D)/I(G)$) is usually used to characterise the in-plane structural disorder of sp^2 carbon. However, a general method that can be used to detail identify the origin of D peak enhancement is still ambiguous due to both of the well-established model have neglected the effect of edge structures^{109,118–120}, which the presence of such crystal disorder could enhance the intensity of D band^{109,117}. This effect can be significant since the graphene samples synthesised by solution assisted graphite exfoliation are focused in the thesis. These synthesis methods

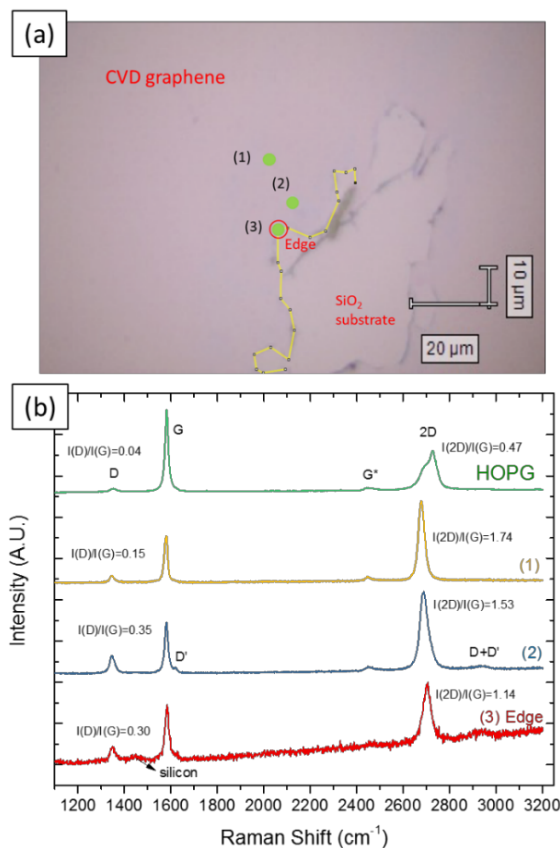


Figure 3.11 : (a) shows the optical microscope image of a CVD graphene deposited on $300\text{ nm SiO}_2/\text{Si}$ wafer substrate. The edges and measured spots are labelled. (b) Shows the Raman spectra measured from the different spots.

usually result to a relatively small lateral size (mean value $\leq 1000\text{nm}$), the effect of graphene edges can therefore be critical and lead to an imprecise estimation of L_a or L_D . Moreover, since a 100X objective lens is unavailable for the Raman system, the laser beam can only be focused into a 3-5 μm laser spot. Therefore, the probe size is generally bigger than the lateral size of graphene in our experiment, the contribution for the D band could not be distinguished. To overcome this problem, I have developed a statistical method to identify whether the contribution of D-band was from flake edges or bulk, in which the detail will be presented in chapter 5. On the other hand, for rapid identification of number of graphene layers, the 2D peak was quantified and used to study the number of coupled graphene layers, in which the result compared with the observation obtained by AFM and TEM, the detail is presented in Chapter 6.

IV. Transmission Electron Microscopy (TEM)

A conventional Transmission Electron Microscopy (TEM) mainly consists of three main components : (1) the electron source system; (2) the electron optics system and (3) image recording system (see figure 3.12).

1) The electron source system

Provide electron source using an electron gun, which may be a tungsten filament or needle. The electron gun is connected to a high voltage source (typically $\sim 100\text{--}300\text{ kV}$), with sufficient electric current, the gun will begin to emit electrons by thermionic or field electron emission into the vacuum.

2) Electron optics system

The electron optics system of a TEM allow for beam manipulation and convergence. This provides the ability to change magnification by modifying the current intensity at the coil, and electromagnetic lenses. A conventional TEM consists of three stages of beam manipulation, using the condenser lenses, the objective lenses, and the projector lenses. The condenser lenses are responsible for primary beam formation, while the objective

lenses focus the beam that have interacted with the specimen. The projector lenses are used to expand and re-construct the transmitted beam onto the phosphor screen or other imaging device.

3) *Image recording system*

Designed to record the formed image. Conventional TEM can direct project image on phosphor screen for observation. However, modern TEM direct project and record images on CCDs, in which the image can be recorded digitally and signal to noise ratio is improved.

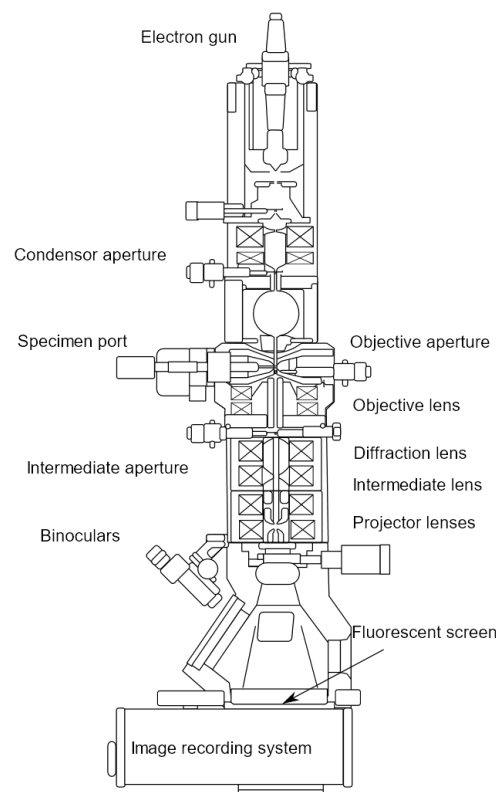


Figure 3.12 : schematically shows the layout of components in a conventional TEM. (Ref: <https://goo.gl/31xDsE>)

Contrast formation

The contrast between two adjacent areas in a TEM image is originated from the difference in the electron densities at the image plane. Due to the scattering / interaction between the incident beam and the specimen, the amplitude and phase of the electron wavefunction is

altered, results in *amplitude contrast* and *phase contrast*. Although most of images consists of both contrast components, one can dominate another in a certain condition. At lower magnifications the image contrast is mainly contributed by different absorption of electrons from the specimen material, which can be due to the difference in material composition (amplitude contrast). At higher magnifications, wave interactions start to dominate and modulate the transmitted electron wavefunction. Thus, the images contrast can be formed by differences in phase of transmitted beams. As such, the image is not only dependent on the number of electrons transmitted, but also the superposition electron wavefunction. Since the sensitivity of phase difference, this effect is an advantage and can provide more structural information about the specimen.

In this project, TEM measurements were conducted using an FEI Titan³ Themis 300 S/TEM operated at 80 kV, which is below the threshold for knock-on damage¹⁴³. Bright-field images were acquired using an objective aperture of 17.9 mrad. Magnifications of 55,000 x and 295,000 x were used for the development of the mean greyscale ratio method (MGVR) and folded edge methods for graphene thickness determination respectively. SAED and EELS measurements were recorded in diffraction mode with a selected area aperture inserted, giving a circular projection on the specimen of

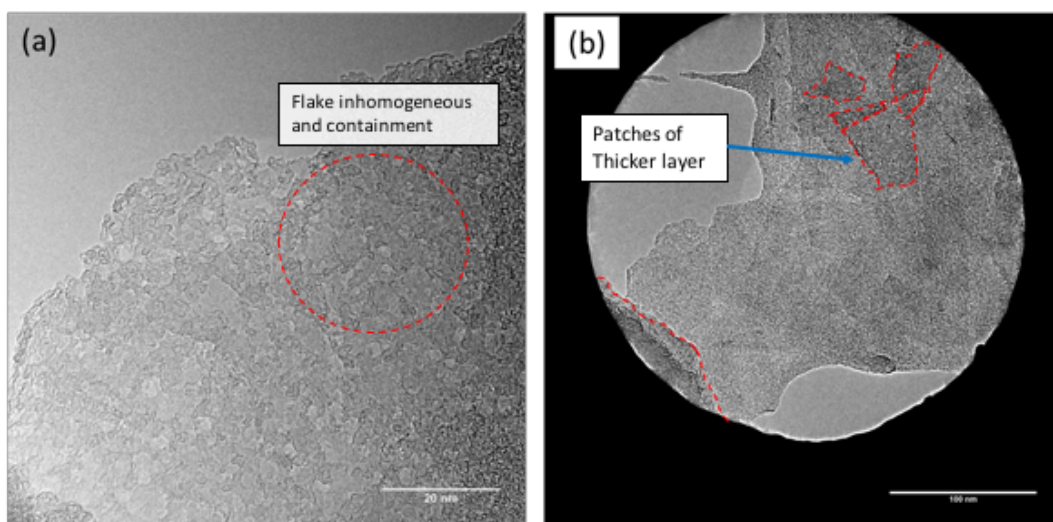


Figure 3.13: Bright-field TEM image of a free-standing graphene flake recorded at 80 kV: (a) the sample region is covered with darker patches of few nanometers, which are assigned as surface containment or incomplete regions. (b) Shows inhomogeneous region relative to the aperture size, where signal from the region with different thickness or flake orientations could be collected. (2DtechTM graphene sample)

approximate radius 100 nm. As seen in figure 3.13, various inhomogeneous patches were present inside the circular projection, indicating the homogeneous regions of the graphene sample were much smaller than the aperture size, leading to each measurement being an average. The flake inhomogeneity was assigned to surface contamination or incomplete delaminated regions, which was unable to be completely controlled or excluded, and could be the major limitation for the precise characterisation.

3.3. Data quantification and interpretation

Quantifying and interpreting data is an important step to link experimental observation to theoretical understanding. In this section, the methodologies used to quantify the experimental data will be introduced.

I. Select Area Electron diffraction (SAED)

SAED patterns were collected together with the bright field microscope images. As introduced in chapter 2, the SAED pattern shows reciprocal lattice of the material, which a single crystal sp^2 carbon region is expected to have a six-fold symmetry for its diffraction pattern. As seen in figure 3.14, the lattice spacings can be measured from the centre to a diffraction spot, which were measured to have lattice spacings of 0.213 ± 0.006 nm ($\{1010\}$ plane) and 0.122 ± 0.004 nm ($\{1120\}$ plane) respectively. As introduced in Chapter 2, the intensity profile can be distinguished between a monolayer or a multilayer graphene by assuming the graphene samples retain AB stacking from the graphitic precursor, (monolayer: $I_{(1100)}/I_{(2110)} > 1$ and multilayer: $I_{(1100)}/I_{(2110)} \leq 1$)^{70,14}.

Polycrystalline regions were also analysed by SAED. Owing to the 6-fold symmetry of graphene lattice, the relative misorientation of graphene grains lay between 0 to 30° can be

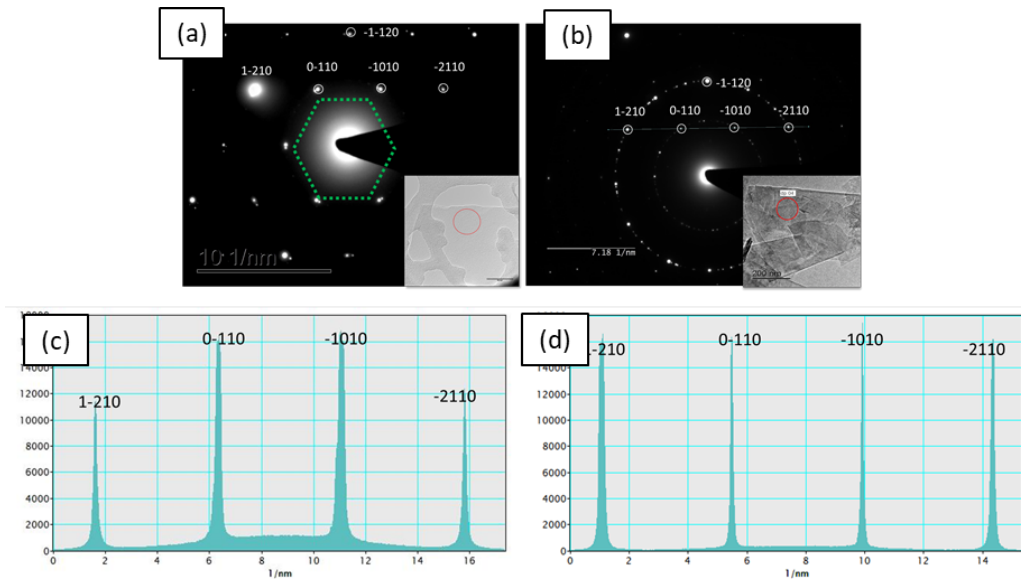


Figure 3.14: Shows the SAED pattern of (a) a monolayer graphene and (b) a multilayer polycrystalline graphene. (c) The diffraction profiles correspond to $\{1010\}$ and (d) $\{1120\}$ planes. (c) and (d) shows the intensity profile along (1100) to (2110). The monolayer layer graphene having an $I_{(1100)}/I_{(2110)} > 1$ profile, while a multilayer graphene shows $I_{(1100)}/I_{(2110)} \leq 1$ as introduced in chapter 2. (2Dtech™ graphene sample)

resolved, a value of $(60^\circ - \theta)$ is measured for orientation angles $\theta > 30^\circ$. Figure 3.15 shows an example SAED pattern of a misoriented graphene region, the intensity profile between the (01) and (10) diffraction spots was plotted and the angle of grain misorientation can be obtained from the intensity profile using well-established peak finding methods. Several

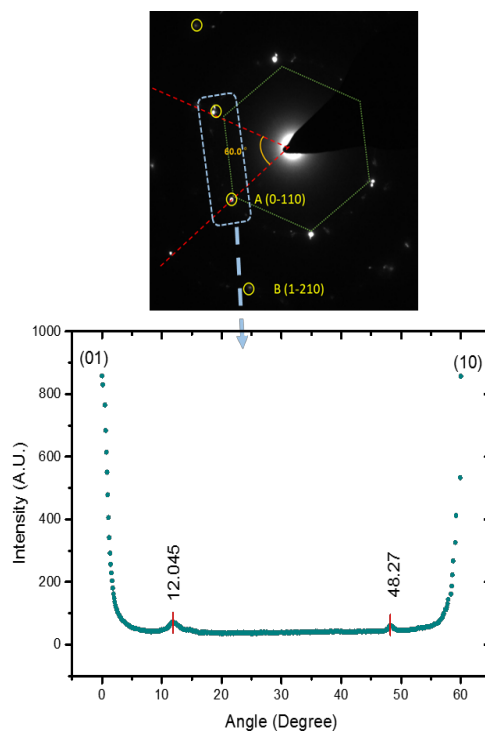


Figure 3.15: The angle of misoriented grains can be measured by analyse the angular intensity profile between the (01) and (10) diffraction spots.

SAED patterns were taken, the grain misorientation angles obtained were measured and studied statistically, and further detail is presented in chapter 5.

II. *Electron Energy Loss Spectroscopy (EELS)*

Electron energy loss spectroscopy (EELS) is a technique analyse the energy distribution of transmitted electrons. An EELS instrumentation is typically incorporated into a TEM (see figure 3.16), which use high energy electrons (60 – 300 kV) to probe the sample material. The Magnetic Prism Spectrometer is the key to obtain the energy distribution of transmitted electrons. The EELS system directed the transmitted electrons into a magnetic prism spectrometer. The magnetic prism spectrometer consists of an electromagnet with magnetic field B perpendicular to the incident electron beam. With the magnetic field, the trajectories of electrons are deflected into a circular orbit due to the Lorentz force. The trajectory of electron can be described with the radius of curvature $R = (\gamma m_0 / eB)v$, where v is speed of transmitted electron; $\gamma = 1/(1 - v^2/c^2)^{1/2}$ is relativistic factor; m_0 is

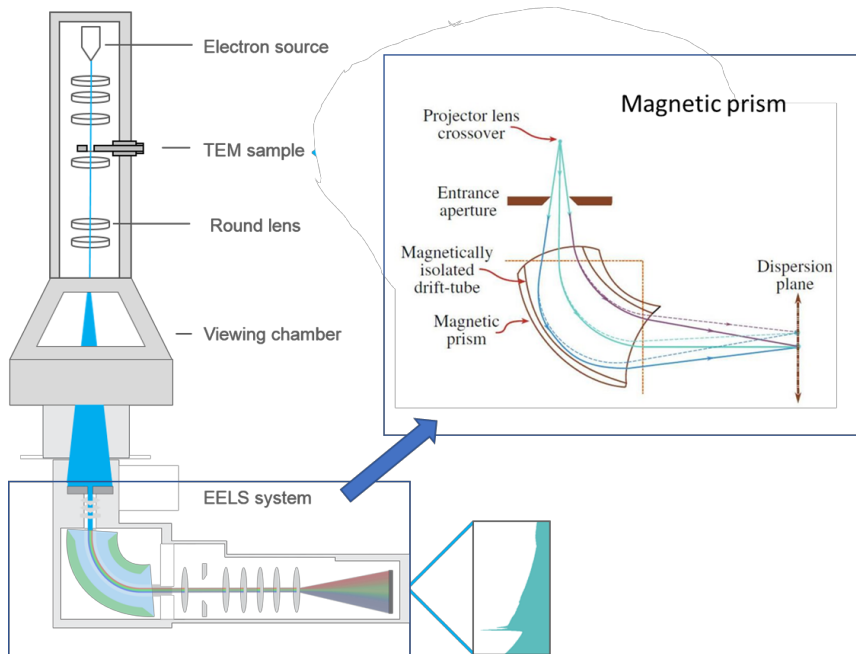


Figure 3.16: Schematically shows the layout of EELS system. The transmitted electrons were sent into a magnetic prism spectrometer, which consists of an electromagnet with magnetic field perpendicular to the incident electron beam. With the magnetic field, the trajectories of electrons are deflected into a circular orbit due to the Lorentz force.

the rest mass of an electron. As seen in figure 3.16, the transmitted electron has been turned by 90° and dispersed by its velocity (v). Since the energy of electrons (E) is related by its velocity by $E = m_0c/(1 - v^2/c^2)^{\frac{1}{2}}$, electrons that have lost higher energy from the specimen have lower energy left, therefore a lower electron velocity (v) and a smaller radius of curvature (R). An energy distribution of the transmitted electrons can be obtained.

The EELS spectra in this project were acquired in the FEI Titan3 Themis 300 S/TEM using diffraction mode and with a selected area aperture inserted. The convergence angle was 1.0 mrad and the incident collection angle was 5.4 mrad. The EELS spectra were measured close to the magic angle¹⁴⁵ in order to remove sample orientation effects. The energy resolution was measured as the full width at half maximum (FWHM) of the Zero-Loss Peak, which was 0.53eV with spectra being recorded with an energy dispersion of 0.025 eV/pixel.

i. Quantify the Low-loss EELS

The probability of an electron being inelastically scattered increases as sample thickness increases, result in the decreased contribution of the Zero-Loss Peak (ZLP) in the whole low-loss spectrum ¹⁴⁶. Therefore, the log-ratio method was used to quantify the variation in the ZLP and hence to estimate the local thickness (t) of a specimen. Here, the relative thickness of the specimen (t_r) can be calculated as ¹⁴⁶:

$$t_r = \frac{t}{\text{IMFP}} = \log\left(\frac{A_t}{A_0}\right) \dots(\text{equation . 3.4})$$

where IMFP (nm) is the inelastic plasmon mean free path, defined as the average distance between inelastic plasmon loss events, t (nm) is the absolute sample thickness, A_t the area under the entire low-loss spectrum and A_0 is the area under the zero-loss peak.

Figure 3.17(a) shows an example low-loss spectrum of a thin graphite flake. To calculate the relative thickness of the sample, the ZLP data was approximated by “logarithm tail model” in GMS3 software, As seen in figure 3.17 (b), the experimental ZLP was filtered over an energy range between 2.0 eV and 4.0 eV, using the logarithm tail model, and the peak intensity, width and integrated area is then obtained from the GMS3 software.

Although the relative thickness of specimen (i.e., $\frac{t}{IMFP}$) can be calculated via the log-ratio method, determination of the absolute thickness t requires a value for the inelastic mean free path (IMFP). The IMFP is dependent on the material properties of the specimen such as atomic number or crystallinity¹⁴⁶, and is also sensitive by the operating conditions (i.e., energy of primary electron beam, collection angle and convergence angles)¹⁴⁶. Egerton et al. has suggested that the log-ratio method is valid for the specimen thickness 4 times larger than the IMFP, but the application to ultra-thin specimens has not yet been evaluated¹⁴⁶. Applying the thickness estimation method to graphene, an ultra-thin material, can test the ability and limitation of the thickness estimation method. The experimental results are presented in Chapter 6.

ii. Quantify the Core-loss EELS

As mentioned in Chapter 2, the core-loss EELS spectra is used to extract information about the crystallinity of the specimen. Zhang et al. proposed a comparison method to quantify the content of sp² bonding in graphite material. They suggested the *planar sp² content* (C_{sp^2}) is proportional to⁸⁷:

$$C_{sp^2} \propto \frac{R_{\text{specimen}}}{R_{\text{HOPG}}} = \frac{\left(\frac{I_{\pi^*}}{I_{\pi^*} + I_{\sigma^*}} \right)_{\text{specimen}}}{\left(\frac{I_{\pi^*}}{I_{\pi^*} + I_{\sigma^*}} \right)_{\text{HOPG}}} \dots (\text{equation 3.5})$$

, where I_{π^*} and I_{σ^*} are the intensity of the π^* and σ^* peak respectively, and R_{HOPG} is the $\frac{I_{\pi^*}}{I_{\pi^*} + I_{\sigma^*}}$ of an HOPG sample.

Zhang et al. and Daniels et al. suggested that the intensity near 287eV raised by the presence of non-six-member rings, caused by distortion in the nearby basal plane ^{86,87,147}. Mironov et al. suggests that the content of the *non-planar sp² is proportional to* ⁸⁸:

$$C_{\text{non-planar sp}^2} \propto \frac{I_R}{I_R + I_{\pi^*}} \dots(\text{equation 3.6})$$

, where I_{π^*} is the intensity of the π^* peak in equation 3.5. the fitting residual between the π^* and σ^* peaks was quantified by two Gaussian peaks: the G1 and G2 peak, the combination intensities is referred as I_R ⁸⁸.

Figure 3.17(c) compares the core-loss EELS spectra between a highly crystallised and a defective graphene region. Quantifying the core-loss EELS spectrum was performed by fitting the experiment spectrum with six Gaussian peaks, as shown in figure 3.17 (d). The π^* peak centred at 285eV, the peak width was constrained to be: 0 eV < FWHM < 0.6 eV. The σ^* peak is centred at 292.8eV, the width was constrained between: 0 eV < FWHM < 1.5 eV. The G1 and G2 peak are used in equation 3.9, centred at 287 eV and 288.7 eV respectively, having peak width between 0 eV < FWHM < 1eV. The G3 peak centred ~ 295 eV and is deemed to be originated from the presence of heteroatom ^{87,88}. Above the G3 peak is the G4 peak, which is raised by multiple scattering resonance peak (MSR) ^{87,88}. Although the G3 and G4 peaks were not utilised in equation 3.8 and equation 3.9, they are fitted to approach the whole core-loss EELS spectra. The G3 peak was set to be centred round 295eV; the G4 peak is higher than 300eV. Both peaks were constrained to have a width between 0 eV to 6 eV. By using the quantification method mentioned above, a high crystalline graphene (HCG) flake with the highest R value in the sample was used as the reference for other graphene flakes, in which a $R_{\text{HCG}} = \left(\frac{I_{\pi^*}}{I_{\pi^*} + I_{\sigma^*}} \right)_{\text{HCG}} = 0.560$ was obtained. For subsequently graphene / thin graphite specimen measurement, the

relative sp^2 containment was calculated as $C_{sp^2} \propto \frac{R_{\text{specimen}}}{R_{\text{HCG}}}$, in which the value R_{HCG} was used as the reference in this project. The experiment results will be discussed in Chapter 5.

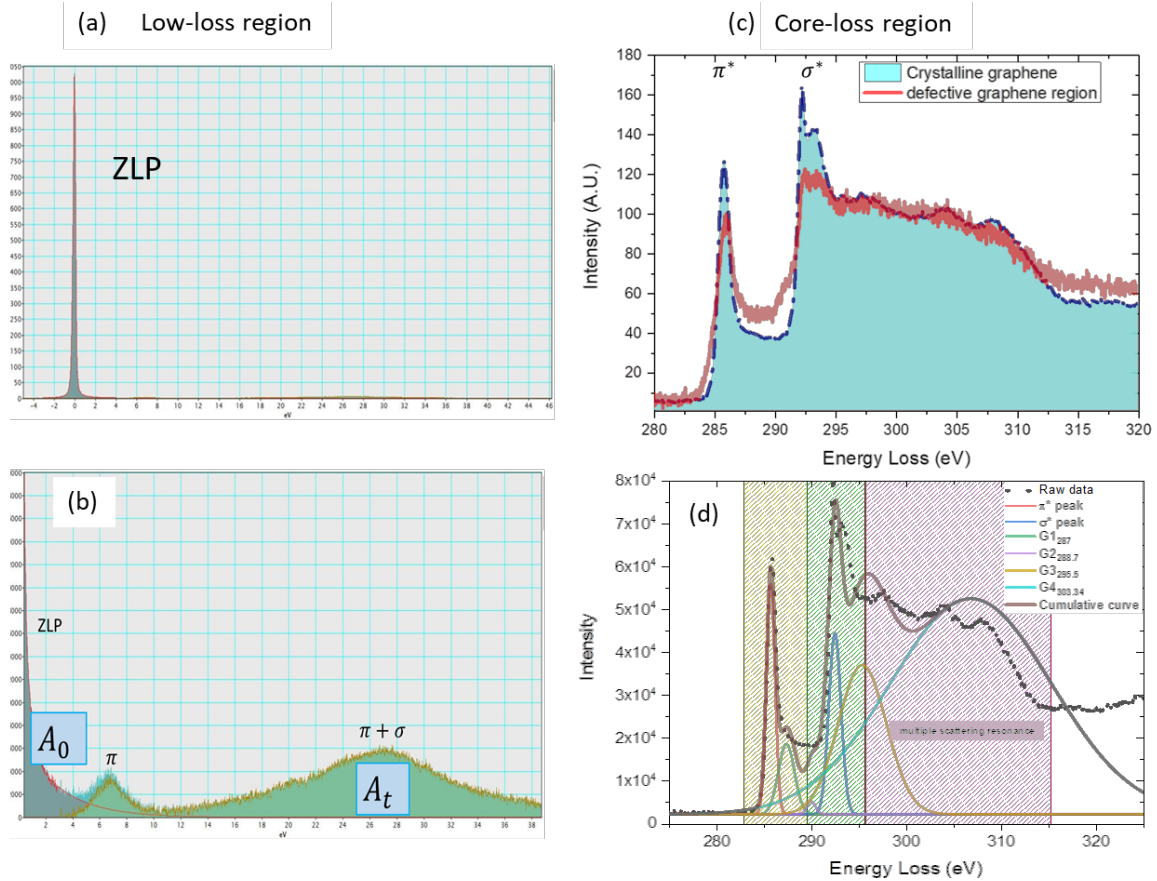


Figure 3.17: Quantify the EELS spectra obtained from thin graphite. (a) and (b) shows low-loss EELS region, where the Zero-Loss Peak (ZLP) is loaded. (b) shows magnified spectra from (a), in which the plasmon peaks became obvious. The ZLP was approximated by the logarithm tail model. A_0 and A_t are the integrated area for ZLP and the total spectra respectively. (c) and (d) shows core-loss EELS region. (c) Compares core-loss EELS obtained from a high crystalline and defective graphene region (spectra are normalised). (d) The core-loss EELS spectra are de-convoluted to six Gaussian peaks. a high crystalline graphene (HCG) flake with the highest R value found in our sample was used as a reference for other graphene flakes, in which a R value was obtained.

III. Mean Greyscale ratio

As mentioned earlier in Chapter 2, the incoming electron beam interacts and is scattered by the specimen forming an image whose contrast provides information about the

transmitted electron beam intensity, and can be described by the dynamical theory. A relationship between specimen thickness and the intensity of transmitted electron beam was shown in equation 2.8, with the thin film approximation for the two beam case, proposed by Rubino et al. ³⁴:

$$\frac{I_{tr}}{I_{in}} = \left[1 - \frac{t}{\delta} \right] \dots (\text{equation . 3.7})$$

, where I_t and I_0 are the value for the intensity of transmitted beam on a graphene region and vacuum region respectively. $\delta = \frac{\xi_0'}{2\pi}$ is the absorption constant for the material.

To adapt the technique proposed by Rubino et al. for the determination of graphene thickness, lower magnification (55,000X,) bright field images were used, so that the transmitted beam intensity would be the major contribution to the image contrast. However in this work, the transmitted beam intensity was measured near the zone axis (ZA), where the six diffraction spots are apparent. Also, an objective aperture of 17.9 mrad was used, which is differs from the work performed by Rubino et al. in that the transmitted beam intensity was measured with an objective aperture of 3 mrad and a 7° sample tilt. The present experimental condition is shown in figure 3.18(a) inset, where the objective aperture (orange dash circle) has not excluded the six-fold diffraction pattern from graphene, result in extra diffraction losses from the (100) reflections³⁴. Furthermore, unlike Rubino et al. who performed measurements at 300 kV acceleration voltage, an 80 kV accelerating voltage was used in our work, which could lead to an increased interaction between the electron beam and the specimen. As seen in Figure 3.14 (a), an example graphene TEM BF image was obtained near the zone axis, where the six-fold SAED diffraction pattern is shown as inset. The spectrum of grey values was generated from a 150 pixel×150 pixel area, sampled from each region of interest (ROI). The sample images were transferred to 8-bit and the grey values are quantified from 0 to 255. The generated spectra were exported from ImageJ to OriginPro for data processing.

As shown in figure 3.18(b), the information on grey values can be easily extracted from TEM images, the grey scale values obtained from vacuum regions generally show a higher

value than in the flake region. However, inhomogeneity in the specimen and uneven illumination in the TEM image can result to significant deviations, which it is still the main limitation for the development of this technique. For example, in the bottom panels of figure 3.18 (b), the flake inhomogeneity has caused the baseline tilt in the the greyscale profile, which limits the image pixel size sampled. On the other hand, due to the

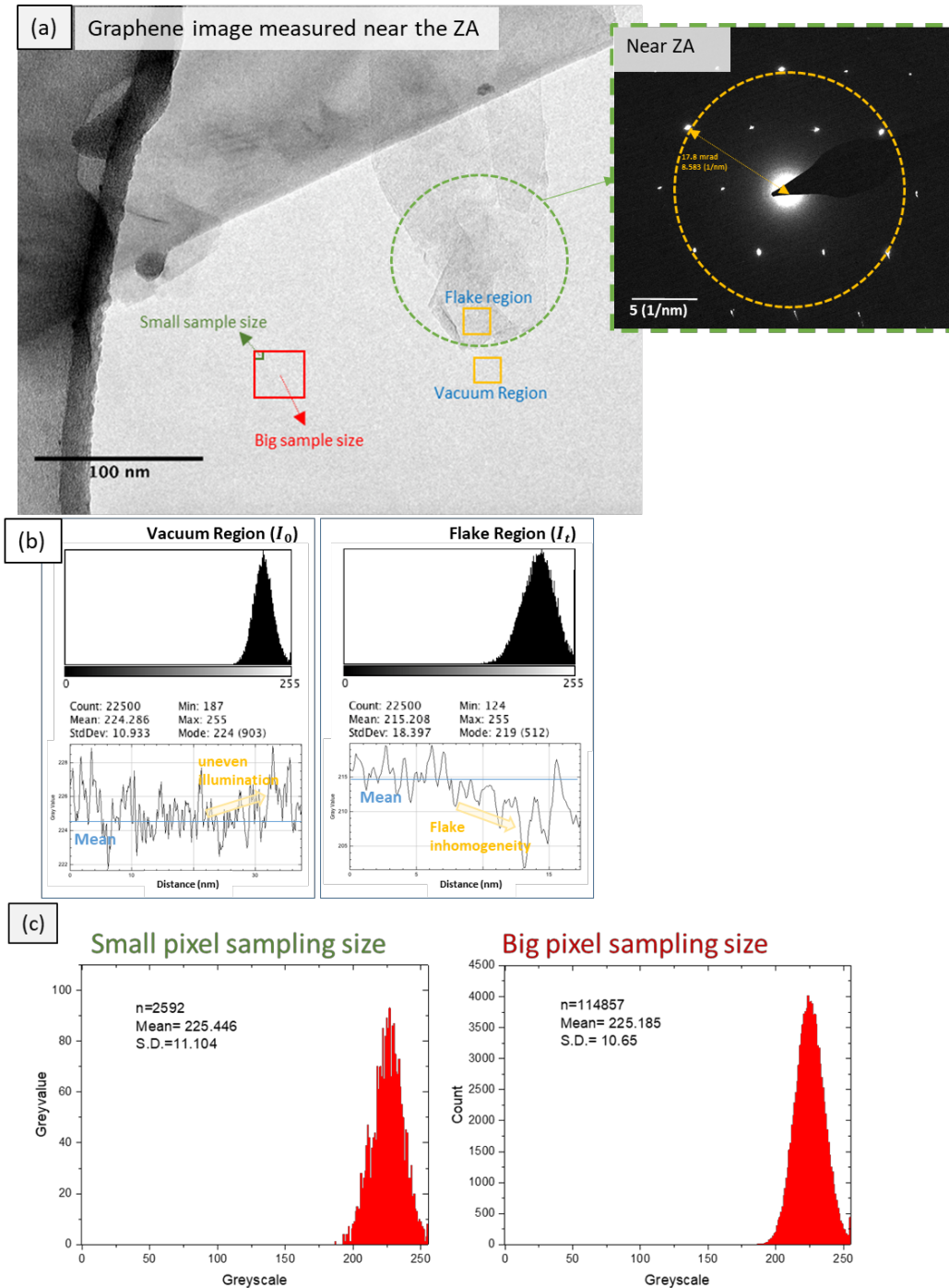


Figure 3.18: Extraction of information from image grey values. (a) Shows the difference of mean value in vacuum and flake regions. The flake inhomogeneity can be a problematic issue for such image sampling. (b) The fluctuation can be significant when sampling size is too small as seen in the difference of standard deviation. The mean value will remain similar due to Centre Limit Theorem (CLT). Uneven illumination can cause baseline tilt even in the vacuum region.

unavoidable shot noise in each image, a small sampling size could result in a greyscale profile dominated by signal noise, which results in uncertainties when obtaining the average greyscale value. Thus, maximising the pixel sampling size is crucial. Example histograms are shown in Figure 3.14(c), the greyvalue distribution of a vacuum region is taken from figure 3.18(a). The histogram of greyscale is approximated by Gaussian distribution and the standard deviation represents the degree of signal fluctuation, which is dominated by shot noise due to the absence of a graphene flake in the ROI. Statistic analysis shows a higher standard deviation for smaller pixel sampling and vice versa, however, the mean value remained similar and represents the general greyscale value over the ROI due to the Centre Limit Theorem (CLT). The mean value was used to characterise the greyscale over the ROI to avoid the effect of noise. Owing to the flake inhomogeneity mentioned earlier, the largest ROI that could be universally used in the experimental condition is found to be $\sim 150 \text{ pixel} \times 150 \text{ pixel}$ with a 55,000X magnification image.

Although the effect of shot noise can be minimised by a larger pixel sampling size, the presence of flake inhomogeneity still cannot be excluded, as well as the presence of uneven illumination causing uncertainty when obtaining the greyscale value. Notwithstanding, estimating thickness by the greyvalue method is still considered as one of the most convenient and universal approach to study graphene in the TEM, and experimental result are discussed further in Chapter 6.

IV. Folded edges

Calculating the flake thickness by observing the folding of graphene edges is one of the most reliable and straight forward methods available. This method is therefore used as the main reference method for developing the thickness estimation from the mean greyscale values. As shown schematically in figure 3.19(a), there are various kinds of folded edges of graphene that are observed: closed, partially open and fully open edges. The open edge and the imperfect partially folded edge were the most common type found in the SEAG sample. This was probably due to the top-down manufacturing method that was used and

the fact that inter-flake random collisions cannot be avoided during ultrasonication. Therefore, a flake edge often consists of multiple-folding, scrolling or incoherent stacking 22,72.

Figure 3.15(b) shows an example TEM image of a typical folded graphene edge. A clear distinct line on the folded graphene edge is obtained where the graphene layers become parallel to the incident electron beams 22,34. The FFT in figure 3.19(b) also shows these lines have the interlayer spacing of graphene (0.34 nm shown as red circle; the red triangle

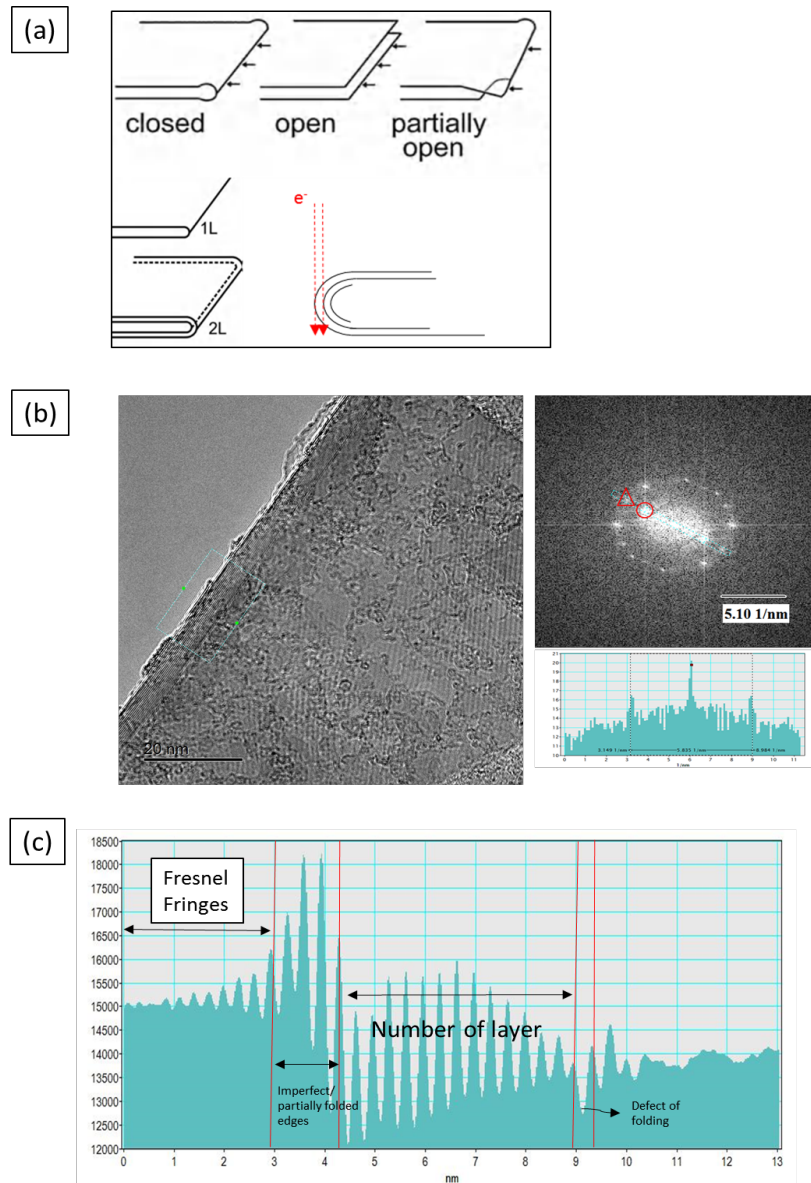


Figure 3.19: Graphene edges used for estimation of the number of graphene layers. (a) Schematic diagram showing the different types of graphene edges. (b) An example TEM image of folded graphene edge. FFT showing these periodic lines have a spacing of 0.34 nm (red circle), while some imperfect partially folded regions can also be observed; (c) Line profile corresponding to the blue rectangular in panel (b). The distance between peaks corresponds to the interlayer spacing and the number of peaks represents number of layers (14 layers in this case).

corresponds to 0.21 nm). This clear periodic interlayer spacing is seen in the intensity profile in figure 3.19(c), and the number of graphene layers can be estimated by counting the number of peaks observed. However, the presence of imperfect folding or Fresnel fringes arising as a result of defocus can give rise to errors, although these can sometimes be observed as irregular spacings (see figure 3.19(c)).

V. *Image processing*

To remove unwanted signals in the images, image processing techniques were applied via FFT. A High-pass Fourier-filtering technique was applied to remove uneven illumination. As seen in figure 3.20 (a), the uneven illumination on the left side image can be removed with the use of a 5 pixels smooth cut off near 1.27 nm^{148,149}.

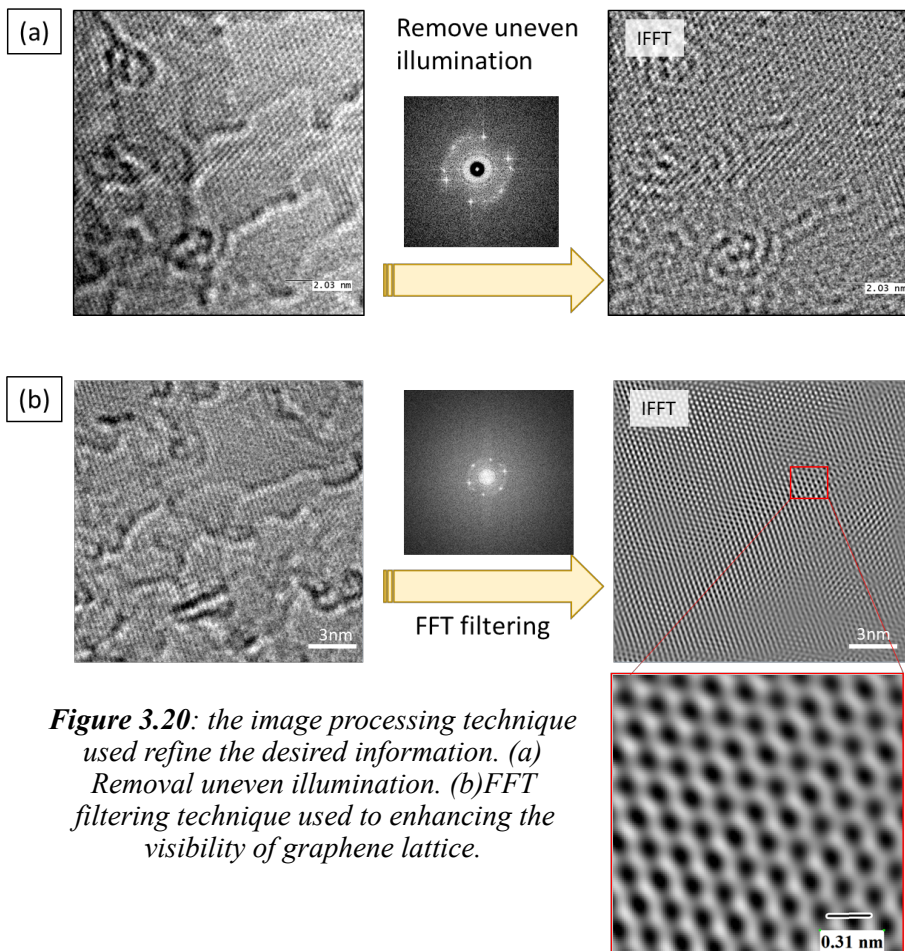


Figure 3.20: the image processing technique used refine the desired information. (a) Removal uneven illumination. (b)FFT filtering technique used to enhancing the visibility of graphene lattice.

A similar technique can be used to enhance the visibility of the graphene lattices in the image. As seen in figure 3.20(b), the original image that consisted lattice information was firstly transferred to a diffractograms, followed by the selection of and masking the spatial frequency of interest, clear lattice image can be reconstructed by inverse FFT (IFFT) of the filtered diffractograms. After unwanted signal was removed and refined, lattice defects as well as grain boundaries could be observed in the reconstructed image.

VI. Edge detection

To analyse graphene images automatically, edge detection is one of the most crucial processes. Owing to the difference in contrast or colour between the specimen and background, the interface can be approximated by quantifying the digital images. There are several edge detection algorithms such as: Canny, Fuzzy logic and Sobel ¹⁴⁹, which are widely available on imageJ, scikit-image or Matlab. In this work, the image processing was performed by a combination of imageJ and scikit-image software packages.

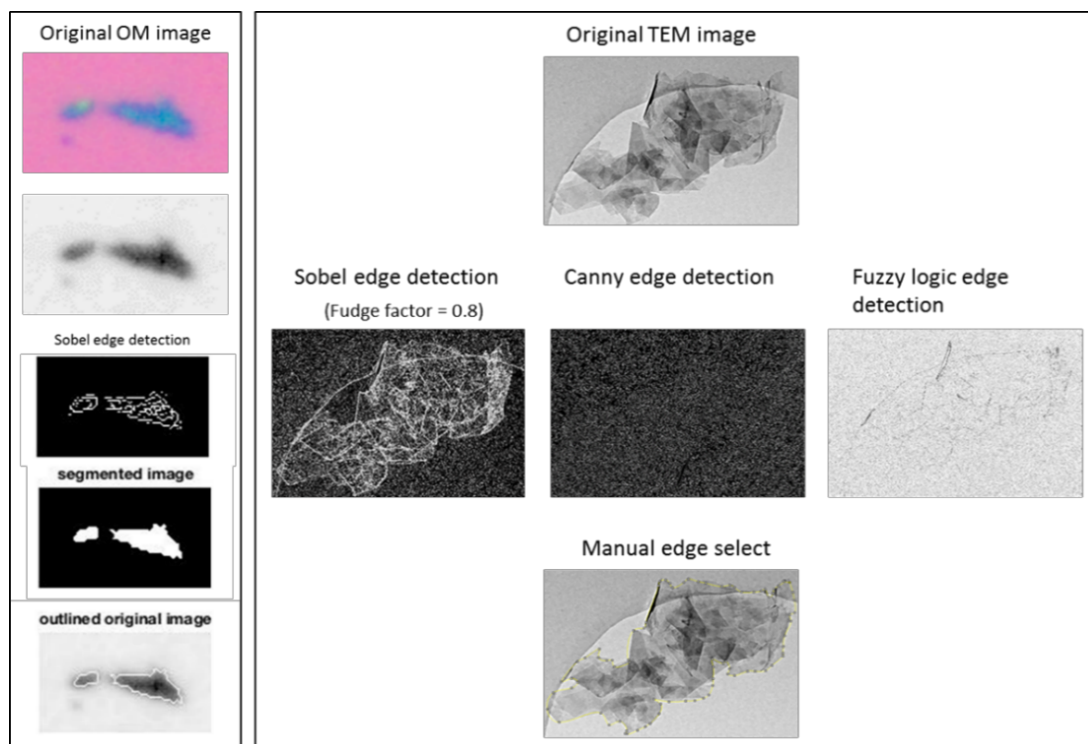


Figure 3.21 Applying edge detection techniques on optical microscope image and TEM image.

To perform the edge detection algorithm, a grey value image is required. As seen in Figure 3.21, different edge detection algorithms have been applied to TEM images, and various parameters tested. However accurate edge detection on graphene flake is still difficult to achieve due to the low contrast differences between the flakes and the background. Thus, generally, the assist of manual selection was often needed for accurate edge detection. In contrast, it was much easier to determine the graphene edges using optical microscopy images owing to and the significant colour differences between the flakes and substrate which allowed the outlines of graphene flakes to be identified by a Sobel edge detection algorithm (fudge factor=0.1). However, it should be noted that due to the resolution limit of optical microscopy, inaccuracies in edge detection still exist, and these are further discussed in chapter 4.

VII. Adaptive local thresholding algorithm (ALTA)

TEM images are complicated due to sample inhomogeneity and the limitation of aperture size. The region of interest (ROI) cannot be easily segmented from the background by applying pixel thresholding. This is because the traditional global thresholding algorithm (GTA) treats every image pixel as an individual object and thus only works well when the target particles have sufficient contrast from the background. For an image that has a noisy background, or the image contrast is unevenly distributed, the global thresholding algorithm is no longer suitable. As example is shown in figure 3.22(a), the global thresholding algorithm incorrectly identified several neighbouring grains as a big grain, with the noise pixels that exceeded the threshold value being taken into the statistics. The selection resulted to a particle size distribution composed of a few large grains and many small noise pixels/particles as shown in figure 3.22(a).

An adaptive local thresholding algorithm (ALTA) was therefore developed in order to improve the accuracy of autonomous thresholding ¹⁵⁰. Unlike the global thresholding algorithm which uses a threshold value for the entire image, the ALTA divides the original image into several subdivisions, allowing a more suitable threshold value to be calculated

for each subdivision (based on an iterative approach). An example is shown in figure 3.22(b), where the ALTA detected neighbouring grains individually and most of the noise pixels are excluded, giving a reasonable grain detection. The ALTA was therefore applied to the dark-field TEM images for grain size statistics and the results will be presented in chapter 5.

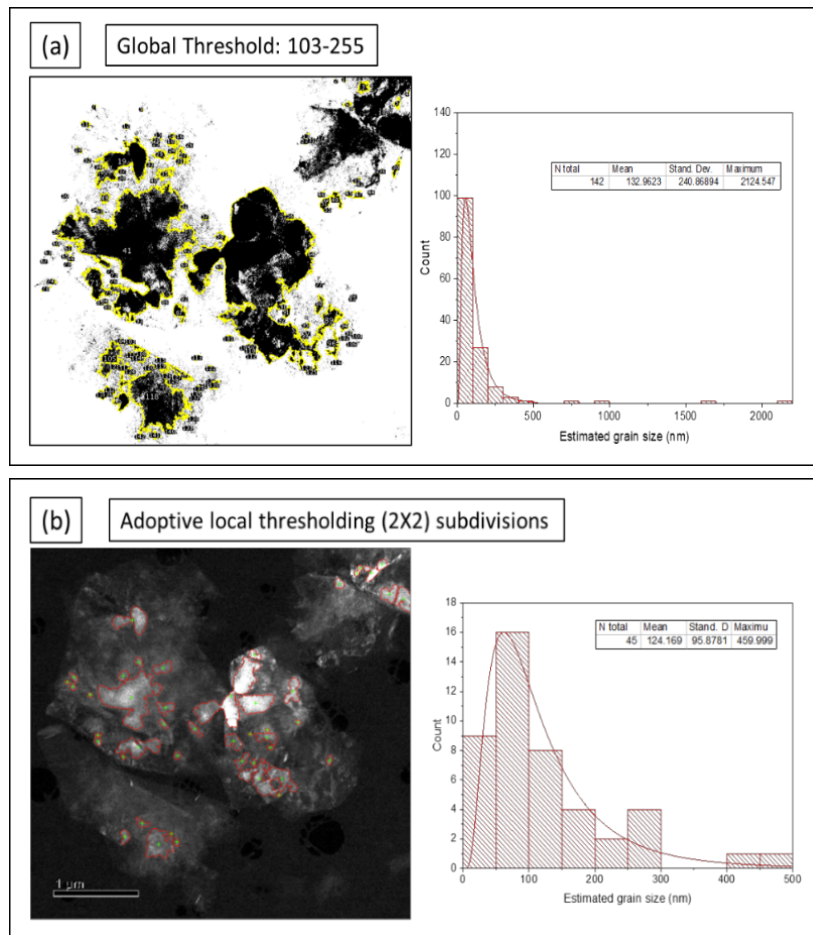


Figure 3.22: An example of applying adaptive local thresholding to TEM images to obtain the grain size distribution in a graphene flake: (a) The application of global thresholding; (b) The application of adaptive local thresholding with different number of subdivisions.

Part two

Results and Discussion

4.

Determination of Graphene Lateral Dimension

Lateral flake size is one of the most important factors that affects various properties of graphene. The variation in size and geometry causes the change in ratio between edge and bulk structures, resulting in spatial confinement in specific dimensions that alters its electrical and mechanical behaviour ^{151–154}. Experimental studies the lateral size of graphene may be initiated for various reasons. The fundamental study of graphene lateral geometry ranges from flake interactions in solvents to the electronic structure of various shapes ^{155–159}. Studies can also be conducted for practical needs such as applications in thin graphene film deposition ^{12,14,160,161}.

Ideally, the ability to track the graphene flakes while determining the flake size distribution over a continuous time interval is the most satisfactory method. This should give information on the number of separated graphene flakes and all aggregates ^{162–164}. The only way of obtaining such information unambiguously is to use a technique that can directly visualise and count graphene flakes and also discriminate between different primary graphene flakes, in terms of shapes, thicknesses and aggregation states. Methods are generally limited because of the difficulties of visualising ultra-thin Nano-flakes and the fact that many of the properties which could be used to identify the material are still unknown.

In this chapter, I intend to demonstrate methodologies to determine the lateral dimension distribution of graphene flakes via direct flake tracking microscopic techniques (TEM and Optical microscopy) as well as fast but less direct techniques based on the light scattering. **Figure 4.1** illustrates the procedure, which is used in this section. TEM was first carried

out to determine the lateral dimension of exfoliated primary graphene flakes and aggregated flakes. This lateral size distribution is used as a benchmark in the further experiments (Figure 4.1(a)). Secondly, an optical microscope measurement was performed; the flake lateral size distribution is obtained by use of digital image processing on a Fabry-Perot interferometer that makes graphene visible under reflective optical microscope (Scheme 4.1(c)). Light scattering techniques are subsequently performed to obtain the dimension distribution (Scheme 4.1(b)). Optical and hydrodynamic parameters used for the DLS analysis such as the diffusion coefficient, refractive index and absorption coefficient of graphene flakes are discussed and investigated (Scheme 4.1(d)). To the best of my knowledge, no precise or reliable parameters for graphene flakes dispersed in IPA exist in literature. Therefore, approximations are used for these parameters in (b) (c) (d). In all cases, the commercialise 2Dtech Aquagraph series graphene sample was used. The obtained distributions are compared to the TEM and OM data; the absolute and related deviation are calculated and discussed (Scheme 4.1(e)).

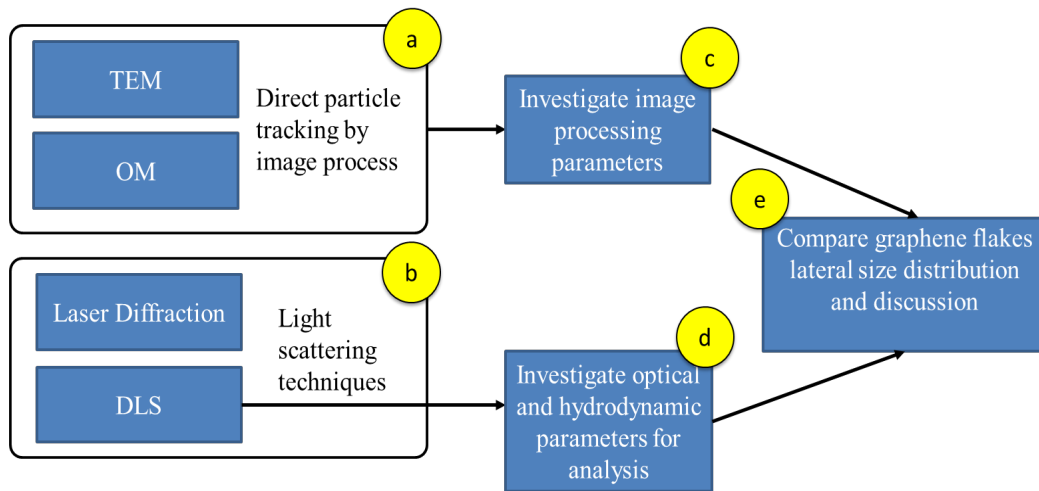


Figure 4.1: Procedure to determine the lateral size distribution of graphene flakes.

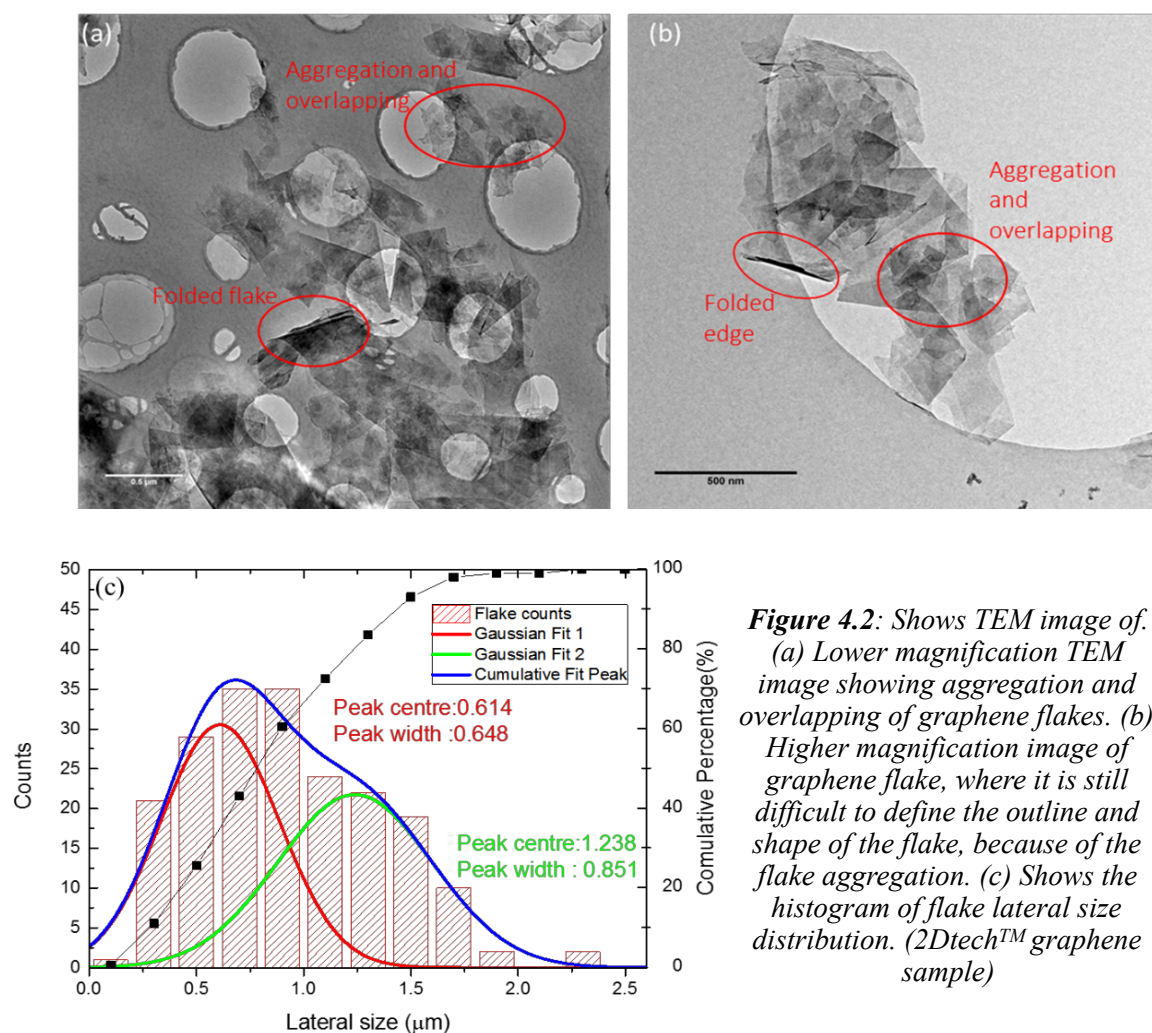
4.1. TEM image analysis

I. Graphene flake size distribution

The first stage of this work was to study the lateral size distribution of flakes using TEM. Because TEM is the most straightforward and precise technique to image freestanding graphene flakes, it was used to set up the benchmarks for the graphene lateral size study. This was achieved using graphene samples provided by 2Dtech Aquagraph series. As it was aimed to develop a general method for lateral size measurement, the graphene suspension was dropped and casted on a holey carbon grid; the same suspension was then analysed using optical microscopy, laser diffraction particle sizing and DLS.

As seen in Figure 4.2 (a) and (b), typical bright-field TEM images of graphene flakes are shown. The graphene flakes are often aggregated or partially folded (indicated in figure 4.2 (a)), complicating images and making them hard to quantify. A higher magnification of graphene flake image is shown in figure 4.2 (b); the flake is attached and suspended at a carbon hole. Even though many thin graphene areas are evident, the aggregation, overlapping and folded edges make it difficult to define the outlines and shapes of these graphene flakes. The graphene flakes were then categorised into primary and aggregated flakes. Primary flakes are fundamental flakes that cannot be separated into smaller flakes except by the application of higher energy, while aggregated flakes are flakes that comprise two or more primary flakes attached together.

To determine the lateral dimension of graphene flakes, the shape and outline of these graphene flakes were approximated as polygons (this approximation is considered reasonable due to the fracture edge of flakes being often Zigzag or Armchair crystal faces^{9,165,166}). Length measurement was taken along the major axis, known as Feret diameter, which represents the longest distance between any two points along flake edges.



In this study, a total of 199 flakes were selected from several TEM images and these flakes were taken for lateral dimension distribution statistics. The total mean lateral size was $0.934 \pm 0.430 \mu\text{m}$, and the size distribution of the graphene flakes is shown in 4.2 (c). This histogram consists of two Gaussian distributions, one of the peak centred at $0.614 \mu\text{m}$ with a peak width of $0.324 \mu\text{m}$, and another Gaussian centred at $1.238 \mu\text{m}$ with a broader peak width of $0.426 \mu\text{m}$. This bimodal distribution curve could indicate two kinds of particles in the sample ¹⁶⁷, namely primary flakes with a larger spacing between the flakes, and aggregated flakes which may overlap or be entangled with each other as mentioned earlier.

Figure 4.3 (a1) and (b1) shows an example TEM images of primary and aggregated graphene flakes. Length measurements are illustrated by the yellow lines. The aggregated flakes and primary flakes were selected, and their size distributions are shown in figure 4.3 (a2) and (b2). Among these selected flakes, the primary flakes demonstrated a smaller lateral dimension, only ranging from c.a. $0.2\mu\text{m}$ to $1.6\mu\text{m}$, and only one flake was found

to be smaller than $0.2\mu\text{m}$. The mean value of the primary flakes was $0.619\ \mu\text{m}$ with standard deviation of $0.25\ \mu\text{m}$ (figure 4.3 (a2)). The aggregated flakes exhibited a higher lateral dimension difference, the lateral flake dimension ranging from c.a. $0.4\mu\text{m}$ to $2.4\mu\text{m}$. The mean value of the flake lateral size was $1.236\mu\text{m}$ and the standard deviation was $0.34\ \mu\text{m}$. Most of the aggregated flakes ($>98\%$) exhibited lateral dimension bigger than $0.5\mu\text{m}$ (figure 4.3 (b2)).

As mentioned in Chapter 2 and Chapter 3, the greyscale of TEM images can provide some information on specimen thickness. Because the intensity of transmitted electrons decreases with increasing sample thickness, this results in thicker flakes appearing darker in TEM images ⁷². From the selected graphene flakes, the Mean Greyscale Value Ratio (MGVR) exhibited a mean value of 0.881 ± 0.092 for primary flakes and 0.709 ± 0.183

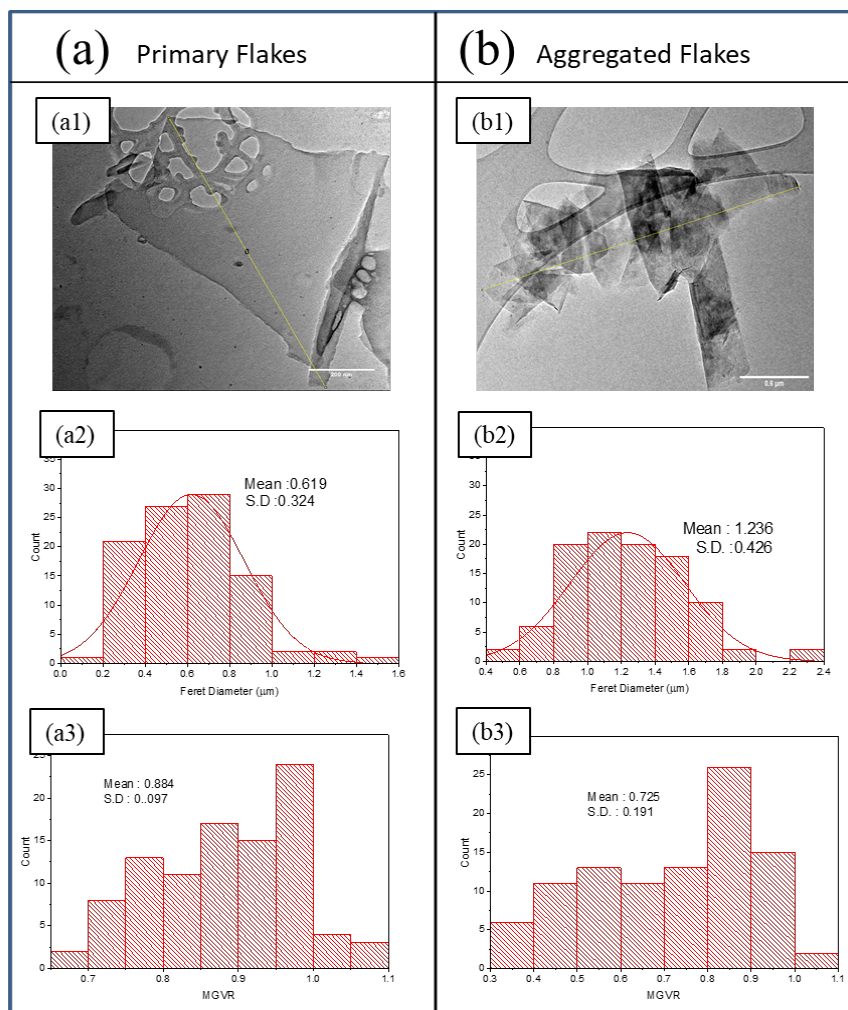


Figure 4.3: Shows Bright field TEM image of (a) primary graphene flakes and (b) aggregated graphene flakes. Yellow lines in (a) and (b) illustrate the method used to determine the flake lateral dimension. Lateral Size distribution of primary and aggregated flakes are shown in (a2) and (b2) respectively. (2Dtech™ graphene sample)

for aggregated flakes. The histograms of MGVR are shown in figure 4.3 (a3) and (b3). Although a precise thickness determination is unavailable at this stage, the difference in MGVR between primary and aggregated flakes suggests that the flake aggregation is preferable in vertically rather than horizontally.

II. The shape of Graphene Flakes

Fragments or aggregates of graphene can result in a variety of shapes and flake edge densities. This is an important consideration when applying graphene in electronic or mechanical devices. In previous literatures, edges and crack paths of graphene were studied by Molecular Dynamics (MD) ^{166,168–170}. It has been reported that crack paths are highly dependent on the direction of the initial crack, the fracture of graphene being the competition between bond breaking and bond rotation at the tip of the crack. TEM is a powerful tool used to investigate the shape and size of graphene flakes due to its precision and the ability to study morphology of graphene flakes.

Figure 4.4 demonstrates the relationship between graphene flake lateral dimension and graphene flake shape. Examples of bright-field TEM images of bigger and smaller flakes are shown in Figure 4.4 (a) and (b). Sharp flake tips or edges can often be found in these graphene flakes. The sharp edges or tips could be due to the crack propagation along the zigzag or armchair edges during the milling synthesis process (indicated by red and green dash lines). A typical sharp edge on a thin graphene flake is shown in Figure 4.4 (c), it is clear to see that the angle of the fracture edges ($\sim 36.895^\circ$) is close to a zigzag-armchair fracture angle (30°) indicated in the inset of figure 4.4 (c). The Shapes of graphene flakes can be described by circularity, defined as:

$$Circularity = 4\pi \times \frac{Area_{(polygon)}}{Perimeter^2_{(polygon)}} \dots (equation 4.1)$$

, where a number closer to 1 indicates a more circular flake. Figure 4.4 (d) shows a histogram of circularity for selected graphene flakes. Only one of the selected flakes has a circularity between 0 to 0.1, while most of the flakes have a circularity between 0.2 to 0.9, meaning these flakes are unlikely to be needle or tube-like in shape. The mean value of circularity for the flakes is 0.649 and the standard deviation is 0.157, which implies that most of these flakes are somewhat rounded.

A scatter plot and linear regression was used to obtain the relationship between flake dimension and flake shape. The result is shown in 4.4 (e). Pearson's correlation test demonstrates a significant but weak correlation between the flake shape and flake dimension ($r = -0.395$). Though the relation between circularity and flake dimension cannot be well predicted by an empirical linear regression model, it shows a trend of

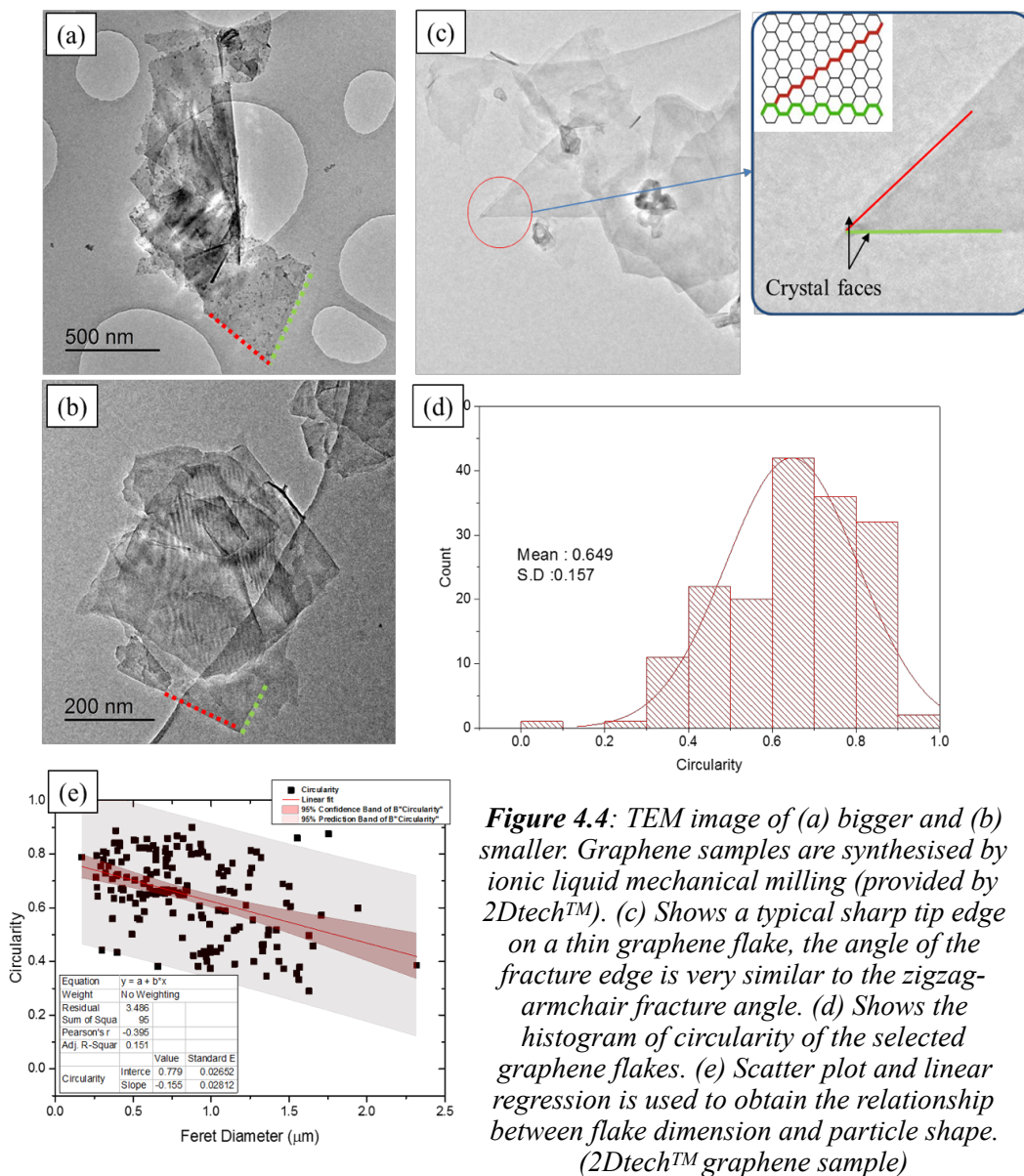


Figure 4.4: TEM image of (a) bigger and (b) smaller. Graphene samples are synthesised by ionic liquid mechanical milling (provided by 2DtechTM). (c) Shows a typical sharp tip edge on a thin graphene flake, the angle of the fracture edge is very similar to the zigzag-armchair fracture angle. (d) Shows the histogram of circularity of the selected graphene flakes. (e) Scatter plot and linear regression is used to obtain the relationship between flake dimension and particle shape. (2DtechTM graphene sample)

smaller flakes having a more rounded flake shape and vice versa. The inverse relation between flake circularity and flake dimension could be explained by ways of two main possible causes: (1) Random collision during the synthesis process and (2) flake re-aggregation. Random collision during the milling process could cause sharp edges to fractures, forming larger fracture edge angles and resulting in smaller graphene flakes having higher circularity than the larger flakes. Re-aggregation of small flakes could also be an explanation of this trend. More rounded small flakes may tend to re-aggregate to form larger graphene flakes, which demonstrate irregular and less circular shapes. A combination of these two mechanisms can explain the trend between flake shapes and flake dimensions.

4.2. Graphene lateral dimension

distribution from Optical Microscopy

Optical microscopy is a relatively user friendly and widely available technique to study sub-micrometre scale objects. However, the resolution of the optical microscope is limited due to the utilisation of visible light. Traditionally, the lateral resolution of optical microscope can be estimated by Rayleigh's criterion ¹⁷¹, and for a 100X objective lens with numerical aperture (NA)= 0.95, the best lateral resolution would be just slightly higher than 0.25 μ m and only samples thicker than 2 μ m can offer sufficient contrast for observation.

Since graphene is much thinner than the axial resolution limit and is highly transparent under visible light, making graphene visible is therefore one of the most crucial steps. To make graphene visible under the optical microscope, a finely optimised substrate and an optical setup is required to enhance the contrast between the graphene samples and the background substrate. For example, on a highly transparent substrate such as silicon

dioxide, optical reflection microscopy gives a higher contrast ratio for graphene flakes than transmission optical microscopy because the reflected light from a graphitic flake is different from the low background reflection of the transparent substrate ¹⁷².

By utilising the reflected light from a Fabry–Perot structure composed of an optimised thickness of silicon dioxide on a single crystal silicon wafer (shown in Figure 4.6(a)), a higher contrast between graphene and the substrate can be achieved by generating a optical path difference, resulting in a interference of each reflected light beams. The origin of the contrast can be explained by Fresnel’s equation ²⁰. Consider the normal incident light from air ($n_0 = 1$) onto a graphene, SiO₂ and Si trilayer system, the reflected light intensity from the system can then be described by^{20,98}:

$$r(\lambda) = \frac{r_a}{r_b} \dots (\text{equation 4.3})$$

$$r_a(\lambda) = (r_1 e^{i(\beta_1 + \beta_1)} + r_2 e^{-i(\beta_1 - \beta_2)} + r_3 e^{-i(\beta_1 + \beta_1)} + r_1 r_2 r_3 e^{i(\beta_1 - \beta_1)}) \dots (\text{equation 4.4})$$

$$r_b(\lambda) = (e^{i(\beta_1 + \beta_1)} + r_1 r_2 e^{-i(\beta_1 - \beta_2)} + r_1 r_3 e^{-i(\beta_1 + \beta_1)} + r_2 r_3 e^{i(\beta_1 - \beta_1)}) \dots (\text{equation 4.5})$$

, where λ is the wavelength of incident light, $r_1 = (n_0 - n_1)/(n_0 + n_1)$, $r_2 = (n_1 - n_2)/(n_1 + n_2)$ and $r_3 = (n_2 - n_3)/(n_2 + n_3)$ are the reflection coefficient for different interfaces, n_1 and n_2 are refractive index of graphene and the SiO₂ layer respectively (schematically shown in figure 4.6(a)), the refractive index of Si substrate n_3

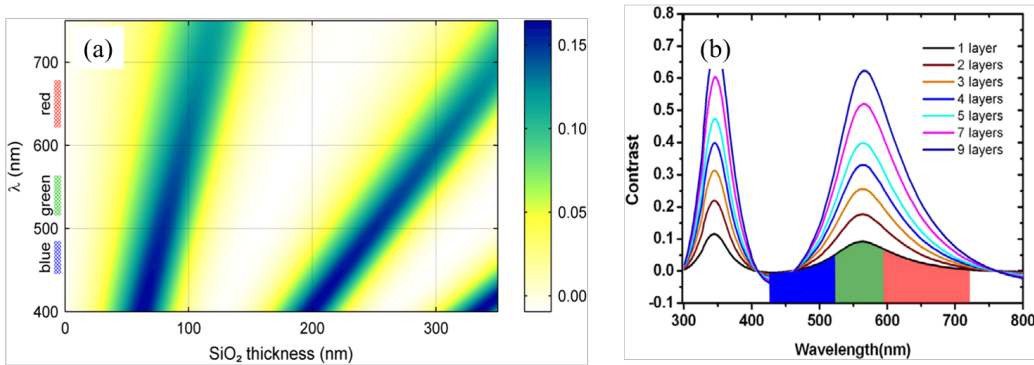


Figure 4.5: Theoretical calculation of (a) colour plot for the expected contrast as a function of SiO₂ thickness and wavelength; (b) theoretical calculation results of contrast spectra of different graphene thicknesses on a SiO₂(285 nm)/Si substrate under normal incident light. (Figures adopted from Ref²⁰ and Ref⁹⁸)

can be considered as semi-infinite^{20,98}, most of light are reflected at the interface.

$\beta_1 = 2\pi n_1(\frac{t}{\lambda})$ and $\beta_2 = 2\pi n_2(\frac{d_2}{\lambda})$ are phase differences when light passes through the

medias and are determined by the optical path difference of two neighbouring interfering light beams. t is the thickness of graphene, which can be estimated as $t = N \Delta d$, N is the number of graphene layers and Δd is the thickness of each graphene layers ($\Delta d \approx 0.335 \text{ nm}$ for AB stacking graphene). The reflection spectrum $R_0(\lambda)$ from the SiO₂/Si wafer substrate and the reflection spectrum $R(\lambda)$ from the graphene sheet can be obtained by knowing the refractive index and thickness of each media ($n_1 = 2.0 - 1.1i$ from reference ⁹⁸ ; $n_2 = 5.6 - 0.4i$ from reference ²⁰). By using this theory, the image contrast can then be described as ²⁰:

$$C(\lambda) = \left(\frac{R_0(\lambda) - R(\lambda)}{R_0(\lambda)} \right) \dots(\text{equation . 4.6})$$

, and the optimised contrast can then be obtained by simulating across the whole visible light range ⁹⁸.

Figure 4.5 (from references ²⁰ and ¹⁷³) shows the theoretical simulated contrast spectra for different SiO₂ and graphene thicknesses. The expected contrast as a function of SiO₂ thickness and wavelength is shown in Figure 4.5 (a), which can be used to select an appropriate thickness for SiO₂ layer to maximise contrast variation for the observation of graphene: approximately 90nm and 280nm under white light or green light ²⁰. The theoretical contrast spectra for different graphene thicknesses on a SiO₂ (285 nm)/Si substrate under a normal incident light is shown in Figure 4.5 (b) (from reference ¹⁷³ and ¹⁷⁴). The calculation based on the Fresnel equation predicts that for graphene less than 10 layers thick, the maximum contrast peak is at around 550 nm. The peak position shifts to shorter wavelength with decreasing graphene thickness, indicating that thinner graphene flakes reflect a lower proportion of green light, so that they appear blue-purple, whereas thicker flakes reflect a higher proportion of green and red light, therefore appear yellowish.

Figure 4.6 shows an example of graphene flakes visualised under the optical microscope. The Fabry-Perot structure was manufactured by thermally growing a 284.1 ± 0.75 (nm) thick oxide on a Si-wafer and was used to enhance the contrast as shown schematically in Figure 4.6 (a). An image of the dried graphene suspension on the SiO₂/Si wafer substrate is shown in Figure 4.6 (b). In this work, an Olympus BX51 series reflection light microscope was employed for the Optical Microscopy analysis, using a 100x objective lens (N.A. = 0.95) and a 163 ms exposure time; white balance and RGB colour ratio were optimised by the pre-installed AxioVision software. An example image is shown in Figure 4.6 (c), where the thin and thick flakes are labelled in the image; thin flakes appear blue and thick flakes are displayed in brown or yellow which agrees with the theoretical prediction.

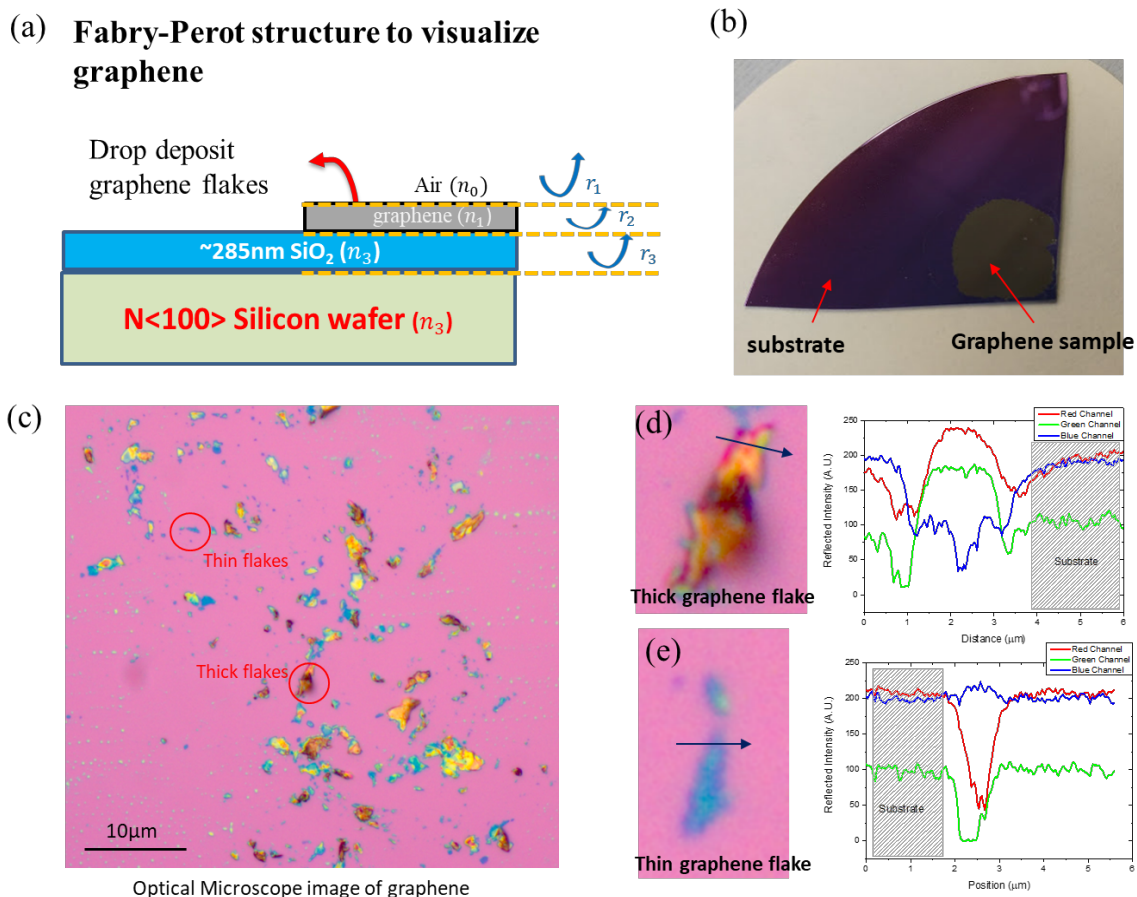


Figure 4.6: Shows (a) schematic diagram of the Fabry–Perot structure composed of an optimised thickness of silicon dioxide layer (284.1nm) on silicon wafer to enhance contrast between graphene sample and the substrate; (b) a photo of graphene ink deposited on the 284.1nm SiO₂/Si wafer substrate from naked eyes ; (c) reflective optical microscope image from 100X, NA=0.95 objective lens; (d) and (e) shows the RGB channel split of thicker and thinner graphene flakes.

The optical microscopy images of the thin and thick flakes were digitally split into RGB channels to quantify the reflected spectrum as a function of graphene thickness. Figure 4.6 (d) and (e) shows the reflected RGB intensity across thick and thin graphene flakes respectively. For these cases, the RGB intensity in the background remains at similar values, implying the background signal is very stable. The reflected intensities of each channel encounter notable change on the thick and thin graphene flakes, indicating a significant contrast is obtained. Figure 4.6(d) and inset shows that the red and green channels increase significantly at the flake boundary and remain constant within the thick graphene sample. The proportion of reflected R : G : B intensity on the thick graphene flakes is around 240 : 180 : 100, which results in yellow-or brown-like flake images. The RGB intensity change across a thin graphene flake is shown in Figure 4.6 (e), in which the ratio of the red and green channels drops significantly on the flake, but the blue channel remains at constant value. The ratio of R : G : B intensity is 50 : 2 : 213 on the thin graphene flake, resulting in a blue-or purple-like image.

Nevertheless, both thin and thick graphene flakes encounter significant change in the green channel, in which the wavelength of green light is around 550 nm, indicating a sensitive optical response of the graphene / graphite material under the wavelength region. By using the refractive index of graphene is $2.0 - 1.1i$, Ni et al. proposed an empirical method to obtain the thickness of graphene layers using the optical image contrast shown in equation 4.6, expressed as⁹⁸:

$$C = 0.0046 + 0.0925N - 0.00255N^2 \dots (\text{equation 4.7})$$

, where N is the number of thin graphene layers can be calculated as:

$$N = \frac{-0.0925 + \sqrt{0.0925^2 + 4 \cdot 0.00255 \cdot (0.0046 - C)}}{2 \cdot (-0.00255)} \dots (\text{equation 4.8})$$

Using the intensity of green channel (~550nm) and equation 4.6, equation 4.7 and equation 4.8, the thickness of graphene can be estimated via the contrast in green channel. Take the flake in figure 4.6(e) for example, it generates a contrast of 0.96, which was

estimated to have a thickness more than 10 layers (~18 to 20 layers). However, such a thickness estimation method may not be suitable for estimating the thickness of a much thicker flake. Taking the flake shown in figure 4.6(d) for example, the flake reflects more green light than the substrate region, resulting in a negative contrast value, in which equation 4.7 and 4.8 is therefore inapplicable. This can be due to the refractive index of the thick graphite flake being far from that of thin graphene, making such thickness estimation method not valid (detailed sensitivity evaluation is presented in chapter 6).

I. Detecting graphene flakes from optical microscope images

The stable reflection spectrum from the substrate and significant reflection spectrum change through graphene flakes makes it possible to identify graphene flakes from the background under a reflection optical microscopy. The significant change of the reflection spectrum at the flake boundaries allows us to extract the outlines of graphene flakes via digital image processing. Moreover, the obvious change in the reflected RGB ratio with graphene thicknesses can provide a rapid method for determining lateral dimension of flakes distribution quantitatively and thus calculate the yields of thin graphene flakes produced by another synthesis process.

The process of obtaining the graphene lateral dimension distribution from optical microscopy image is briefly shown in Figure 4.7. The original optical microscope image contains background, thin graphene flakes (blue areas), and thick graphene flakes (yellow and dark brown areas). To autonomously select flakes of interest, the original image was firstly split to RGB channels, where the green channel is used to distinguish thin flakes and thick flakes from the background, owing to the green channel encountering the most significant change between thick and thin flake at the boundaries, which is also physically meaningful for the optical response of graphene (see figure 4.6(d) and (e)). By applying the thresholding process, array values of the background regions were normalised but the

array value remains the same in flake regions, the regions of flakes of interests can be therefore extracted by adjusting the threshold values.

After flakes of interests were decided, edge detection process was performed. The Sobel edge detection algorithm was used to determine the lateral dimension of selected graphene flakes. However, owing the spatial and colour resolution of optical microscope, fault image pixel selection can occur when noise pixels are consisted in the image. Thus, to avoid such errors, selected areas with a dimension smaller than 200 nm or circularity > 0.9 are discarded. This selection process criteria is reasonable, because the optical microscope cannot resolve flake dimension < 200 nm. In addition, the TEM observation has shown that most of flakes are bigger than 200nm with circularity between 0.3 and 0.9. An example histogram of graphene lateral dimension distribution is shown in Figure 4.7. The

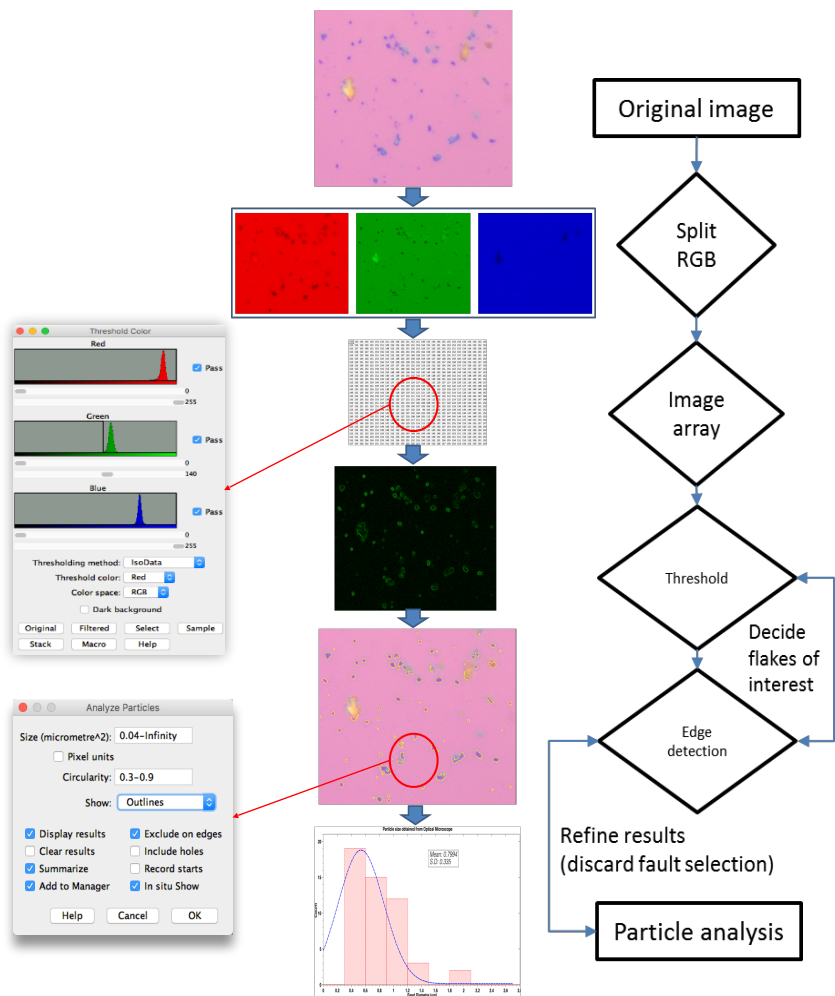


Figure 4.7: shows the process for obtaining graphene lateral dimension from optical microscopic images. Left side shows the outcomes from each process. Right side shows image process and operators that were used to obtain graphene flake dimension distribution.

histogram was obtained by analysing optical microscopic image, using the selection criteria mentioned above.

i. Imprecisions in flake edge detection

The process of obtaining the graphene lateral dimension distribution from optical microscopic image is briefly shown in Figure 4.7. Here I discuss some factors that can causes inaccuracy when obtaining graphene lateral dimension distributions form optical microscopy. The thresholding range is one of the most common parameters that can affect the output of the dimension distribution.

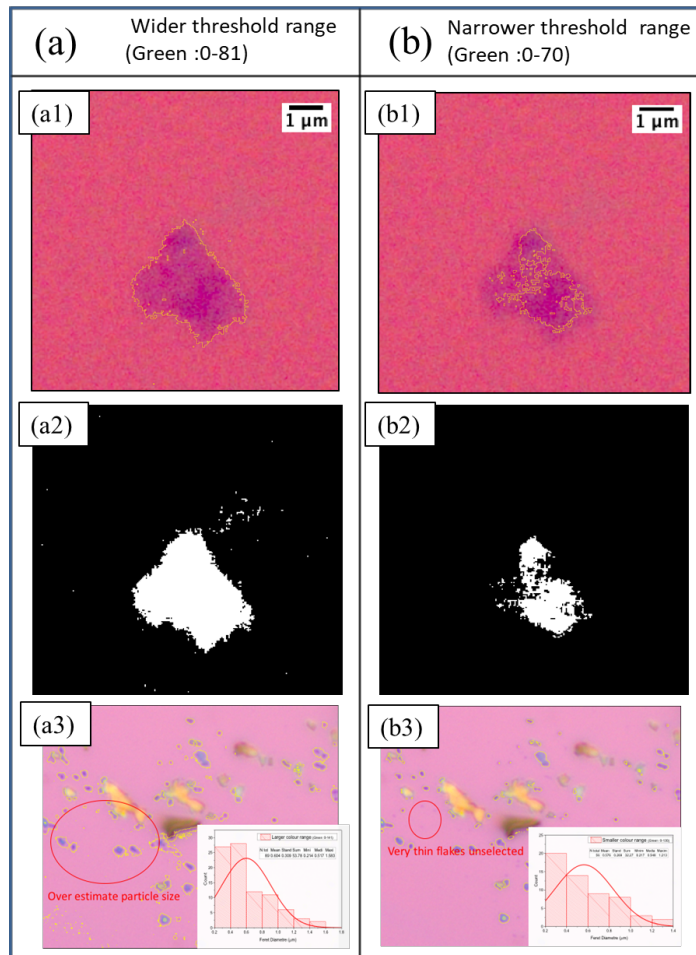


Figure 4.8: shows lateral dimension distribution affect by the colour selection threshold. (a) A wider colour threshold or (b) narrower colour selection range can affect flake diameter that was measured. (a1) and (a2) demonstrates larger flake dimension can be measured with wider colour threshold, while the dimension could be overestimated (labelled as red circle in (a3)). Narrower colour threshold can result to smaller flakes dimension, as seen in (b1) and (b2), but many of the thin flakes cannot be detected with such colour threshold (indicated in red circle in (b3)).

Figure 4.8 shows detection of graphene flakes edges using different green channel threshold value. The selection outcomes from the wider threshold and the narrower threshold are shown in figure 4.8(a) and figure 4.8(b), which the green channel threshold range were set as 0 to 81 and 0 to 70 for the wider threshold and the narrower threshold respectively. As the yellow lines indicated in figure 4.8 (a1) and (b1), a bigger flake will be obtained when using a wider threshold and vice versa. Figure 4.8 (a2) and (b2) showing the binary images after the initial microscopic images were threshold in order to enhance the differences in selected flake outline. As seen in the binary images, fractal flakes and many multiple small spots were consisted in the image. This is owing to the insufficiency of spatial and colour resolution that uncertain flake edges and fault pixels can presented and unable to be completely avoided by the global threshold method.

As seen in figure 4.8 (a2) and (b2), a different thresholding value could result in a deviate Feret diameter measured, a 19.36% difference in dimension difference were obtained. However, the difference in dimension distribution is not much affected when obtaining the dimension distribution from a large area / amount of flakes (larger sample dimension). This can be seen in Figure 4.8 (a3) and (b3), the obtained mean lateral dimension is 0.604 μm and 0.576 μm for a wider and narrower threshold range respectively, just ca. 28 nm and 4.86% in difference. This is because the increased detection in thin flakes are usually very small in lateral dimension, compensates the overestimated lateral dimension of bigger flakes. By using the green channel threshold between 0-81, it was estimated that the graphene flakes can generate contrast of 0.2, with thickness between 2-21 layers can be selected (based on using equation 4.8). For much thinner graphene flakes, it is difficult to be identified based on current optical microscope setup due to the lack of image resolution.

ii. Calculating yield of thin graphene via Optical Microscope using colour selection

The difference in colour between different graphene thicknesses allows us to estimate the yield of thin graphene flakes. This technique can be used to investigate how many thin graphene flakes are produced in a fast period. Figure 4.9 demonstrates a simple method to calculate the yield of thin graphene flakes from the optical microscopic image. By converting the optical images to the HSB (Hue, Saturation, Brightness) space, thin and thick flakes can be easily selected from its colour. As previously shown in figure 4.6, thin graphene flakes appear in blue or purple, so the selection of blue to purple regions in the Hue space can easily define the boundary of thin flakes (shown in figure 4.9(a) and inset). Yellow and brown thick flakes can be selected from, by using the yellowish colour region (figure 4.9(c) insets).

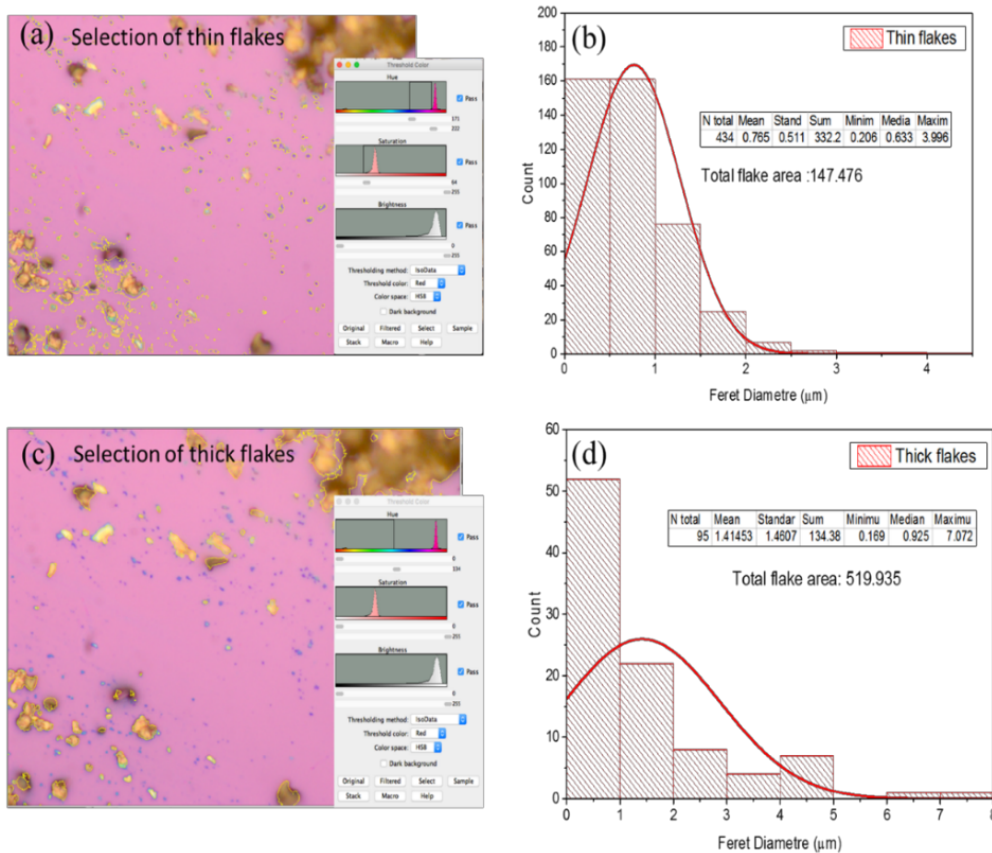


Figure 4.9: Shows an example of obtaining the yield of thin graphene flakes. (a) Thin graphene flakes and (c) thick graphene flakes are selected in the microscope image by converting the image into HSB space (insets). (b) And (d) shows the histogram of obtained thin and thick graphene flakes respectively. Total flake area is used to estimate the yield of thin graphene flakes. (2Dtech aquagraph SAEG sample were used)

Using the flake selection method introduced in the previous paragraph, in the 2Dtech™ graphene sample, it was found a total of 434 thin graphene flakes and 109 thick flakes were consisted and identified in the $50\mu\text{m} \times 50\mu\text{m}$ optical microscope image. In general, thick flakes demonstrated larger lateral dimension, the mean lateral dimension of thin and thick flakes is $0.765 \pm 0.511 \mu\text{m}$ and $1.414 \pm 1.461 \mu\text{m}$ respectively. It is unknown whether the existence of these thick flakes is caused by incomplete delimitation of the graphite flakes during the synthesis process or thin graphene flakes re-aggregation during sample deposition. However, the difficulties of distinguishing single flakes from the aggregated islands makes it impossible to calculate the yield from the number of thin and thick flakes. To make a reasonable estimation of the graphene yield, integrated flake area is one of the only few choices. In this case, a total flake area from thin graphene flakes is $147.47 \mu\text{m}^2$, while the area of thick flakes is $519.93 \mu\text{m}^2$, given a estimated yield of 22.1% for thin flakes. This technique can be useful for rapid characterisation and quantification of the yield of graphene, which can also be a practical application to exam the quality of deposited graphene film.

II. Lateral dimension distribution of thin graphene flakes

To obtain reliable statistics for the overall lateral dimension distribution of thin graphene flakes, a number of optical microscope images were analysed. Images were converted into RGB stacking, the green channel was used to filter the thin flakes from the background and thick flakes. With graphene flakes that has contrast value between 0.020 to 1 in green channel were chosen, a total of 6572 thin flakes with lateral dimension $>200\text{nm}$ and circularity between 0.3 to 0.9 were selected for statistical analysis.

A representative optical image is shown in Figure 4.10(a). With the 2Dtech™ graphene In Aquagraph series graphene sample used, the analysed image gives mean lateral dimension of $0.776\mu\text{m} \pm 0.345\mu\text{m}$ shown in figure 4.10(b). The raw histogram of the dimension distribution and commutative flake dimension percentage are plotted. The distribution

histogram consists of two Gaussian distributions, which are plotted and analysed in figure 4.10(c). One Gaussian peak is located at $0.625 \mu\text{m}$, with narrower peak width of $0.368 \mu\text{m}$ (indicated by the red line). The other Gaussian peak is located at $1.243 \mu\text{m}$, with a broader peak width of $0.489 \mu\text{m}$ (indicated by the green line). The broadening and asymmetric lateral dimension distribution can be explained by consisting both primary graphene flakes and aggregated flakes laying on the substrate¹⁶⁷. Also, the unintentional selection of both primary flakes and aggregated flakes is because of the lack of resolution of the technique. Thus, even though a thin flake selection method was employed in the experiment, the resolution still cannot distinguish primary flakes from aggregated flakes.

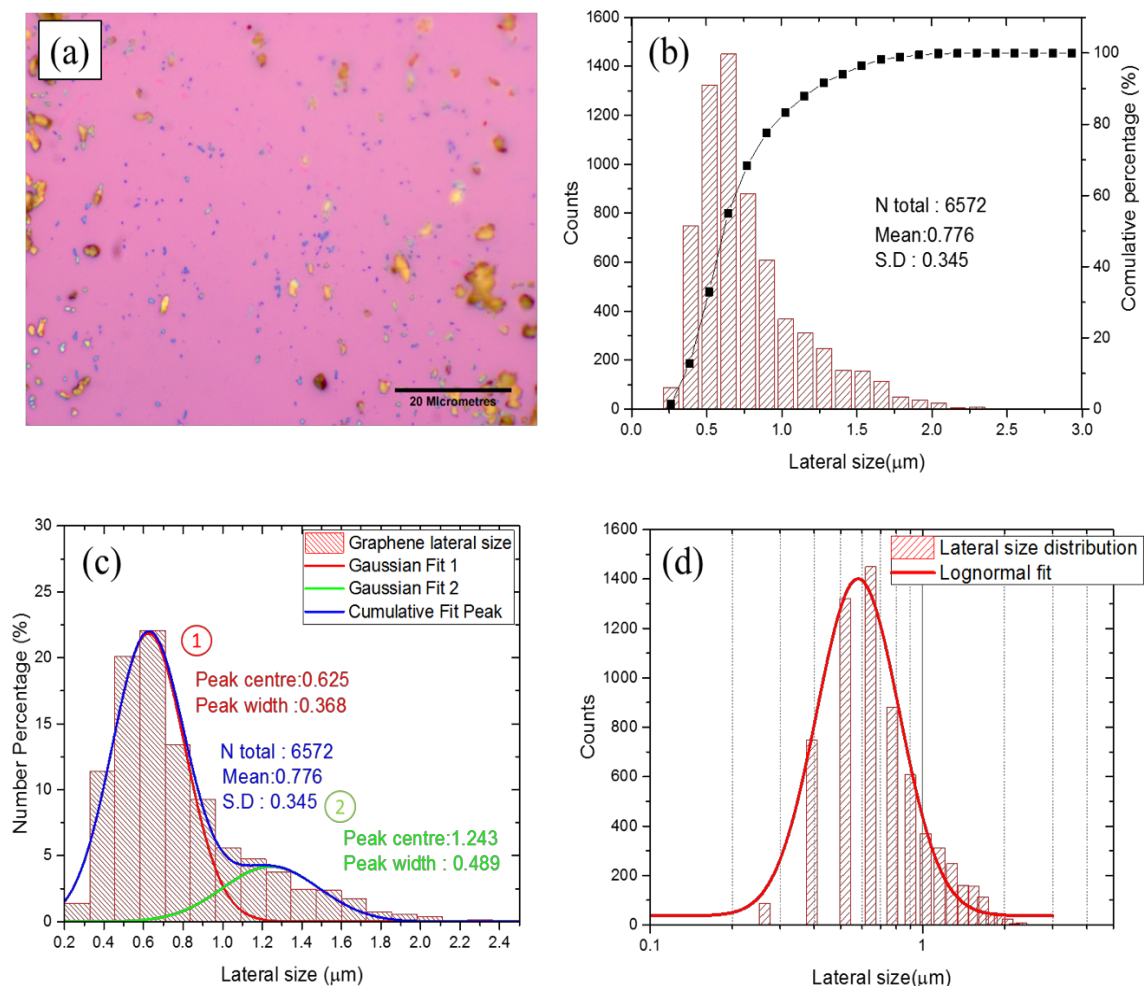


Figure 4.10: (a) OM image of thin and thick graphene flakes deposition onto SiO_2/Si wafer substrate via drop coating; (b) Cumulative percentage and Histogram of lateral dimension distribution on 6572 selected flakes; (c) The data was fitted with multi-Gaussian function with two individual Gaussians. Peak 1 represented lateral dimension distribution of primary flakes, Peak 2 represents aggregated flakes. (d) The distribution was fitted with lognormal distribution; a single symmetric distribution is obtained. (2Dtech aquagraph SAEG sample were used).

To further understand the flake distribution on the substrate, figure 4.10 (d) shows a plot of a histogram fitted with a lognormal function. The histogram shows a more symmetric distribution after the x-axis was converted to a log scale which can be fitted with Gaussian distribution (normal distribution), especially for flake dimension $< 1.1\mu\text{m}$. The finding indicates that the lateral dimension difference between primary flakes and aggregated flakes is not big; this can be explained by the graphene flakes having a tendency to stack vertically rather than horizontally.

From figure 4.10, the well distributed obtained histogram from OM images shows the technique can be used to detect multiple graphene flakes in order to make sufficient and reliable statistics. However, observation of the bimodal flake dimension distribution indicates that both primary flakes and aggregated flakes were included even when thicker flakes were excluded during flake selection process, meaning that the current selection technique does not have the capacity to differentiate primary flakes from the aggregated flakes with a high degree of detail.

III. Comparison with TEM

Having determined the graphene lateral dimension distribution by TEM and OM, I now proceeded to analyse the discrepancy between these approaches. The mean lateral dimension of flakes is $0.776\mu\text{m} \pm 0.345$ from OM observation, whereas the value is $0.934\mu\text{m} \pm 0.430$ for TEM. This difference arises from the quantity of graphene flakes selected for statistics. For TEM observation, only 199 flakes were selected to obtain the lateral dimension distribution, nearly half of these flakes were larger aggregated flakes which result in a higher mean flake dimension. In contrast, over 6572 graphene flakes were analysed by OM and the primary and aggregated flakes cannot be resolved in this case. This gives an unbiased flake dimension distribution where the number of primary flakes is much higher than the aggregates.

Figure 4.11 (a) which shows a comparison of the lateral dimension distributions obtained by OM and TEM where the flake counts in previous histograms were normalised and

expressed as a number percentage. From the OM analysis, the primary Gaussian peak is centred at $0.625\mu\text{m}$ which corresponds to the primary peak at $0.619\mu\text{m}$ obtained from TEM with only 0.9% of difference. The secondary peak from OM analysis is a Gaussian peak centred at $1.243\mu\text{m}$, with only 0.5% difference compared with from the TEM observation, which is higher in relative intensity.

The deviation between OM and TEM observation is further evident by the cumulative frequency plot as a function of lateral dimension. As shown in Figure 4.11 (b) The median value for TEM is $0.917\mu\text{m}$, 250 nm larger than the value obtained from OM. This highlights the flake counting efficiency of the TEM method, where a similar number of primary flakes and aggregates were taken into statistics, resulting in a larger median number. Figure 4.11 (c) shows the direct and relative deviation of the graphene flake diameter as a function of the TEM measured value. The blue vertical line indicates the direct and relative deviation at the median value. Several discontinuous breakpoints are evident in the plot graph, as well as the TEM cumulative percentage curve. Conversely,

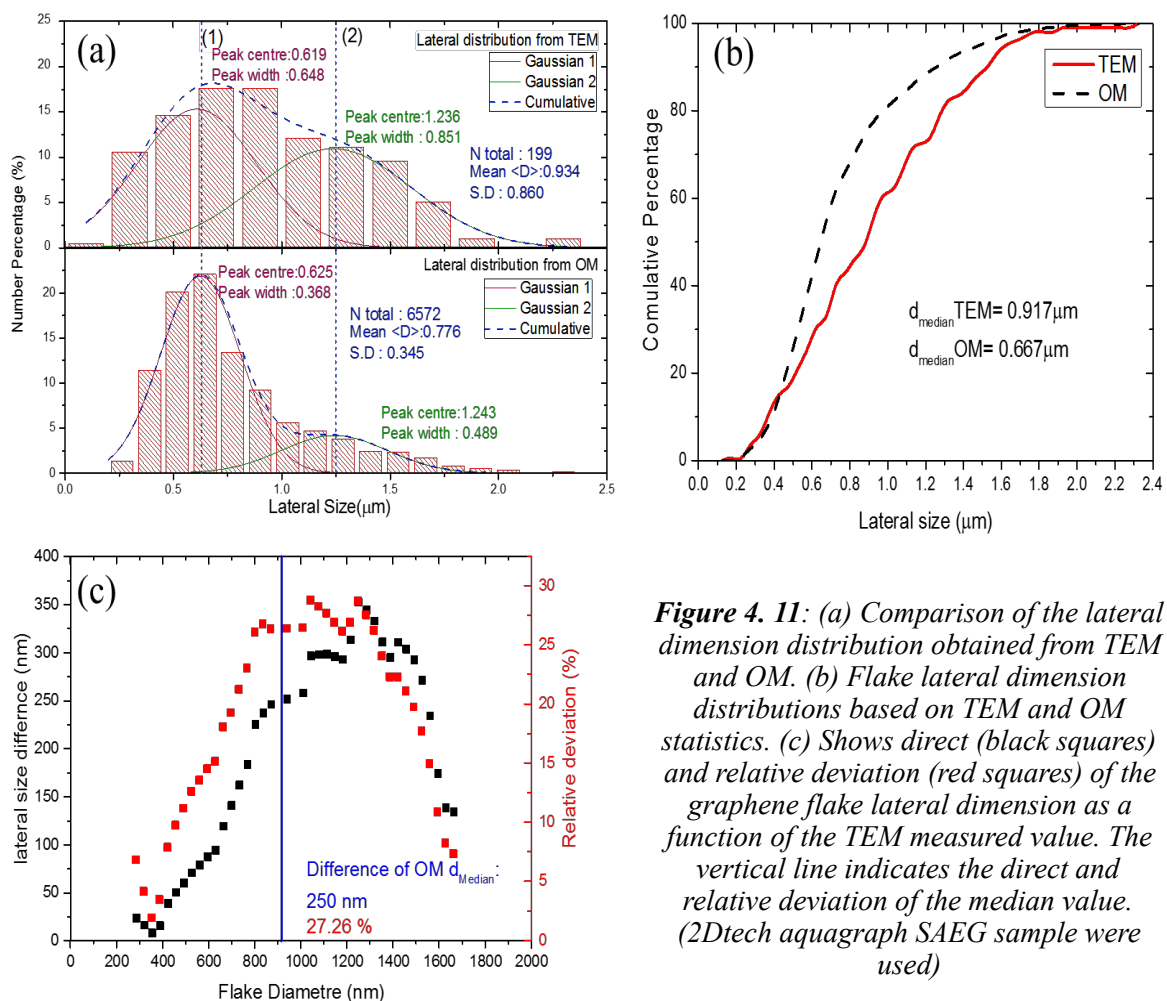


Figure 4. 11: (a) Comparison of the lateral dimension distribution obtained from TEM and OM. (b) Flake lateral dimension distributions based on TEM and OM statistics. (c) Shows direct (black squares) and relative deviation (red squares) of the graphene flake lateral dimension as a function of the TEM measured value. The vertical line indicates the direct and relative deviation of the median value. (2Dtech aquagraph SAEG sample were used)

the cumulative percentage from OM shows a much smoother curve, indicating that sufficient flakes were selected for statistical analysis.

In summary, the graphene lateral dimension distribution can be obtained from optical microscope images. Utilising a Fabry-Perot structure as the substrate enhances the contrast between the graphene sample and background. This provides a rapid technique to extract the lateral dimension distribution of graphene flakes from the optical microscope images. Analysis shows that the obtained distribution curve corresponded to the TEM observation. A small difference with the TEM observation is found, which implies that the lateral dimension distribution of the sub-micrometre graphene flakes can be effectively obtained by the image analysing technique.

4.3. Light scattering techniques

Light scattering techniques are investigated to develop an in-situ method for particle size distribution (PSD) in a dispersion. A suspension of particles illuminated by a light beam causes some of the light to be scattered. In general, the wavelength of light and the scattered angle depends on the particles size, shape and refractive index. Measurement of extinction or turbidity of photons is the simplest way of deriving information on particle size in suspensions. However, more detailed information requires more complicated techniques by measuring the angular distribution of scattered light ¹⁶³.

A well-known theory (Mie theory) is often used for spherical particle sizing, involving several approximate approaches. For studies of sub-micrometre or nanoscale particles, it usually requires certain assumptions to simplify the system. Nevertheless, it is often impossible to calculate a detailed particle size distribution because of complicated light-matter interactions that occur at this scale ¹⁷⁵⁻¹⁷⁷.

In general, there are two light scattering techniques for particle sizing: static light scattering, which measures average scattered light intensities and gives information over a wide range of particle sizes. Dynamic light scattering is another widely used technique that gives values of diffusion coefficients of particles from which size information can be derived. However, this method relies on the Brownian motion of particles, so it is only suitable for smaller particles (no larger than 3 μm depending on the density and hydrodynamic friction of the particles).

The goal of this part of the study is to develop a simple, fast and in-situ method to measure the lateral dimension of dispersed graphene flakes. This method should be straightforward and commonly available. In fact, many commercialised instruments can be used to measure the size of colloidal particles. Here, we employ two commonly used particle sizing techniques based on light scattering (1) Laser diffraction particle sizing and (2) Dynamic light scattering (DLS). These techniques are reported to work well for spherical particles but are less reliable for non-spherical geometries. For non-spherical objects like carbon nanotubes (CNT) or graphene, the relationship between diffusion coefficient and dimension can be much more complex. Therefore, data analysis can be much more difficult, and the errors can be significant. In this section, we try to develop a simpler approach to obtain graphene lateral dimension distribution, by discovering a semi-empirical relationship between the data given by the light scattering techniques and lateral dimension distribution obtained from optical microscopy. This correlation relationship can then be used to refine the real graphene lateral dimension distribution from the light scattering data.

I. Laser diffraction particle sizing

Laser diffraction particle sizing is a static light scattering technique. The technique utilises a monochromatic laser light beam that is passed through the particle sample and focused on the centre of a forward scattering detector. Figure 4.12 (a) shows a schematic plot of the system setup; all light scattered in a specific direction is projected in one point

of the focal plane that is independent of the particle's position in the measurement cell. In the case of spherical particles, a specific diffraction pattern is produced with a ring in the centre, the intensity decreasing outwards from the centre of the ring. The radius of the ring depends on the diameter of the spherical particle, so the information of particle size and shape can be extracted by analysing the diffraction pattern ¹⁶².

A commercially available laser diffraction system (Malvern Mastersizer 2000 series) was used in the study. A 633nm He-Ne gas laser with max output of 4mW and beam diameter 0.63mm provided the light source. The flow cell system was firstly pre-filled with IPA and 15 seconds of period measurement with 5000 snaps was used to acquire the background signal. The graphene suspension was sequentially injected into the flow cell system. The measurement of the sample takes 15 seconds and 5000 snaps of spectrum. To avoid turbulence and uncertainty in the signal from the flow cell, the speed of the pump was set as low as 700rpm; the stirring speed was set at 500rpm.

With the commercialise 2Dtech Aquagraph series graphene sample used, the raw particle size distribution (PSD) data is shown in figure 4.12 (b). The flake size ranges from 0.83 μm to 30 μm , but most of the flakes are smaller than 13 μm . For laser diffraction particle sizing, it is difficult to get a diffraction signal from particles smaller than 0.5 μm , because of the limitation of the optical setup. As a result, the resolution of the technique is not high enough to differentiate primary flakes and aggregated flakes. Figure 4.12 (c) shows lognormal fitting of the number PSD (Particle Size Distribution) obtained from laser diffraction particle sizing. A symmetric Gaussian distribution was observed after the x-axis transfer to log scale, the peak centre is located at 2.077 μm and peak width is 0.469 μm .

A significant difference in PSD values was found when using laser diffraction particle sizing and microscopic techniques. This can be caused by equipment sensitivity. For the microscopic techniques, flakes ranging from 200 nm to 3000 nm can be easily selected and analysed; while particles larger than this range are considered as agglomerates. Conversely, flakes smaller than 500nm (which is the size range of most primary flakes) cannot be detected by the laser diffraction technique. For the laser diffraction technique,

bigger agglomerates can easily be detected, resulting in a significantly higher flake size distribution.

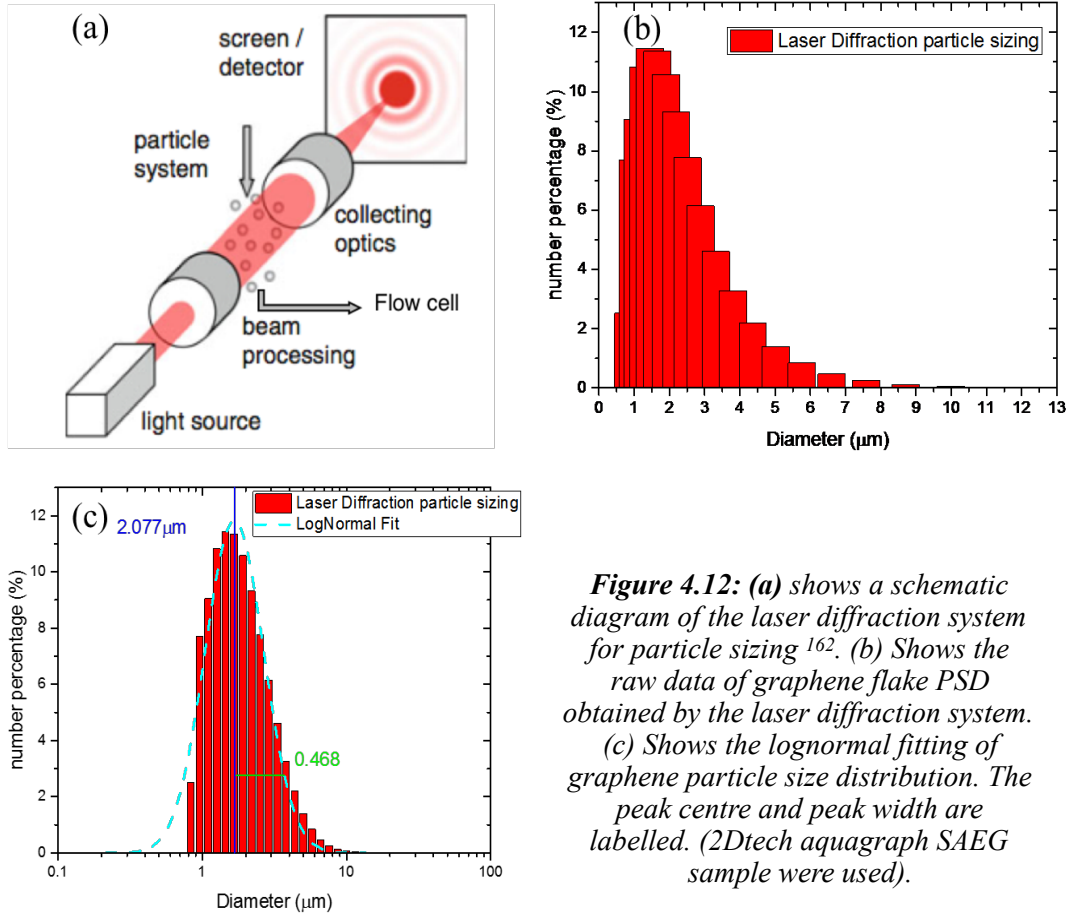


Figure 4.12: (a) shows a schematic diagram of the laser diffraction system for particle sizing ¹⁶². (b) Shows the raw data of graphene flake PSD obtained by the laser diffraction system. (c) Shows the lognormal fitting of graphene particle size distribution. The peak centre and peak width are labelled. (2Dtech aquagraph SAEG sample were used).

II. Dynamic light scattering

The basic principle of dynamic light scattering (DLS) is that the wavelength of light scattered from a moving particle will have wavelengths from the incident light, according to the Doppler Effect. In a colloidal dispersion, random Brownian motion of the particles causes scattered light to vary randomly in frequency. The interference between the scattered light from the different particles cause random fluctuations in the light intensity which is detected by a stationary sensor. The DLS technique resolves the fluctuated light intensity over a period and information on moving particles can be extracted by measuring the auto-correlation of the intensity distribution as a function of time. Smaller, faster-

moving particles will show a faster change in their intensity fluctuation versus time and this effect can be used to quantify the particle size. Thus, in a stable temperature condition, the translational diffusion coefficient D of a particle can be derived from the Stokes-Einstein equation:

$$D = \frac{KT}{6\pi\eta a} \dots (\text{Equation 4.9})$$

, where T is the absolute temperature, K is Boltzmann's constant, η is the liquid viscosity, and a is the hydrodynamic radius of the spherical particles. In general, static fluid layers with respect to the particle was taken into consideration when a particle moves through the liquid medium ^{178,179}.

In this study, a commercially available DLS instrument, Malvern Zetasizer Nano ZS was used. Unlike the sample preparation for microscopy in which graphene flakes were deposited onto a substrate for observation, for DLS the graphene suspension was contained in a cuvette cell. Using a 633-nm laser, the diluted graphene suspension sample is prepared in a quartz cuvette cell, having a 10-mm path length. Because the parameters are highly temperature-sensitive in Brownian motion, the sample is equilibrated to 25°C for 120 seconds prior to each measurement. The solvent is IPA, which has a viscosity value at 25°C of 2.32 (cP). By operating in backscatter mode (173° scattering angle), it was possible to detect the particle size using the equipment's automatic optimised beam-positioning system. This auto-beam-position setting optimises the focus position and attenuation of the incident laser before the data collection, which can reduce multiple scattering of the light from the concentrated sample area. Different analysis algorithms are available in the software from Malvern Zetasizer Nano ZS to derive particle size distribution. Intensity particle size distribution (PSD) is the most direct expression in the software, where the algorithms analyse the correlation of scattered light and outputs the relative intensity of light scattered by different particle sizes. This algorithm requires only solvent viscosity and refractive index. However, because of the larger scattering cross-section of larger particles, intensity PSD mode is particularly sensitive to the presence of large particles or aggregates based on the Mie theory. The software of the Zetasizer allows

user-programmed mode to obtain detail of the number distribution of dispersed particles. The conversion requires refractive index and absorption of the sample particle. The calculation is usually reliable for spherical particles, but in our system, the exfoliated layered graphene is clearly not spherical, and the optical properties are still under discussion.

i. Approximated refractive index of graphene for obtaining lateral dimension distribution

To compare the DLS data with the lateral size distribution obtained from the microscopy techniques, approximate optical properties of graphene and graphite were applied to obtain the number PSD. The refractive index of graphite and exfoliated graphene were calculated based on the experimental work of Weber et al.⁹⁹ and A. B. Djurišić¹⁸⁰, where the optical properties of graphite and graphene were obtained from direct measurement using spectroscopic ellipsometry⁹⁹ (see figure 4.13). The wavelength-dependence refractive index can be derived¹⁸¹. In our system, the sample is under 633 nm He-Ne Laser illumination and the real part of refractive index (n) and extinction coefficient (k) of graphene are obtained as 2.730 and 1.355 respectively. When complicated refraction phenomena are neglected, the group refractive index (n_g) can be calculated from^{171,181}:

$$n_g = n - \lambda \frac{dn}{d\lambda} \dots \text{(Equation 4.10)}$$

, here λ is the wavelength of the laser in vacuum and the chromatic dispersion ($\frac{dn}{d\lambda}$) is approximated by 0.797 near the laser wavelength⁹⁹. The group refractive index of exfoliated graphene under 633nm of laser illumination is then estimated to be 2.225. A similar calculation was performed on graphite, where the group refractive index was obtained as 1.942. The material absorption is also required to derive the number PSD. The absorption $\alpha = \sigma t$, where σ is absorption coefficient of the sample and t is sample thickness. The absorption coefficient of graphite and graphene can also be estimated as:

$\sigma_{\text{graphite}} = 0.03116 \text{ (nm}^{-1}\text{)}$ and $\sigma_{\text{graphene}} = 0.02656 \text{ (nm}^{-1}\text{)}$ ¹⁸¹. By providing the optical parameters and the molecular weight of the solvent and solute, the software of Zetasizer not only allows the derivation of particle size distribution, but also the properties of graphene suspension. The suspension concentration can also be calculated based on Rayleigh's equation ^{179,182}, and the information about the sample sedimentation can be provided by the outputted correlation function.

However, it is important to note that the calculations discussed above are based on standard graphite and polycrystalline CVD monolayer graphene, where the factors of incompletely delaminated graphene, defects and multi-interface reflections in the graphene suspension are neglected, due to the current inaccessibility of accurate parameters. Thus, the analysis is only valid in ideal conditions and optimisation of optical parameters is still needed for our system. However, though an accurate measurement is still unavailable, the measurement based on these calculated parameters can still provide insights of the suitability when adopting the ideal graphene properties to the unconventional solution processed sample as discussed.

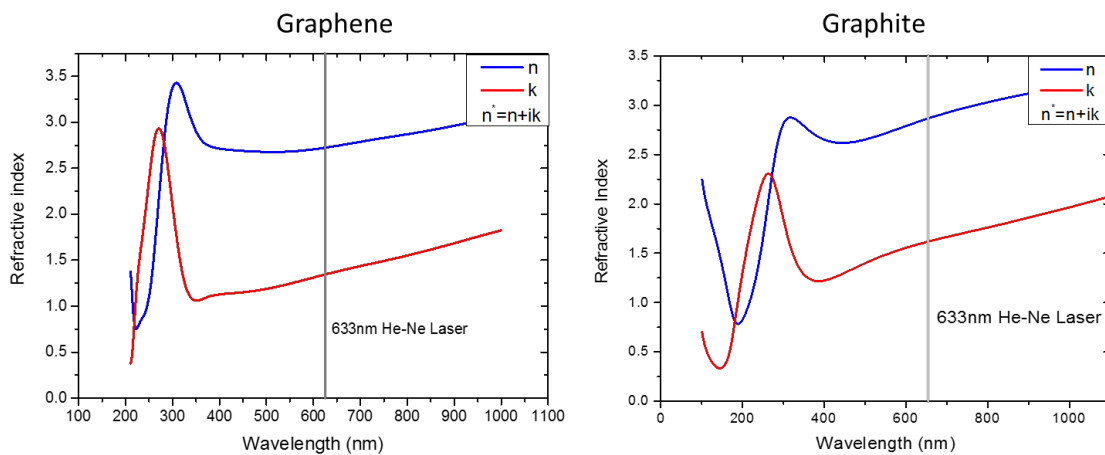


Figure 4.13: Shows simulated Refractive index and Extinction coefficient of graphene and graphite. The grey line says wavelength of He-Ne laser that is used in the DLS equipment. (Based on Weber et al. and A. B. Djurišić's work ^{99, 180})

ii. Obtaining graphene lateral dimension from DLS

To investigate a suitable optical setup for DLS study, different values for the refractive index (RI) and material absorption (α) between graphene to graphite were tested. The number PSD spectra were obtained from a slightly diluted stock 2Dtech sample, using various optical parameters: (1) Refractive index of graphene with 1nm of thickness, where absorption is $\sim 3\%$ of incident light, the optical parameter will be ($RI_{\text{graphene}}; \alpha_{1\text{nm}}$); (2) Refractive index of graphite with 3nm of thickness which $\sim 10\%$ of incident light was absorbed ($RI_{\text{graphite}}; \alpha_{3\text{nm}}$); (3) Refractive index of graphite with 5nm of thickness, $\sim 15\%$ incident light absorbance ($RI_{\text{graphite}}; \alpha_{5\text{nm}}$). The obtained number PSD spectra are shown in figure 4.14 and quantified by Gaussian distribution, in which this spectra data fits well with the Gaussian model (with $0.9 < r\text{-square} < 1$) . The PSD spectra obtained using graphene refractive index ($RI_{\text{graphene}}; \alpha_{1\text{nm}}$) demonstrates the narrowest peak width

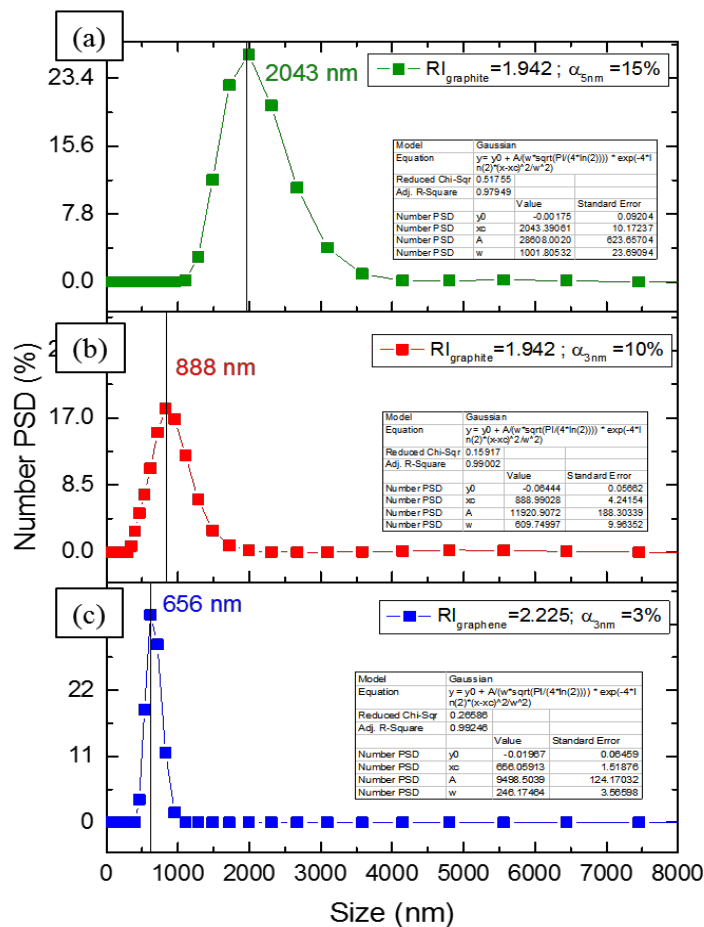


Figure 4.14: Shows number PSD obtained using different optical property settings. (a) Number PSD obtained from the refractive index of graphite with 15% absorbance (b) Number PSD obtained from refractive index of graphite, with 10% absorbance (c) Number PSD obtained from refractive index of graphene, with 3% absorbance (2Dtech aquagraph SAEG sample were used)

(FWHM=246 nm). The peak centre $X_c = 656$ nm (shown in figure 4.14(c)). Wider number PSD spectra were obtained when utilising the refractive index of graphite. Figure 4.14 (a) and (b) shows the width (FWHM) of DLS peaks of 609 nm and 1001 nm for $(RI_{\text{graphite}} ; \alpha_{3\text{nm}})$ and $(RI_{\text{graphite}} ; \alpha_{5\text{nm}})$ respectively. The centres of peaks are also shifted to higher lateral size, where $(RI_{\text{graphite}} ; \alpha_{3\text{nm}}) = 822$ nm and $(RI_{\text{graphite}} ; \alpha_{5\text{nm}}) = 2015$ nm.

The number PSD obtained from $(RI_{\text{graphene}} ; \alpha_{1\text{nm}})$ and $(RI_{\text{graphite}} ; \alpha_{3\text{nm}})$ are not too different from the results of microscopy image analysis. The distribution obtained from $(RI_{\text{graphene}} ; \alpha_{1\text{nm}})$ corresponds to the primary flakes obtained from OM, where the peak centres are 622 nm and 625 nm for DLS and OM (see figure 4.10(c)). The number PSD obtained from $(RI_{\text{graphite}} ; \alpha_{3\text{nm}})$ is also similar to the combined distribution of primary and aggregated flakes. The peak centre of DLS measurement is 822 nm where the values are 776nm and 934nm from OM and TEM observation respectively.

III. Comparison to direct image tracking technique

However, the particle size distribution obtained from DLS can be highly influenced by the concentration and inhomogeneity of the graphene suspension. The optimised position of the laser beam in DLS can vary over time and this can significantly affect the outputted particle size distribution.

To minimise the uncertainty caused by sample inhomogeneity and to carefully compare the DLS result with the data obtained from microscopy methods, the stock 2Dtech Aquagraph series graphene sample was sediment for 48 hours to fractionate the graphene flakes by size. Two optical parameters, $(RI_{\text{graphene}} ; \alpha_{1\text{nm}})$ and $(RI_{\text{graphite}} ; \alpha_{3\text{nm}})$ were used to obtain number PSD in the DLS experiment. The lateral dimension distribution of thin graphene flakes is also obtained from OM and compared with the DLS results. The primary peak position of the number PSD from DLS was used, the value will be referred to as X_c . Figure 4.15(a) shows a photograph of a 20-ml graphene suspension sample sediment for 48 hours. It is clear to see that the transparency of the sample gradually decreases towards the bottom of the sample. The fractionated sample was taken out

sequentially every 4-ml (roughly 1 cm depth in the container). The fractionated samples were labelled 1L for the top layer to 5L for the bottom layer. The flake size distributions of each sample were measured by both DLS and OM and the results are normalised and expressed in number percentage shown in figure 4.15 (b)-(f). Further analysis and the deviation between these measurement techniques are shown in figure 4.16.

In general, the number PSDs obtained from DLS correspond to the OM results, but the deviation is evident when comparing the mean lateral dimension $\langle L \rangle$ of OM observation to the peak centre from DLS (X_c) measurement. The absolute difference and relative deviation of the measured flake dimension between these techniques are shown in figure 4.16 (a). It is clear to see that for flake dimension < 1000 nm, the deviation between $\langle L \rangle$ and X_c is small, the value of relative deviation is less than 22% in this region. However, the deviation becomes significant when the flake dimension > 1000 nm. The deviation between these two techniques could be due to re-aggregation of graphene flakes during the OM sample preparation process. Thin graphene flakes can re-aggregate on the substrate when the solvent evaporates, resulting in larger mean values obtained by OM than by DLS measurement. However, when the concentration of the suspension exceeds a certain point, the aggregation of thin flakes can even happen in-situ in the suspension, resulting in similar X_c and $\langle L \rangle$ values (see figure 4.15 (e) 4L). For flakes >1000 nm, the significant deviation between the OM and DLS measurements can be caused by the existence of agglomerates. The boundary of agglomerates is difficult to recognise and define by the OM technique and their hydrodynamic properties can also be very different from thin graphene flakes, resulting in a significant deviation between OM and DLS data. The discrepancy can be reduced by picking up thick flakes in OM rather than thin flakes. Though the particle size distributions still do not match up very well, the deviation between X_c and $\langle L \rangle$ can be reduced to less than 25% when analysing thick graphite, these results are shown in figure 4.15 (f) 5L and figure 4.16 (a).

For DLS measurement, minimal differences were obtained by utilising graphene ($RI_{\text{graphene}} ; \alpha_{1\text{nm}}$) or thin graphite ($RI_{\text{graphite}} ; \alpha_{3\text{nm}}$) optical parameters. The deviation of number PSD obtained from graphene ($RI_{\text{graphene}} ; \alpha_{1\text{nm}}$) or thin graphite ($RI_{\text{graphite}} ; \alpha_{3\text{nm}}$) are shown in figure 4.16 (b). In the first two fractionated suspension layers, a slightly

larger number PSD is obtained using the refractive index of graphite (RI_{graphite}). The distribution becomes almost identical when it comes to the third and fourth fractionated layers (see figure 4.15 (b)-(e)). However, the deviation became large at the bottom layer of the fractionated suspension (figure 4.15 (f)). This could be caused by distinctive hydrodynamic and optical property differences between thin flakes and thick

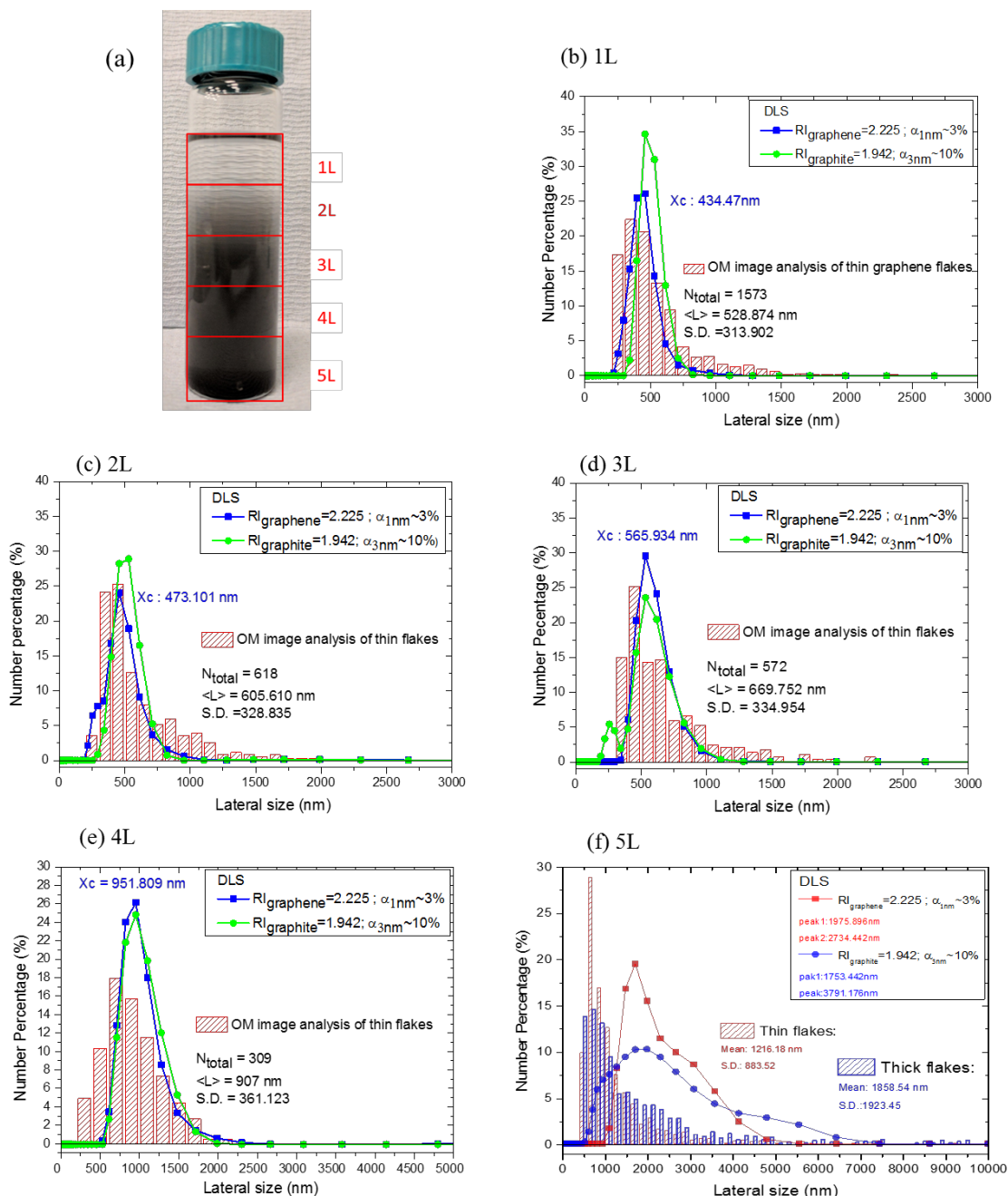


Figure 4.15: shows graphene lateral dimension distribution of a fractionated sample. (a) Fractionated graphene lateral dimension by sedimenting the stock sample for 48 hours. The 20ml fractionated sample was sequentially taken out and split into 5 layers, labelled 1L-5L. (b)-(f) shows the lateral dimension distribution of graphene flakes obtained from DLS and OM for these 5 fractions (2Dtech aquagraph SAEG sample were used)

agglomerates. In general, number PSD obtained from either optical setup matches with flake size < 1000 nm, where the differences are less than 20%.

Figure 4.16 (c) shows the mean graphene lateral dimension $< L >$ as a function of sample layer depth. It is clear to see that larger graphene flakes can be found in the deeper layers. Fitting the data to an exponential:

$$< L > = L_0 + A_1 \exp\left(x - \frac{x_0}{\tau_1}\right) \dots (\text{equation 4.2})$$

, g a v e $L_0 = 424.626 \pm 35.28$ (n m) , $A_1 = 45.556$, $x_0 = 0.307$ (c m) , a n d $\tau_1 = 1.664 \pm 0.13$. The value x is the position originating from the surface of the suspension in units of centimetres. Thus, the lateral dimension of the graphene flakes can be estimated via the position (x) that the observer takes out the sample. This represents sedimentation of larger flakes under the influence of gravity.

The primary peak position from the number PSD (X_c) was plotted against $< L >$, the plot is shown in figure 4.15(d). The X_c values using different optical properties are close to each other and scale linearly with $< L >$ on the log-log plot in the sub-micrometre region. This means that the X_c is correlated to $< L >$ by a power law. Fitting the data with $X_c = a < L >^b$, gives an exponent $b = 1.594 \pm 0.12$ and $a = 0.018 \pm 0.015$. The relationship can provide a simple estimation of graphene lateral dimension distribution by measuring the DLS number PSD. Using the data in figure 4.16 (d), we can write:

$$< L > = (12.433 \pm 4.33) X_c^{(0.627 \pm 0.05)} \dots (\text{equation 4.11})$$

This DLS method using approximate optical properties of graphene flakes offers a simplified and rapid method to estimate graphene lateral dimension distribution in liquid phase dispersions. This alternative approach provides similar precision to the direct imaging technique using OM and TEM for graphene flakes of sub-micrometre in dimension, for which the direct imaging technique such as TEM and AFM are much more time-consuming and labour-intensive characterisation techniques.

However, it is important to appreciate the drawbacks of the empirical approach. Firstly, due to the sensitivity limitation of the instrument, the increment of the x-axis is quite big, meaning there are still some uncertainties and a degree of unreliability with the DLS data. Each of the number PSD spectra presented is averaged from 3 measurements, providing more reliable results. It is also clear to see from figure 4.15 and 4.16, , when the flake size exceeds 1000 nm, the uncertainty of DLS increases significantly. This uncertainty can be affected by sample concentration, the light scattering event being too low to be detected when the absorbance per unit length is lower than $0.001m^{-1}$.^{178,179}

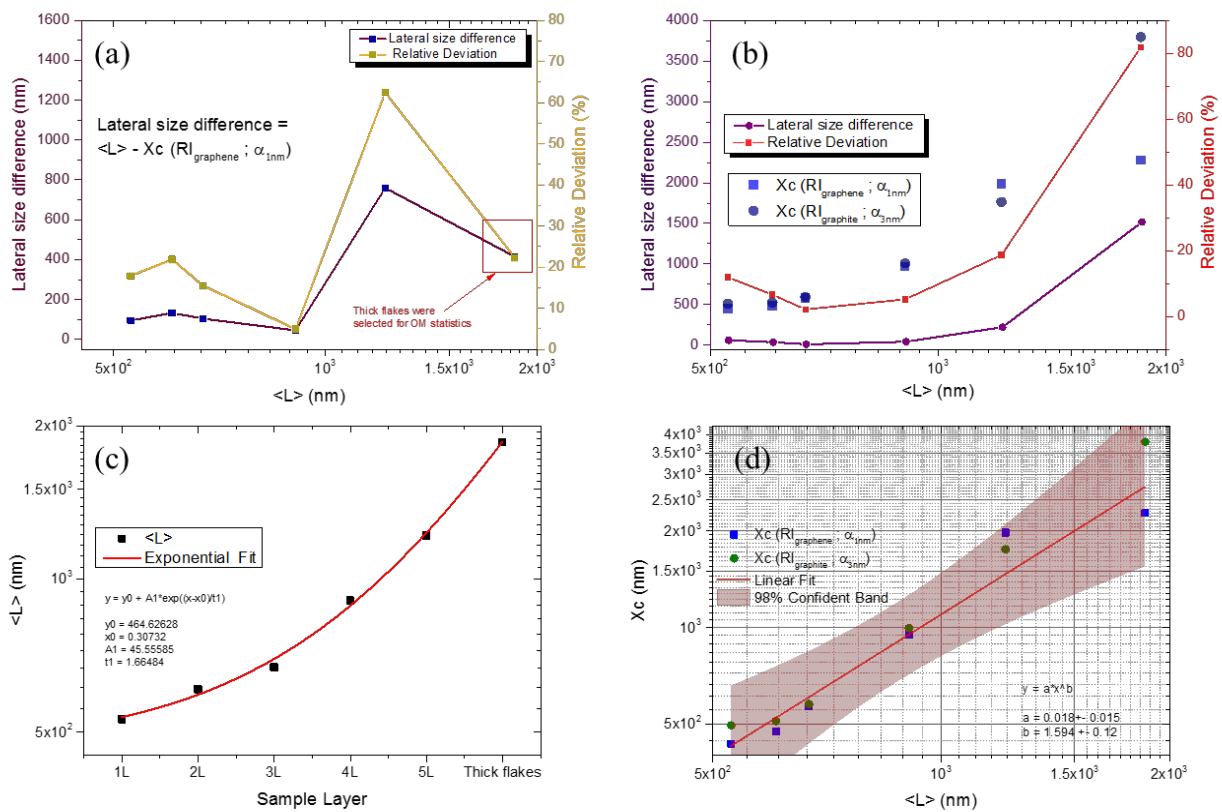


Figure 4.16: (a) absolute (purple squares) and relative deviation (brown squares) of the difference in graphene sheet diameter determined by OM and DLS as a function of the OM measured value, (b) The absolute (Red squares) and relative deviation (purple circles) between number PSD obtained by graphene ($RI_{\text{graphene}}; \alpha_{1nm}$) and thin graphite ($RI_{\text{graphite}}; \alpha_{3nm}$) as a function of OM measured $\langle L \rangle$. (c) Mean lateral dimension value $\langle L \rangle$ obtained from OM as a function of sampling position, the red line is fitted exponential dependence (d) Number PSD position Xc versus flake mean lateral dimension $\langle L \rangle$, Red line is fitted power law dependence of Xc with $\langle L \rangle$. (2Dtech aquagraph SAEG sample were used)

4.4. Conclusion

In this chapter, a method to estimate the lateral dimension distribution for exfoliated graphene in liquid was developed. To do this, we started with the most precise technique by deriving the graphene lateral dimension from TEM images; the result was used as a benchmark for the other techniques. An image analysing technique that can obtain lateral dimension distribution of graphene flakes rapidly by analysing optical microscopy (OM) images was developed. The technique can distinguish thin and thick graphene flakes from their reflected spectrum on SiO₂/Si substrates. Multiple optical microscopy images were analysed, and the lateral dimension distribution of thin graphene flakes was obtained. A very good correlation with an error of 0.9% and 0.5% for the mean value of primary flake and aggregated flake lateral dimension is obtained respectively. The limitations and possible uncertainties of the image analysing technique were also discussed.

To develop an in-situ observation of the graphene lateral dimension distribution, light scattering techniques were undertaken. Static laser diffraction particle sizing was firstly tested, but the technique is limited by its resolution. In contrast, Dynamic light scattering is a more sensitive technique to derive flake lateral size. To compare the DLS data with previous image tracking techniques, approximate optical properties of graphene and thin graphite flakes were used to obtain number PSDs from DLS. Sedimentation based size selection method was employed to prepare dispersions of graphene and heterogeneity in the sample. In all cases, the lateral flake size distributions were firstly measured using OM. The same dispersion was then characterised by DLS. We found that the number PSDs outputted from DLS fit quite well with the size distribution measured from OM, especially for flakes smaller than 1000 nm (relative deviation <22%). This finding allows us to write an empirical expression that correlates the flake size distribution from OM to the DLS data, which can provide a fast and simple method to obtain a good estimation of the mean lateral size of graphene dispersed in liquid.

The methodology demonstrated in this section offers the possibility to monitor the lateral dimension of graphene accurately whilst avoiding time-consuming methods such as AFM

or TEM. This is valuable for quantifying one of the important properties of solution processed graphene and can be used to improve the industrial scalability of graphene manufacturing processes.

5.

Determination of graphene crystal imperfections

The crystal structure is one of the most crucial factors that determine the various chemical and physical properties of graphene. Ideally, graphene is consisting of a perfect two-dimensional honeycomb sp^2 -carbon lattice, but in reality, several crystal imperfections are usually exhibited in a graphene flake. As introduced in chapter 2, the crystal imperfection in real graphene can include in-plane lattice distortion/defects, edges or inter-plane uncompleted delaminated patches or twisted layers. These crystal imperfections usually appear spontaneously during material synthesis and in thin particles surface imperfections have a large influence on the overall character of the particle. The properties of graphene can be very sensitive to these imperfections ^{46,78,183}.

Atomic resolution microscopy such as STM and TEM are common methods to characterise the imperfections in graphene. Using conventional STM or TEM systems, the structural disorders such as vacancies, grain boundaries or foreign molecules can be visualised and characterised. However, one of the biggest challenges is the low throughput of such microscopic measurements, make such characterisation methods expensive and time-consuming to represent the highly inhomogeneity SAEG graphene samples ^{184,185}.

Raman spectroscopy and XRD provides a platform to characterise structural disorder in graphite/graphene-related materials in a shorter time scale and over larger area. However, as mentioned in Chapter 3, characterise the SAEG graphene using XRD can be biased and impractical. A general model for Raman spectroscopy that can be used to quantify the structural disorder in SAEG graphene is still lacking. This owing to the limitation of probe

size in conventional equipment, the experimental study is difficult and can only rely on empirical methods. ^{121,186–189}.

To assess structural imperfections in SAEG graphene, a practical characterisation method based on Raman spectroscopy was developed. As seen in figure 5.1, the structural imperfection in 2Dtech SAEG graphene sample were firstly characterised by TEM and the image data were analysed. On the other hand, a CVD graphene sample was used to clarify the effect of graphene edge on the Raman spectra, with random sampling method was utilised, a statistical analysis method was presented. The same sampling method was then applied to the 2Dtech aquagraph sample, the structural imperfection was calculated by the existing model, the results are compared with the TEM data.

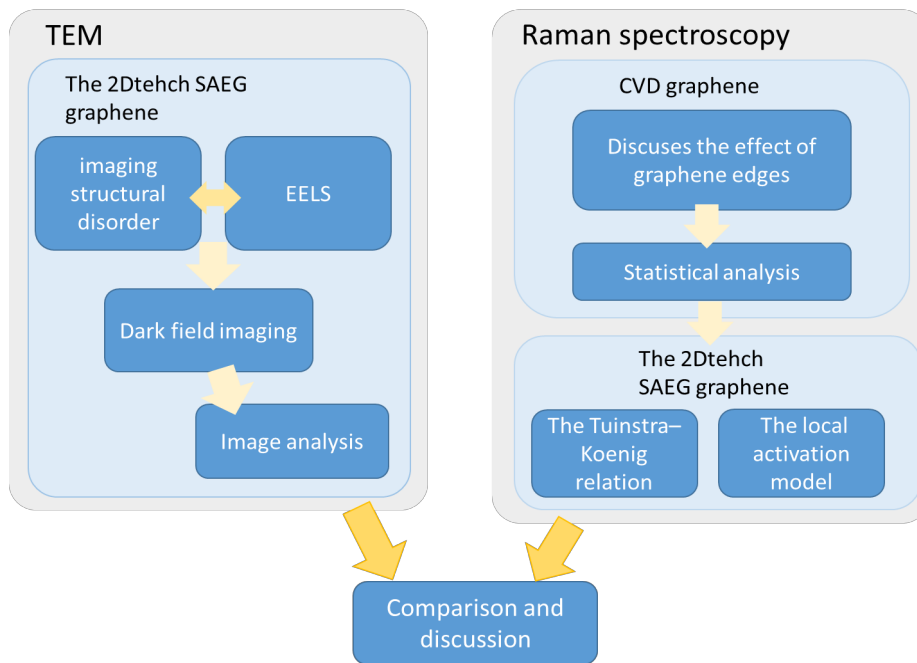


Figure 5.1: Procedure to determine the structural imperfection in graphene flakes.

5.1. Characterise graphene crystal

imperfection by TEM

I. Imaging crystal imperfections

High-resolution TEM images consist of information about graphene lattices. Figure 5.2 shows a high-resolution bright-field TEM image, which was conducted using 80keV acceleration voltage and 240,000X of magnification. The image comprised by three major regions: graphene flake, a vacuum region and amorphous carbon film from the TEM grid, they are labelled as (1), (2) and (3) respectively.

Owing to unique features shown the images, regions of different materials can be identified. One of the most significant features is the periodic patterns appears in the image. To identify and quantify the periodic structure in the image, a 300×300-pixel sampling was taken from each region. As shown in figure 5.2(b), the amorphous film shown the highest in image entropy while the vacuum region is the lowest, meaning the feature of randomness in amorphous film is higher than in the vacuum region (denoted as s)^{190,191}. The histogram of grey value shows high standard deviation in the region of amorphous carbon, but much less in the vacuum region. This indicates that the randomness of grey value in the image of amorphous carbon region is not originated from the shot noise, but the disorder of the amorphous crystal.

As mentioned in chapter 2 and 3, FFT is a well-established technique to quantify a periodic structure. As shown in figure 5.2 (b) (2), a diffusive pattern was obtained from the vacuum religion, indicating no periodic features is presented. This is contrary to the FFT obtained from the graphene region, which shows a series of bright spots that is symmetrically arranged in a hexagonal pattern. These bright spots show a reciprocal space periodicity of $\sim 4.75\pm 0.68$ (1/nm) (shown as inset), which corresponding to 0.21 ± 0.04 (nm) in real space and hence the {110} plane of sp² carbon. Nevertheless, the FFT derived diffraction pattern of amorphous carbon film have demonstrated a broad ring at $\sim 1.85\pm 3.44$

(1/nm) outward from the centre, showing the amorphous carbon does not contain a well-defined lattice spacing

Therefore, the lattice in a graphene flake can be visualised and characterised by applying image process technique (introduced in chapter 3) on the HRTEM images. Figure 5.3 (a) shows example images of monolayer and multilayer graphene regions lattice obtained from the 2Dtech SAEG sample. It is clear to see significant non-uniformities in these high-resolution images, which can be due to the presence of surface contaminants or the

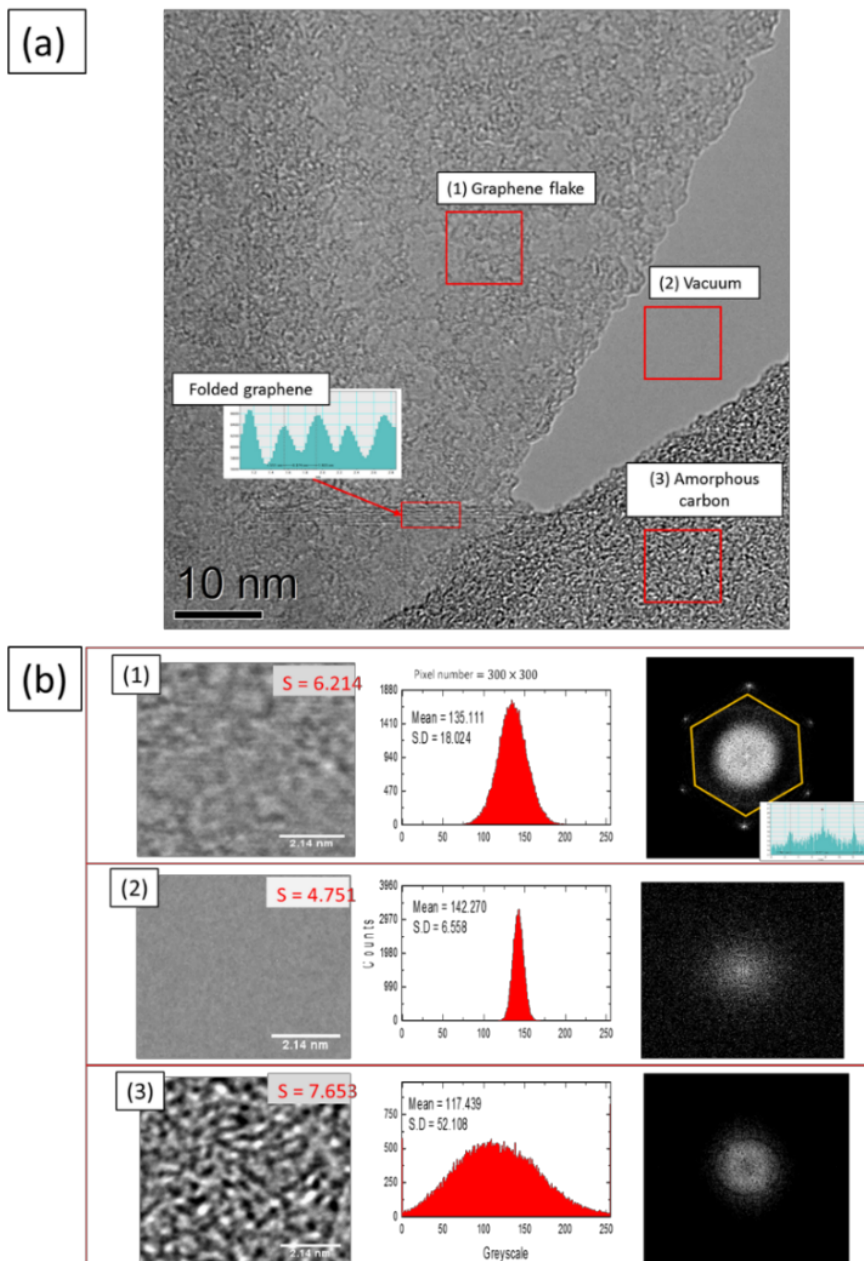


Figure 5.2: (a) Shows a bright-field HRTEM image that consists (1) graphene flake, (2) vacuum background and (3) amorphous carbon film. (b) Shows processed images of each areas. Histograms of greyscale shows image homogeneous of each area and FFT was applied to analyse periodic patterns in the microscopic image. (2Dtech aquagraph SAEG sample were used)

presence of different types of structural anomalies such as ripples. The insets display an FFT of these images, the $\{1100\}$ spots are seen, but the $\{2110\}$ spots are blurry. However, the comparatively obvious $\{2110\}$ spots appear in multilayer region, and the consistency of several series of oriented spots indicates the region may comprise grain boundaries or twisted layers.

Figure 5.3 (b) shows a graphene lattice obtained from IFFT. This image proves the hexagonal lattice structure of the graphene. The intensity profile analysis in figure 5.3 (c) plots along the left red line showing the hexagon structure has a width of $\sim 2.5\text{\AA}$, which is close to the expected value (2.46\AA , as referred to figure 2.1). Figure 5.3 (d) shows the intensity profile along the blue line, which provides the length of the sp^2 C-C bond, which is measured as $\sim 1.4\text{\AA}$, close to the expected value of 1.42\AA ⁷⁵.

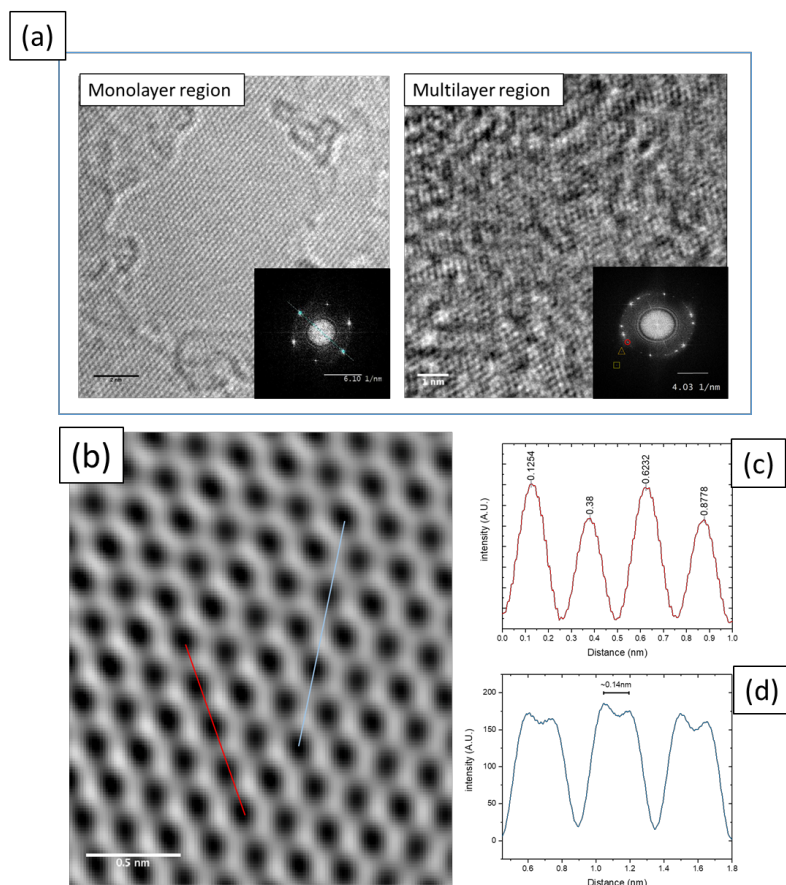


Figure 5.3.: High-resolution TEM images of 2Dtech SAEG graphene flakes. (a) HRTEM images of a monolayer and multilayer graphene region, insets show FFT (equivalent to an electron diffraction pattern) of the image. (b) A refined image of part of monolayer region in (a). (c) Intensity profile analysis along the red line shows a hexagon width of $\sim 2.5\text{\AA}$. (d) Intensity profile along the blue line measured the length of sp^2 C-C bond to be $\sim 1.4\text{\AA}$. (2Dtech aquagraph SAEG sample were used)

i. Topological defects and grain boundaries

However, not all the imaged regions appeared to be monolayer or free of structural defects in our sample. As seen in figure 5.4, topological defects are commonly found in such a SAEG graphene flake (highlighted by the red square in figure 5.4 (a)). These topological defects were reported due to an in-plane bond rotation / stretching between two atoms, resulting in the transformation of hexagon lattices to several heptagons and pentagons^{45,192}. The presence of topological defects could thereby induce strain / stress to the lattice, which could further distort the bond lengths or angles to the nearby graphene lattices⁴⁴, introducing inharmonic vibrational modes and shortening phonon lifetime as introduced in chapter 2.

Not only topological defects, grain boundaries are another common crystal imperfection in a graphene flake that separates a coherence two-dimensional domain into few different coherent regions. However, the grain boundaries in multilayer graphene could appear in two distinct configurations, as schematically shown in figure 2.6. The grain boundary can exhibit in an atomically bonded arrangement as for the monolayer graphene (Figure 2.6 (b)) or formed by an interlayer overlap as previously shown in figure 2.6(c)). The interlayer overlap grain boundaries were experimentally observed. An example of AB-stacked interlayer overlapping grain boundary is shown in Figure 5.4(b). The yellow line

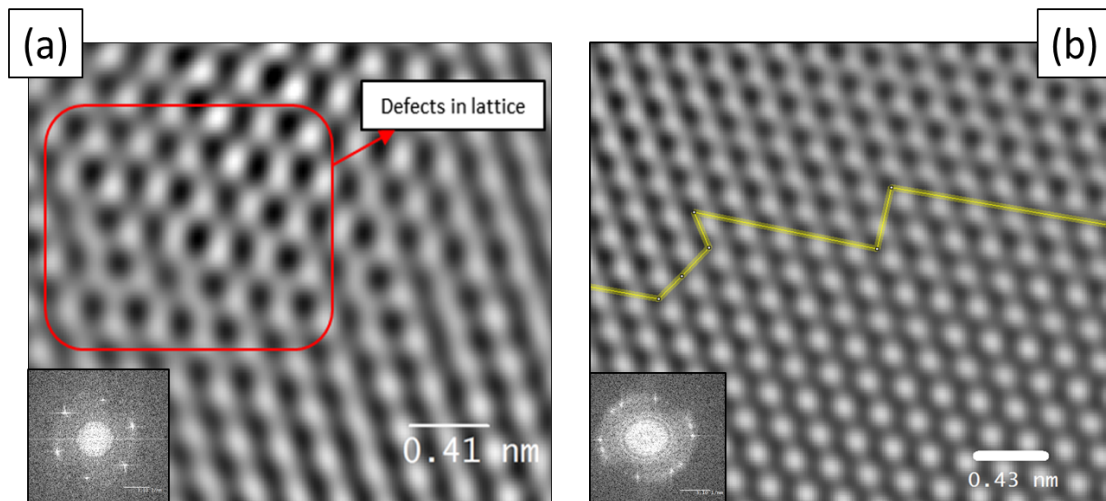


Figure 5.4: Refined TEM image shows crystal imperfections in a graphene flake. (a) the topological defect found in a monolayer graphene region. (b) the interface between monolayer and bilayer (lower part of the image). The insets are corresponded FFT. (2Dtech aquagraph SAEG sample were used).

have divided the domain into an upper and lower region, where the atoms in the upper region appear in white-contrast and are switched to black-contrast in the lower bi-layer region^{45,193}, indicating that an overlapping of graphene layers is presented in the region. An atomically bonded grain boundary was not found in the project, although it was believed to exist in our sample, it was hard to be found by using the proposed direct imaging technique. Nevertheless, it should be noticed that the atomic columns can appear white or black depending on the defocus condition. Therefore, such an image is difficult to provide direct information about the real graphene stacking configuration, other techniques such as SAED should be carried out to complementarily determine the stacking configuration of graphene^{45,77,78,194}. Nevertheless, although such an image may not be precise to determine the stacking configuration of graphene, it still qualitatively shows an evidence of that the interlayer overlapping grain boundary could be presented in a multilayer graphene.

ii. Misorientation and Turbostratic graphene

1) The Moiré Pattern of Turbostratic graphene

As introduced in chapter 2, the properties of a graphene flake are not only affected by the existence of the presence of uncompleted delaminated graphene regions, but also determined by the stacking configurations, as well as the relative twisted angle between two or more stacked graphene layers^{195–200}.

The presence of the Moiré pattern can be accounted to the existence of turbostratic graphene / graphite structures, where the graphene layers are weakly bonded and could have a rotation with respect to each other^{195,197,198,200}. This turbostratic graphene / graphite structure is commonly observed in the solution-assisted-exfoliated graphene sample, due to several delaminated graphene sheets, in which could re-aggregate and form a multilayer graphene flake. An example of the Moiré pattern is shown in figure 5.5(a), which is an evidence that the turbostratic graphene flakes are presented in the graphene sample. The twisted graphene region has shown a superlattice size of L , which is larger than the real lattice of graphene and can be seen in figure 5.5 (a) and its IFFT in Figure 5.5 (c). The

misoriented angle can be obtained from the FFT diffraction pattern, which was measured at a value of $11.96^\circ \pm 0.11^\circ$. To compare such an experimental observation to theoretical study, the relationship between the commensurate twist angle (θ) and the Moiré superlattice periodicity (\mathcal{L}) was plotted via the theoretical work from reference ¹⁹⁹. J. M. B. Lope's dos Santos et al. suggested that the Moiré superlattice periodicity (\mathcal{L}) in a bilayer graphene is a function of the commensurate twist angle (θ), expressed as:

$$\theta = \cos^{-1}[(3i^2 + 3i + 1/2)/(3i^2 + 3i + 1)] \dots (\text{equation 5.1})$$

$$\mathcal{L} = a \times (3i^2 + 3i + 1)^{\frac{1}{2}} \dots (\text{equation 5.2})$$

, where $a = 2.46\text{Å}$ is the lattice parameter of graphene and i step integer which takes on the values of 1, 2, 3, Using this relationship, a twisted angle of 12.01° was calculated to have a superlattice periodicity (\mathcal{L}) of 23.46Å , which is close to the value obtained from panel (b) and (c), indicating such a theory is valid for our observation. However, it is worth mentioning that the superlattice periodicity (\mathcal{L}) can vary significantly with a slight change in the twist angle especially when the commensurate twist angle (θ) angles $< 10^\circ$

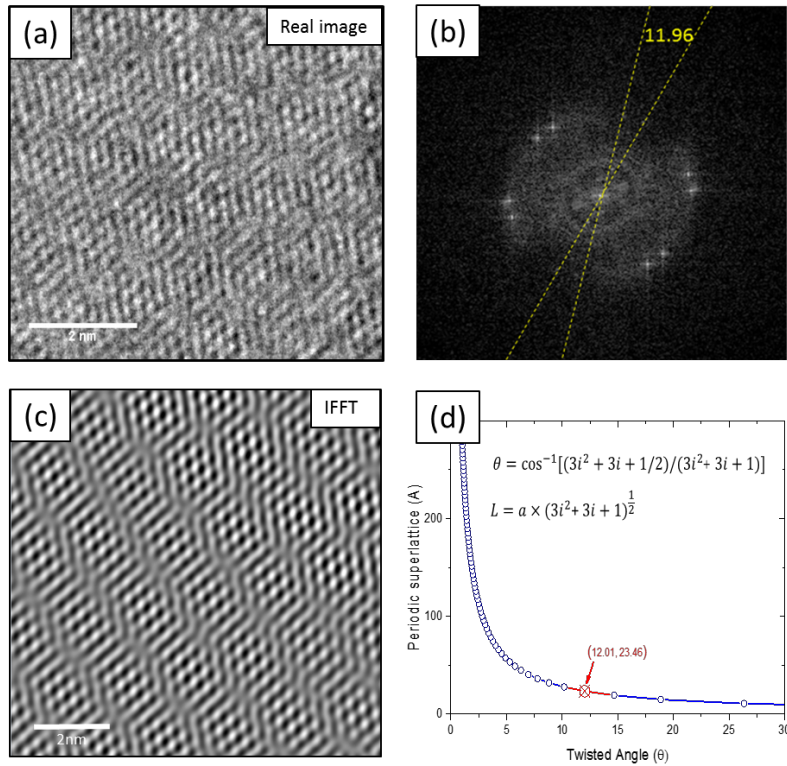


Figure 5.5: Shows Moiré pattern in TEM image. (a) Moiré pattern in a region of twisted graphene. (b) The FFT of the twisted region, which show the twisted angle is 11.96° . (c) The IFFT of image (a). (d) Plot the angle-dependent periodic superlattice based on J. M. B. Lope's dos Santos work ¹⁹⁹. The marked points denote the twists angle of the image. (2Dtech aquagraph SAEG sample were used)

61,62,198, and the size of superlattice periodicity (\mathcal{L}) might be too big to be recognised with a slight change in θ .

2) Characterise misoriented graphene flakes using electron diffraction

Another way to investigate the relative misoriented graphene is by analysing the SAED pattern. As introduced earlier in chapter 3, the misoriented angle of a graphene region can be obtained by analysing the intensity profile between (10) and (01) diffraction spots.

Figure 5.6 shows the histograms of the twisted angle in the selected graphene flakes. Among the SAED patterns obtained, over 25% of multilayer graphene sheets have a relative orientation of $\theta > 25^\circ$, with a few of them misoriented by $\theta \leq 5^\circ$, contrary to monolayer graphene sheets where a small misorientation angle ($\theta < 5^\circ$) is the majority. A small misorientation angle ($\theta < 5^\circ$) in monolayer graphene can be caused by the presence of

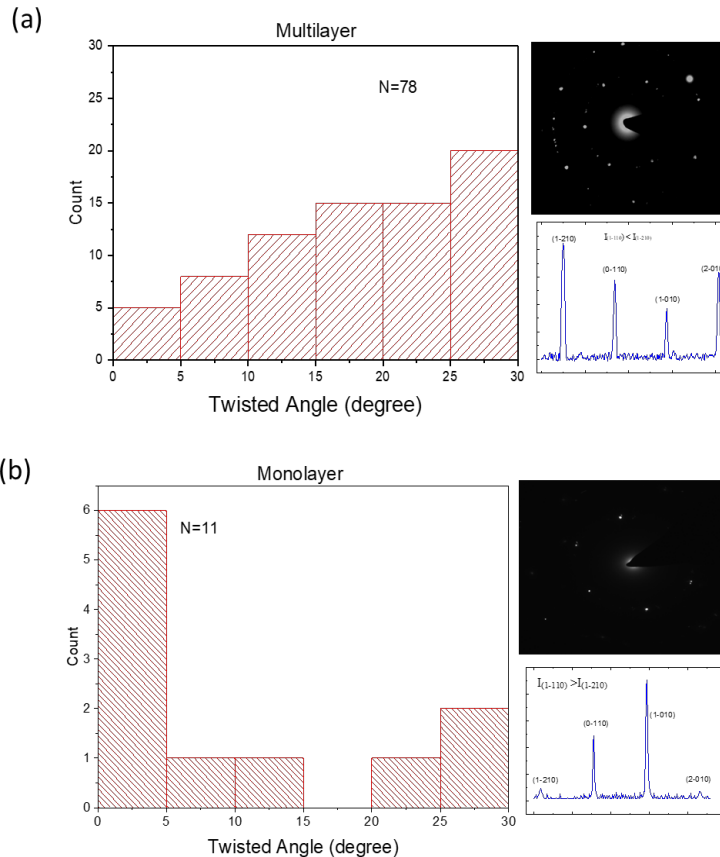


Figure 5.6: Histogram shows the angular distribution of (a) multilayer and (b) monolayer graphene. Insets show the intensity profile along $I_{(1-110)}$ to $I_{(1-210)}$ were used to categorise a mono/x graphene region. (2Dtech aquagraph SAEG sample were used)

in-plane dislocations, in which the monolayer graphene domain is divided into several misoriented grains ^{48,77}. The high-angle ($\theta > 25^\circ$) misorientation grains in monolayer graphene can be raised by the in-plane atomically bonded grain boundaries, which is formed by arrays of alternating pentagons and heptagons in the graphene periodic hexagonal structure ^{48,77} as shown in figure 2.5. However, in figure 5.6, it was found that the low-angle misorientation ($\theta < 5^\circ$) grains presented higher proportions in the sample, which could be due to the fact that misorientation grains are more energetically favourable because they can be formed only when few defects or dislocations exist in a two-dimensional graphene domain ^{47,48,77,78}.

However, unlike the angular misorientation distribution in monolayer graphene, it is difficult to conclude and explain the angular misorientation distribution obtained from the multilayer graphene flakes. The reason is that in a multilayer graphene flake, not only in-plane atomic bonded grains boundaries but also interlayer overlapping could both be present and cause misorientation in a flake, making the origin of a misoriented flake difficult to isolated. In addition, for the weakly bonded Turbostratic graphene / graphite flakes, they can twist at any possible angle, making the proposed electron diffraction technique to distinguish and interpreting the origin of the misorientation grains/flakes is difficult.

II. Crystal Structural imperfection studied by EELS

As mentioned in chapter 2 and 3, the core-loss EELS spectrum can be used to investigate the content of sp^2 bonding and non-planar sp^2 bonding in the graphene flakes in comparison to a reference sample.

Figure 5.7(a) shows example EELS spectra obtained from the edge (region A) and the bulk (region B) of a graphene flake. As seen in the figure, a strong zero-loss peak (ZLP) was obtained from region A contrary to a much lower ZLP in Region B. This means a much lower relative thickness in region A. The shift of π peak and the variation of $\pi+\sigma$ peak also show a different dielectric property between these regions. In spite of the

difference found in the low-loss region, obvious differences are also observed in the core-loss EELS: the π^* and $\pi^* + \sigma^*$ peaks are sharper in region B than in region A, implying a higher sp^2 contentment or a lower non-planar sp^2 fraction consists in the regions. The table in figure 5.7(b) shows the quantified results (based on Zhang's method as introduced in Chapter3): the sp^2 fraction in region B is significantly higher than in region A, while the non-planar sp^2 fraction in region A is higher than in region B.

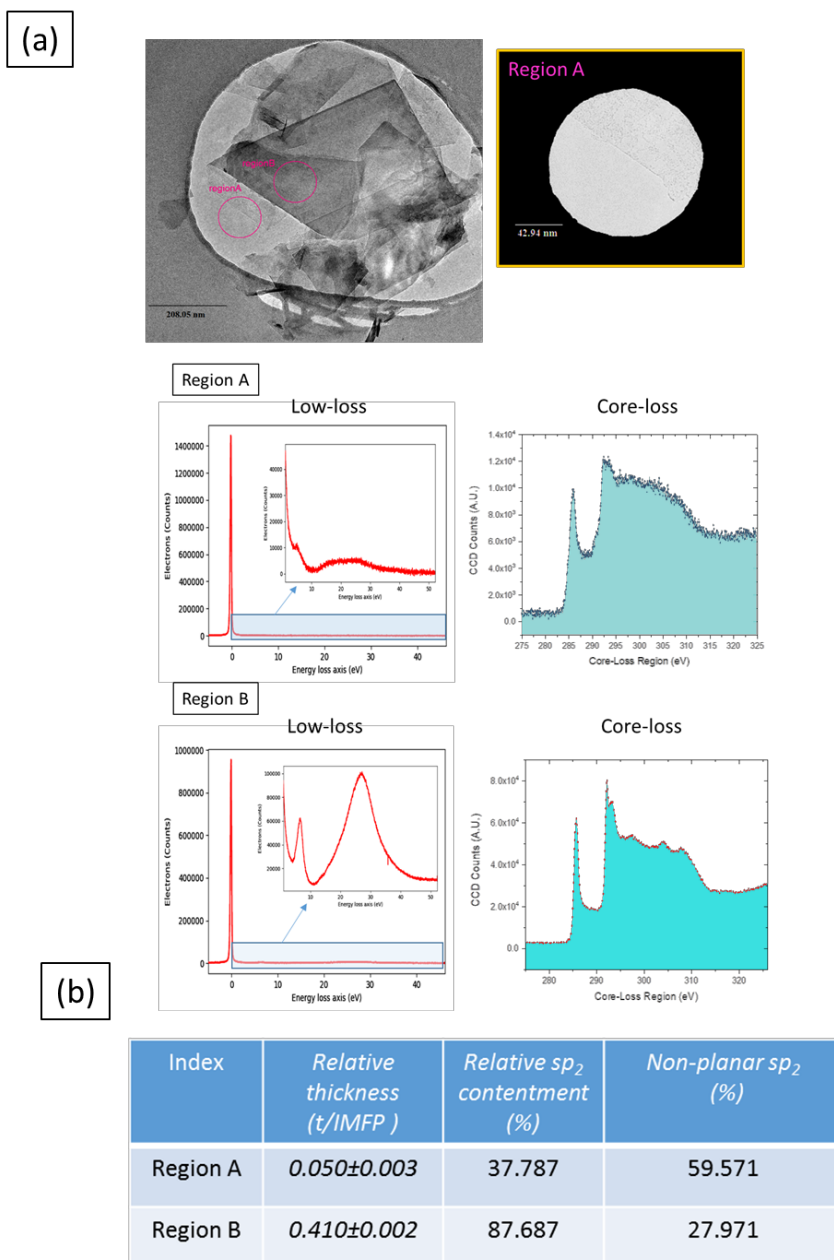


Figure 5.7: shows EELS spectrum of a graphene flake. (a) the EELS measured from different regions of a graphene flake. The log-ratio method was used to estimate the relative thickness and the corresponded core-loss spectrum are quantified to estimate the fraction of sp^2 and non-planar sp^2 bonding. (b) Shows table of data quantified from the EELS spectra. (2Dtech aquagraph SAEG sample were used)

Similar measurements were performed on 25 regions on different milling SAEG graphene sheets. Among these samples, the *relative sp² containment* shows a mean value of 69.01 ± 14.23 % and the mean value of the *non-planar sp² fraction* is 52.82 ± 11.46 %. The relative thicknesses of these selected regions ranging from 0.037 to 0.41.

The relationships between relative thickness and *relative sp² containment* / *non-planar sp² bonds fraction* are shown as scatter plots in figure 5.8. The relationship between the *relative sp² containment* and its *relative thickness* is unclear, as seen in figure 5.8(a). However, a slightly lower *relative sp² containment* (mean value = 62.85 ± 17.81 %) was obtained in the thinner regions ($t/IMFP < 0.2$) than in the thicker regions (mean *relative sp² containment* = 71.86 ± 12.94 % for regions having $t/IMFP > 0.2$). A corresponding, inverse trend was found in the scatter plot of the *relative thickness vs. non-planar sp² fraction*. As seen in figure 5.8(b), a higher *non-planar sp² bonds fraction* was obtained from the thinner regions ($t/IMFP < 0.2$) than in the thicker regions ($t/IMFP > 0.2$), where

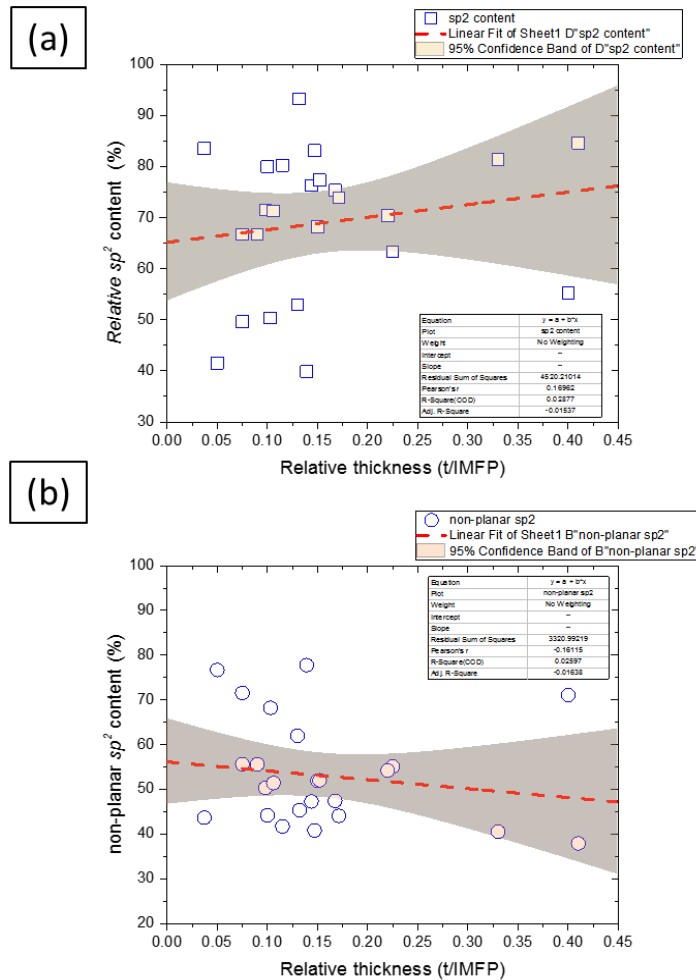


Figure 5.8: Scatter plots show the relationship between graphene relative thickness and the fraction of sp² (a) and non-planar sp² bonding (b). (2Dtech aquagraph SAEG sample were used)

the mean *non-planar sp² bonds fraction* were estimated at $54.07\pm 11.73\%$ and $46.92\pm 8.975\%$ respectively.

The trend including that the *relative sp² containment* and the *non-planar sp² bonds fraction* varies with relative thickness can be interpreted as the instability of chemical or physical properties in the thinner regions. Since it is not always possible to avoid causing damage to a graphene flake during the top-down synthesis process, a higher concentration of vacancies, topological defects, dangling bonds, edge sites or absorbed heteroatoms are therefore being introduced to the flake, especially in the thinner region of a graphene flake where its chemical and physical properties are less stable due to its large aspect ratio and surface area. Nevertheless, even though the crystal imperfections can be quantified and was observed being unevenly distributed in graphene, a rigorous conclusion cannot be made due to the lack of spatial resolution in the presented technique. This is because the EELS spectra were acquired in diffraction mode, the projected aperture size is usually bigger than the flake inhomogeneity, the obtained spectrum may comprise a significant amount of edge sites or containments (absorbed heteroatoms), causing an imprecise estimation of the *relative sp² containment / non-planar sp² bonds fraction*. Even so, the trend indicate that thinner graphene regions may contain higher proportions of *relative sp² containment / non-planar sp² bonds fraction* could still hold true, but a study that measures EELS in STEM mode may provide a much better spatial resolution for a better understanding of defects / vacancy distribution within a graphene flake ^{54,201}.

III. Local structural imperfection analysed by dark-field TEM imaging

i. The size distribution of graphene in-plane grains

As introduced in chapter 2, the formation of the TEM Dark-Field (DF) image is originated by the diffracted beams that pass through the objective aperture, and information about structural imperfections can present as bright contrast on the dark background and thus

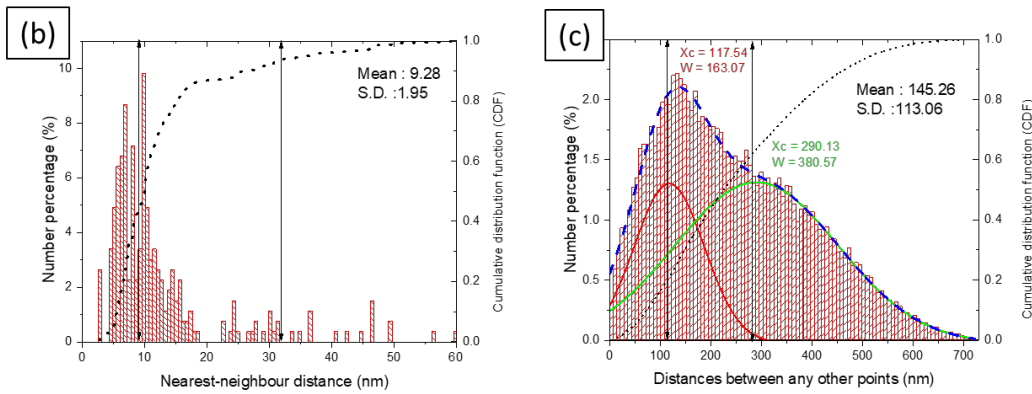
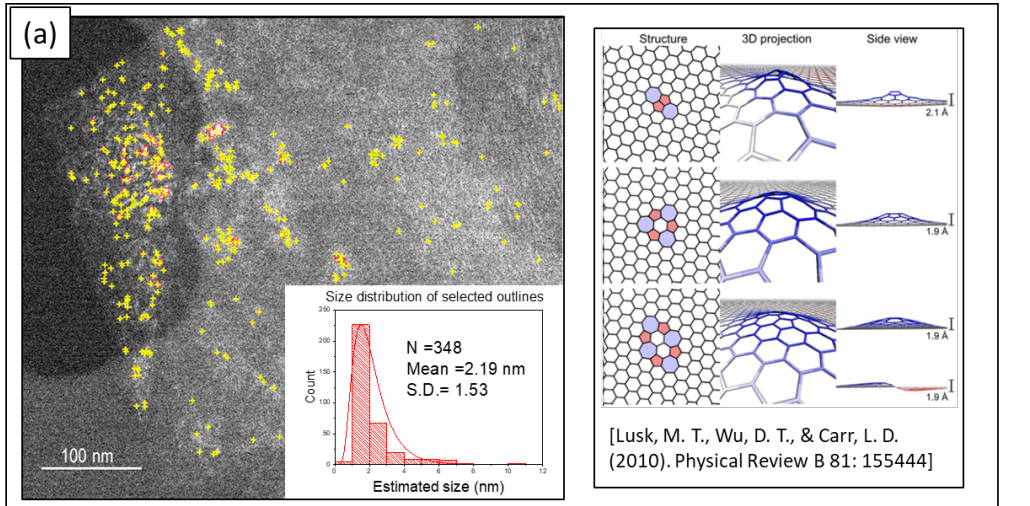


Figure 5.11: Analysis spatial distribution of defect in a graphene flake. (a) shows a higher magnification DF image. The bright spots were assigned as point defects because the out- of -plane distortion. The defects are identified by the ALTA algorithm and marked as yellow crosses. (Insets): Size distribution of the selected defects. (b) Shows the histogram CDF of the nearest-neighbour distances between the defects. (c) Shows the histogram and CDF of the distances between a defect to any other defects. (2Dtech aquagraph SAEG sample were used)

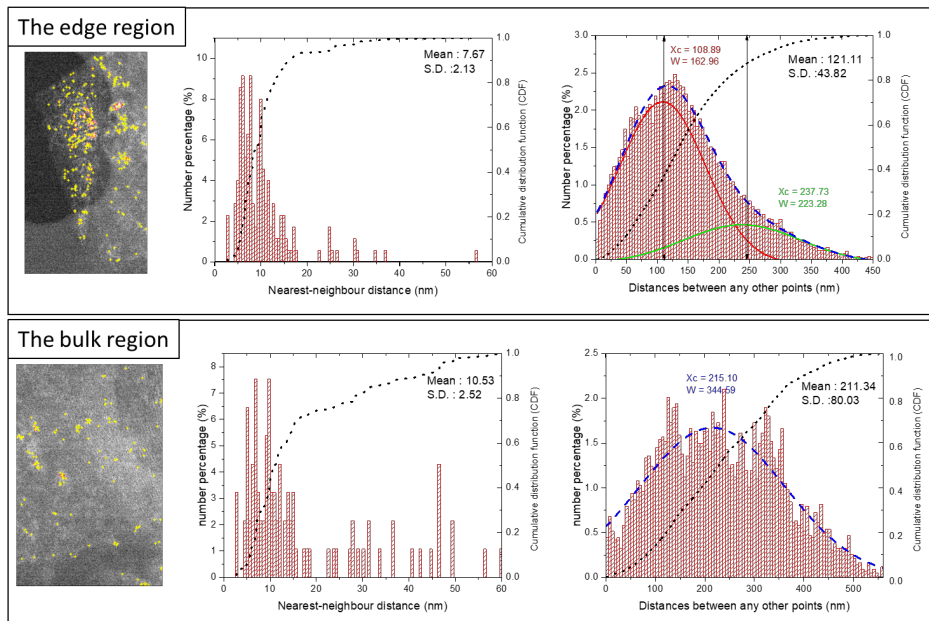


Figure 5.12: compares the spatial distribution of defects in the edge region and the bulk region. (2Dtech aquagraph SAEG sample were used)

can give a more accurate / useful method to visualise the structure imperfection in a graphene sheet ^{76,202}.

However, there are still several difficulties in analysing the obtained DF images, and they are: (1) The apparent isolation of individual grains/defects/flake wrinkles from the other kind of crystal imperfection. (2) The uneven and complex background. The former is

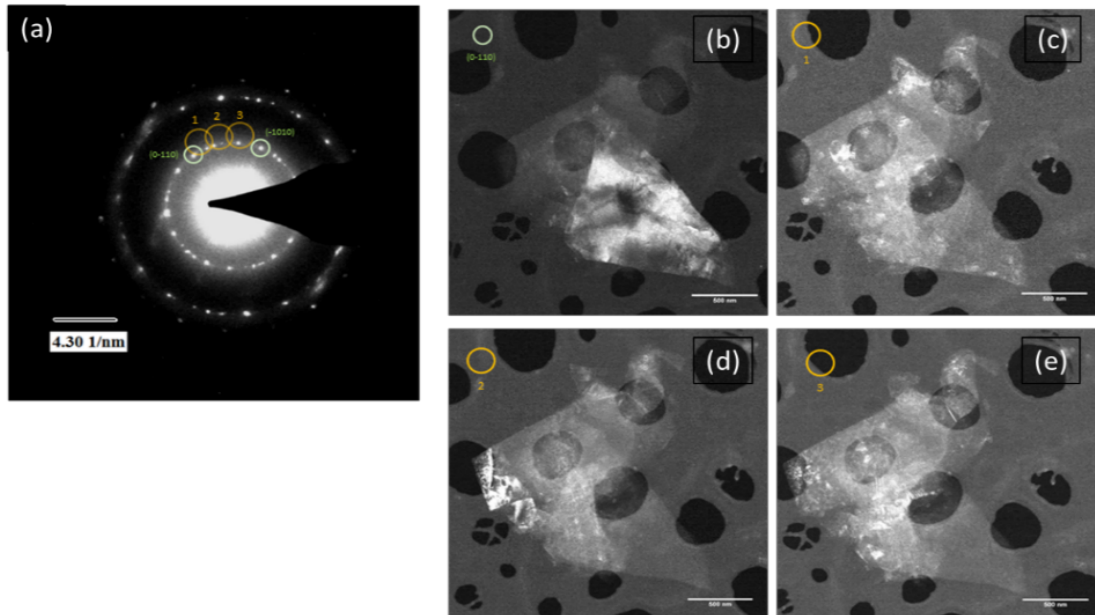


Figure 5.9: shows DF image of misoriented grains / patches. (a) SAED pattern of the selected flake. Yellow circles highlight misoriented diffraction spots between the (0-110) and (-1010). (b)-(e) shows the DF image formed by the first-order diffraction spots between (0-110) and (-1010). (2Dtech aquagraph SAEG sample were used)

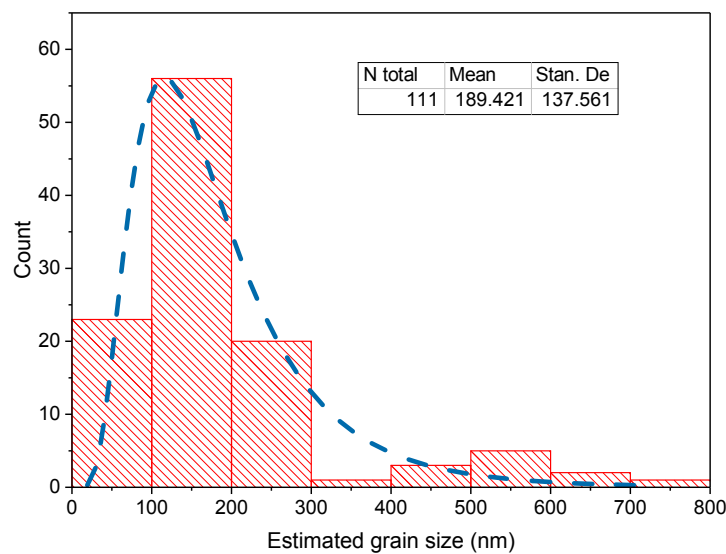


Figure 5.10: shows the distribution of grain size obtained from few graphene flakes (2Dtech Aquagraph series). (2Dtech aquagraph SAEG sample were used)

limited by the sample inhomogeneity and the finite size of the objective aperture, which leads to a complex background and thus an improved image recognition technique is needed to identify the objects of interest from the background.

As seen in Figure 5.9, even though the dependency of DF images formed by different diffraction spots can be used to isolate the in-flake grains⁷⁶, an image with a clear background is difficult to be obtained. Therefore, the Adoptive Local Thresholding Algorithm (ALTA) mentioned in chapter 3 was used to help the segmentation of the grains from DF images¹⁵⁰. By applying such an algorithm to a few selected DF images, the grain size distribution can be obtained by segmenting the DF images. Figure 5.10 shows the histogram of grain size distribution obtained from the 2Dtech graphene sample. The grain size (L_a) here is expressed by the diameter of a circle that has the same area as the selected irregular shaped grains. On the basis of statistics derived from a sample of 111 grains, a mean value of 189.421 nm and a standard deviation of 137.56 nm were obtained from the 2Dtech graphene sample.

ii. Spatial distribution of topological point defects

As mentioned in chapter 2, the in-plane defects can cause out-of-plane distortion of the flake in the range of a few nanometers and appear as bright spots in a higher magnification DF image, and information about the spatial distribution of point defects can be extracted by analysing the position of the bright spots in the image^{202,203,76}.

Figure 5.11 shows a higher magnification DF image; the ALTA algorithm was used to extract the outlines and positions of the defects / distortion in the image. The position of defects is defined by the geometrical centre of mass from the selected outline, which is labelled as yellow crosses in the figure. After the position of each defect is determined, the distances between defects can be calculated by the Euclidean method. The spatial distributions of the point-defects are described by two different methods: (1) The nearest-neighbour distances (G-function) and (2) The distances between a point to any other points (H-function)^{204,205}.

Figure 5.11 (b) shows the histogram and the cumulative distribution function (CDF) of the nearest-neighbour distances between the defects. As seen in the figure, the CDF rises rapidly at short distances, then levels off at larger distance value, indicating that these defects appear nearby or tend to cluster. This can be seen in the histogram, where a multimodal distribution consists of an intense peak at short distances, and a few weak peaks at large distances were obtained.

Figure 5.11 (c) shows the histogram and the cumulative distribution function (CDF) of the distances between a defect and any other defect. As seen in the figure, the bimodal distribution consists of two Gaussian peaks at 117.54 and 290.13(nm), plotted in red and green respectively. The bimodal distribution also indicates that the defects are unevenly spaced but clustered.

Figure 5.12 compares the spatial distribution of defects in the edge region and the bulk region. As seen in the figure, defects in both regions tend to cluster, but the bulk region showed a stronger but broader peak at the large distance value, indicating a higher defect concentration in the edge region than in the bulk region.

5.2. Characterising crystal imperfection by Raman spectroscopy

In this section, the aim is to develop a characterisation protocol based on Raman spectroscopy, so that the disorder of graphene can be rapidly quantified and used to characterise the SAEG graphene. To do so, a pristine monolayer CVD graphene was initially used to develop the robust procedure for investigation of SAEG graphene. Secondly, a correlation test was developed to identify the contribution of edge structure. This was followed by a random sampling method, which was intentionally developed to avoid biased or misleading data collection. The developed measurements routine was then

applied to the SAEG graphene, and with the assistance of statistics techniques, the L_D or L_a was calculated via the local activation model and Tuinstra–Koenig relation.

I. Effect of graphene edges

As introduced earlier in Chapter 3 and 4, graphene samples manufactured by solution assisted exfoliation gave rise to a relatively small lateral size (mean value $\leq 1000\text{nm}$) and thus the effect of graphene edges can be significant. Also, the laser beam of the Raman system can only be focused into a 3-5 μm diameter laser spot, making the probe size much bigger than the lateral size of graphene, and the contribution of graphene edge to the D band enhancement is thereby undistinguishable.

As seen in figure 5.13, a small flake from the fragmented CVD graphene film was chosen to compare with the SAEG graphene flakes from 2Dtech. As displayed in the spectra, the D band intensity obtained from the small lateral size graphene flakes are significantly higher in comparison with those of the HOPG and the bulk CVD graphene regions, indicating the effect of edge could be significant in terms of the D band intensity, thus making the estimation of defect density imprecise.

To overcome such a problem, a method is proposed to improve the characterisation technique based on the theories introduced in chapter 2. As mentioned earlier, the presence of topological defects could induce strain/stress to the graphene lattice, and introduce inharmonic vibrational modes thereby shorten phonon lifetime. Thus, these topological defects will not only cause the enhancement of the D band, but also broaden the G band due to the introduction of inharmonicity in the sp^2 natural phonon frequency. This can be explained by way of the graphene phonon dispersion diagram shown in figure 2.15. The induced inter-atomic strain disturbed the graphene hexagonal symmetry, resulting in the mixing of the in-plane LO and TO phonon modes near Γ point, result to a broader G band^{105,116,206}. Therefore, when the width of G band (FWHM (G)) was observed to increase with the I(D)/I(G) ratio, the enhancement of the D band can be assigned to the

topological defects. This is contrary to a perfect edge structure or atom vacancy where the nearby hexagonal lattices are not distorted, and the $I(D)/I(G)$ ratio should be independent of the width of the G band (i.e., the nature sp^2 phonon frequency remained undisturbed 105,109,116,206,207). Such understanding of the D peak enhancement and the G peak broadening mechanism provides a platform that can be used to identify which structural disorder is the major contributor to the D band enhancement, and to be used to evaluate the precision of the graphene defect models in small graphene flakes.

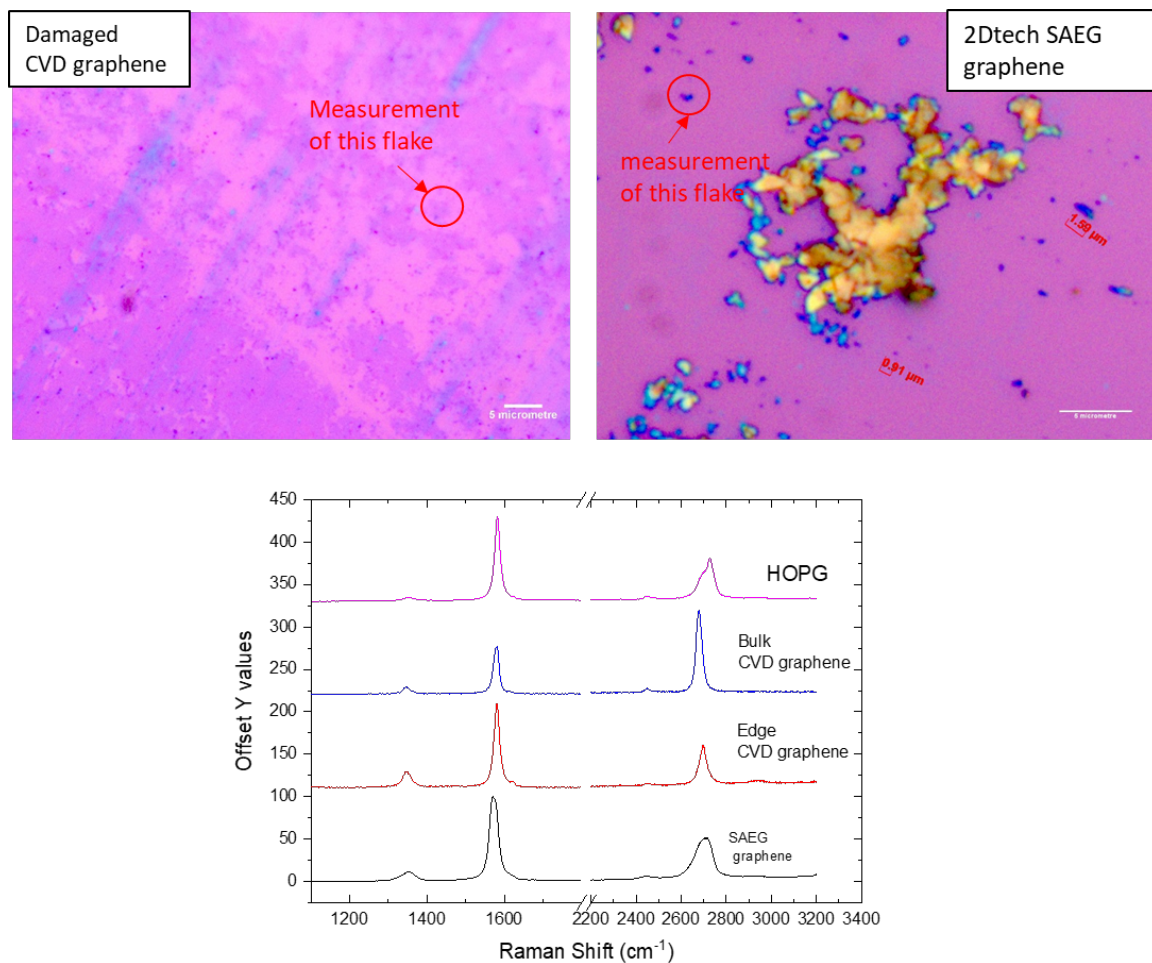


Figure 5.13: (top) shows optical microscope images of graphene flakes in damaged CVD film and SAEG graphene provided by 2Dtech™ graphene sample. (bottom) shows the differences between Raman spectra measured in a bulk graphene region and regions surrounded by graphene edges.

II. A correlation method to indicate the contribution of edge structure

A correlation method was used to test this hypothesis. Several bulk regions (far from the edge) and edge regions in the CVD graphene sample were selected using the optical microscope image. 20 Raman spectra were collected from each region for analysis. As seen in figure 5.14, the I(D)/I(G) ratio was plotted versus the FWHM(G), a linear regression was used to test the correlation between the I(D)/I(G) and the corresponded FWHM(G). A strong correlation between I(D)/I(G) and FWHM(G) was obtained in the bulk regions, with a Pearson r value of 0.807. This contrasted with the plot obtained from the edge region, where a weak correlation was attained (Pearson r value = 0.266).

However, the edge region has seen in Figure 5.14(b) still shows a weak correlation between FWHM (G) and I(D)/I(G) in the edge regions. This could be because of the absence of perfect edges in the CVD graphene sheet when it was partially torn during the transfer process, leading to the generation of defects near the edges. Also, it is possible that the presence of zig-zag edge transformed to a 5-7 or 5-8-5 defect edges as shown in figure 2.7, in which could also cause the broadening of G band. In fact, it was observed that the thin edge regions are usually accompanied with topological defects (see figure 5.8), which contributed to the broadening of G band and making the Pearson r value non-zero. Despite so, the hypothesis that the G band will always broaden with D band intensity would still valid for identifying topological defects in the bulk graphene regions. Thus, in this thesis, for an I(D)/I(G) and FWHM(G) that has Pearson r value ≥ 0.8 will be considered having the main D band enhancement originate from the bulk region. Similarly, for Pearson r value ≤ 0.3 will be considered have the D band enhancement comes from the edge regions.

Nevertheless, the existence of D' band can limit the utilisation of such a correlation method and affect the analysis results. This is owing to the position of D' peak is just next to the G peak and is enhanced as the D peak increases. Thereby, it can significantly influence the accuracy of the measurement of FWHM (G). Also, it has been reported that

for highly damaged graphene ($n_D > 10^{14} \text{ cm}^{-2}$ or $L_D < 10 \text{ nm}$), the G and D' peaks will start merging and become indistinguishable^{115,116}. In this case, the FWHM (G) will always increase linearly with I(D)/I(G) increases and the correlation method will no longer be suitable for identifying the contribution of graphene edges.

In conclusion, we have demonstrated the significant influence of edge structure on the Raman spectra. Hence, the earlier proposed local activation model and Tuinstra–Koenig empirical relation could be imprecise when applied to small lateral graphene flakes due to the significance of edge structure. To evaluate the usability of such models, several Raman spectra will be obtained from the 2Dtech SAEG sample, the coherence length (L_a) and defect density will be estimated via the local activation model and Tuinstra–Koenig relation to compare with the prior TEM observation, where the errors and the limitation of current graphene defect model will also be discussed.

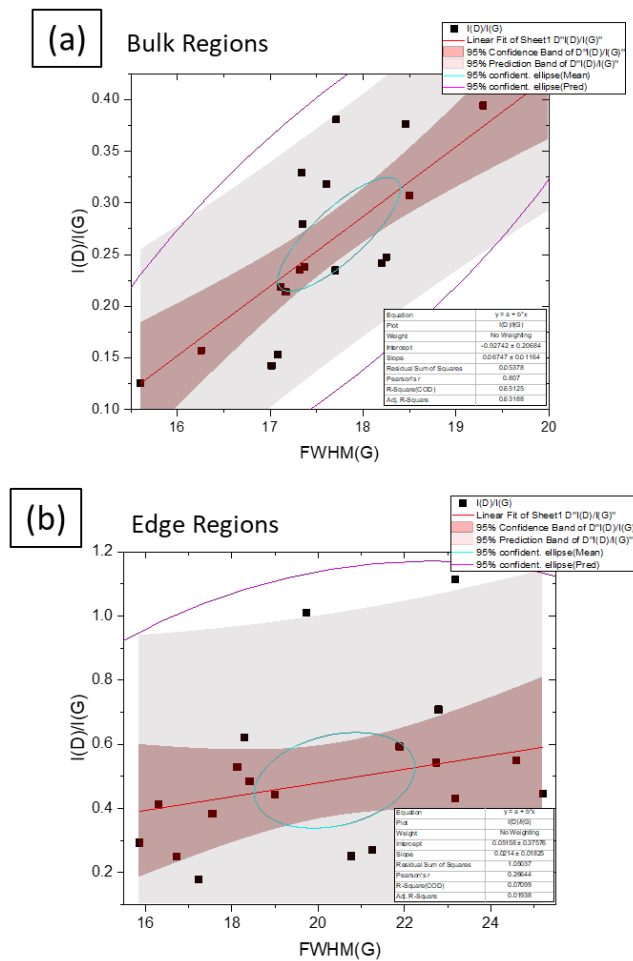


Figure 5.14: shows the linear regression results of I(D)/I(G) ratio and FWHM(G) in (a) graphene bulk regions and (b) graphene edge regions. Data obtained from CVD graphene.

III. Characterisation of the structural disorder of SAEG graphene (2Dtech aquagraph sample)

Figure 5.15 shows the Raman-based measurement of 20 randomly selected 2Dtech aquagraph SAEG graphene flakes on a 1cm×1cm SiO₂/Si substrate. Among these flakes, a mean I(D)/I(G) ratio of 0.155 and a standard deviation of 0.053 were obtained. Similar to figure 5.14, a linear regression was applied to correlate the FWHM (G) to I(D)/I(G) ratio. As shown in figure 5.16(b), the regression showed a weak correlation between FWHM (G) to I(D)/I(G) ratio, where a Pearson r value 0.311, indicating the edge structure appears to be the main contribution to the D band enhancement. Thus, applying the local activation model or Tuinstra–Koenig relation to estimate the defect density (L_D) or

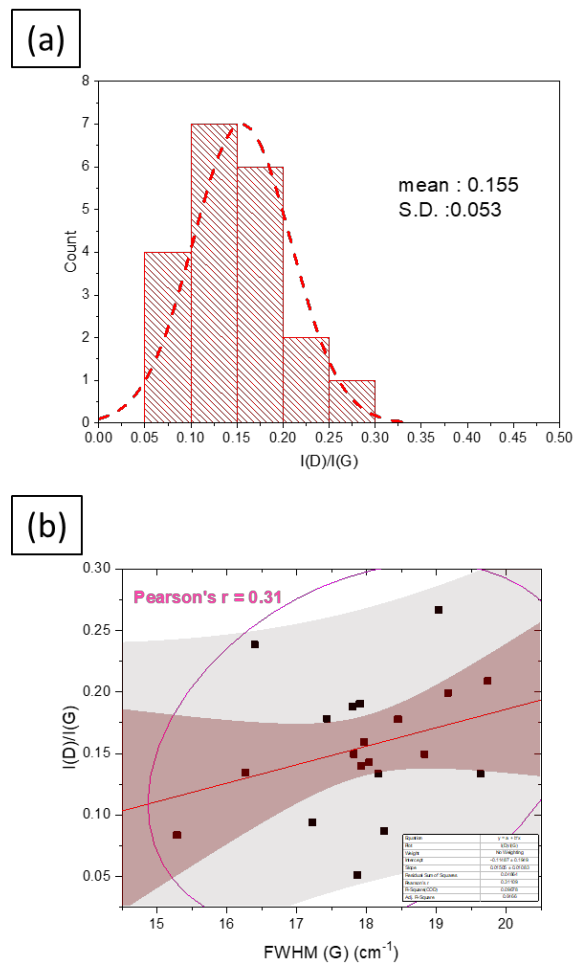


Figure 5.15: (a) shows the I(D)/I(G) ratio distribution of the 2Dtech SAEG graphene. (b) the correlation test suggests the D band intensity in the sample originated from the flake edges. (2Dtech aquagraph SAEG sample were used)

coherence length (L_c) could be inaccurate when such small SAEG graphene flakes were used.

i. Sampling method and required sampling size

1) Sampling method

A random sampling method was used to perform the Raman measurement. The graphene suspension was initially drop cast onto a 1cm×1cm SiO₂ (285 nm)/Si substrate for microscope observation. As seen in figure 5.16, a virtual coordinate was set onto the sample using the stage of microscope, where the 1cm×1cm substrate was then divided into 10×10 grids. Each grid has a ~1mm×1mm area and can also be located by the stage of the Raman spectroscopy. By generating two series of random numbers between 0 to 10, the grid to be measured can be decided. The Raman measurement were performed on a graphene flake within the computer-decided grid. Since a 1mm×1mm grid appears very large under the microscope, it is always possible to find a graphene flake for obtaining Raman spectra.

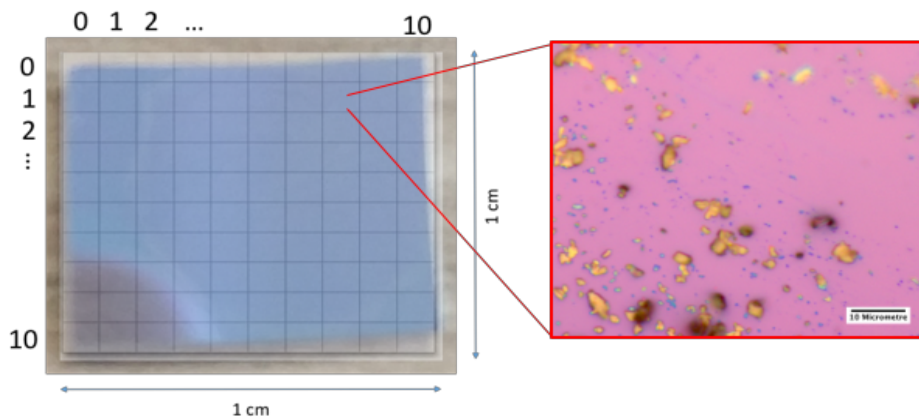


Figure 5.16: describes the random sampling method used to characterise the SAEG graphene flakes. Image in left shows the concept of a virtual coordinate on a 1cm×1cm SiO₂ (285 nm)/Si substrate used for deciding the Raman measurement. The inset shows that plenty of graphene flakes can be found in a grid.

2) required sampling size

A sufficient sampling is important to make a measurement representative. Figure 5.17 shows the histograms of I(D)/I(G) ratios obtained from different sampling numbers based on the random sampling method. As seen in the figure, the distributions tend to form a normal distribution with an increase of sampling size, while the mean value does not change significantly as sampling size increases. This is owing to the accordance of the central limit theorem (CLT), which states that with a system having a finite level of variance (finite energy states), the sample mean value will be approximate to the system when the sampling size is sufficient. Thus, it is possible to represent the property of a large population of flakes with a sufficiently large sample size.

The population of graphene flakes in a 100cc suspension will be of the order of 7×10^{13} (considering each graphene flake has lateral size of ~ 1000 nm, with five graphene layers, the concentration of suspension was measured to be $\sim 1.12 \pm 0.16$ (mg/ml)). The number is much higher than the sampling size we can measure. Therefore, in this situation, we use

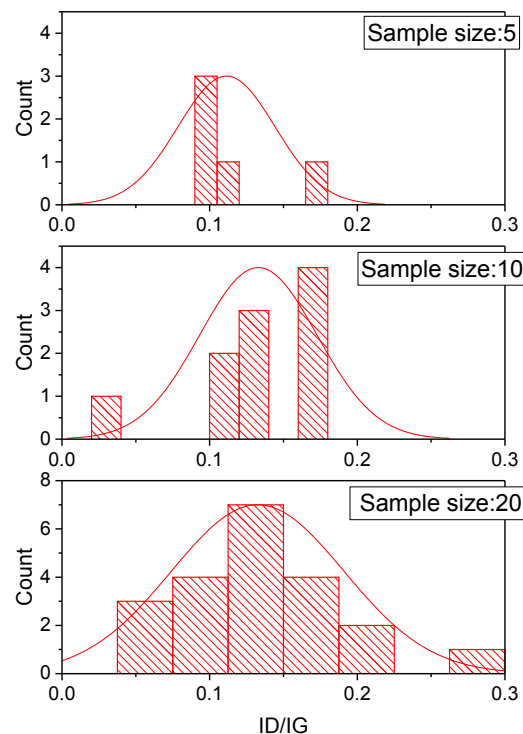


Figure 5.17: shows the histograms obtained from different sampling sizes. The distributions tend to form a normal distribution as increase of sampling size, but the mean value does not change significantly as sampling size increases. (2Dtech aquagraph SAEG sample were used)

Student's t distribution to estimate the population mean (μ). The value was estimated using:

$$\bar{x} - t \frac{\varsigma}{\sqrt{n}} < \mu < \bar{x} + t \frac{\varsigma}{\sqrt{n}} \dots (\text{equation 5.3})$$

,where n is the sample size, \bar{x} is the mean value of sample and ς is sample standard deviation. The value of t is decided by the degree of freedom and the chosen confidence interval, which can be found in standard tables for $n < 30$.

With 20 randomly selected flakes, we have calculated the sample mean (\bar{x}) and standard deviation (ς) as 0.132 and 0.058 respectively. With 99% of the confidence interval and $t = 2.528$ (degree of freedom =20), a $0.10 < \mu_{I(D)/I(G)} < 0.164$ can be determined. However, the important question is how many flakes should be measured in order to effectively represent a solution processed graphene sample? This varies sample by sample, depending on how accurate the measurement is required to be and how many differences there are between the flakes. Take the 2Dtech sample for example and assuming $E = 0.05$ (the error that we can tolerate), then the confidence interval is 99%.

We can estimate $n \geq \left(\frac{tS}{E} \right)^2 = \left(\frac{2.528 * 0.058}{0.05} \right)^2 = 8.599$, meaning we can make a fairly accurate I(D)/I(G) measurement if we take a random sample of 9 flakes from the 2Dtech graphene suspension.

5.3. Comparison Raman spectroscopy with the TEM results

I. Estimate L_a via Tuinstra–Koenig relation

As introduced in chapter 2, the coherence length (L_a) can be estimated by the obtained Raman spectra via the Tuinstra–Koenig relation:

$$L_a(nm) = \frac{560}{E_{laser}^4} \left(\frac{I_D}{I_G} \right)^{-1} = (2.4 \times 10^{-10}) \lambda_{laser}^4 \left(\frac{I_D}{I_G} \right)^{-1} \dots (equation 5.4)$$

, where the value of L_a is only depend on the $\left(\frac{I_D}{I_G} \right)$ ratio and the wavelength of excitation laser (E_{laser}). The excitation laser in the Raman system is 514nm (2.41eV), and the coherence length of the observed graphene flakes L_a can be easily calculated by the $I(D)/I(G)$ ratio.

The bottom histogram in figure 5.18 shows the coherence length distribution (L_a) estimated by the Tuinstra–Koenig relation, in which the mean L_a was estimated to be 123.65 nm in the 2Dtech graphene sample. Considering that the mean lateral dimension of each primary flake is $\langle L \rangle \sim 600$ nm (see chapter 4), several different grains (domains) are present in each primary flake: considering a square primary flake with lateral dimension L , the shape of each grains (domains) is perfect circle, then the number of grains presented in the primary flake is estimated to be : $\left[L/(\sqrt{2}L_a) \right]^2$, in which the value is ~ 12 for $L = 600$ nm; $L_a = 123$ nm. Figure 5.18 further compares L_a estimated via the Tuinstra–Koenig relation to L_a obtained by the DF TEM image. It was found that the coherence length (L_a) measured by the Tuinstra–Koenig relation method were estimated to be 62.77 nm smaller than the measurement from DF TEM ($L_a = 189.42$ nm), which is around 33.13% in difference. Such a difference could be caused by the effect of edge structure in the SAEG

graphene that significantly contributes to the D peak enhancement, making the value of L_a underestimated.

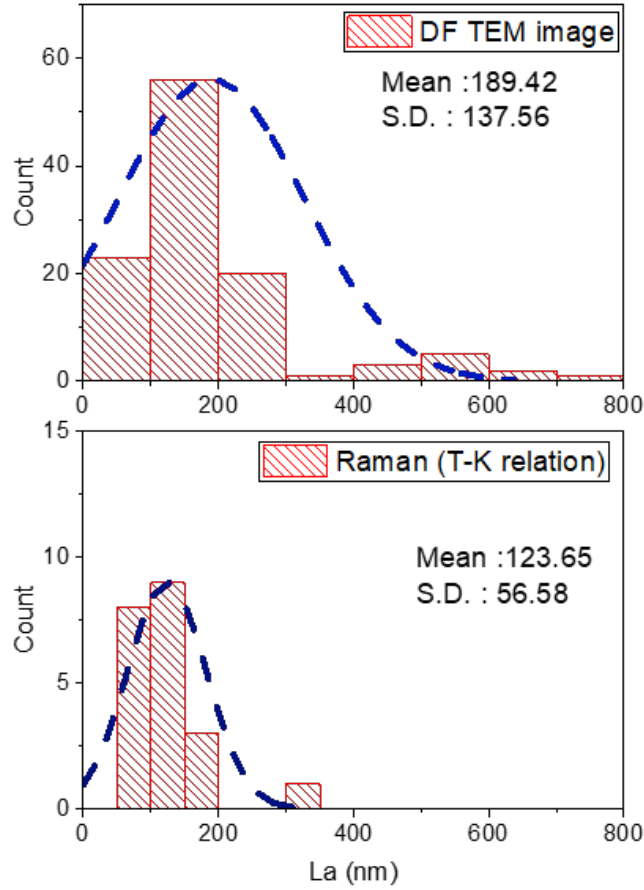


Figure 5.18: Comparison of the grain size distribution obtained by DF TEM to the L_a from Tuinstra-Koenig relation. (2Dtech aquagraph SAEG sample were used)

II. Estimate L_D via local activation model

As introduced in Chapter 2, the semi-empirical derived local activation model suggests the $I(D)/I(G)$ ratio increases as the concentration of defect and is a function of the average distance between two defects (L_D)^{115,116}:

$$L_D^2(nm^2) = \frac{(4.3 \pm 1.3) \times 10^3}{E_L^4} \left(\frac{I_D}{I_G}\right)^{-1} \dots(\text{equation 5.5})$$

, where E_L is the photon energy of the excitation laser in eV and the value of 4.3 ± 1.3 is a constant that derived from the empirical experimental study. The value of 4.3 was then used for estimating the L_D of our sample.

Figure 5.19 compares the L_D estimated via local activation model with the spatial distribution of defects obtained by the DF TEM image analysis. As seen in the figure, the statistics shows that the mean value of the distances between any other two point defects is 146.28 nm, which is very different from the average L_D of 38.35 nm estimated via the local activation model. However, the estimation is much more precise when the nearest-neighbour distances were used for such a statistic. As mentioned in the earlier sections, the multi-modal distribution from the nearest-neighbour distances consists of an intense peak at short distances and a weak peak at large distances. The short distances defects are the defects that clustered, having a range of ~ 10 nm and may be difficult to distinguish by the Raman spectroscopy method. In fact, for $L_D \sim 10$ nm, the local activation model is about to

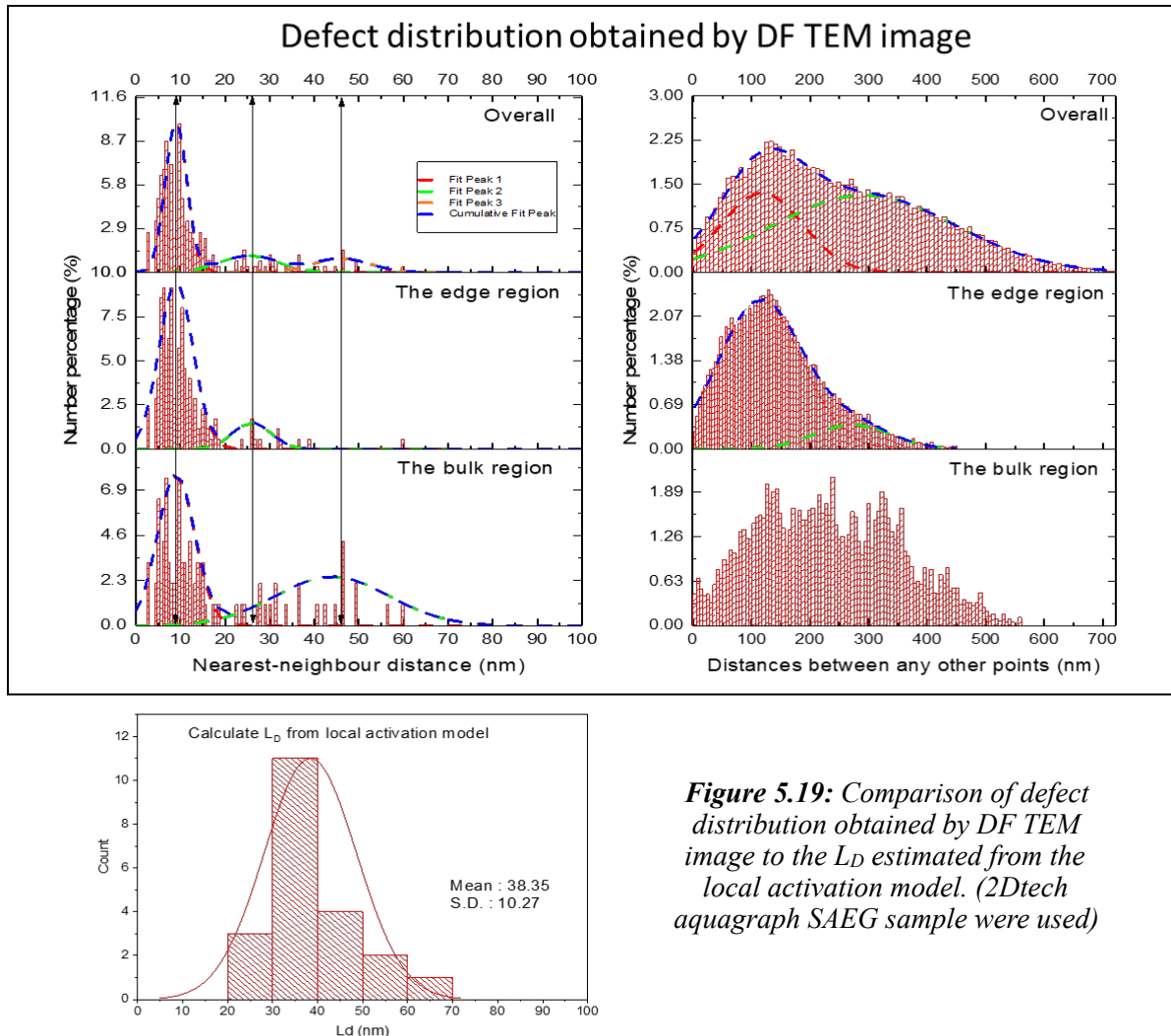


Figure 5.19: Comparison of defect distribution obtained by DF TEM image to the L_D estimated from the local activation model. (2Dtech aquagraph SAEG sample were used)

saturate, and the trend that the I(D)/I(G) ratio increases with defects concentration could be no longer valid (see figure 2.16(b)). This is because of the disordered area have already take-over of the activated area in such a defect concentration (n_D)^{115,116}.

However, the long-distance defects distribution with nearest-neighbour distances between ~20 to ~40 nm is close to the value of L_D estimated by the local activation model. Although an exact spatial distribution of defects cannot be obtained by Raman spectroscopy, it seems that the defect density estimation from the local activation model has underestimated the defect concentration in the edge region but overestimated the defect concentration in the bulk regions.

5.4. Conclusion

In this chapter, the aim was to develop a more rapid method to assess the crystalline imperfections in graphene. Initially, the existence of crystal defects in graphene has been demonstrated using bright-field TEM images, where both in-plane and inter-plane crystal imperfections are visualised. Electron diffraction (ED), electron energy loss spectroscopy (EELS) and dark-field (DF) imaging techniques were employed to characterise these crystal imperfections in the graphene flakes. It was found that a small misorientation angle ($\theta < 5^\circ$) presented higher proportion for monolayer graphene sheets, which can be originated by the presence of in-plane dislocations, dividing the a monolayer graphene domain into several misoriented grains. The high-angle ($\theta > 25^\circ$) misorientation grains were also present in significant proportions a significant proportion in monolayer graphene, which can be raised by the in-plane atomically bonded grain boundaries that formed by arrays of alternating pentagons and heptagons in the graphene periodic hexagonal structure. However, the reason that causes misorientation in multilayer graphene cannot be identified in this stage. It is due to both the in-plan atomically bonded grain boundaries and out-of-plane interlayer overlapping being present and causes misorientation in a multilayer graphene flake.

The *relative sp^2 containment* and *non-planar sp^2 bonds fraction* in a graphene flake can be obtained by quantifying their EELS spectra. It was found that a thinner graphene region tends to have lower *relative sp^2 containment* but higher *non-planar sp^2 bonds fraction*, which can be due to several unavoidable damage-causing events that can occur to a graphene flake during the top-down synthesis process, a higher concentration of vacancies, topological defects, dangling bonds, edge sites or absorbed heteroatoms could therefore be introduced to the flake, especially in the thinner region of a graphene flake where its chemical and physical properties are less stable because of its large aspect ratio and surface area.

Although the graphene crystal imperfections can be quantified and was observed being unevenly distributed EELS, a rigorous conclusion cannot be made because of the lack of spatial resolution. The TEM Dark-Field (DF) image is therefore used to quantify the crystal imperfections and its spatial distribution in a graphene flake. By using such a technique, a mean value of grain size of 189.421 nm with a standard deviation of 137.56 nm was obtained for the 2Dtech graphene sample. The spatial distribution of in-plane defects can be obtained due to the out-of-plane distortion from the topological defects, which could make the regions of defects appear as bright spots in the DF image. Information about spatial distribution of topological point defects can therefore be extracted by analysing the position of the bright spots in the image. A multimodal distribution that consists of an intense peak at short distances, and a few weak peaks at large distances was obtained. This indicates an uneven spatial distribution of topological point defect and indicates that these defects appear nearby or tend to cluster.

However, though the TEM observation gives a direct characterisation for the detailed disorder in a small graphene region, the low throughput makes such measurement expensive and time-consuming. Raman spectroscopy has long been considered as a rapid method for quantifying the structural disorder in graphite-related material, but a general model that can be used to reflect the origin of defects is still ambiguous and unavailable in conventional Raman spectroscopy due to the limitation of probe size. The effect of graphene edges could be one of the most significant uncertainties when characterise graphene using Raman spectroscopy. Since graphene samples that were manufactured by

solution assisted exfoliation produce a relatively small lateral size (mean value $\langle L \rangle \leq 1000$ nm) thus the effect of graphene edges can be significant. Also, the laser beam of the Raman system can only be focused into a 3-5 μm diameter laser spot, making the probe size much bigger than the lateral size of graphene, and the contribution of graphene edge to the D band enhancement is thereby indistinguishable. A simple method based on linear correlation and random sampling was proposed to indicate the source of disorder in the graphene sample with significant edge structure. It has been shown that both the presence of edge structure can cause the coherence length (L_c) to underestimate via the Tuinstra–Koenig relation. The average distance between defects (L_D) can also be imprecise when estimating using the local activation model. The results obtained from Raman spectroscopy was compared to the TEM study, and the differences between them were assigned to the uneven distribution of defects in graphene flakes.

In summary, we have shown the existence of graphene crystal disorder using TEM. A characterisation protocol based on Raman spectroscopy was developed to quantify the graphene crystal imperfection. We have shown that the estimation from previous proposed models could be imprecise due to the significant effect of graphene edge structure. Nevertheless, with the implementation of statistical analysis, the characterisation protocol can be used to quantify and represent the structural disorder of heterogeneous and large population graphene samples.

6.

The thickness of graphene

The thickness of graphene plays a significant role in determining the electronic and optical properties as result of alternations in band structure. For example, the semi-metal character of pristine graphene can be changed to semiconducting, by control of the number of layers in a graphene flake as mentioned in Chapter 2 ^{2,40,208,209}.

To characterise such an important property for the ultra-thin material, microscopy techniques such as TEM and AFM are the most widely used techniques. However, the low throughput of these techniques, along with the uncertainty regarding the influence of substrate morphology or an unavoidable buffer layer (water layer or the possible C-H contaminant ^{139,210,211}, see section 6.3 III) makes such characterisation inaccurate and time-consuming.

Although the shape and position of the Raman 2D band offers a possibility of characterising the number of coupled graphene layers ^{21,212,213}, a standardised quantification method that could be used to determine the number of graphene layers by Raman spectroscopy is still unclear. Especially a systematically study that correlates the observation from TEM and AFM is still unavailable due to the uncertainty of the AFM measurement and the difficulties of transferring the same graphene flake onto a different substrate for observation. Therefore, the precision of utilising Raman spectroscopy to characterise the thickness of graphene is still arguable, in particular with reference to the small lateral size SAEG graphene.

In this chapter, the thickness of graphene flakes was initially determined by TEM, where the mean grey scale value (MGVR) and folding edge method were used. The well-established relative thickness (i.e., $\frac{\text{flake thickness}}{\text{inelastic mean free path}}$) was determined via low-

loss EELS spectra, where the inelastic mean free path in graphene/graphite was estimated. In order to develop a rapid thickness characterisation for the solution assisted exfoliated graphene (SAEG), empirical equations have been derived based on regression of the variation of the 2D band in Raman spectra of the graphene. All of these techniques were applied to the 2Dtech SAEG graphene sample, with the assistance of AFM measurements, and the results were compared to each other. The limitations and causes of error were also discussed.

6.1. Determination of graphene thickness using TEM

I. The mean greyscale value ratio (MGVR) in bright-field images

As mentioned earlier in Chapter 3, calculating the flake thickness by observing the folding of graphene edges is one of the most reliable and straightforward but time-consuming method available. On the other hand, the MGVR method is considered as a less time-consuming method to estimate the thickness of graphene using TEM, but an accurate assessment is needed for a more universal application.

i. Correlation between MGVR and graphene folded edges

In this study, a total of four flakes were selected through the presence of folded edges, where the flake thicknesses were determined using the folding edge method and the associate MGVR values were measured by selecting an appropriate region of interest (ROI) on the flake. The MGVR values were plotted against the thickness estimated by the

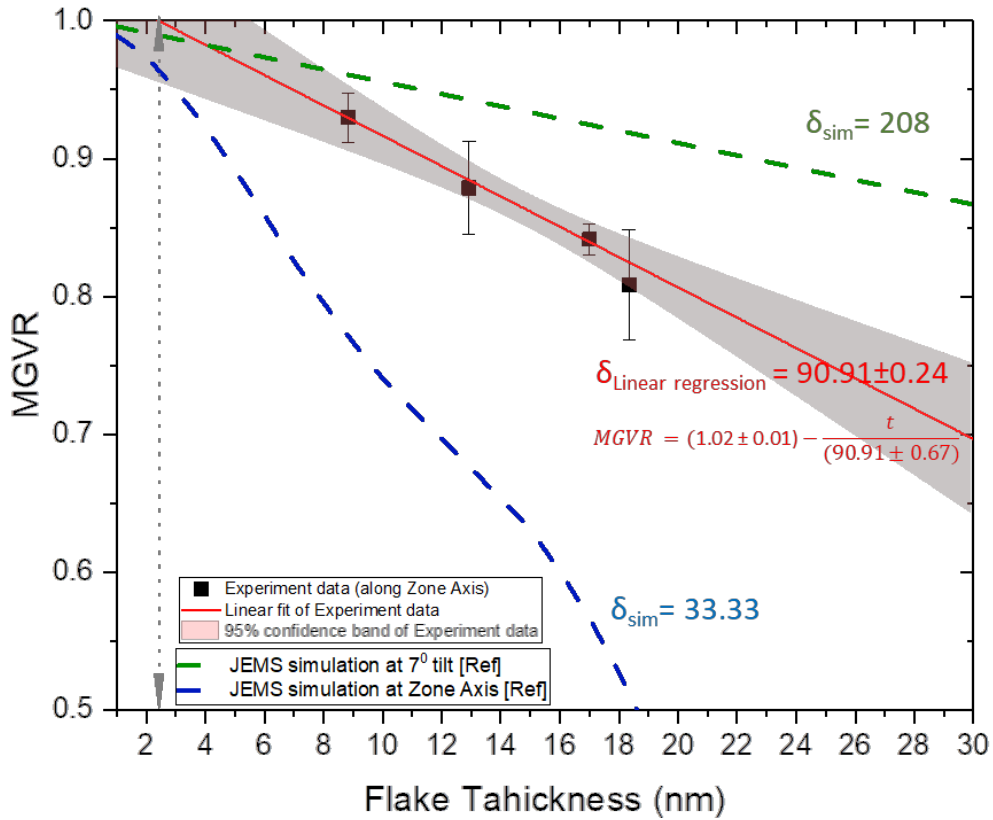


Figure 6.1: Plot of MGVR measured at Zone axis (ZA) vs Flake thickness obtained through folding edge method (scatters). The linear relationship seems to hold true as the flake gets thinner but exhibits a resolution limit of ~3 nm thickness (see dotted lines). The simulations were conducted by Rubino et al. using the JEMS software. (The green dash line): shows the simulation of MGVR vs flake thickness decays in a sample tilted 7° from ZA, where the experimental result fits with the simulation curve. (The blue dash line): shows the simulation of MGVR vs flake thickness decays at ZA. The slope of the curves gives the value of the absorption constant δ for graphite..(2Dtech™ graphene sample)

folding edge method, here the thickness determined by the folded edge was doubled to account for the folded flake. The 1st standard deviation (1σ) in the MGVR over the ROI was shown as error bars.

As shown in Figure 6.1, an inverse linear correlation exists between the MGVR and the flake thickness obtained through the folding edge method, which seems to agree with the linear relationship proposed by Rubino et al. ³⁴. The thickness of flakes can be calculated using the linear relationship obtained as:

$$t = \left((1.02 \pm 0.01) - \frac{I_{tr}}{I_{in}} \right) \times (90.91 \pm 0.67) \dots (eq. 6.1)$$

, where t is the thickness of graphene in nm , I_{tr} and I_{in} are the values for the intensity of transmitted beam on a graphene region and vacuum region respectively. However, on inspection, two issues arise in the experimental linear trend.

Firstly, the y-intercept value of 1.026 ± 0.012 was obtained when applying linear regression to the experimental data, indicating that the MGVR of the flake region will be higher than the MGVR of the vacuum region as the flake gets thinner. This means that the flake region will show a brighter image than the vacuum region, which is unphysical. Thus, based on the linear fit, the maximum resolving limit on such a MGVR method for the non-tilted sample (i.e. zone axis) would approximately occur at ~ 3 nm thickness, which is roughly 8 graphene layers.

Secondly, when the linear regression is compared to the experimental results obtained by Rubino et al. a steeper negative slope of MGVR vs. flake thickness was obtained at zone axis than the MGVR vs. flake thickness obtained at 7° sample tilt. This result in a shorter mean absorption distance ($\xi'_0 = 2\pi\delta$, δ were defined as the material dependent absorption constant, which can be analogous to the penetration depth in an optical system ³⁴), in which a $\delta_{exp} = 90.91 \pm 0.67$ nm was obtained from the experiment, significantly shorter than $\delta_{exp} = 225$ nm derived from Rubino et al's experimental work. In fact, the MGVR measurement performed at 7° sample tilt that was proposed by Rubino et al. agrees very well with both analytical expression based on two-beam case (see equation 2 in reference ³⁴) and the JEMS simulation. This is owing to the fact that the two beam approach is still valid when only one significant reflection beam presents. However, the MGVR should decays fast at zone axis than the measurement conducted at 7° sample tilt (see the blue dash line in figure 6.1) due to additional diffraction losses. This trend can be derived by JEMS simulation because the software deliberated the crystal structure with the many-beam reflection condition, in which the analytical expression derived by two-beam case will no longer be valid. As seen in the red-line in figure 6.1, due to the higher crystal symmetry structure at zone axis than at a 7° sample tilt, the experimental MGVR value obtained at zone axis therefore leads to additional diffraction losses from (100) refraction, resulting in the more rapid intensity loss as number of graphene layer increases ³⁴, and a shorter mean absorption distance.

Even though the JEMS simulation shows that the MGVR measurement at zone axis should have a faster decay than in a lower symmetric sample-tilt condition, the experiment conducted in this project demonstrated that the MGVR decay measured at zone axis is much slower than the JEMS simulation conducted by Rubino et al. (compare the experiment data to the blue dash line in figure 6.1). This discrepancy can be due to the different operation voltages that have been used. Instead of using a 300-kV operation voltage like Rubino et al., an 80-kV operation voltage was used in our study, which could lead to a different reflection or absorption property responded from the material. Besides, a 3 mrad objective aperture was used in Rubino et al.'s study, in which is much smaller than the objective aperture of 17.9 mrad used in our case. This meant that the BF image contrast may arise not only due to the contribution of (002) reflections, but also significantly affected by several diffraction losses. Nevertheless, it is still possible that the inverse linear relationship between MGVR and flake thickness obtained in our experiment holds true despite it deviates from the JEMS simulation.

ii. Sensitivity and detection limits

The main source of uncertainties in this MGVR method for thin flake measurement originates from the Poisson's noise of the BF images, in which the level of noise can be estimated via ³⁴:

$$\sigma_I = \sqrt{I(\tau)} \dots (eq. 6.2)$$

, where the value of $I(\tau)$ is the intensity (brightness) of an image pixel, which is related to the detected number of electrons per pixel arrived the CCD ^{34,66}. However, since the images were transferred to 8-bit, the true intensity was compressed to between 0 and 255, and the level of noise was thereby estimated to be ~ 16 units of greyscale. From equation 6.1, the thinnest graphene can be estimated by such contrast method at zone axis ($\delta_{\text{exp}} = 90.91 \pm 0.67$ nm) is ~ 5.27 nm, which is around 15-18 graphene layers.

However, since the Poisson noise was considered as random errors, it is reasonable to assume the value of each pixel as an independent measurement of the transmitted electron intensity. The Poisson distribution thus can be approximated by a Gaussian distribution when a large number of pixels were taken into statistics^{34,66}. The measured value of intensity $I_s(\tau)$ would be the mean value of the n pixels that are measured on a homogeneous graphene region. Then the noise would be^{34,66}:

$$\sigma_s = \sqrt{I_s(\tau)/n} \dots (eq. 6.3)$$

Thus, from equation 6.1, a monolayer graphene (0.34nm) can only cause a difference of 0.953 unit in greyscale between the vacuum region and the graphene region. The pixels needed to resolve such a monolayer graphene can be calculated as: $0.953 > \sigma_s = \sqrt{I_s(t)/n}$, which n should be larger than 280 pixels ($n > 18323$ pixels for a 99% confidence). Thus, it was estimated an uniform ROI larger than $\sim 3.6 \text{ nm}^2$ ($\sim 229.77 \text{ nm}^2$ for a 99% of confidence) on a monolayer graphene is needed for a 55,000X magnification to identify its thickness by the MGVR. Ideally, the 150 pixel \times 150 pixel sampling ROI used in the project should nearly have the ability to distinguish monolayer graphene from the vacuum region. However, the highly inhomogeneous SAEG graphene samples make the process of finding an appropriate ROI near a reliable folded edge time-consuming, and it is difficult to achieve such an accurate assessment. In addition, the noises in an image do not only originate from the Poisson's noise discussed above, uncertainties such as hydrogen contamination, uneven illumination, sample drift or diffraction contrast...etc are often present. Utilising a higher definition image form could improve such a resolution, but a longer processing time would be needed. Also, it was reported that an alternative image acquisition technique such as acquiring and summing multiple images can minimise the Poisson noise or utilising cross-correlation algorithm to eliminate the effect caused by sample drift³⁴.

II. Correlation between MGVR and relative thickness determined using EELS

A total of six flakes were selected for EELS measurement. The relative thickness (t_R) was calculated using the log-ratio technique introduced in Chapter 3, and the MGVR was determined by selecting the appropriate ROI. Subsequently, the MGVR was plotted against the relative thickness to obtain the relationship. A strong inverse linear correlation between the MGVR and the relative thickness was then obtained as seen in figure 6.2.

Similar to what was found in figure 6.1, the y-intercept value increases to > 1 when the flake gets very thin. This shows the difficulty in applying the MGVR method for the thickness estimation when the flakes are very thin. On the other hand, the MGVR decays with the relative thickness increases, which is also similar to the trend obtained in Figure 6.1. Assuming the inelastic mean free path (IMFP) as 100 nm (for 100KeV, $Z= 6$; $\alpha=0$;

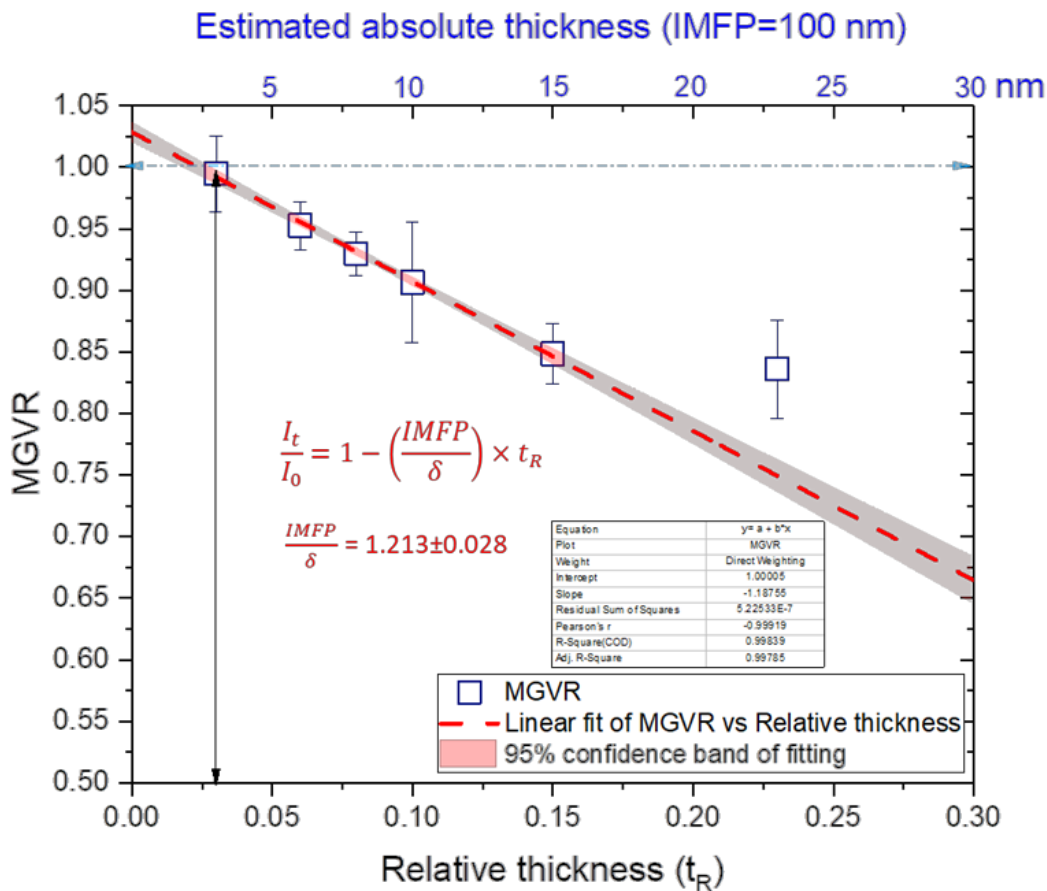


Figure 6.2: Plot of MGVR vs Relative thickness obtained through EELS method – the linear relationship holds true for relative thickness up to the value of ~ 0.15 . (2Dtech™ graphene sample)

$\beta=10\text{mrad}$, from Malis et al. ²¹⁴), the resolution limit was estimated to be ~ 2.3 nm, which is $\sim 6 - 7$ graphene layers.

Combining equations $\frac{I_t}{I_0} = (1 - \frac{t}{\delta})$ and $t_R = \frac{t}{IMFP}$, we can derive the equation:

$$\frac{I_{tr}}{I_{in}} = 1 - \left(\frac{IMFP}{\delta} \right) \times t_R \dots (eq. 6.4)$$

. The equation describes the relationship between the material dependent absorption constant (δ) of electron beam and the inelastic mean free path can be obtained from the slope in figure 6.2. In this case, a value of $IMFP = (1.213 \pm 0.028) \times \delta$ was found from the measurement performed at zone axis (0° sample tilt). The δ is describing the absorption constant of the incident Bloch wave, while the IMFP is the mean distance that an electron could encounter and inelastic scattering event. The relationship between δ and $IMFP$ indicates that the incident electron wave intensity has undergone significant decay before it encountered inelastic scattering events. This could imply that the log-ratio method might be less sensitive than the MGVR method. In fact, the log-ratio method has only been widely discussed and evaluated for thick specimens, where the thickness of specimen is significantly larger than its IMFP, the applicability for ultrathin material like graphene is still debatable. Therefore, the IMFP of graphene and the applicability of log-ratio method will be further discussed in the following sections.

i. Obtaining inelastic mean free path of graphene

With reference to figure 6.1 and figure 6.2, the linear relationships between MGVR and absolute thickness obtained from the folded edge, and the MGVR vs. relative thickness, the inelastic mean free path (IMFP) for a non-tilt thin graphene/graphite sample can be derived. To explore this possibility, the thickness of flakes was calculated using the linear relation from equation 6.1, where the $\frac{I_{tr}}{I_{in}}$ term was substituted by the MGVR value of

flakes that were chosen for the EELS method, the absolute thickness of the flakes was then estimated. The IMFP of the flakes were derived by dividing the absolute thickness by the relative thickness. In order to compare such a result to the existing model for IMFP estimation, another set of IMFP values were calculated via GMS 3 using the low-loss EELS spectra. The calculation of inelastic mean free path in GMS 3 was based on Mali's study, estimated as:

$$IMFP_{(nm)} = \frac{106F\left(\frac{E_0}{E_m}\right)}{\ln(2\beta\left(\frac{E_0}{E_m}\right))} \dots(\text{equation . 6.5})$$

, where E_0 is the operating voltage; $E_m \approx 7.6Z_{eff}^{0.36}$ is the mean energy loss, which Z_{eff} is the effective atomic number of the specimen material; β is the collection semi-angle in mrad; F is the relativistic factor dependent on the operating voltage; the convergence semi-angle was used for incident beam parameter correction. The calculation of IMFP proposed by Malis et al. is derived by using a semi-experimental approach originated from the scattering theory ^{67,214,215}. Values of experimental conditions including operating voltage = 80 KeV, collection semi-angle = 5.4 mrad, incident convergence semi-angle = 1.0 mrad, and effective atomic number = 6 for carbon were given to the program prior to performing such a calculation ²¹⁵.

These two sets of IMFP were compared with each other. As seen in figure 6.3, the IMFP values estimated using the calculated absolute thickness were of varying difference against the IMFP calculated using GMS 3 with a deviation of approximately $\pm 11.4\%$. The relative thickness of the 6th flake (reading left to right) 6 is 0.23, which has a higher percentage of error than other flakes for the estimated IMFP. Such a deviation might be caused by its higher thickness, for which a different plural scattering is starting to play an important role and making the estimated IMFP much different to the other thinner flakes, which also evident in figure 6.2. Besides the possible plural scattering effect, the interference from the presence of inhomogeneous layer regions or a different density of defects in the aperture zone, may lead the inaccurate thickness estimations and IMFP calculations when using the method proposed.

Moreover, calculating IMFP using GMS 3 was based on equation 6.5, in which the equation was parameters on the scattering events with zero-damping dipole model ^{67,214}. This may lead to a more precise IMFP estimation for the sample material that the outer electrons are weakly bonded to the nuclei. Thus, such a method was only judged by Zhang having an accuracy of around $\pm 10\%$ for a polycrystalline Au film when the collection angle is less than 5 mrad ²¹⁴⁻²¹⁶, the applicability on such an sp^2 carbon material is still unclear. Nonetheless, the data in figure 6.3 exhibits a closer agreement in the thin flake regions, which may imply the zero-damping dipole model used by Malis et al. could

| Flake | Relative thickness (t/IMFP) | MGVR | Estimated thickness from MGVR using eq. 6.1 (nm) | Estimated IMFP (nm) | IMFP from GMS 3 (nm) | Differences (%) |
|-------|-----------------------------|------|--|---------------------|----------------------|-----------------|
| 1 | 0.03 | 0.99 | 2.91 | 97.04 | 118.33 | 17.99 |
| 2 | 0.06 | 0.95 | 6.72 | 111.95 | 104.33 | 6.98 |
| 3 | 0.08 | 0.93 | 8.82 | 110.19 | 120.50 | 8.55 |
| 4 | 0.10 | 0.91 | 10.92 | 109.16 | 116.50 | 6.30 |
| 5 | 0.15 | 0.85 | 16.20 | 108.03 | 118.93 | 9.17 |
| 6 | 0.23 | 0.84 | 17.32 | 75.31 | 114.00 | 33.94 |

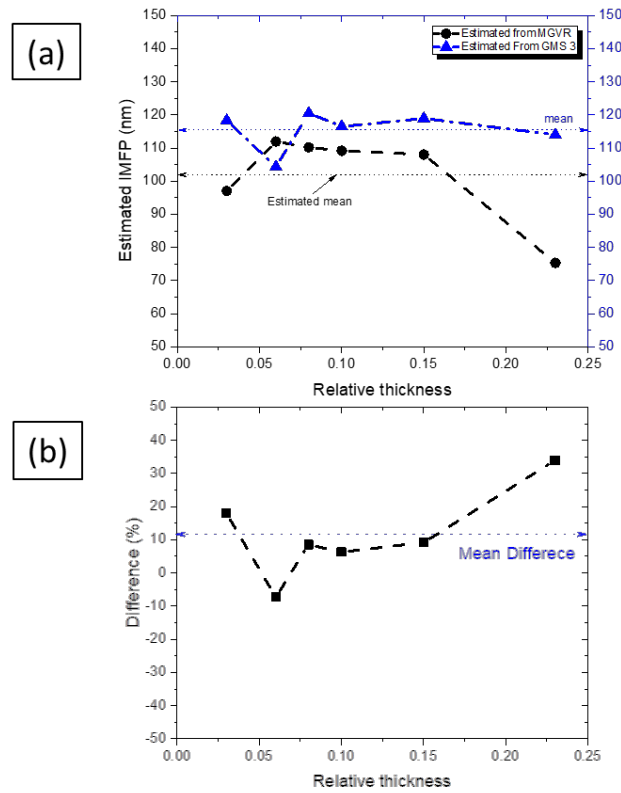


Figure 6.3: Comparison between IMFP estimated through absolute thickness and IMFP estimated through GMS 3; the flakes are listed in increasing relative thickness for ease of reference. (a) compares the IMFP obtained from MGVR to the IMFP obtained from GMS 3. (b) plots the difference of estimated IMFP vs. relative thickness..(2DtechTM graphene sample)

be a better approximation for thin graphene, but a conclusion cannot be drawn at this stage for lack of rigorous understanding of how real dielectric properties vary according to graphene thickness. Also, although there is an overlapping region between the method using GMS 3 and the method derived using MGVR with relative thickness, it is not possible to determine which method is more accurate, because both methods can be affected by the uncertainty of obtaining an accurate absolute thickness of graphene. In addition, the IMFP estimation obtained from MGVR method is influenced by the absorption of Bloch wave (δ); whilst the Mali's semi-empirical equation is based on scattering theory, which is also inaccurate when the specimen is very thin. This is not only due to the additional diffraction losses for the Bloch wave, but also the arising of surface plasmon in thin graphene, a shorter IMFP will be calculated via the MGVR method due to the over-estimation of relative thickness.

Nevertheless, despite the inaccurate and uncertainty of obtaining an IMFP value for graphene, such a comparison shows the discrepancy between estimating IMFP using MGVR and Mali's semi-empirical equation, which demonstrated the difficulties of applying the concept of inelastic mean free path to a thin crystalline solid and concurs with the suggestion made by Egerton in his book ^{66,67,217}.

III. The plasmon bands in multilayer graphene / graphite

As mentioned earlier, the log-ratio method gives an easy and general approach to estimate the thickness of specimens. However in practice, the approach has only been judged to be valid for $t/IMFP$ as large as 4 (within errors of about 10% ⁶⁷), while an over-estimated thickness might be obtained for very thin specimens $\frac{t}{IMFP} < 0.1$ due to the significance of surface plasmons ^{67,68}. As shown earlier in the section, among the six selected graphene flakes, five of them were measured to have relative thickness ≈ 0.1 , which might be one of the reasons that cause the discrepancy in the IMFP estimation.

The arise of surface plasmons can be observed when looking closer at the low-loss EELS spectra. A noticeable change in both peak shape and position as a function of graphene thicknesses is seen, which could be used as an alternative method for characterising the thickness of graphene for flakes that have a relative thickness smaller than 0.1. The change in peak position and shape for different graphene thicknesses is shown in figure 6.4. In the figure, the ZLP tail was approximated by the logarithm tail model in GMS 3 and open or folded edge methods were used to determine the number of graphene layers (refer to figure 3.19(a)). Thickness of the HOPG sample was estimated to be ~ 360 layers (relative thickness = 1.05 and absolute thickness = 121.95 nm using the built-in “compute thickness” function in GMS 3).

As seen in figure 6.4, a clear π plasmon peak shift towards the lower energy losses is accompanied by a $\pi + \sigma$ plasmon peak broadening as the number of graphene layers decreases. To further quantify such a peak variation, the magnified and normalised π plasmon peak is shown in Figure 6.5 (a). By observing the peak maximum position, the π plasmon peaks was found to have shifted from 7.12 eV in HOPG to ~ 4.91 eV in the regions that consisted of 3 layers. This observation concurs with a similar study from T.

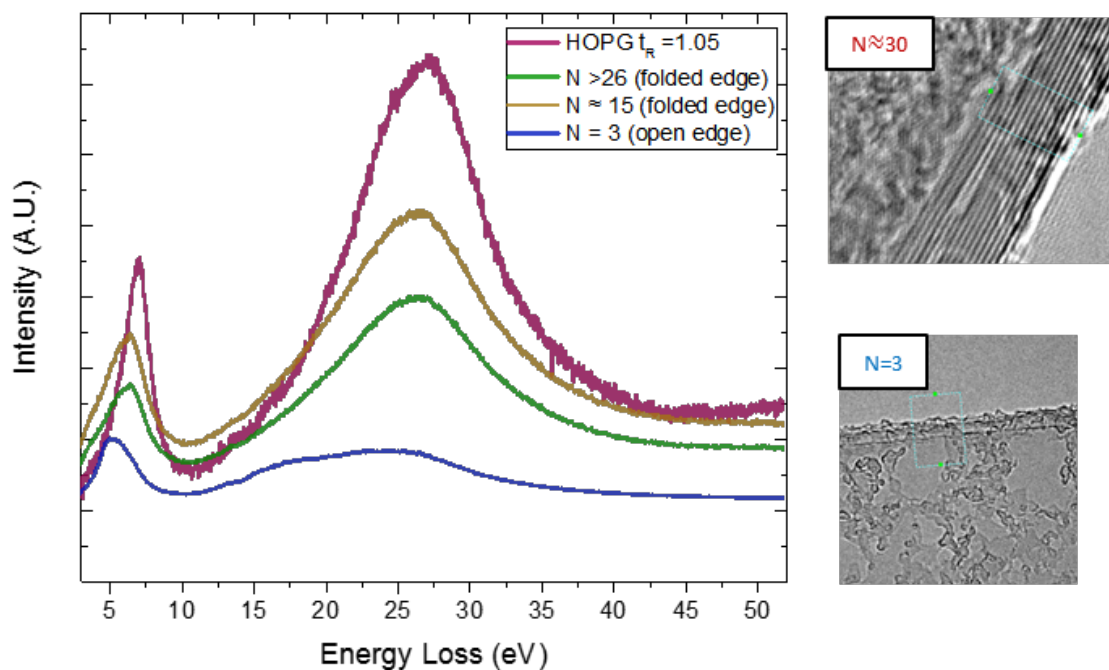


Figure 6.4: EEL spectra of 3, 15, 26 layers of graphene and compared to a HOPG specimen (relative thickness = 1.05). The ZLP was approximated by the logarithm tail model and subtracted via GMS3. The number of graphene layers in a flake was characterised by the folded edge or the open edge in the corresponded TEM images (seen in the insets).

Eberlein et al. ²¹⁸ on free-standing graphene , where they reported the centre of the π plasmon peak to be 4.7 eV for a monolayer free-standing graphene, and 7 eV for a 30-layer graphite flake.

iii. The evolution of graphene plasmon peaks for thickness determination

Since the plasmon peak is originated from collective oscillations of outer atomic electron of the material, the shape of the plasmon peak will be the response of a damped harmonic oscillator with eigenfrequency ω_p that is forced by an external perturbation with frequency ω . Considering the damping energy is given by Γ_p , the power dissipated by the forced damped harmonic oscillator is a Lorentzian curve. Thus, the plasmon peaks should able to be fitted by Lorentz peaks if the behaviour of the material's outer atomic electron follows the proposed damped harmonic oscillator model. Therefore in order to reasonably quantify the variation of the plasmon peaks, the Lorentzian curve fitting was used. As seen in figure 6.5, the position of the π plasmon peak in the low-loss EELS spectrum was fitted by a single or two Lorentzian peaks, the variation of the π plasmon peak was then quantified and plotted as a function of number of graphene layers. A relationship between the position of π plasmon peak and the number of graphene layers for non-tilt, $dq \rightarrow 0$ measurement was expressed by an empirical equation as:

$$x_{M(\pi)} = (7.15 \pm 0.27) + (-2.55 \pm 0.42)e^{-\frac{N}{(27 \pm 9.13)}} \dots (eq. 6.6)$$

, where $x_{M(\pi)}$ the position of maximum value in the π plasmon peak and N is the number of graphene layers. Utilising the equation, the number of graphene layers can be estimated by the position of the π plasmon peak, and such a variation potentially indicates the variation in electron band structure as the number of graphene layers increases.

Also shown in figure 6.5(a), π plasmon peak in HOPG presented only a single Lorentzian peaks, centered at 6.9 eV. As the flakes get thinner, an extra surface plasmon peak at ~ 5 eV

is starting observable and the contribution to the π plasmon peak increases as graphene gets thinner. Figure 6.5 (c) shows the ratio between the integrated area of surface plasmon and bulk plasmon. The contribution ratio of surface plasmon increases from 0 in the HOPG sample to more than 0.9 in a trilayer graphene, the trend can be fitted with an exponential decay curve, which indicated the main contribution of π plasmon peak is surface plasmon when the specimen is very thin, while the bulk plasmon dominates when the specimen is thick.

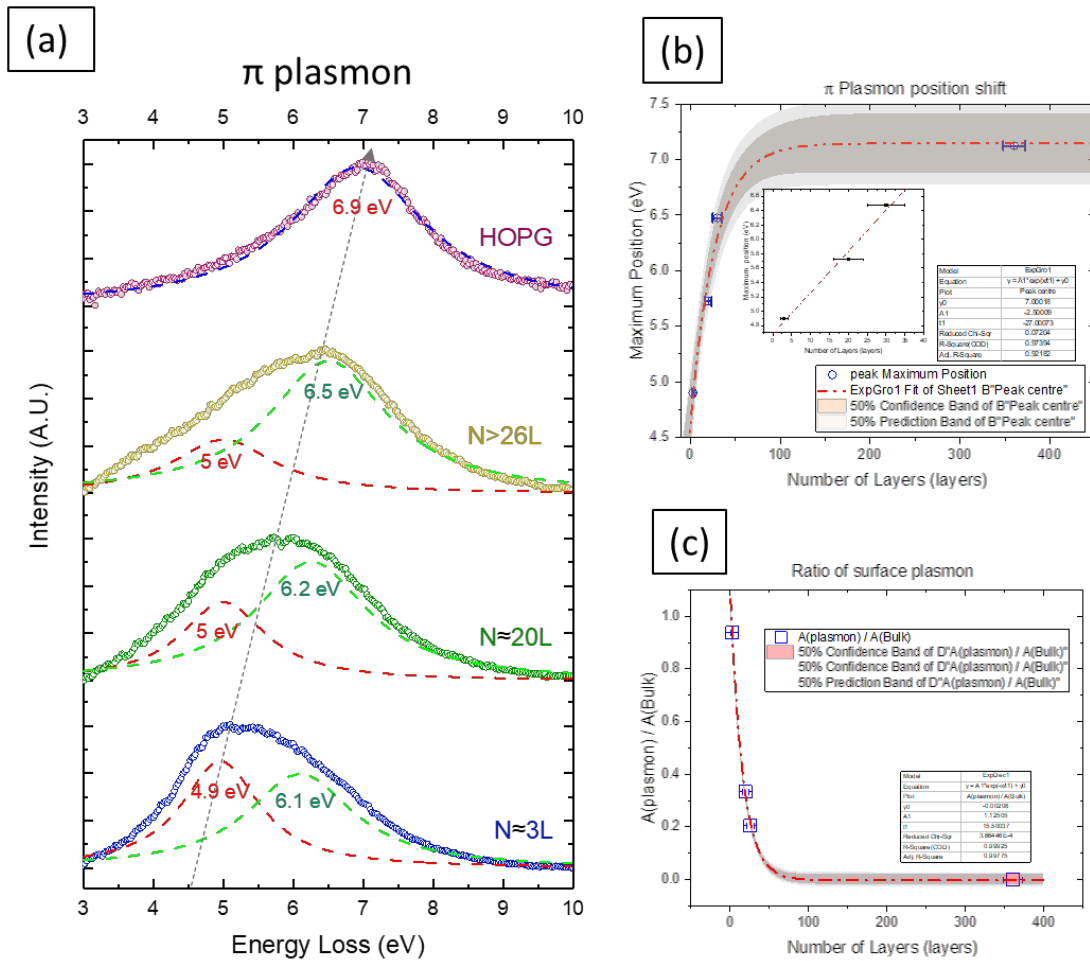


Figure 6.5: shows variation of π plasmon peak with the number of graphene layer. (a) fit with two Lorentz peaks to the π plasmon peak. (b) Plot the peak position as a function of number of graphene layers. (c) The ratio of surface / bulk plasmon peak as number of graphene layers increases.

Besides the observation in the π plasmon region, the surface plasmon excitation mode was also found in the $\pi + \sigma$ plasmon region for thin graphene flakes and repeatedly observed in the thin graphene regions (< 15 layers). Shown in figure 6.6(a), the thin graphene region ($N = 3$), an additional surface plasmon peak centered at 18.5 arises

accompanied with the ~ 26 eV bulk plasmon peak was observed. Such a surface plasmon peak is absent for the thick graphene and the HOPG sample, where only a bulk plasmon peak centred at ~ 26 eV can be observed. The latter peak centre kept moving toward to the higher energy as the graphene layers increased, resulting in the surface plasmon excitation mode vanishing and the bulk plasmon mode remained. As implied by the ratio plot shown in the lower part of figure 6.6(b), the $\pi + \sigma$ plasmon structure for the flake that is more than 25 layers thick is almost identical to the ~ 360 -layer thick HOPG.

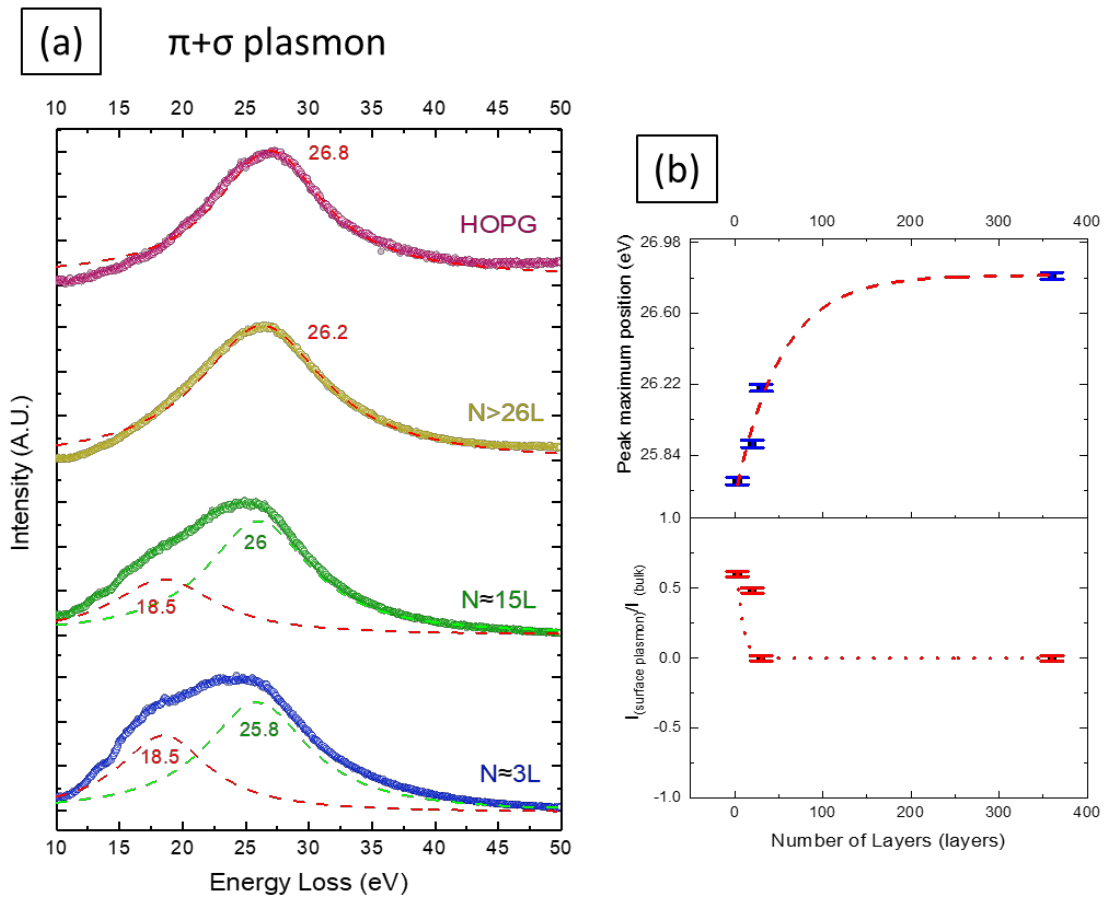


Figure 6.6: shows variation of plasmon peak with the number of graphene layer. (a) two plasmon modes in the plasmon peak and can be fitted with two Lorentz peaks. (b) shows peak position and the ratio of surface plasmon peak vary with the number of graphene layers, the trend was fitted with exponential growth and exponential decay respectively.

iv. Discussion

When comparing the result from figure 6.5 and 6.6 to the log-ratio method, the variation of plasmon peaks of graphene shows a more sensitive trend with flake thickness. Thus, a graphene thickness estimation based on the evolution in the plasmon peak variation seems to be a better indicator for graphene flakes that have relative thickness < 0.1 .

Moreover, studying the variation in the plasmon structure not only provided a simpler method for the identification of graphene thickness, such an observation could also indicate some information about the variation of electron band structure as a function of number of graphene layers coupled. This is because the plasmon structure in graphene can be interpreted as charge oscillations confined to certain planes and coupled via interlayer coulomb interactions. This means that when the coupling is weak, the plasmon excitation on each of the graphene layers may act like separated isolated graphene sheets, while a strong interlayer coupling gives rise to the degeneracy of these plasmon modes and leads to the formation of different plasmon bands. P. Wachsmuth et al. suggested a layered electron gas model (LEG) to interpret the dispersion and the shift of plasmon peaks ²¹⁹. However, the study was mainly focused on few-layered graphene, with large emphasis on the momentum-resolved EELS experiment and simulation. It is therefore still worth performing a systematic detailed experimental study on how the electron band structure evolves from graphene to graphite. Nevertheless, it should be noted that applying the conventional 3D electron model to interpret the plasmon peaks in graphene could be inaccurate. This is because the plasmon vibration in the 3D system is now confined in 2D, which results in a highly anisotropic electron movement in that the mobility of electron is only high along the basal plane. In addition, with the unique band structure of graphene, a more complicated Lindhart model is needed for correlating the plasmon behaviours to the graphene dielectric properties. However, despite the incomplete understanding of graphene dielectric properties, the observed variation of plasmon peaks shift as a function of graphene thickness could be roughly explained by the presence of both in-plane and out-of-plane collective electron oscillations modes in graphene and graphite ^{83–85,220}.

Therefore, although it could be concluded that the plasmon peak has a positive shift trend with the increase in the number of graphene layers, the corresponding band structure or dielectric properties cannot be accurately derived from this set of experimental data. Not only because of a lack of suitable dielectric model to be used for graphene, but also because the commercial EELS data treatment software (GMS 3) relies on sum rule to calculate the sample thickness and dielectric function, which can be very inaccurate in this case. A further study on EELS data treatment is needed to bypass the dependence on the software's thickness estimation method ²²¹, so that the Kramers-Kronig can be correctly applied and to be used to determine the dielectric properties of graphene. If this can be achieved, performing the momentum-resolved EELS measurement with band structure simulation could enable the possibility of linking the observation from EELS experiment to the dielectric properties that evolve with graphene layer increases ⁸⁵.

Besides all the observation mentioned in the section, it is worth noting that the presence of crystal defects or mean contamination of the region of interest can both affect the low-loss EELS spectrum. Previous studies applied STEM and HAADF imaging to discern such uncertainties, but these techniques were not applied in this project ^{218,219}.

6.2. The 2D (G') band dispersion in Raman spectroscopy

As mentioned in chapter 3, Raman spectroscopy can not only be used to characterise the crystalline imperfections of the graphene samples, but the number of graphene layers (N) can also be identified by the shape and position of the Raman 2D peak. The shape of the 2D band at $\sim 2700\text{ cm}^{-1}$ is known to change with the changing number of graphene layers ^{21,212,222}. Thus, a 2D peak analysis procedure was developed to quantify the change in

bandshape, in order to estimate the number of graphene layers constituting a flake when using Raman spectroscopy.

I. The 2D peak evolution and band overlapping

As shown in figure 6.7, the 2D peak was de-convoluted into four vibrational elements: (1) 2D_{1B}: the peak centre is at ~ 2660 cm⁻¹. This is the lowest frequency peak of the 2D (G') band and could correspond to the P₂₂ process as introduced in Chapter 2 ^{113,223}. (2) and (3) The 2D_{1A} and 2D_{2A} at ~ 2685 cm⁻¹ and ~ 2710 cm⁻¹ respectively, two of which correspond to the P₁₂ and P₂₁ process and have higher relative intensities than the other two in multilayer graphene. (4) The 2D_{2B} at ~ 2730 cm⁻¹ is the highest frequency of the 2D band, the vibration mode is associated with the P₁₁ process, which also has the largest wavevector (q_{11}) and hence higher frequency ^{113,223}. All the peaks are de-convoluted by the Levenberg-Marquardt algorithm and the Lorentz peak model in OriginPro in which each peak width (FWHM) was constrained to be ≤ 30 cm⁻¹, and a good deconvolution result can be obtained with Adj. R-Square value ≥ 0.97 . All spectra and well-established data was taken from Ferrari's previous work ²²² for regression reference as it was recorded under the same experimental condition (514 nm excitation laser).

As seen in figure 6.7, the monolayer graphene exhibits only a Lorentz peak at ~ 2685 cm⁻¹(2D_{1B}), while when $N \geq 2$, three additional peaks became evident. This is because the possibility of (2D)G' band scattering processes increases as the number of graphene layers increase ^{112, 224}. Malard et al. suggested that there are already 15 possibilities for a trilayer graphene, but the frequency spacing between each peak is not large enough for them all to be resolved ¹¹². Although the scattering gets even more complex for multilayer graphene ($N > 3$), the G' band spectra start to merge with each other and become simpler in terms of their appearance. For a highly oriented pyrolytic graphite (HOPG, $N \rightarrow \infty$), the G' band can be de-convoluted into only two bands (2D_{1A} and 2D_{2A}). This was explained as a result of the number of double resonance events allowed in in the three-dimensional structure ¹¹¹, and was discussed in detail using a geometrical approach by Cancado et al. ¹¹¹.

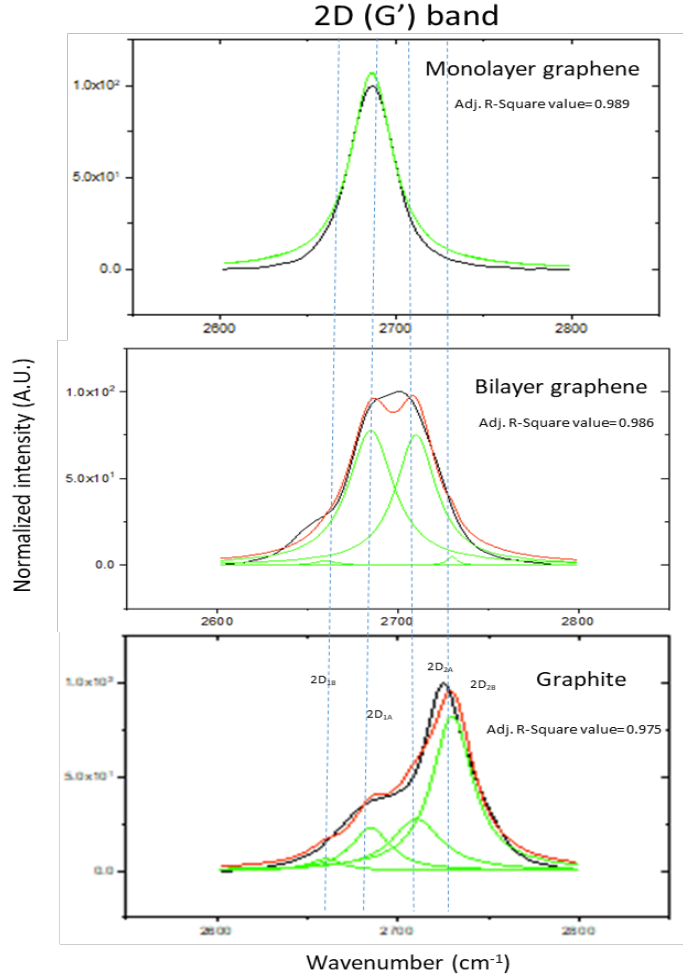


Figure 6.7: Quantifies the change in shape and position of the Raman 2D peaks with number of layers. The shape and position of the 2D peaks were deconvoluted into four vibrational elements.

i. Regression of the 2D peak evolution

In order to utilise such a variation of the 2D (G') peak, the ratio of integrated area: $A_{2D2} / A_{2D1} = (2D_{2A} + 2D_{2B}) / (2D_{1B} + 2D_{1A})$ was plotted versus the number of graphene layers. As seen in figure 6.8, the A_{2D2} / A_{2D1} ratio increases with the number of graphene layers (N) from 0 for monolayer graphene to ~ 2.4 for HOPG. An empirical equation was then obtained by fitting the A_{2D2} / A_{2D1} ratio against (N), where the number of graphene layers (N) could be obtained as:

$$N = \frac{1}{(-0.209 \pm 0.068)} \times \ln\left(1 - \frac{A_{2D2}/A_{2D1}}{2.434 \pm 0.289}\right) \dots (eq. 6.7)$$

From figure 6.8, it can be seen that the A_{2D2}/A_{2D1} ratio increases with the number of graphene layers (N) but reached a plateau and approximates to graphite, this phenomenon potentially indicates the band overlapping as number of coupled graphene layer increases (see section 2.2 II, figure 2.9). Although the number of coupled graphene layers could possibly derived using equation 6.7, such an equation is difficult to apply to estimate the number of graphene layers in practice This is not only because the steep slope in the $N < 10$ region makes an accurate estimation of graphene layers very difficult, but also the complex peak fitting process and the relatively weak 2D peak in damaged graphene make the application of such a technique to the SAEG graphene difficult and time-consuming.

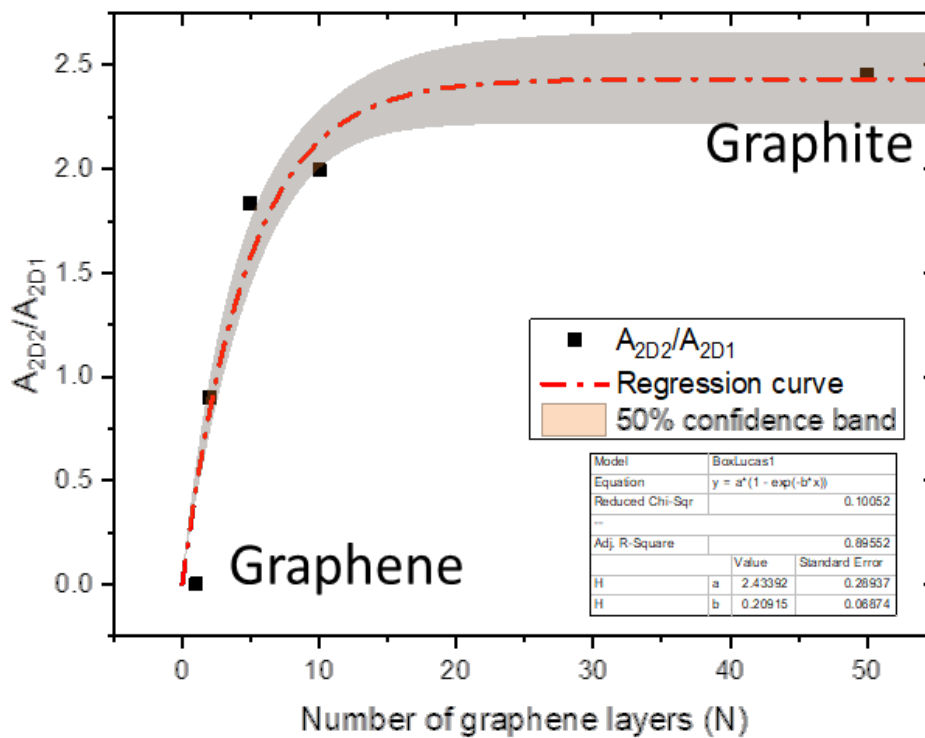


Figure 6.8: shows a regression between A_{2D2}/A_{2D1} vs. number of graphene layers.

ii. Simplified empirical equations for practical graphene thickness estimation

Instead, an alternative method was then developed to simplify the characterisation process for identifying the number of graphene layers in the SAEG sample using Raman

spectroscopy. As seen in the inset in figure 6.9, not only does the peak shape of the 2D band change with an increase in the number of graphene layers, but also the peak position shifts from $\sim 2685 \text{ cm}^{-1}$ in graphene to $\sim 2725 \text{ cm}^{-1}$ in graphite. This information can be gathered by simple differentiation of the 2D peak, where a requirement of a sharp 2D peak and complex peak fitting process can be bypassed. Figure 6.9 plots the 2D peak centre and peak centroid as a function of number of graphene layers. For a monolayer and bilayer graphene flake, the 2D peak centre and peak centroid are almost in the same position. This is due to the symmetrical peak shape of the 2D peak. The difference between the peak centre and peak centroid position increases with the number of graphene layers, since the peak shape becomes asymmetric as the Raman scattering property is getting closer to graphite.

The relationship between peak centre and the number of graphene layers can be fitted with an exponential growth function, where the number of graphene layers can be estimated via the empirical equation as:

$$N = (-1.944 \pm 0.23) \times \ln \left(\frac{((2725.57 \pm 0.39) - X_c)}{65.4 \pm 4.96} \right) \dots (eq. 6.8)$$

, where X_c is the position of peak centre and N is the number of graphene layers in the flake of interest.

For the sake of convenience, the estimation of the number of graphene layers was further approximated by a linear relationship in the region of $N < 10$:

$$N = \frac{1}{(4.76 \pm 0.84)} \times (X_c - 2685), \text{ for } X_c < 2720 \text{ (cm}^{-1}\text{)} \dots (eq. 6.9)$$

, in which for a graphene lake that is thicker than 8 layers, the 2D peak centre present will present at frequency slightly higher than 2720 cm^{-1} and will be approximated as graphite.

The purpose of studying the 2D peak shift of graphene in Raman spectroscopy is to develop a fast identification for the number of graphene layers in a flake. In spite of utilising a comparably direct the band overlapping phenomenon to estimate the number of graphene layers, the technique based on the evolution 2D peak centre position is still considered one of the easiest and practical method to identify the number of graphene layer coupled in a flake.

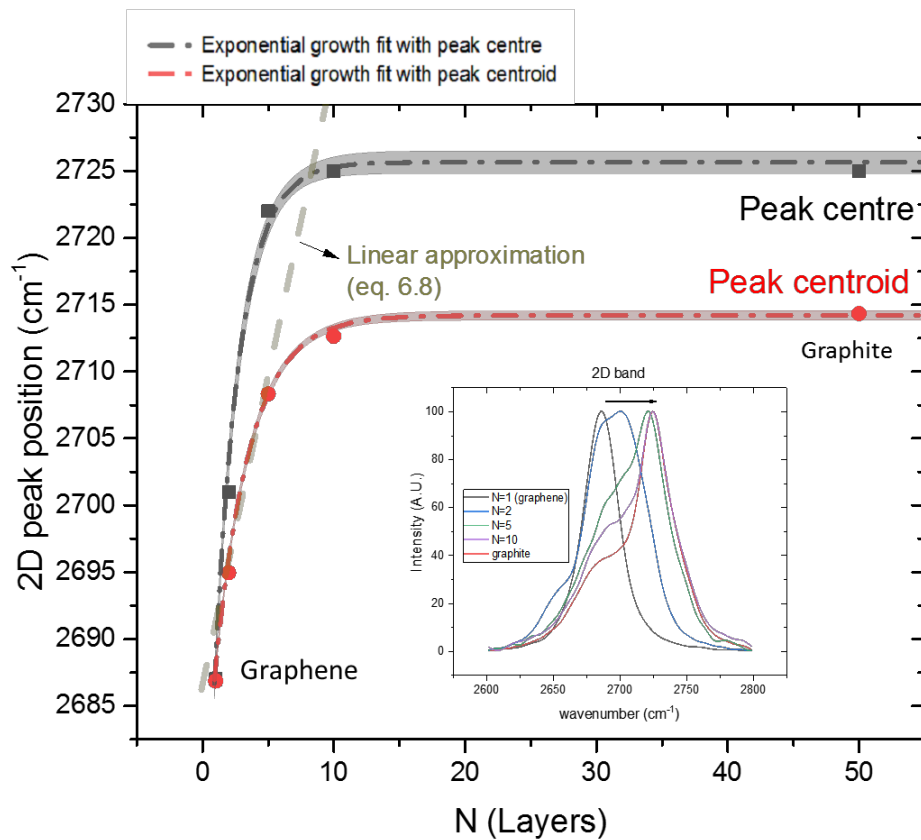


Figure 6.9: shows a regression between the 2D peak positions vs. number of graphene layers. The dash line indicates is the curve fitted with exponential growth.

6.3. Obtaining flake thickness distribution for the SAEG graphene ((2Dtech aquagraph SAEG sample were used)

Owing to the random collision processes during the synthesis of SAEG graphene, some flakes will be exfoliated into few-layer graphene, while some will remain as thick graphite, as shown in the optical microscope images in Chapter 4.2. Various techniques developed in the earlier sections of this chapter were applied to estimate the thickness of the SAEG graphene from 2Dtech.

I. Thickness distribution obtained by MGVR

As discussed in section 4.1, a total of 199 graphene flakes were selected in the TEM. These flakes were categorised as either primary flakes or aggregated flakes. Among all the selected flakes, a mean MGVR value of 0.795 ± 0.168 was observed. However, the MGVR exhibited a mean value of 0.881 ± 0.092 , and 0.709 ± 0.183 for primary and aggregated graphene flakes respectively. Figure 6.10 shows the thicknesses of selected graphene flakes estimated from the MGVR using equation 6.1, where a mean value of 21.03 ± 15.31 nm was obtained. Figure 6.10(b) and figure 6.10(c) shows the thickness distributions of the primary flakes and aggregated flakes respectively; both histograms exhibit a bimodal distribution curve. An overall mean thickness of 13.214 ± 8.358 nm was found in the primary flakes, with two Gaussian peaks centred at around 7.5 nm and 25nm. The aggregated graphene flakes exhibit around twice the thickness of the primary flakes, with an overall thickness estimated to be 28.86 ± 16.67 nm. The bimodal thickness distribution can also be fitted with two Gaussians, which centred at around 15 nm and 40 nm respectively. These bimodal thickness distributions in both primary and aggregated

flakes could be due to the presence of folded edge or flake overlapping regions present in an image, which is also evidence that the graphene flake aggregation is preferable vertically rather than horizontally.

However, it should be mentioned that the presence of uneven illumination, interference of the holey carbon film, as well as curved or aggregated flakes in the image can make it difficult to apply the MGVR method for large-scale thickness determination. Nevertheless, despite all the drawbacks mentioned for the MGVR method, this technique can still provide a fast screening for graphene thickness identification.

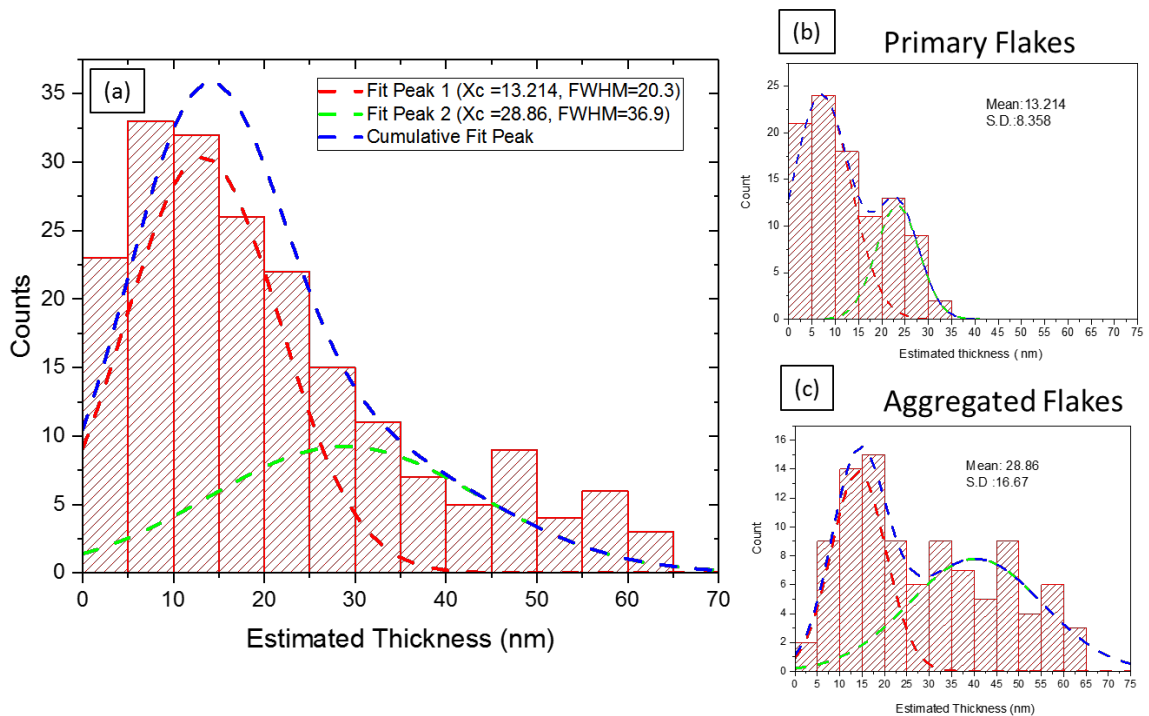


Figure 6.10: Histograms show graphene thickness via MGVR method. The primary flakes show a mean thickness of 13.214 ± 8.358 nm, which about half of the thickness is shown by the aggregated graphene flakes (28.86 ± 16.67), an evident that the graphene flake aggregation is favoured vertically rather than horizontally. (2Dtech aquagraph SAEG sample were used)

II. Thickness distribution obtained using the 2D band dispersion in Raman spectroscopy

As referred to in sections 3.3 and 5.2, a random sampling method was applied to the SAEG graphene sample, and a series of 2D band spectra was acquired. The top panel of figure 6.11 shows a histogram of the 2D peak position from the selected graphene flakes. The centre of 2D peak ranges from 2699 cm^{-1} to 2725 cm^{-1} , but no intense 2D peak centred at 2685 cm^{-1} was observed, indicating that clean monolayer graphene flakes are absent in the sample. Around half (47.6%) of these selected flakes exhibit 2D band at frequency $> 2720 \text{ cm}^{-1}$, indicating that many of these graphene flakes are incompletely delaminated and remained graphitic or multilayer graphene properties.

The thickness was estimated via equations 6.7, 6.8 and 6.9. As seen in figure 6.11, the thickness histograms obtained from equations 6.7 and 6.8 exhibit a lognormal distribution,

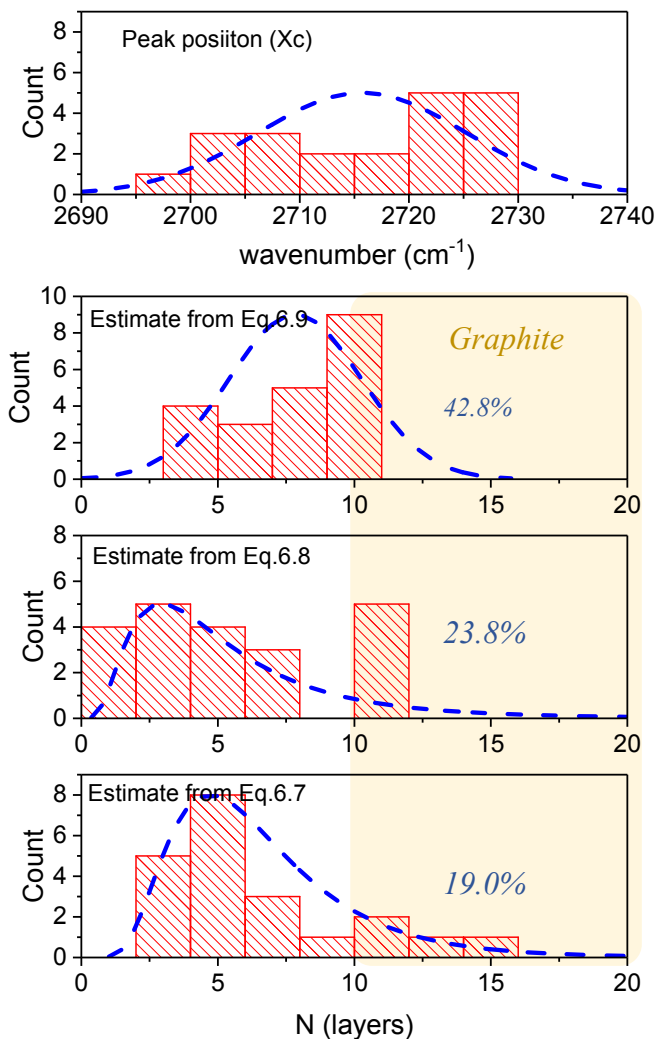


Figure 6.11: shows the thickness distribution estimated via the 2D band in Raman spectra. With random sampling, the histogram of 2D peak centre is shown in the top panel. The corresponding thickness distribution were determined via eq. 6.7, eq. 6.8 and eq. 6.9. The yellow boxes indicated the flakes that are identified as graphite. (2Dtech aquagraph SAEG sample were used)

where the mean thickness was estimated to be 6.51 (6 - 7) layers and 7.84 (7 - 8 layers) from equations 6.7 and 6.8 respectively. Furthermore, a significant proportion of graphene flakes were categorised as graphite as the estimated number of graphene layers were larger than 10 ($N > 10$): 19.0% and 23.8% of the SAEG graphene sample was categorised as graphite from equation 6.7 and 6.8 respectively (see yellow boxes in figure 6.11). The thickness estimation performed by Equation 6.9 shows poor precision in terms of the number of graphene layers. Since Equation 6.9 approximate equation 6.8 as a linear relationship for $N < 10$, it is the simplest way to estimate the number of graphene layers. However, the variation of 2D peak against the graphene thickness is much more

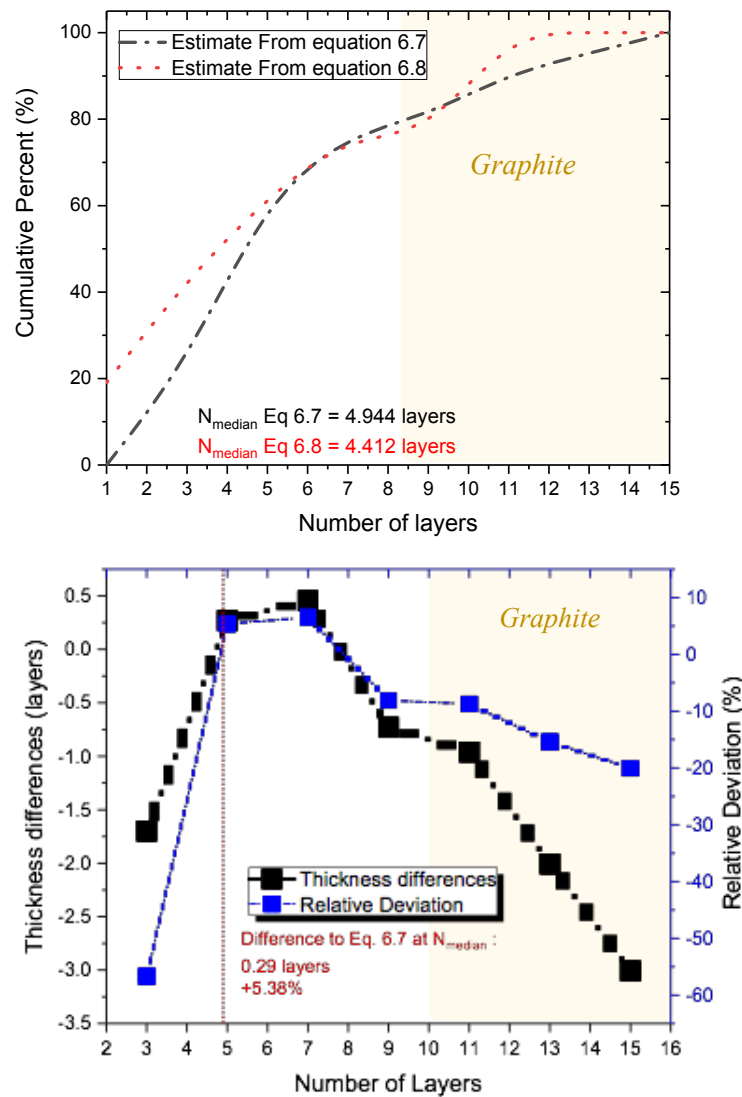


Figure 6.12: Analysis the differences between obtaining thickness distribution via eq.6.7 and eq. 6.8. The estimation through eq.6.8, generally sees the graphene thinner; the difference is small for graphene thickness between 4 to 10 layers. 2Dtech™ graphene sample

complicated and the linear relationship cannot accurately quantify such a variation and results in a poor thickness estimation.

Overall, equation 6.7 might be the most precise way to describe the variation in 2D band versus the number of graphene layers. This is because the method not only takes the shift in peak position into account, but also the 2D band broadening and contribution of relative peak intensities. However, the peak deconvolution process is complicated and time-consuming. Equation 6.8 provides a comparably simpler method. Figure 6.12 analyses the difference between the estimated graphene thicknesses derived using equation 6.7 and 6.8. As seen in the figure, even though equation 6.8 generally estimates thinner graphene, the difference is small for graphene thickness between 4 and 10 layers. Furthermore, equation 6.8 identifies 23.8% of the flakes as graphite, which is only about 4.8% more than the identification from equation 6.7. Therefore, the equation 6.8 has a similar ability to differentiate the number of graphene layer as equation 6.7, however it has an easier data treatment method and a shorter processing time.

6.4. Comparison between different characterisation techniques

There is a significant difference when obtaining SAEG graphene thickness between the MGVR method and the Raman 2D band dispersion method. As highlighted in figure 6.10 and 6.11, the mean thickness for the primary flakes using MGVR was estimated to be 13.214 nm, in which is ~ 40 layers of graphene. Conversely, the Raman measurement shows a mean thickness of 6~8 layers, which should have a thickness < 3 nm. In order to understand the cause of this deviation, an extensive AFM study was used.

I. Comparison between optical reflection spectrum and AFM

Figure 6.13 shows comparisons of the AFM measurement to the optical microscope image. Owing to the accuracy of the piezoelectric stage on the AFM, it allows us to locate the flake of interest on the substrate and compare it with the result obtained by using the optical microscopy technique. We have focused on a large but thin graphene flake, which was synthesised via electrochemical exfoliate HOPG and was found by optical microscopy. As seen in figure 6.13(b), the thinnest part of the graphene flake was estimated to be ~ 1 nm. The same flake was measured by the reflection spectra from optical microscope, as shown in figure 6.13(c). The image was separated into RGB channel and the green channel was used for the thickness measuring. With 400 pixel sampling, the background (substrate) reflection intensity have a mean value of 82.707 (see figure 6.13(d)). The thicker part of the graphene flake was found to have a mean reflection of 55.917. The contrast is therefore calculated to be 0.324 (equation 4.6), a thickness of 3.86 layers (1.312nm) was estimated (see section 4.2). However, The same region was measured to be ~ 8 nm from the AFM profile, which is significant thicker than the measurement obtained from the reflection spectrum. In order to test the limitation of the technique based on optical reflection, the thinnest region in the graphene flake was measured. The region demonstrated a mean reflection intensity of 69.333, which was estimated to have a thickness of 1.78 layers (0.6025 nm). Similarly, a much thicker result was obtained using AFM, where the thickness was estimated to be ~ 1 nm from the AFM profile. This could be due to the effect that the distortion induced by the finite AFM tip radius, or often reported, the existence of a buffer layer between the graphene samples and the substrate; a graphene monolayer can be measured to be as thick as 1nm under AFM ^{139,140}. In spite of the lack of precision from the AFM technique, it seems that the optical reflection spectrum method can resolve very thin graphene regions. From figure 6.13, the optical reflection spectrum technique has the ability to differentiate the contrast a graphene region as thin as ~ 1 nm from the substrate. Although a precise thickness precision assessment is still unavailable in this stage, the ability to visualise thin samples is already much higher than other conventional techniques. However, similar to the MGVR method,

such a technique is still depend on the number of pixels can be sampled, which is also limited by the availability of the size of homogeneous graphene regions. Therefore, with the a homogeneous graphene and higher resolution AFM/STM, the precision and accuracy of such an optical reflection technique can be further evaluated or even improved.

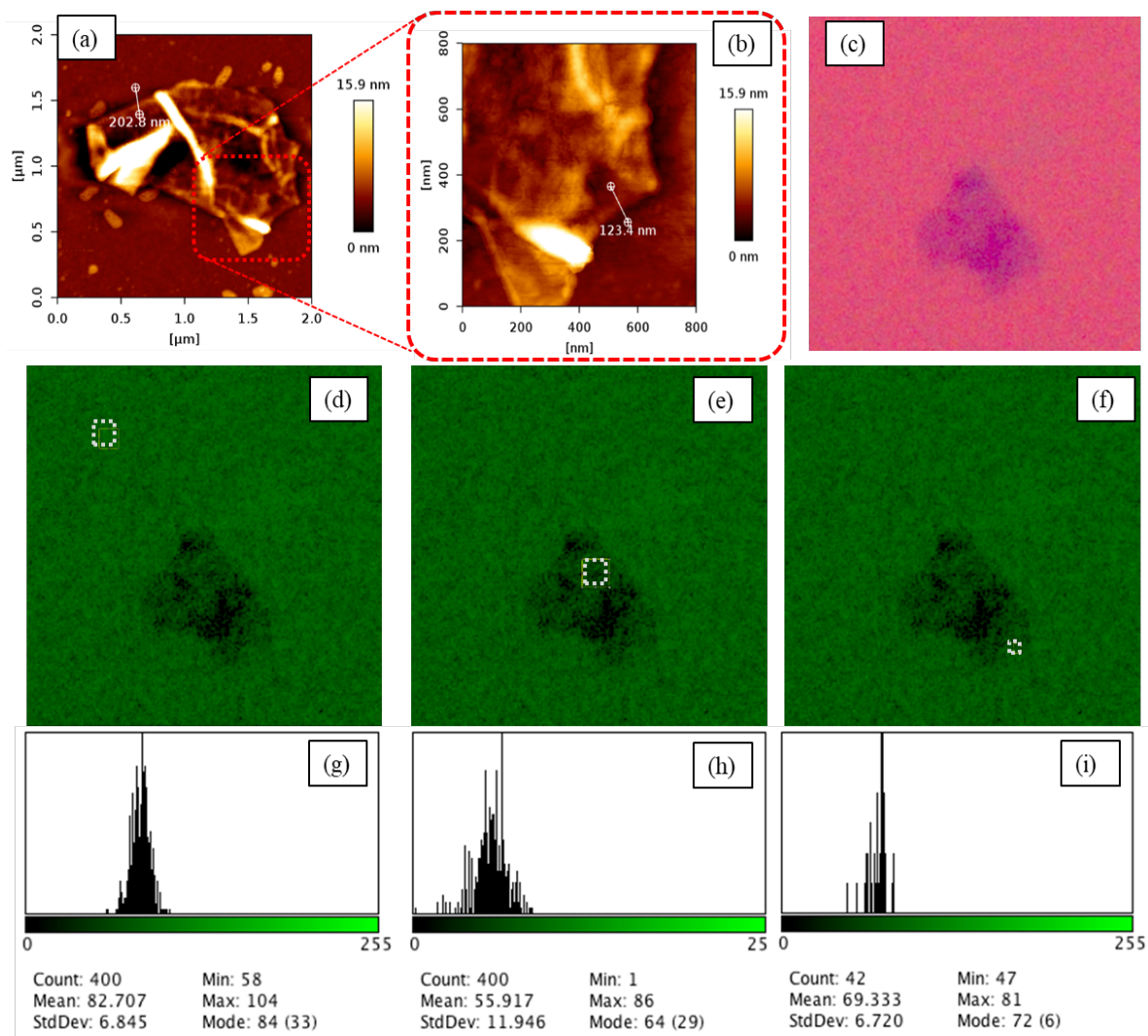


Figure 6.13: compares the thickness measured by AFM and OM. (a) AFM image of a thin graphene flake. (b) magnified image of a thin area of (a), the thinnest region was measured to be 1nm thick. (c) OM image of the graphene flake. (d)-(f) shows the reflection green channel intensity of (c), different regions of green channel intensity were sampled for thickness estimation. (g)-(f) shows histogram of reflected intensity obtained from substrate, thick and thin graphene regions respectively.

II. Compare the results between AFM and Raman spectroscopy

Figure 6.14 shows an AFM image of the 2Dtech SAEG sample on a 285nm thick SiO₂/Si wafer substrate. The very thick islands were avoided using the optical microscope, so that the cantilever could be operated in a small range. As seen in figure 6.14 (a), the measured graphene flakes have a thickness below 5 nm, while small circular spots (~ 0.65 nm in z-direction) were assigned as contaminants in the graphene suspension, which therefore spreads over the image both on flakes and the substrate. Figure 6.14 (b) plots the profile of an example flake. As seen in the profile, even though the measured height fluctuates, due to the possible presence of contaminant or the surface roughness, the profile fluctuation always occurs upon a plateau region with a discrete height (1 nm, 2 nm, 3 nm... etc). This is reported to be the evidence for the existence of a buffered layer between the graphene and substrate, also the possible C-H contaminant on graphene surface ^{139,210,211}. Such a buffer layer and contaminant may not have been expelled even when the flakes re-aggregated, resulting in a discrete height measured by AFM. Virtually no literatures have reported a 0.34 nm interlayer spacing in SAEG graphene samples. In contrast, a 0.34 nm interlayer spacing has been observed in an incompletely delaminated flake synthesised by mechanical exfoliation ²²⁵.

Figure 6.14 (c) shows the thickness distribution obtained from the AFM image. In total 48 flakes with a thickness >1nm were taken into statistics. A mean value of 3.11 nm was obtained among these flakes. Assuming the buffer layer to be present only between the substrate and the graphene flakes, which could be 1 nm thick (see inset of figure 6.14(b)), then these graphene flakes could be approximately 6-8 layers thick. However, when comparing the AFM result to the estimation using Raman spectroscopy, the difference was marginal. Using equation 6.7 with Raman spectroscopy, a mean 7-8 graphene layers was estimated in the 2Dtech aquagraph sample, which was estimated to be 2.38-2.72 nm, not too far from the observation using AFM on the sample (a mean value of 3.11 nm). This could be because the Raman spectroscopy “sees” flakes with thickness >> 10 layers as 10 layers, the statistics are therefore biased in favour of thinner flakes. Therefore, though the

thick flakes were avoided when performing the AFM measurement, the differences between the number of graphene layers estimated via AFM and Raman is coincidentally small.

The discrepancies discussed in the earlier paragraphs show that a precise thickness characterisation method is difficult to achieve for large-scale measurement. It is because of the limitations in current equipment, that the precise number of graphene layers cannot be easily quantified. Also, the fact that many of the properties vary when comparing graphite with graphene, all of the relevant properties still need to be fully identified before an accurate measurement of graphene/graphite thickness can be achieved. Nevertheless,

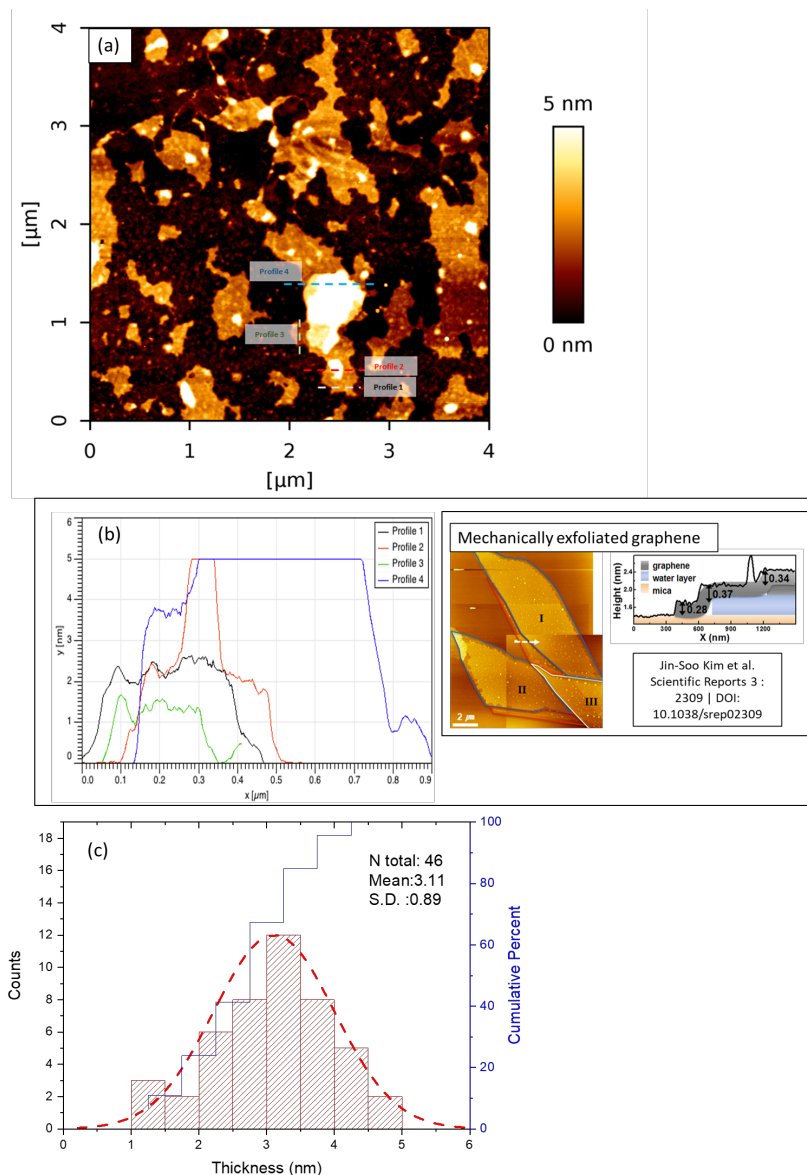


Figure 6.14: Thickness measurement of the 2Dtech SAEG sample on a 285nm thick SiO₂/Si wafer substrate performed by AFM. (a) an AFM image of the SAEG sample. (b) the height profile of an example graphene flake. (c) shows the thickness distribution obtained from the AFM image. (2Dtech aquagraph SAEG sample were used)

despite obtaining the precise number of graphene layers, identifying the level of graphitic character is rather more important and can be used to improve the graphene synthesis process. Therefore, unlike the microscopic methods that utilise probes to measure the physical thickness of graphene layers, Raman spectroscopy directly detects the scattering properties of graphene, which are strongly affected by the band structure and the number of graphene layer coupled ^{21,111,222}. Therefore, despite the limitations and difficulties mentioned earlier, the variation of 2D peak is one of the most practical techniques that can be used to determine the level of graphitic character.

6.5. Conclusion

In this chapter, different methods were used to determine the thickness of SAEG graphene flakes. The most straightforward method involved direct imaging of the edge of the folded graphene flake, which was correlated to the MGVR in order to develop a rapid characterisation for the thickness of graphene. The MGVR measured on zone axis decreased as the number of graphene layers increased and can be approximated by an inverse linear relationship for graphene thicknesses < 30 layers. The inverse linear relationship decays faster than the experimental work at 7° sample tilt conducted by Rubino et al. ³⁴, but decays slower than the JEMS simulation at zone axis, which could be due to a different operating voltage and objective aperture size were used. However, it is still possible that the inverse linear relationship between MGVR and flake thickness holds true despite the fact that the presence of multiple diffraction decay.

The MGVR values were further compared to the relative thickness determined by the log-ratio method in low-loss EELS. The result shows that the decrease in MGVR remains inversely linear relationship to the flake thickness when $t_R < 0.15$. Such a relationship allows us to compare the material depended absorption constant of Bloch wave (δ) to the inelastic mean free path (IMFP) from the slope of the linear relationship. By comparing the IMFP obtained from MGVR to the IMFP estimated via Mali's equation in GMS 3, the

results show that thinner flakes correspond better to with Mali's equation, while a difference of $\pm 11.4\%$ was obtained from six selected graphene flakes, which indicates the well-established log-ratio method may not be suitable for the ultra-thin graphene regions. This can be account to the presence of surface plasmon in thin regions, leading to an over-estimation of relative thickness and affect the accuracy of estimated IMFP from both methods. This suggests that applying the concept of inelastic mean free path to a thin crystalline solid could be difficult.

In order to exploit the sensitivity of the low-loss EELS spectra and improve the thickness determination technique, the variation in the EELS low-loss plasmon band was quantified by Lorentzian curve, and the variation was plotted as a function of number of graphene layers. A clear π plasmon peak shift toward lower energy losses accompanied by a $\pi + \sigma$ plasmon peak broadening was seen as the number of graphene layers decreased, which could be due to the contribution of the surface plasmon mode and was generally attributed to the competition of the out-of-plane and in-plane plasmon excitation modes in graphene and graphite. Potentially, this indicates a change in the electronic band structure from graphene to graphite and can be used to identify the number of graphene layers.

For a rapid investigation of graphene thickness in an ambient environment, the variation of 2D (G') band in Raman spectroscopy was studied. A well-established data was taken from Ferrari's previous work. Based on the variation in peak shape and peak position, several empirical equations were then derived from the variation of the 2D bandshape, in which the trend is similar to the degree of band overlapping as the number of graphene layer increases. These empirical equations were then applied to the same SAEG graphene, showing that whilst the equation based on the variation of peak shape resolves the number of graphene layers, the equation based on the shift of peak position is the most effective method for the characterisation of number of graphene layers.

However, applying these thickness characterisation methods to a SAEG sample resulted in significant deviations in their results. Extensive AFM measurements were performed in order to understand the cause of the deviation. With the assistance of AFM, it was concluded that the optical reflection spectrum method can resolve very thin graphene

samples. However, the presence of flake aggregation and buffer layer could significantly affect the obtained AFM result. Hence, a precise thickness characterisation method may not be practicable for rapid large-scale characterisation. nevertheless, despite it being difficult to obtain the precise number of graphene layers, identifying the level of graphitic character is probably a more practical and important point on terms of improving a graphene synthesis process. Therefore, analysis of the position of Raman 2D band is probably the most practical technique that can be used to determine the level of graphitic character, and the number of coupled layers.

7.

Synthesis of graphene via electrochemical exfoliation and comparison with other methods

In this chapter, the characterisation protocol was applied to different graphene samples synthesised by solution-assisted graphite exfoliation method (SAEG). As introduced in Chapter 3, different graphite cleavage methods are available to exfoliate graphite into graphene, which could also result in different SAEG graphene properties. Traditionally, the slightly changes in the SAEG property are hard to be identify at the nanoscale. However, by applying the previously proposed characterisation protocol to the SAEG samples, it is possible to quantify the nanostructural features of graphene and extract the differences and can be used to optimise the graphene synthesis process. In this chapter, three-dimensional graphites was electrochemical exfoliated to

produce electrochemically exfoliated graphene (ECEG). In order to understand and optimise the relative effectiveness of each exfoliation method, different electrochemical exfoliation conditions were tested. The results were in comparison with two different SAEG samples synthesised by: (1) ultrasonication in IPA (SG) and (2) the commercialised graphene produced by mechanical milling in ionic liquids (2Dtech). The exfoliated SAEG graphene material was characterised by the protocol developed in previous chapters and the mechanism of the graphene exfoliation process is discussed.

7.1. The starting material

As mentioned in Chapter 3, the electrodes for electrochemical exfoliation were manufactured via pressing the graphite nanoplatelets (GNP) from Cheaptube™ in a 2.54 cm diameter die with pressing force between 0.1 ton to 0.5 ton and holding for 300 seconds. The same GNP material was also used for synthesis of SAEG using ultrasonication for comparison. Besides the pressed GNP graphite (PG), a Highly Ordered Pyrolytic Graphite (HOPG, Grade-2 provided by SPI™ 226) was also used as the exfoliation electrode for comparison. The crystal structure of PG and HOPG were initially investigated by X-Ray diffraction (XRD). As seen in figure 7.1, the (002) peak is the most intense feature in all spectra, contrary to the weaker (004) and (110) peaks. Although the (100) and (101) peaks near 44° can be seen in the zero pressed GNP or HOPG, they can not be clearly seen in the pressed-GNP samples due to the much intense (002) peak, indicating a preferential orientation in the (002) direction in these graphite material.

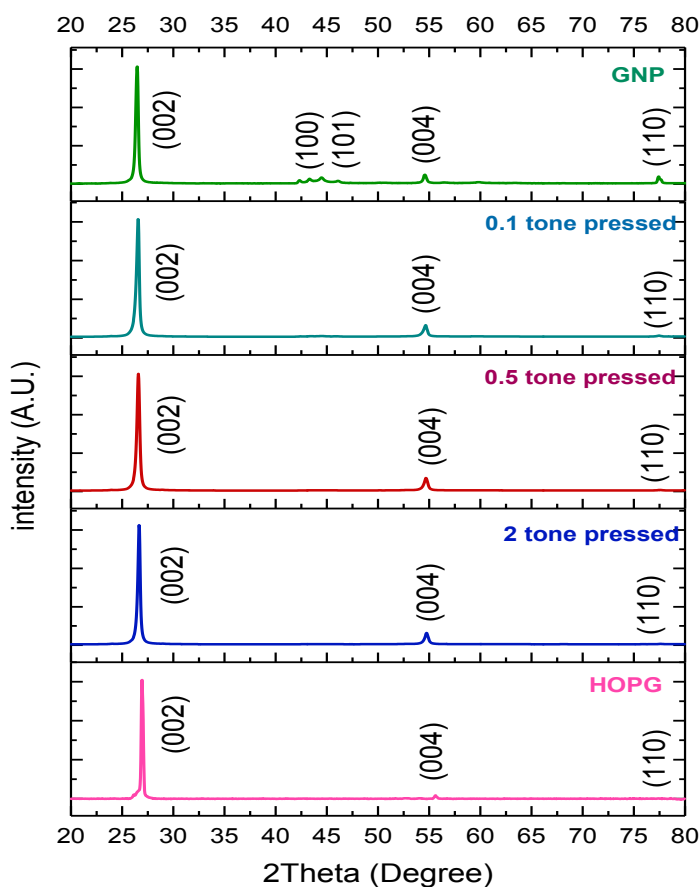


Figure 7.1 XRD of different starting materials. Strong (002) peak in each sample, showing many layers of graphene is consisted in the starting material.

In order to investigate the effect of pressing force on the graphite structure, figure 7.2 (a) extracted and magnified the (002) peak from figure 7.1. and Rietveld refinement was used to identify the peak position and peak broadening effect. As seen in the figure, the peak positions were observed to shift slightly to higher 2θ values as the pressing force increased. Figure 7.2 (b) plots the peak position as a function of pressing force, where the peak position shifted from 26.14° for the non-pressed GNP to 26.57° for the two-tons pressed graphite respectively. The shift of (002) peak possibly indicated a decrease of interlayer spacing based on Bragg's equation (Equation 3.1). As shown in the bottom panel of figure 7.2(b), the interlayer spacing can be fitted by an exponential function as the pressing force increases and was found to be decreased from 0.3420 nm to 0.3365 nm, a $\sim 1.6\%$ change from the non-pressed GNP powder to the two-tons pressed electrode. However, even with a two-tons pressed to the GNP material, a interlayer spacing of 0.332 nm in HOPG still much smaller than the GNP-based samples. This suggesting a minimum energy Bernal-AB-tacking configuration is presented in HOPG (interlayer spacing 0.335nm for AB stacking configuration ⁵⁸). A larger interlayer spacing presented in the

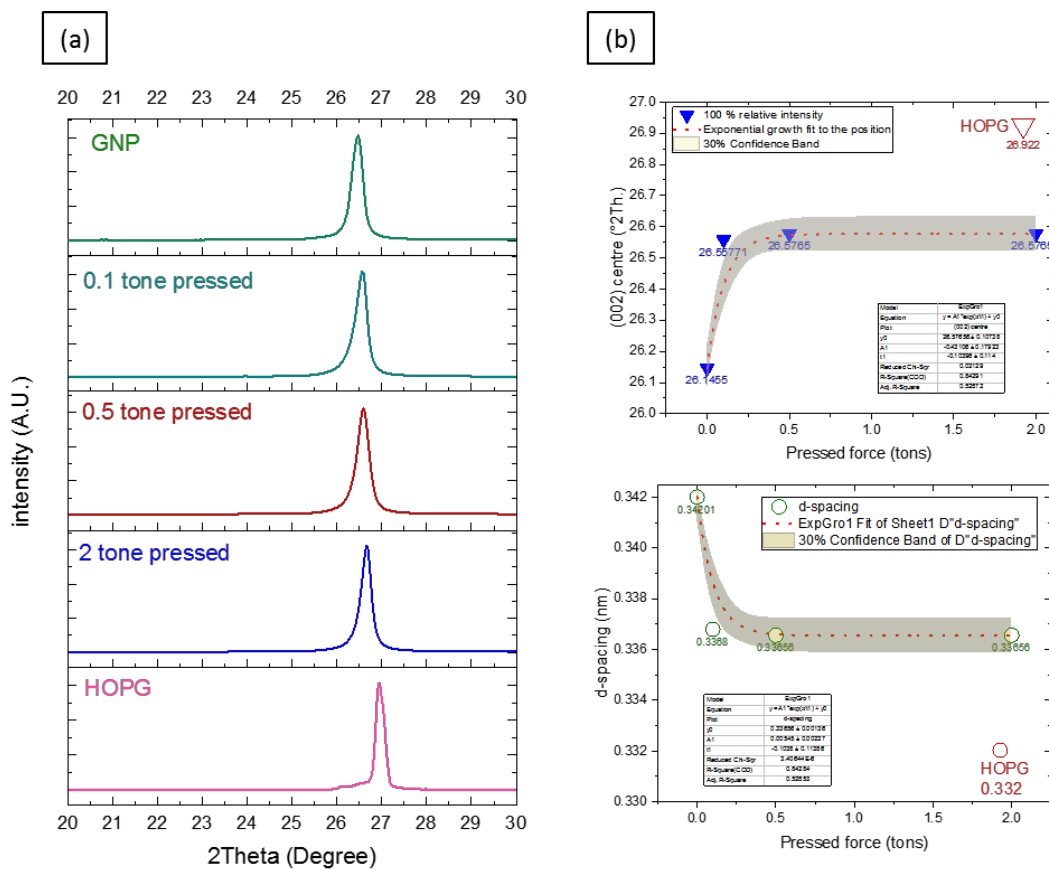


Figure 7.2: shows the (002) peak change as a function of pressing force. (a) the (002) peak extracted from figure 7.1. (b) the peak position and corresponded d-spacing changes as increase of pressing force.

non-pressed GNP could possibly due to the presence of the turbostratic structure consisted in the sample (interlayer spacing 0.344 nm ⁵⁸).

Figure 7.3 shows the SEM images of the non-pressed GNP raw material and the 0.5 ton pressed-GNP electrode. The GNP is seen to consists of many small graphite flakes stacking on top of each other, with a lateral flake size of few micrometers. In contrast the pressed-GNP electrode has a smoother surface morphology, where the surface texture and flake boundaries are still apparent.

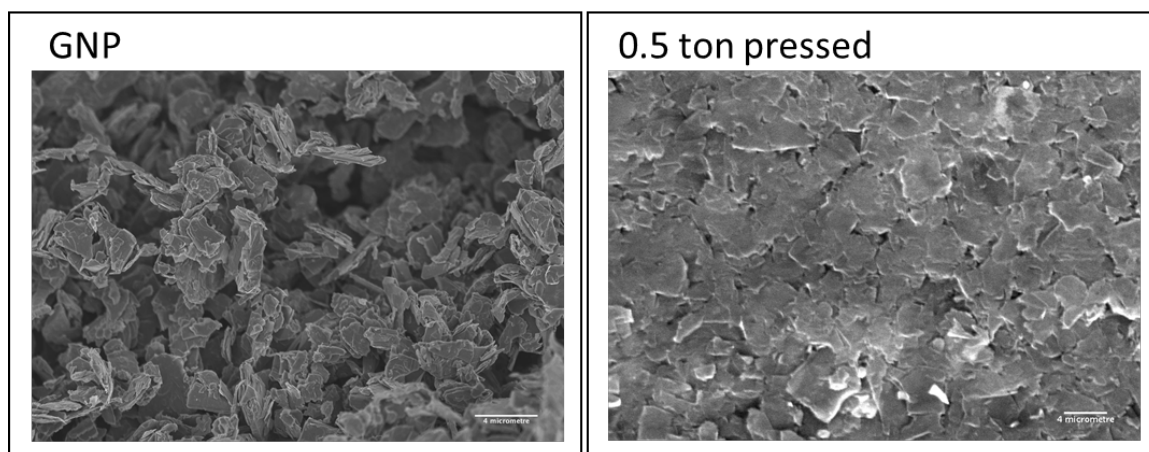


Figure 7.3: SEM image showing surface morphology of the un-pressed graphite nanoplatelets (GNP) and the pressed GNP

7.2. Electrochemical Exfoliation

Electrochemical exfoliation of graphite is considered to be one of the simplest, fast and cost-effective methods for SAEG graphene synthesis due to its short process time and high-quality graphene produced ^{7,12,227}. However, the effectiveness of such an exfoliation method is yet to be evaluated. In this section, the SAEG graphene synthesised via different exfoliation conditions is studied.

I. Active voltage

To investigate the active voltage that can be used for electrochemical exfoliation, the current density was plotted as a function of applied voltage (I-V curve). With a two-electrode electrochemical system ($\sim 1.5 \text{ cm} \times 1.5 \text{ cm}$ Pt cathode and 0.5 ton pressed graphite electrodes anode) in the aqueous 0.1M Ammonium sulfate solution ($(\text{NH}_4)_2\text{SO}_4$ (aq)), the current density can be plotted as a function of applied voltage. Seen in figure 7.4, the I-V curve can be categorised into three regions. (1) the onset region from 0 V to ~ 4 V, where no current density response was observed until the applied voltage reached ~ 4 V. This could imply an equilibrium state at 0 V and an internal chemical potential existed in the electrochemical system that compensated for the applied voltage > 0 V condition; (2) A Tafel's region : the I-V curve can be fitted by the Tafel equation when the biased voltage is < 8 V seen as inset in figure 7.4. (3) The linear region: the current density increases linearly with applied voltage, which is generally ~ 5 V to 25 V in this case.

In the Tafel region, between 0V~ 8 V, the I-V curve can be fitted with the Tafel equation:

$$j(V) = j_0 \cdot \exp\left(\frac{a \cdot n \cdot F \cdot V}{RT}\right) \dots (\text{eq. 7.1})$$

, where V is the overpotential; F is Faraday's constant, R is the universal gas constant and T is the absolute temperature ($\sim 300\text{K}$). The value $n = 2$ is the stoichiometric number of electrons in the anode reaction: $\text{SO}_4^{2-}(\text{aq}) + 4\text{H}^+ + 2\text{e}^- \rightarrow \text{SO}_2(\text{g}) + 2\text{H}_2\text{O}$, in which the corresponding cathode reaction is for Arrhenius expression is $\text{M} \rightleftharpoons \text{M}^{n+} + n \text{e}^-$ used in the Tafel equation ^{22,86}.

By fitting the I-V curve by the Tafel equation, the symmetry factor (a) was extracted to be $a = 0.0045$, which is several orders of magnitude smaller than expected for a common metal electrode electrochemical reaction ($a = 0.5$). The significant lower value of symmetry factor (a) indicates a low electrochemical reactivity and could be an explanation for the reason that the turn on voltage of the electrochemical exfoliation experiment is higher compared to common electrochemical experiments ^{6,228,229}.

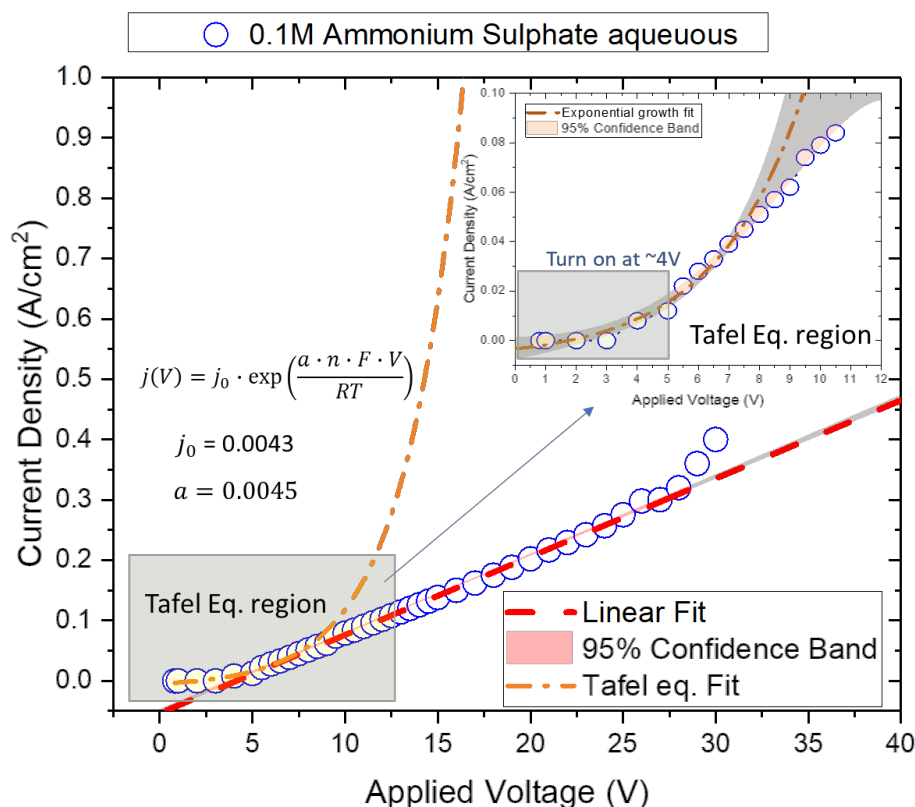


Figure 7.4: *I-V curve of the electrochemical exfoliation experiment with 0.5 ton pressed graphite electrode. The red dash line fitted the experimental data with exponential growth, where a symmetry factor was extracted to be $a=0.0045$*

II. Properties of the SAEG graphene synthesised by electrochemically exfoliate graphite

A fixed 0.1M ammonium sulphate aqueous ($(\text{NH}_4)_2\text{SO}_4$ (aq)) was used as electrolyte, and a 0.5 ton pressed graphite used as the electrode. As described in Chapter 3, after the graphene flakes were exfoliated from graphite, the exfoliated product (a mixture of graphene / graphite and the electrolyte) was collected by vacuum filtration with a membrane filter and repeatedly washed with deionised (DI) water to remove any residual salts, followed by a re-dispersion process in IPA. After a 48-hours sedimentation, the bottom layers were believed to consist of a high concentration of incompletely delaminated graphite chunks and was discarded, the remaining upper part of suspension was taken for further characterisation.

i. Flake lateral size

As discussed in chapter 4, the graphene lateral size distribution can be obtained rapidly via DLS. Figure 7.5(a) shows the lateral distribution of graphene flakes exfoliated at different exfoliation voltages. The lateral size of exfoliated graphene was generally < 1000 nm without a significant linear dependence on the exfoliation voltage used. However, a noticeable pattern between exfoliation voltage and graphene flake size can be observed when the peak centre obtained by DLS (X_c) is plotted against the exfoliation voltage, seen in figure 7.5(b). When the exfoliation voltage is just above the turn on voltage (4 V), a smaller flake size was obtained. The mean flake size ($\sim X_c$) continuously increased as exfoliation voltage increase, whilst the peak shape remained similar. The mean flake size reached a maximum of ~ 825 nm when a 10 V exfoliation voltage was used, which is approximately at the end of the Tafel region (see inset of figure 7.4). The flake size starts to decrease as exfoliation voltage exceeds the Tafel's region and enters the linear region. It was found that exfoliation performed in the linear region produces a smaller flake lateral size and for a 15 V exfoliation voltage, the flake size is even smaller than at 5 V. Although

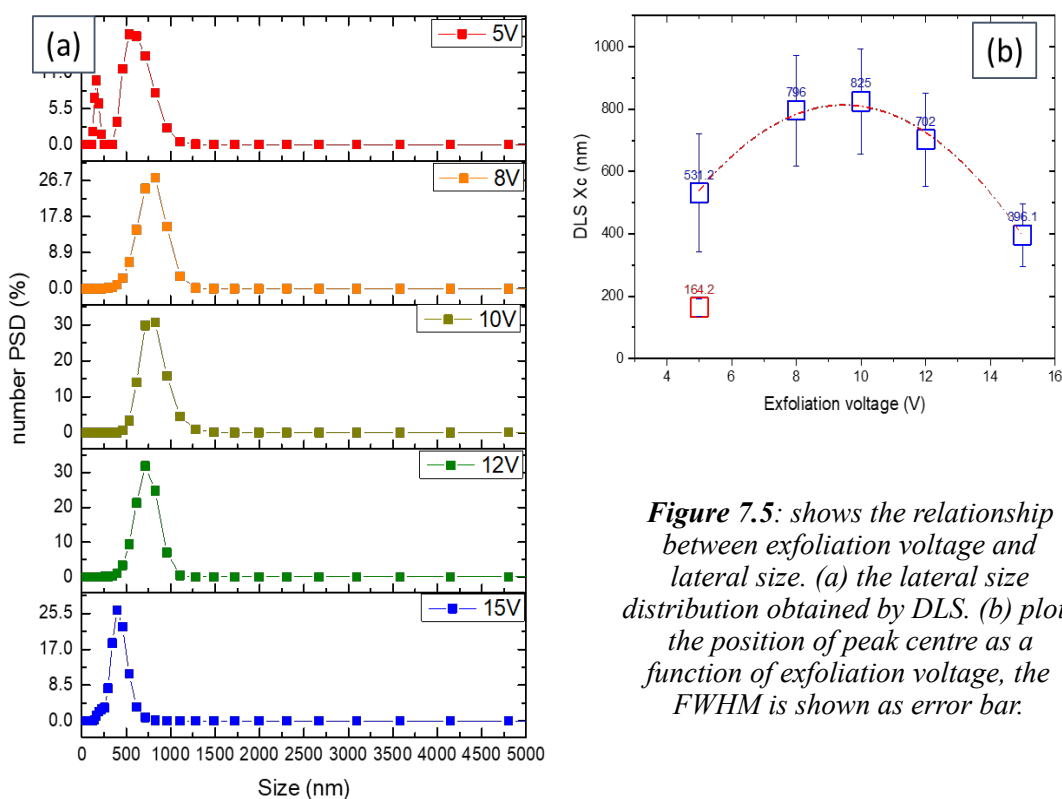


Figure 7.5: shows the relationship between exfoliation voltage and lateral size. (a) the lateral size distribution obtained by DLS. (b) plots the position of peak centre as a function of exfoliation voltage, the FWHM is shown as error bar.

the reason underlying for this dependence of flake size on voltage is unclear, we can conclude that utilising a 8-12V exfoliation voltage can rapidly produce SAEG graphene flakes with a sub-micrometer lateral size.

Figure 7.6 compares the lateral size distribution of the SAEG graphene flakes electrochemically exfoliated from different graphite electrodes. Here the exfoliation voltage was set at 10 V and the same 0.1M Ammonium Sulphate aqueous was used as electrolyte. As seen in figure 7.6(a), the SAEG flakes exfoliated from HOPG exhibited a widest size distribution, with highest mean flake size (X_c) at around 2500 nm. On the other hand, although the mean flake size is similar between exfoliation performed on the 0.5 ton pressed graphite and the 0.1 ton pressed graphite (~700nm), a wider flake size distribution is observed for graphene exfoliated from the 0.1 ton pressed graphite. This could be due to a different ion-insertion rate or pathway involved when a different morphology graphite electrode was used.

Figure 7.6(b) compares the optical microscope images of graphene flakes exfoliated from the 0.5 ton pressed graphite and HOPG. Both of the images exhibit some thinner flakes (blue spots) and a significant number of thicker flakes (brown-yellow spots). However, it

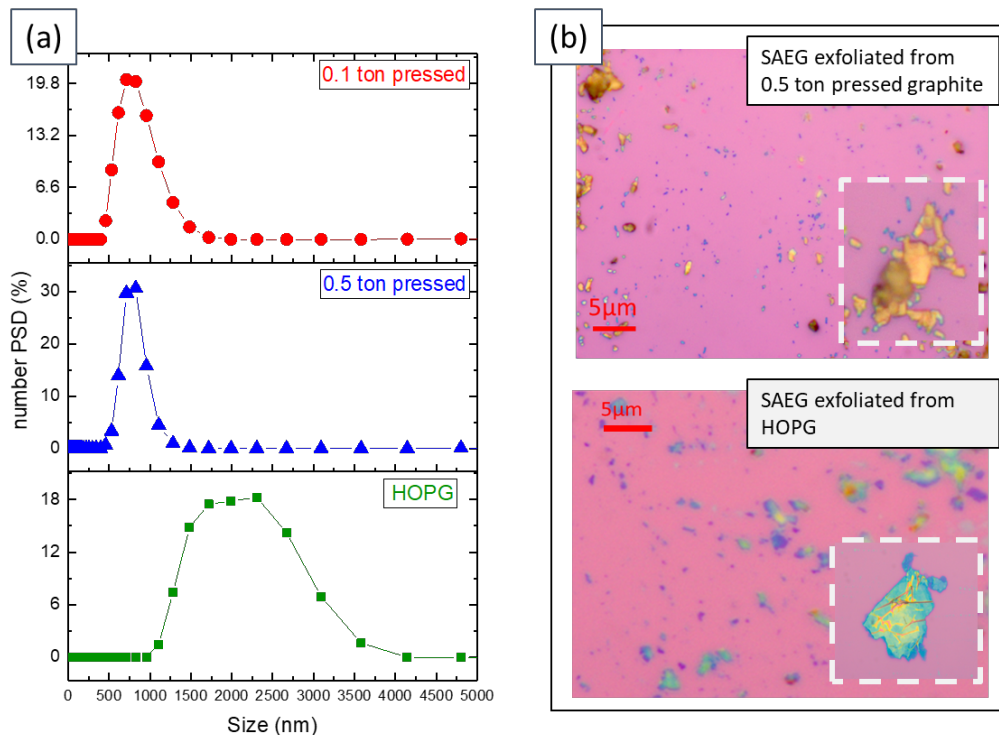


Figure 7.6: shows the lateral dimension of graphene synthesised from different starting material. (a) Lateral size distribution obtained from DLS. (b) The lateral dimension seen by optical microscope. The insets shown a representative image of a thick graphene flake.

is clear that the thinner flakes is significantly larger when HOPG was used. Also, the sample exfoliated from HOPG shows a gradual colour change from brown-yellow-like in the flake bulk region to a blue-like colour in the edge region, implying that the thickness of the exfoliated graphene flakes decrease gradually towards the edge. In contrast, the thick flakes exfoliated from the pressed graphite exhibit a sudden change in colour from the bulk region to the edge region, implying that the exfoliation process cleavage a large fragment of material rather than gently peeling it away, which could also be an evident that the ion-insertion paths are affect by the structure of the starting graphite electrode.

ii. The crystal imperfection

The crystal imperfection of a graphene sample can be characterised by the I(D)/I(G) peak intensity ratio from Raman spectroscopy as discussed in chapter 5. Figure 7.7 (a) shows the histogram of I(D)/I(G) ratio of graphene flakes synthesised using different exfoliation voltages. As seen in the figure, the unexfoliated 0.5 ton pressed graphite sample exhibits the smallest standard deviation in I(D)/I(G) ratio of 0.036, with a mean value of 0.165. This corresponding to the average distance between two defects (refer to the L_D in Chapter 5) of ~ 27.7 nm. On the other hand, the mean I(D)/I(G) ratio remained similar when the SAEG graphene flakes were exfoliated using 5 V and 10 V of biased voltage, with a value of 0.128 and 0.115 respectively. However, the standard deviation of the I(D)/I(G) ratio increases with exfoliation voltage increase. For SAEG graphene flakes exfoliated with 15 V, the standard deviation of I(D)/I(G) was 0.110, while for exfoliation voltage of 5 V and 10 V of exfoliation the value is about 0.06. The increase I the standard deviation of I(D)/I(G) when at high exfoliation voltage used could be caused by a severe ion insertion and the following exfoliation process that promotes different level of oxidation / damage to the graphene flakes. Nevertheless, it is interesting to note that the mean value of the I(D)/I(G) ratio of the un-exfoliated 0.5 ton pressed graphite is slightly higher than for the 5V and 10 V exfoliated graphene. This could be due to the fact that the the graphite surface has encountered external damage during the pressing process, while the exfoliated graphene

flakes could be originating from a deeper location within the material that had encountered less surface damage.

Figure 7.7(b) shows scatter plots that correlates the FWHM(G) to the I(D)/I(G) as introduced in Chapter 5. Seen in the figure, the unexfoliated 0.5 ton pressed graphite exhibits a strong correlation between FWHM (G) and I(D)/I(G) ratio, with the largest Pearson r value of 0.79, indicating that the major contribution of D peak enhancement originates from bulk defects. On the other hand, all the exfoliated graphene flakes show a weak correlation between FWHM (G) and I(D)/I(G) ratio, where the Pearson correlation coefficient $r \sim 0.3$, indicating that the edge structure significantly contributes to the D peak enhancement. This could also indicate that only a minor damage or oxidation have occurred to the graphene flakes during the electrochemical exfoliation.

Unlike electrochemically exfoliated pressed graphite electrode, utilising the same process with HOPG produces significant damage in SAEG graphene flakes. As seen in Figure 7.8 (a), the unexfoliated HOPG exhibits a very low I(D)/I(G) in comparison to the pressed

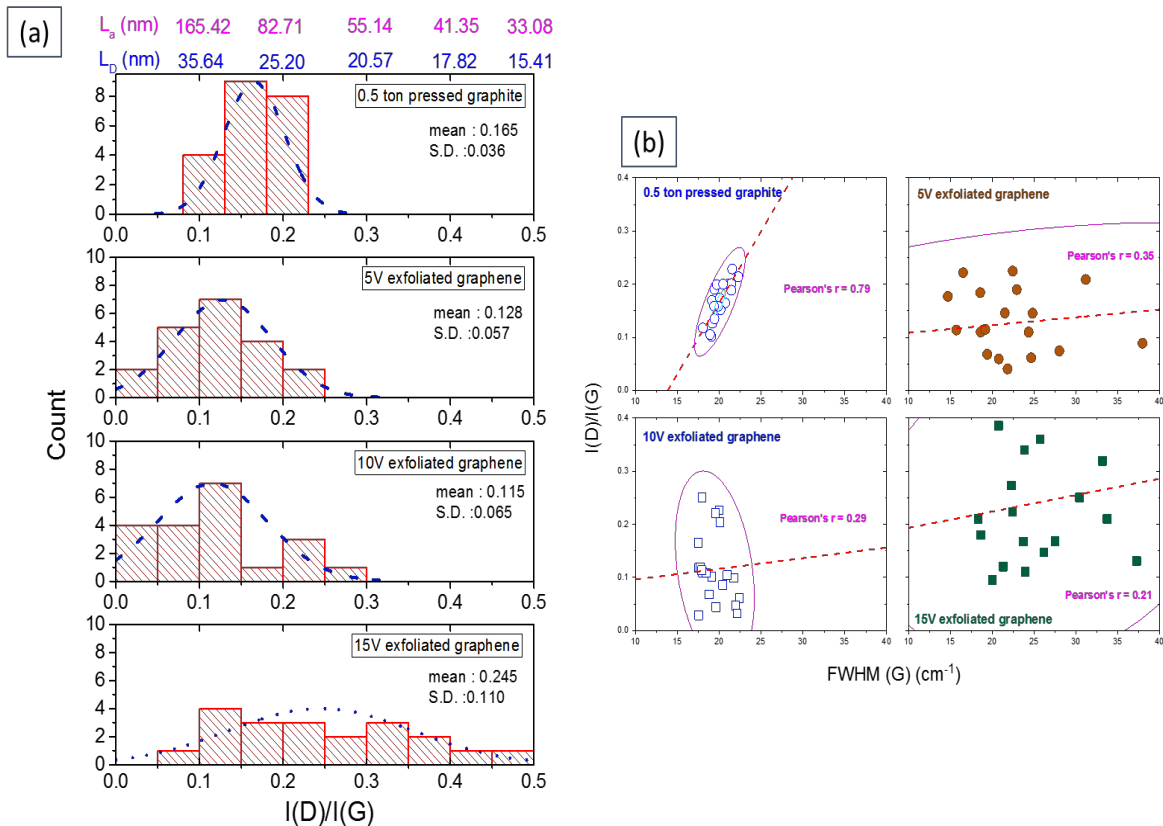


Figure 7.7: Crystal imperfections characterised by Raman spectroscopy : (a) histograms showing the I(D)/I(G) distribution of graphene flakes for different applied voltage. (b) Scatter plots show the correlation between FWHM (G) and I(D)/I(G).

graphite, which indicates a very low concentration of defect and very high coherence length (L_a). However, the graphene flakes that were electrochemically exfoliated from HOPG show a significant higher $I(D)/I(G)$ ratio as compared to exfoliation on the pressed graphite. The mean $I(D)/I(G)$ ratio are 0.806 and 0.814 for 5V and 10V exfoliation, while the value is less than 0.2 when utilising the pressed graphite as electrode under the same exfoliation conditions. Considering the $I(D)/I(G)$ ratio in unexfoliated HOPG is about 0.022 and significantly increases to ~ 0.8 for HOPG exfoliated SAEG flakes, this implies that the exfoliation process could be accompanied by a serious damage or oxidation to the surface of HOPG electrode. The scatter plot further indicates the origin of the crystal imperfections. Unlike SAEG graphene exfoliated from pressed graphite that shows a weak correlation, the SAEG graphene exfoliated from HOPG shows significant correlation between the $I(D)/I(G)$ ratio and $FWHM(G)$, implying that this arises from crystal imperfections in the bulk instead of the edge structure (7.8 (b)).

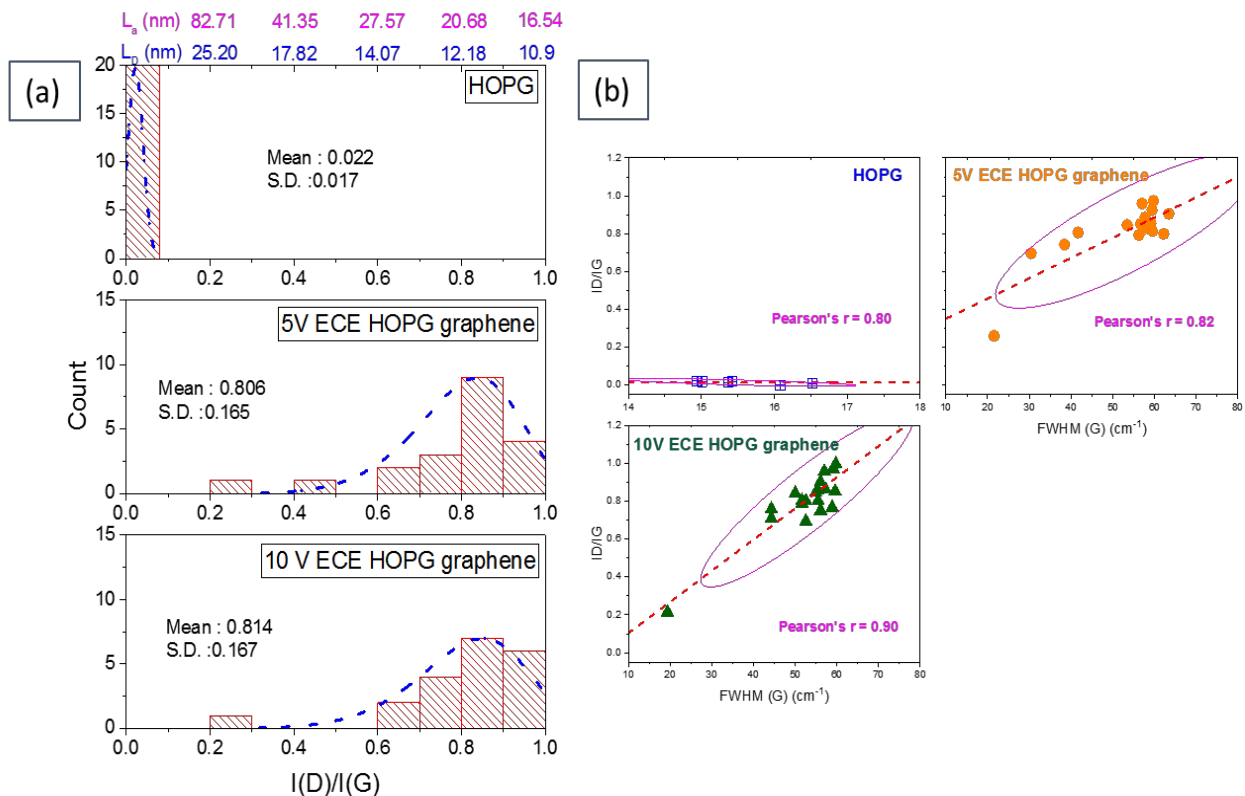


Figure 7.8: Crystal imperfection characterised by Raman spectroscopy (a) histograms showing the $I(D)/I(G)$ distribution of graphene flakes exfoliated from HOPG for different applied voltage. (b) Scatter plots showing the correlation between $FWHM(G)$ and $I(D)/I(G)$.

iii. The thickness of graphene

Figure 7.9 shows the thickness estimation using equation 6.8 on the SAEG samples exfoliated at different voltages. The yellow box indicates flakes that were categorised as graphite due to the estimated thickness being >10 layers. As seen in the figure, the exfoliation performed at 5 volts produced the highest percentage of graphite flakes, around 42.8% of the exfoliated flakes have the 2D peak centred at $\sim 2725 \text{ cm}^{-1}$. The SAEG exfoliated at 15 V yields the lowest percentage of graphite flakes ca. 10%. The SAEG exfoliated at 10V produced around 35% incompletely exfoliated graphite flakes.

A different thickness distribution was obtained when HOPG electrochemically exfoliated (figure 7.10). Since the SAEG graphene flakes synthesised from HOPG exhibit high I(D)/I(G) a high ratio and a broad G peak, the 2D peak is usually weak and subject to a low signal to noise ratio. Thus, a well established Savitzky-Golay method (polynomial order: 2 ; window width: 20 points) was first used to process the noisy signal before extracting the

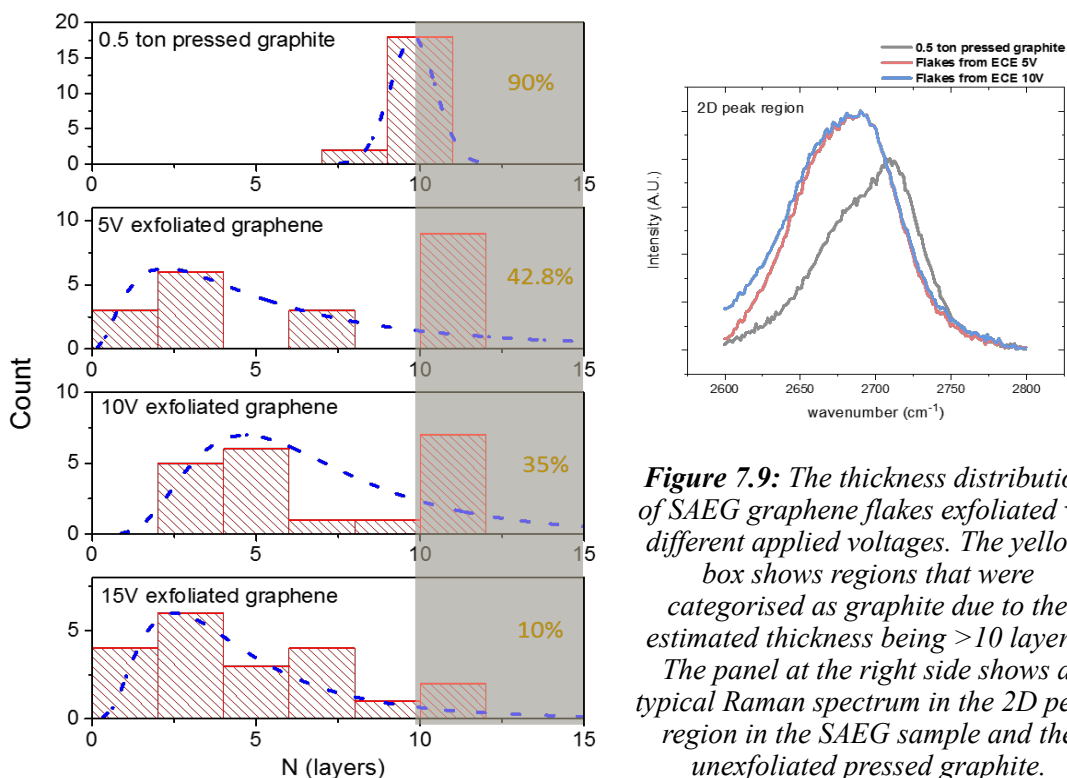


Figure 7.9: The thickness distribution of SAEG graphene flakes exfoliated via different applied voltages. The yellow box shows regions that were categorised as graphite due to the estimated thickness being >10 layers. The panel at the right side shows a typical Raman spectrum in the 2D peak region in the SAEG sample and the unexfoliated pressed graphite.

2D peak position, from which the number of graphene layers was estimated via equation 6.8. The unexfoliated HOPG sample exhibits its 2D peaks at 2725 cm^{-1} , indicating that HOPG is a highly graphitic three-dimensional AB stacking graphite before exfoliation. However, most exfoliated graphene flakes exhibit 2D peaks at lower wavenumber. For 10V electrochemically exfoliated flakes, only 10% of the flakes were categorised as graphite, whilst none of the exfoliated flakes from the 5 V electrochemical exfoliation consisted of more than 10 layers, with one of the selected flakes found to have a symmetric 2D peak centred at $\sim 2687\text{ cm}^{-1}$, which could be a monolayer graphene. This observation shows that although serious damage can occur to the SAEG flakes, electrochemically exfoliated HOPG can produce thinner graphene flakes compared to exfoliation of the pressed graphite.

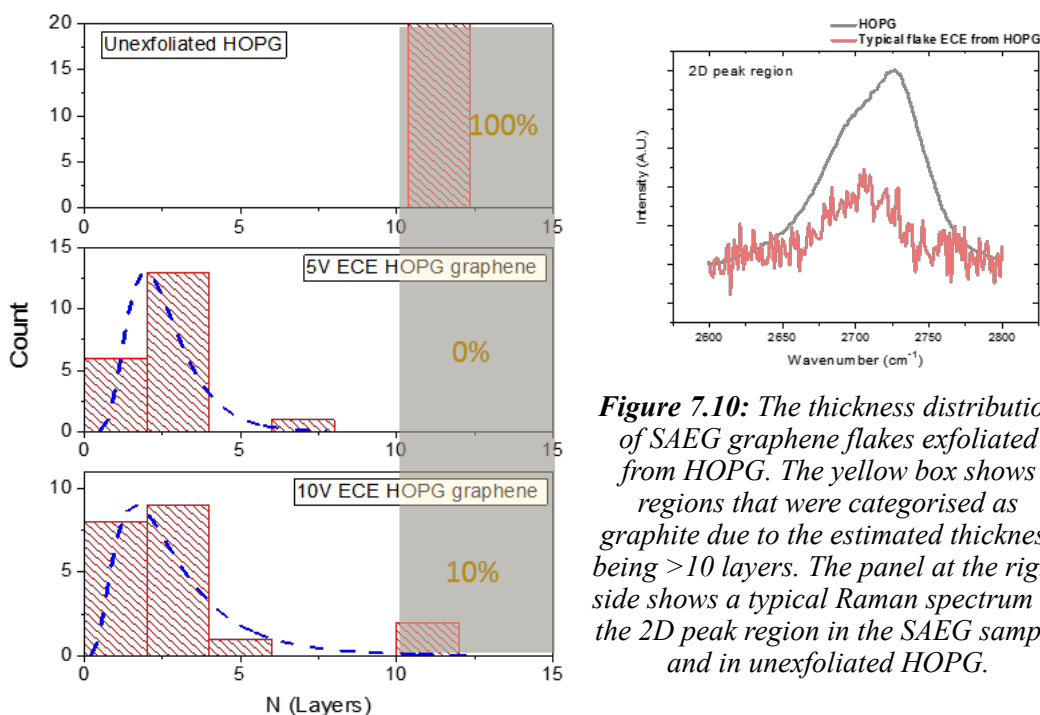


Figure 7.10: The thickness distribution of SAEG graphene flakes exfoliated from HOPG. The yellow box shows regions that were categorised as graphite due to the estimated thickness being >10 layers. The panel at the right side shows a typical Raman spectrum in the 2D peak region in the SAEG sample and in unexfoliated HOPG.

7.3. Comparison to other exfoliation method

The graphene characterisation protocol was also used to study SAEG graphene samples synthesised by sonication in IPA and milling mechanical milling in ionic liquid. The results are compared to the SAEG graphene synthesised by electrochemical exfoliation.

I. Flake lateral size

Figure 7.11 compares the lateral size distribution of graphene flakes obtained via different synthesis method. The SAEG graphene sample synthesised by milling has the sharpest size distribution, where the mean flake size is ~ 712.4 nm as discussed in chapter 4. The SAEG sample synthesised by 10 V electrochemical exfoliation of pressed graphite shows a slightly broader and larger lateral size distribution, with a mean flake size of ~ 825 nm. Electrochemically exfoliated HOPG produces the largest SAEG graphene flakes, with a mean size is of ~ 2305 nm. The graphene sample synthesised via direct sonication of GNP in IPA for 13 days shows a clear two peaks in lateral size distribution obtained from DLS:

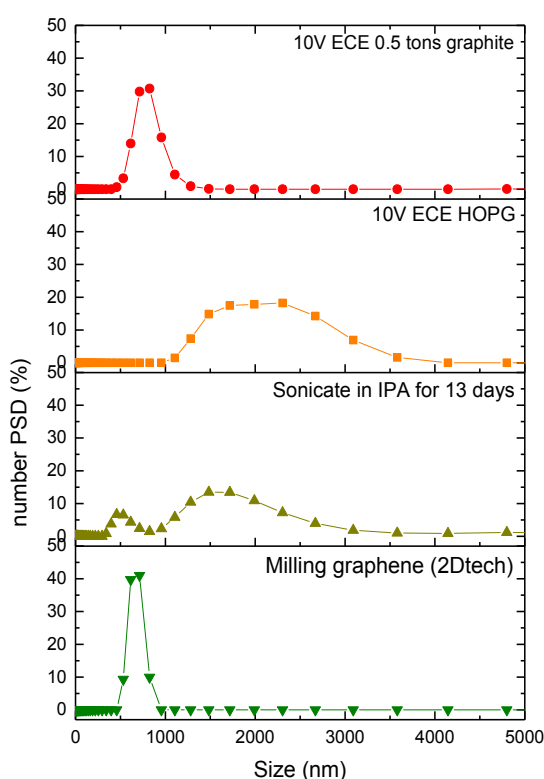


Figure 7.11: The relationship between lateral size distribution and graphene synthesis method that have been used.

a smaller sharp peak and a large broad peak centred at 458 nm and 1484 nm respectively, which could indicate a high portion of re-aggregation or incomplete delimitation of flakes.

II. Crystal imperfections

Figure 7.12(a) compares the crystal imperfections in the graphene flakes synthesised via different methods. SAEG synthesised via 10V electrochemical exfoliation produces the smallest $I(D)/I(G)$ ratio, indicating a low defect density in the flake. Sonication of GNP in IPA for 13 days also produces a low defect density SAEG sample, with a $I(D)/I(G)$ ratio mean value of 0.199. However, the defect density varies significantly from flake to flake in the graphene sample synthesised by the sonication method has a high standard deviation in the $I(D)/I(G)$ ratio of 0.172 was obtained, which is only slightly lower than the value obtained from the electrochemical exfoliation of HOPG. The sample synthesised by

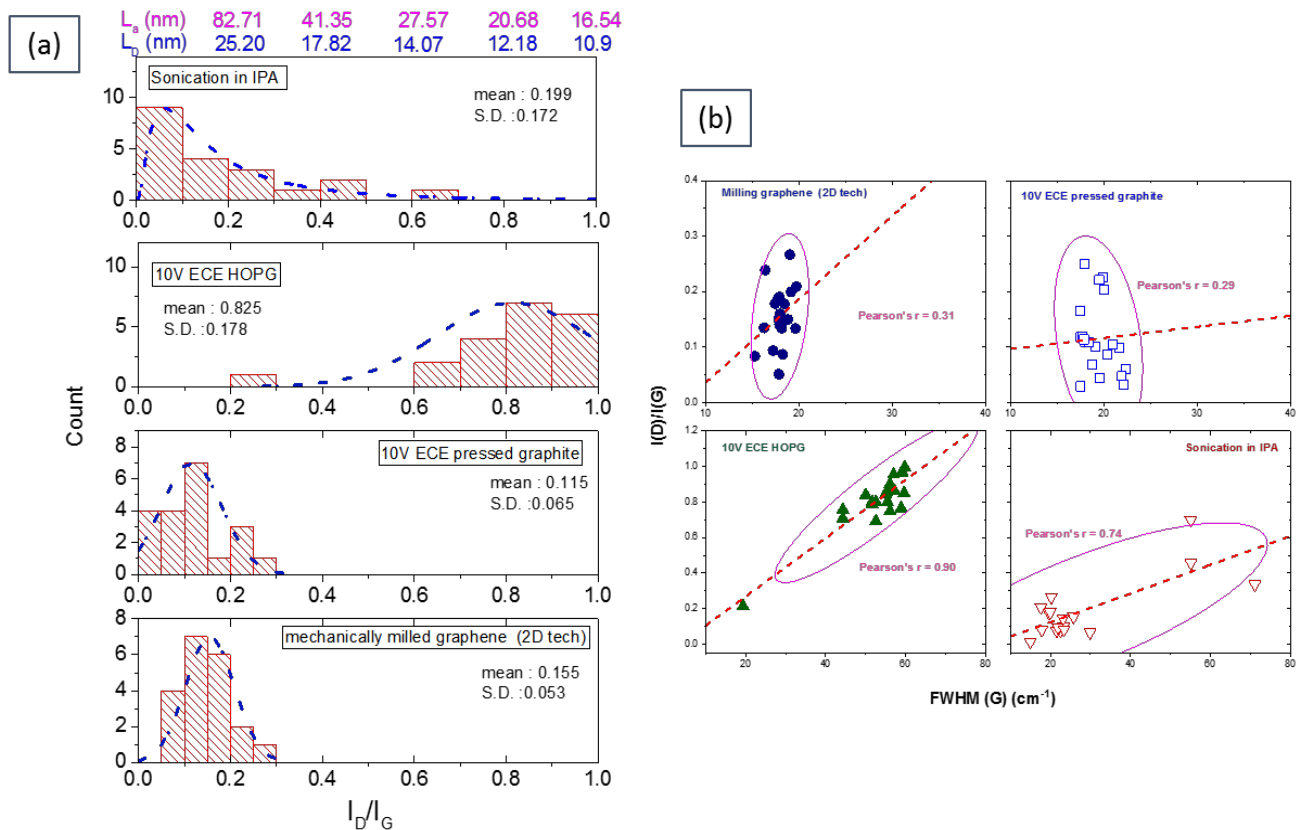


Figure 7.12: Crystal imperfection characterised by Raman spectroscopy (a) histograms showing the $I(D)/I(G)$ ratio distribution of graphene flakes for different synthesis method used. (b) Scatter plots showing the correlation between FWHM (G) and $I(D)/I(G)$ ratio.

mechanical milling in an Ionic liquid also produces good quality graphene flakes, with a low I(D)/I(G) ratio and small standard deviation.

Figure 7.12(b) shows scatter plots that correlate the I(D)/I(G) ratio to FWHM(G). The SAEG samples synthesised by milling and electrochemically exfoliation of pressed graphite both exhibited weak correlation between the I(D)/I(G) ratio and FWHM(G), indicating that the main contribution of the D peak originated from the edge structure. In contrast, the SAEG samples synthesised by electrochemically exfoliating of HOPG and sonicating GNP in IPA for 13 days show a strong correlation between the I(D)/I(G) ratio and the FWHM(G), which indicates that bulk defects could be the main contribution to the D peak enhancement.

III. Graphene thickness

Figure 7.13 shows the thickness distributions from SAEG samples exfoliated via different methods. Although sonicating GNP in IPA is a time consuming method to synthesise graphene, a high proportion of thin graphene flakes can be produced via this method,

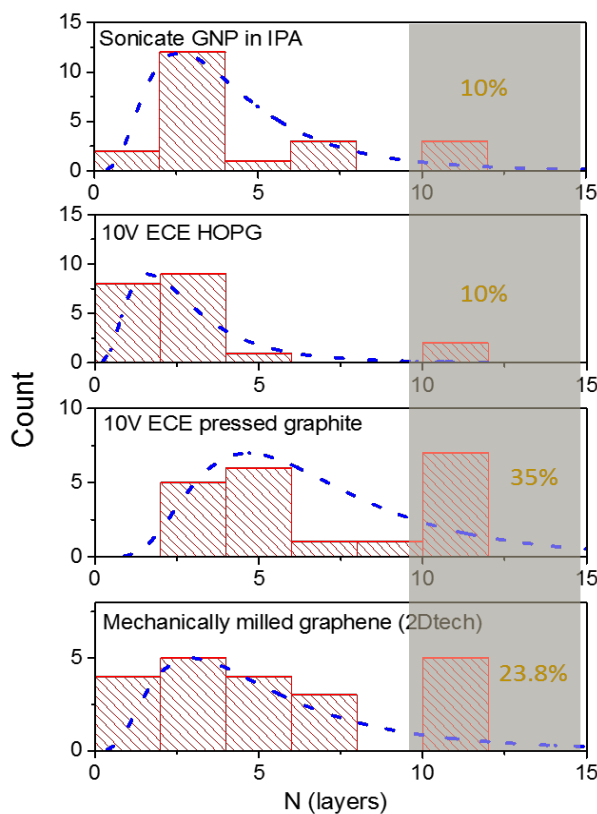


Figure 7.13: The thickness distribution of SAEG graphene exfoliated via different methods. The yellow box shows regions that were categorised as graphite due to the estimated thickness being >10 layers

where only 10% of the selected flakes were categorised as graphite. In contrast, a higher proportion of graphene flakes were deemed to be graphite in the SAEG samples synthesised by milling and electrochemically exfoliating pressed graphite, with 23.8% and 35% of flakes were estimated to consist of >10 layers respectively. Electrochemically exfoliating HOPG may synthesise a high portion of thin graphene flakes, but such a method also produces defective graphene flakes as shown in figure 7.8. Also, electrochemically exfoliating HOPG is relatively time-consuming and the starting material is much more expensive, thus it is considered to be a less effective electrochemical exfoliation method.

7.4. The possible mechanism of electrochemical exfoliation

Understanding the exfoliation mechanism is required if we are to improve the graphene synthesise process. To investigate the mechanism of electrochemical exfoliation, the exfoliated residue is studied and compared with the exfoliated product and the starting material.

The mechanism of electrochemical exfoliation has been explained in previous literature as consisting of the following steps : (i) Applying a bias voltage results in the reduction of water at the cathode, creating hydroxyl ions (OH^-), which attack graphite initially at the edge sites and grain boundaries; (ii) stage (i) causes oxidation at the edge sites and grain boundaries then leading to depolarisation and expansion of the graphite layers, the continuous direct biased voltage making the sulphate ions (SO_4^{2-}) from the electrolyte drift into graphite layers; (iii) Reduction of SO_4^{2-} anions and oxidation of water produce gaseous species such as SO_2 , O_2 , and others ^{25,230,231}, which can provide sufficient force between to separate weakly bonded graphite layers from one another.

To study this hypothesis, both the 0.5 ton pressed graphite and HOPG electrodes were electrochemically exfoliated under the same condition (a constant bias voltage +10V, ~100 seconds in 0.1M ammonium sulphate). After the electrochemical exfoliation process, the SAEG suspension was washed with deionised water and the solid powder collected by the vacuum filtration, which was further scratched off from the filtration paper and placed on a silicon wafer for study by XRD. Both the exfoliated material and the graphite residue were characterised. The change in crystallinity was examined by XRD and scanning Raman spectroscopy, whilst the morphology of the exfoliated graphite electrodes were monitored by SEM.

I. X-Ray Diffraction

Figure 7.14 shows the XRD (002) peak before and after the electrochemical exfoliation. For improved resolution, an increment of 0.03° was used in the 2θ region between 24° ~ 29° . The peak position and peak width was determined by Rietveld refinement with the HighScore software. As seen in Figure 7.14(a), the unexfoliated 0.5 ton pressed graphite exhibits an intense (002) diffraction peak, centred at 26.576° corresponding to an interlayer spacing of 0.333nm, suggesting an AB stacking graphite. However, after electrochemically exfoliation, the (002) peak broadened into two close separate peaks : a broader peak at 26.307° and a sharper peak at 26.576° , which correspond to interlayer spacing of 0.340 nm and 0.336 nm respectively. Such asymmetric broadening could be due to the anisotropic strain in graphite which induced by the exfoliation process. Thus, estimating the coherence length L_c via the Scherrer's equation using such an asymmetric broadened peak width could be unreasonable and highly inaccurate^{232,233}. As seen in the figure, the collected powder shows a low intensity sharp (002) diffraction peak centred at 26.350° . The interlayer spacing was estimated to be 0.339 nm, which is only ~0.8% larger for than the unexfoliated 0.5 ton pressed graphite. The coherence length L_c was estimated to be 42.977 nm, indicating a significant proportion of incompletely delaminated material was present in the SAEG powder. This is confirmed by Raman spectroscopy, where a high

percentage of graphite was produced in the SAEG sample was synthesised via electrochemical exfoliation of the pressed graphite (see figure 7.18).

Figure 7.14(b) shows the (002) XRD peak of HOPG before and after electrochemical exfoliation. Unexfoliated HOPG shows an intense but asymmetric (002) diffraction peak, which can be resolved into a peak centred at 26.121° , with 3.35% relative intensity, a peak at 26.449° with a relative intensity of 4.21% and the most intense peak centred at 26.922° , estimated to have an interlayer spacing of 0.332 nm. The HOPG sample was provided by

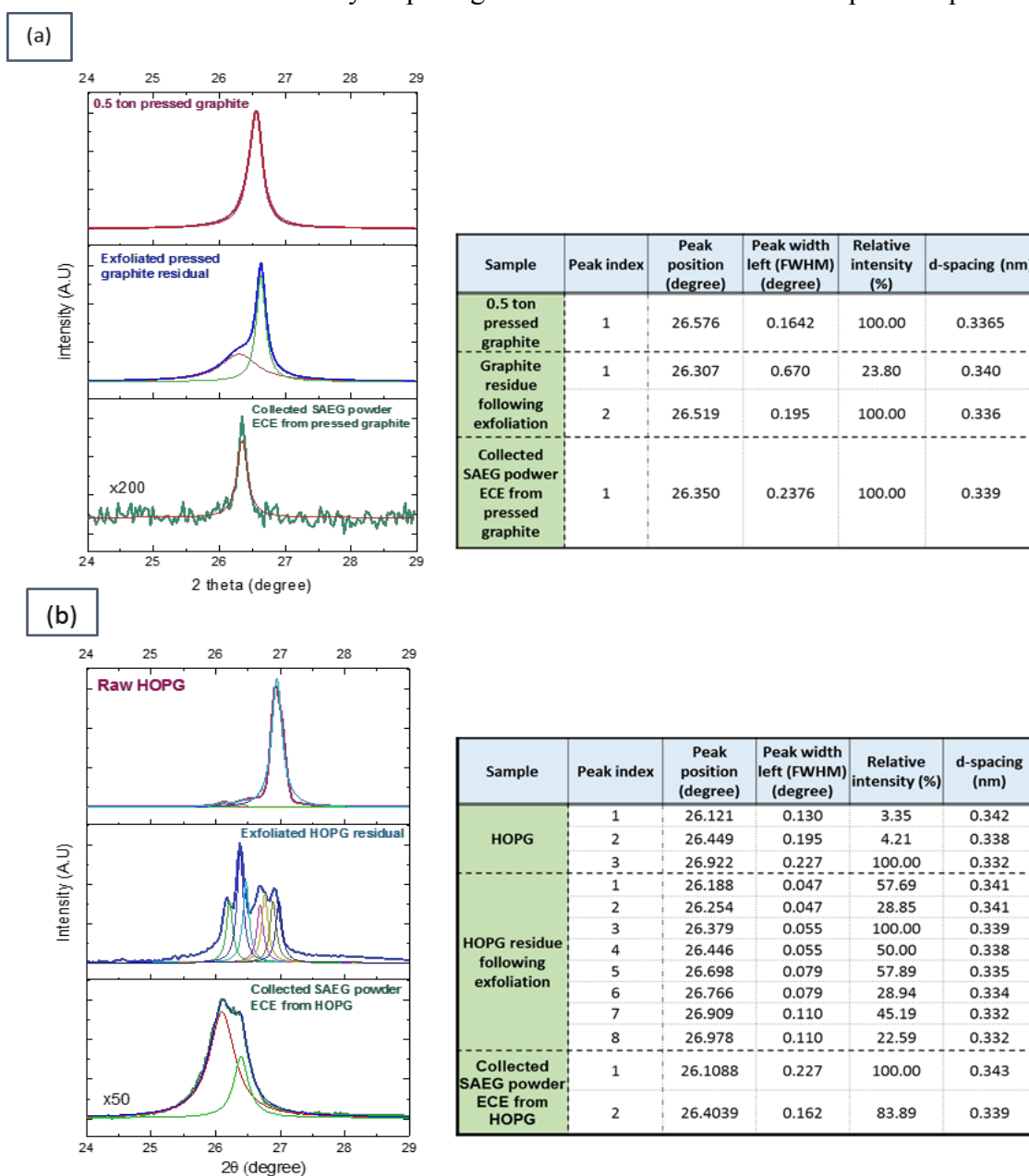


Figure 7.14: XRD (002) peaks of pressed graphite and HOPG before and after applying a bias voltage of +10 V for around 100 seconds in 0.1M $(\text{NH}_4)_2\text{SO}_4(\text{aq})$ aqueous electrolyte solution. (a) 0.5-ton pressed graphite, the residue following exfoliation and the collected powder. (b) HOPG, the exfoliated residual and the collected powder. Associated tables provided the results of Rietveld refinement.

SPI™, the grade 2 sample was claimed to have a lateral grain size (L_a) up to 0.5 mm and a mosaic spread angle of $0.8^\circ \pm 0.2^\circ$, indicating the existence of disorder in (002) direction²²⁶. The spread of (002) peak in the raw HOPG sample were estimated to be 0.552° , and appeared asymmetric, suggesting that anisotropic strain is already existed in the unexfoliated HOPG sample. The following electrochemical exfoliated HOPG residue shows even more peaks in the (002) region. The most intense diffraction peak is centred at 26.379° surrounded by seven minor peaks which not only indicate the presence of anisotropic strain in the sample, but also suggests that the expanded layers are clustered. Eight different peaks were extracted by Rietveld refinement, where the largest interlayer spacings were estimated to be 0.341 nm and 0.332 nm respectively, similar to unexfoliated HOPG. The collected exfoliated graphene powder exhibited only two peaks, centred at 26.101° and 26.404° , corresponding to interlayer spacings of 0.343 nm and 0.339 nm respectively. This indicating a proportion of AA stacking graphene or Turbostratic graphene flakes are presented in the sample (interlayer spacing ~ 0.34). The fewer peaks compared to the HOPG residue following exfoliation could be due to the release of strain after the flakes were exfoliated from the HOPG electrode. The obtained interlayer spacings are larger compared to those of SAEG powder synthesised via pressed graphite. Furthermore, the peak widths indicate that a significant proportion of incomplete delaminated graphite is still present in the powder, which could be due to flake re-stacking during powder collection and was estimated to be 10% from the Raman spectra (see figure 7.13)

II. Scanning Raman spectroscopy

Scanning Raman spectroscopy was further used to study the graphite residue following exfoliation. Figure 7.15 shows the interfacial region between the unexfoliated area and the exfoliated area of the graphite electrode. The region was selected using optical microscopy and a line scan was performed across the interface. The probe size for the Raman spectroscopy was $\sim 1 \mu\text{m}$ and the scanning step was set to be $1 \mu\text{m}$; a total length of $15 \mu\text{m}$ was scanned across the interfacial region. As seen in the photograph in figure

7.15, unlike HOPG where the exfoliated region is obviously expanded, the exfoliated pressed graphite seem to have been etched off by the exfoliation process. Furthermore, no

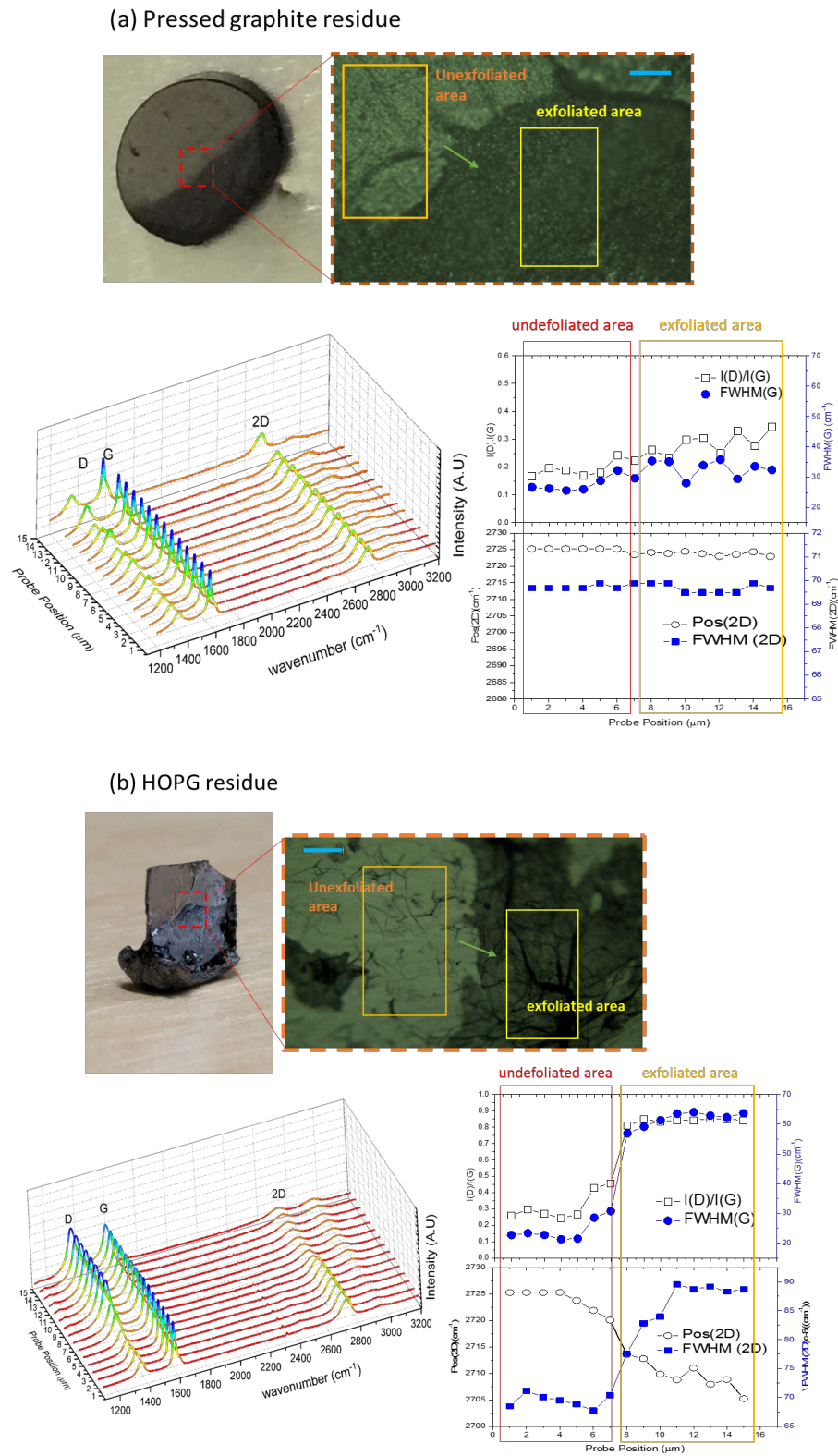


Figure 7.15: The scanning Raman measurement of the pressed graphite and HOPG (a) Measurement on pressed graphite residual shows unclear boundary between the unexfoliated and exfoliated areas. (b) Measurement on HOPG residual shows noticeable spectrum change, a clear boundary between the unexfoliated area and the exfoliated area. (The blue scale bar stands for 20 μm.)

significant change in I(D)/I(G) ratio were observed in Raman spectra when the laser probe was scanned across the interfacial area in the pressed graphite residue. This could indicate that the exfoliation is not accompanied by an increase defect concentration in the graphite or cause serious oxidation. Also, only a very minor decrease in minor the 2D peak position shift was observed in the exfoliated area.

In comparison, a clear boundary between the unexfoliated area and the exfoliated area was observed for the exfoliated HOPG residue. As seen in figure 7.15(b), the HOPG residue exhibits a I(D)/I(G) ratio of ~ 0.3 in the unexfoliated area, with the D peak intensity gradually increasing as the probe position moved towards to the exfoliated area reaching a I(D)/I(G) ratio of ~ 0.85 in the exfoliated area. This increase in the D peak intensity was accompanied by an increase in the G peak width (FWHM(G)), as observed in the exfoliated SAEG flakes, indicating severe structural damage or oxidation occurred to the graphite. The 2D peak also shifted from $\sim 2725 \text{ cm}^{-1}$ to $\sim 2710 \text{ cm}^{-1}$, which could be due to the effect of HOPG expansion.

III. Scanning electron microscopy (SEM)

A significant differences in morphology between the pressed graphite surface and the HOPG surface following exfoliation were also observed by scanning electron microscopy (SEM). As shown in figure 7.16 (a), the exfoliated surface of pressed graphite exhibits a rougher morphology compared to the unexfoliated surface (compare image (1) and (3) in figure 7.16 (a)). In addition, a step-like morphology was found in lower magnification images, but the surface morphology of the step edge appears similar to the exfoliated basal surface, where most of the micro-flakes appear to remain closely packed (see images (2) and (3) in figure 7.16(a)) . SEM images of the exfoliated HOPG surface exhibited significant differences in surface and edge morphology. As seen in figure 7.16(b), after applying a bias voltage for 60 seconds, the edge sites of the HOPG electrode increased, accompanied by expansion of HOPG that can also be observed at the macroscopic scale. Moreover, ripples and edge networks appeared on the exfoliated surface of the HOPG

electrode which could be due to the visible gas evolution result in expansion and swelling of the graphite layers. The observation corresponds to the proposed mechanism of electrochemical exfoliation for graphene synthesis as mentioned in reference ²⁵.

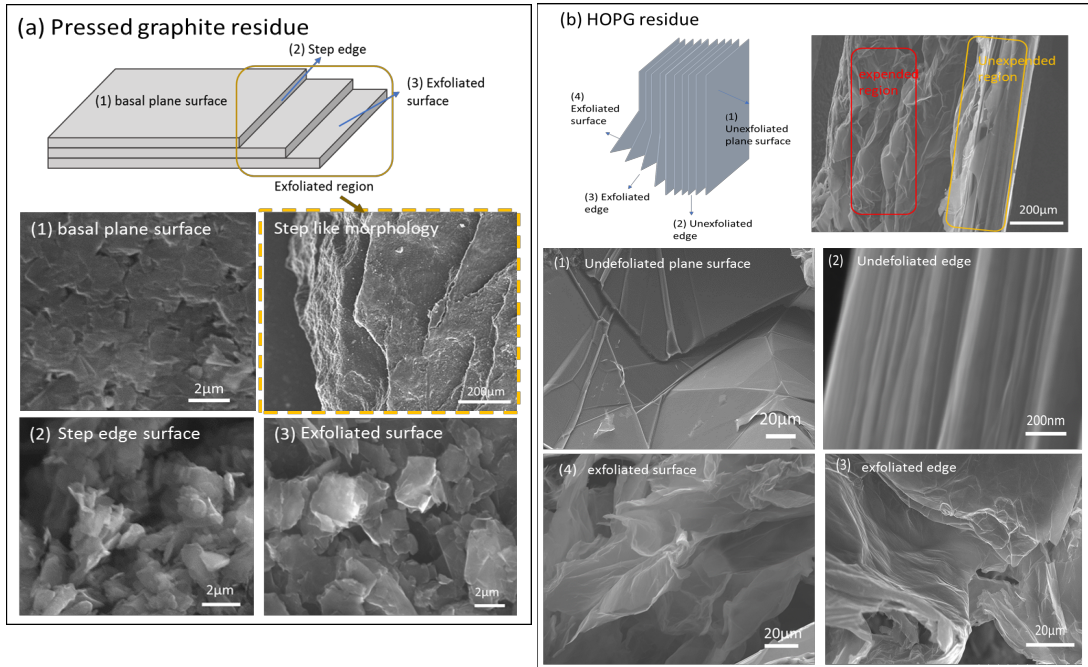


Figure 7.16: SEM images of surface and edge morphology of the pressed graphite and HOPG residue after applying a bias voltage of +10 V for 100 seconds in 0.1M $(\text{NH}_4)_2\text{SO}_4$ (aq) aqueous electrolyte solution.

IV. A proposed model for electrochemical exfoliation

However, the proposed mechanism for electrochemical exfoliation does not explain why different properties of SAEG graphene flakes (i.g., lateral size, crystal imperfection and thickness) obtained when different exfoliation conditions or starting materials were used. This is due to most studies focusing on the electrochemical mechanism for exfoliation rather than the ion insertion process, the latter could significantly affect the obtained SAEG graphene properties. Indeed, ion insertion could be highly influenced by the original graphite structure. Consideration of the electric potential distribution in the graphite electrode structure under a constant bias voltage may improve the understanding of the mechanism of electrochemical exfoliation.

Figure 7.17 (a) reveals an idealised and simplified graphite structure, where the a graphene flake were indicated by black lines and are assumed to be parallel to each other having a coherence length of L_a , (002) d-spacing between each graphene flakes of D . The width of grain boundaries (pores) was assumed to be d . The electric potential distribution within the simplified graphite can be obtained by solving Poisson's equation using a 2D Finite Difference Method (FDM) algorithm²³⁴. Using 401×401 grids with a Matlab code was used for the calculation. The relative electric potential distribution was based on the simplified graphite model, where the flake length $L_a = 200$ grid points; the (002) d-spacing $D = 10$ grid points and the width of pore (flake boundary) $d = 10$ grid point. Such a simplified model cannot represent a real structure, but it could provide an insight of how the electric potential distribution would look like in the graphite structure. Here, the relative permittivity of the electrolyte was assumed to be : $\epsilon_r = 80$ for water at 20°C , and $\epsilon_0 \epsilon_r = 7.09205 \times 10^{-10} \text{ (F} \cdot \text{m}^{-1}\text{)}$, due to the low concentration of ammonium sulphate in the electrolyte. Each graphene layers were biased by 10 V and complicated boundary conditions were neglected and each boundaries were set to be 0 V (uncharged electrolyte environment).

As seen in the figure 7.17(b) , electric potential was concentrated near the edge and the grain boundary regions, implying that both hydroxyl (OH^-) and sulphate (SO_4^{2-}) ions in the electrolyte will drift to these regions before being inserted into the graphite electrode. Since the direction and intensity of electric field implies the resultant electric force on the ions, the vanishing of the electric field at certain point within the interlayer space means that the movement of ions will then be mainly caused by thermal fluctuations, which is much smaller than the effect of electric field. Therefore, the interlayer region where the electric field vanishes is assumed to be where the ion reduction commences causing vigorous gas evolution. By visualising the electric field distribution within the graphite, the possible ion drift pathways and the place where initiate the exfoliation process can be approximated.

In figure 7.17 (b) (c) and (d), dense equal-potential contour lines were concentrated near the graphite surface, grain boundaries (pores) and graphite edge site, but a lesser concentration in the intercalation space between layers. The dense equal-potential contour

lines within the grain boundary could be the reason that the ions preferably to drift into a deeper place through the boundaries (x-direction in figure 7.17(c)) rather than directly insert into the intercalation space of graphite, resulting in exfoliation of thick graphite.

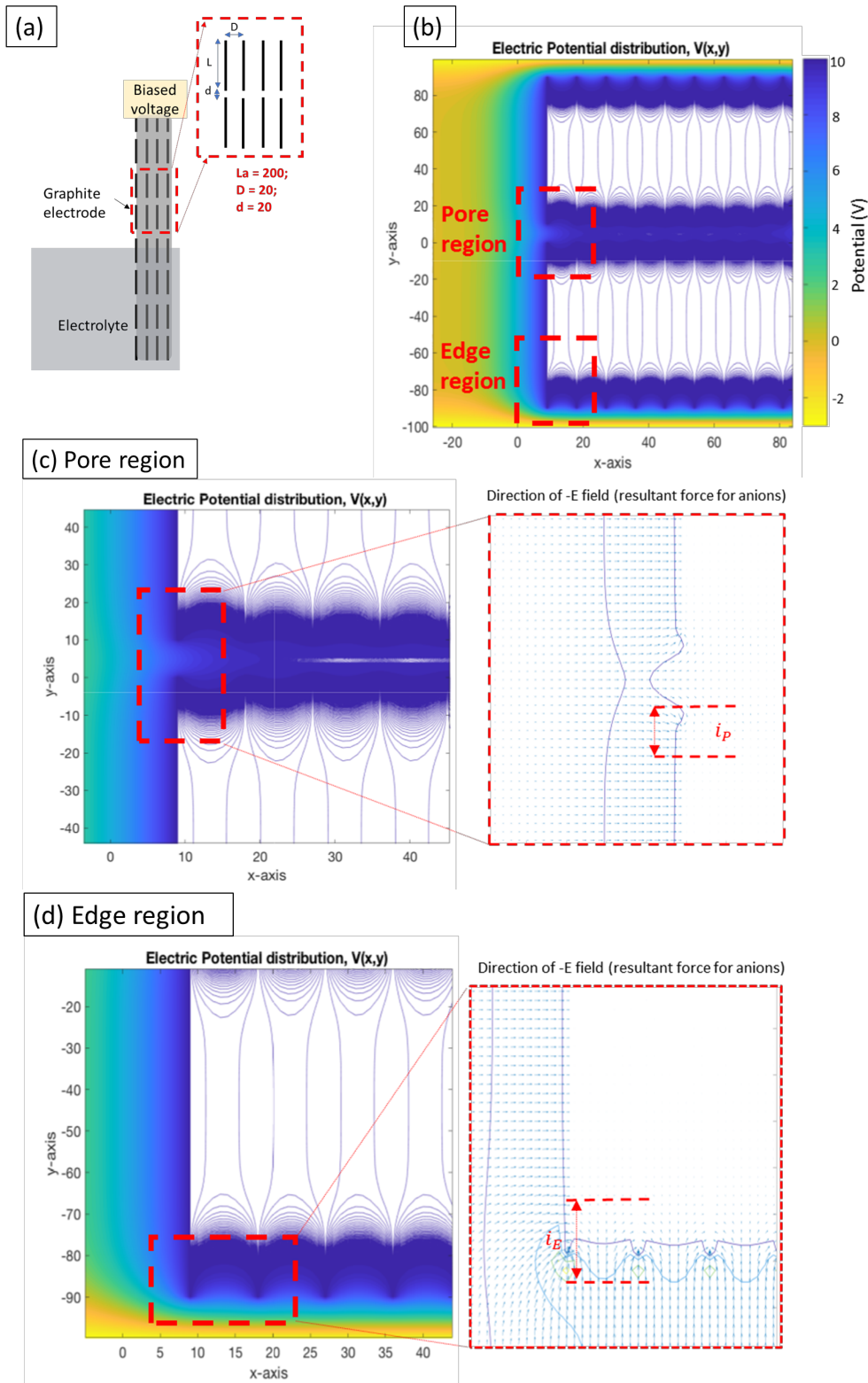


Figure 7.17: Electric potential distribution around graphite electrode. (a) Schematically shows simplified graphite electrode mode used. (b) Electric potential distribution around the simplified graphite electrode. (c) Electric potential distribution around the pore. (d) Electric potential distribution around the graphite edge.

However, there are still possibilities that ions can drift into the intercalation space of graphite through pores. As seen in the right-hand side of figure 7.17 (c), the direction of electric field is observed to turn into the intercalation space near the flake edge and the boundaries near the graphite surface. The electric field then vanishes at a depth of i_p , which is around 6% of the flake length (L). The small i_p could be the reason that oxidation or exfoliation process are often initiated at the flake edge site ²⁵. However, the oxidation and exfoliation process near the flake edge could further enlarge the boundary width (d) or alter the width of interlayer spacing (D) near the flake edge, which further promote the resultant electric field to drift the ions into the interlayer space and initiate vigorous gas evolution until the graphene/graphite is being peeled off from the graphite electrode.

Similarly, dense equal-potential contour lines were concentrated near the graphite edge region. As seen in figure 7.17(d), the direction of the electric field showing that the ions could be drifted into the interlayer space through the graphite edge. Unlike the case near the pores, the intensity of the electric field remained strong within the interlayer space, resulting in a longer vanish depth $i_E \approx 0.12L$. As ions can intercalate further at the graphite edge, gas evolution will be more effective in exfoliating graphene flakes relative to the grain boundaries.

Although the electric potential distribution can provide an insight at how the ions are inserted into the graphite electrode, such a potential simulation can be imprecise due to the finite number of grid point used for calculation. Also, since the electric potential increased rapidly with decreasing distance from the charge, it is often difficult to simulate the potential distribution at the nanoscale. As the position (\vec{R}) gets closer to the point charge position (\vec{R}_{charge}) an unreal value could result (i.e.,

$$V_{(x,y,z)} = \sum_{c=1}^N \frac{Q_c}{4\pi\epsilon \left| \vec{R} - \vec{R}_{charge} \right|}, \text{ when } \vec{R} - \vec{R}_{charge} \rightarrow 0, V \rightarrow \infty$$

)^{89,235}. Therefore, a more complicated Molecular Dynamics simulation is probably required for simulation of the electric potential distribution and to help understand the mechanism of electrochemical exfoliation.

Nevertheless, although the simulation could be inaccurate, the variation of electric potential distribution could hold largely true and can be used to explain the observed experimental results. From figure 7.17, we can conclude that ion insertion is more effective at the graphite edges rather than the pore channels. Thus, for a graphite electrode that has long coherence length (L_a) such as HOPG (i.e., $L_a > 751.90$ nm, $L_D > 75.98$ nm from Raman spectroscopy, the exfoliated flake lateral dimension $\sim 2\mu\text{m}$), the DC potential will mainly drift ions into the intercalation space through the graphite edges. This static potential is continuously applied, which triggers the electrochemical reaction. As shown schematically in figure 7.18(a), gas evolution causes HOPG graphite electrode to expand, and due to its long coherence length, the bubbles kept banding the graphene layers, result in expanding the electrode rather than to tearing off graphene flakes from the graphite electrode. Although some of the flakes might fall off as time increases, the long process time can therefore cause significant oxidation or damage to both the HOPG electrode as well as the exfoliated SAEG flakes, which can be observed as the intense Raman D peak in both the exfoliated graphene flakes and the exfoliated HOPG residue.

In comparison, the pressed graphite has a much shorter coherence length (L_a), suggesting higher concentration of grain boundaries per area (i.e., $L_a = 100.25$ nm and $L_D = 27.74$ nm for 0.5 ton pressed graphite from Raman spectroscopy). Therefore, the biased DC potential could drift electrolyte anions into the intercalation space through both the

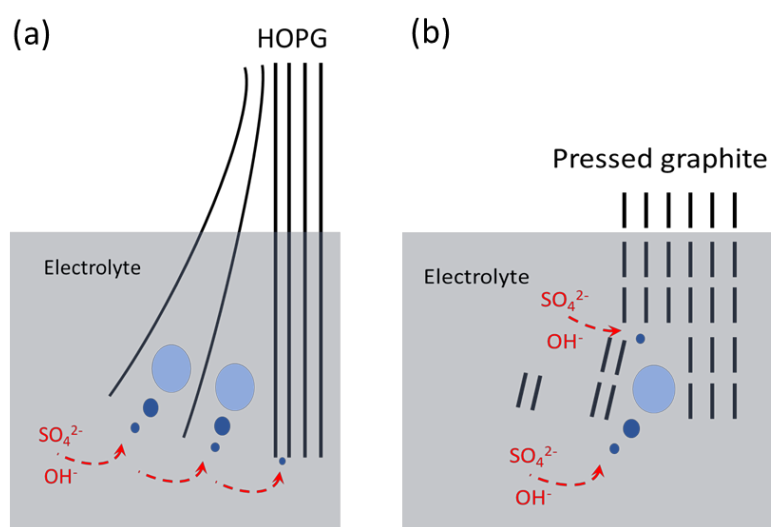


Figure 7.18: Schematic diagram showing the ion insertion and gas evolution for different graphite electrodes.

graphite edges and the grain boundaries. As seen in figure 7.18(b), the extra insertion channel via the grain boundaries making it possible for ions to drift deeper from the graphite surface, which results in exfoliation of a thicker block of graphite rather than thin graphene flakes. Since the short coherence length of the pressed graphite, the graphene/graphite flakes were fractured and etched off before the layers being bended, providing a step-like morphology on the pressed graphite residue. As a consequence, electrochemical exfoliation of pressed graphite is much faster than HOPG. Also, since the graphene/graphite flakes could be peeled off before serious oxidation took place, they exhibit much lower Raman D peaks.

7.5. Conclusion

In this chapter, the graphene characterisation protocol was applied to the SAEG samples synthesised using different exfoliation conditions. To understand the relative effectiveness of each exfoliation method, the starting material was investigated by X-Ray diffraction (XRD). It was found that the position and width of the (002) peak was affected by the pressing force, being slightly shifted to higher 2θ angles with increasing pressing force. This indicated a smaller intercalation space in the high-force-pressed graphite. The pressed graphite was further examined by SEM, where a smoother surface morphology was obtained after the graphite was pressed.

To investigate the applied voltage for the electrochemical exfoliation, the current density was plotted as a function of applied voltage (I-V curve). It was found that electrochemical exfoliation commences when the applied voltage exceeded 4 V and utilising a 10 V bias voltage on 0.5 tons pressed graphite can rapidly electrochemically exfoliate graphite. Using such an exfoliation condition, a relatively large lateral flake size (~ 825 nm) and a low defect density (I(D)/I(G) ratio = 0.115) was obtained, while the yield of graphene was estimated to be only $\sim 65\%$. In contrast, electrochemical exfoliation of HOPG under the

same conditions yielded thinner SAEG samples (> 90% graphene yield), although a higher I(D)/I(G) ratio was obtained.

The exfoliation mechanism was studied by characterising the graphite following exfoliation residue. Unlike the HOPG residue which was significantly expanded, a step-like surface morphology was found in the pressed graphite residue. XRD and scanning Raman observation also revealed a minor change in the pressed graphite after it was electrochemically exfoliated. This could indicate a different exfoliation path when a different graphite structure was used. The electric potential simulation shows that ions may insert into the graphite through both the edge and the flake / grain boundaries. Ions inserted through the graphite edge may provide a more effective exfoliation than through the grain boundaries. This can be used to explain why the exfoliated HOPG residue is expanded and the SAEG flakes produced were highly damaged or oxidised. The additional insertion channel via the grain / flake boundaries in the pressed graphite make it possible for the ions to drift deeper from the graphite surface, resulting in exfoliation of a larger proportion of thicker graphite rather than thin graphene flakes. Also because of the short flake/coherence length of the pressed graphite, the graphene/graphite flakes were peeled off before the graphite expanded, resulting in a step-like morphology in the graphite residual.

Nevertheless, although the model electrochemical exfoliation could be incomplete, the proposed simulation for electric potential distribution and ion insertion path ways could holds largely true, and can be used to explain the observed experimental results. To obtain a more precise model for electrochemical exfoliation, Molecular Dynamics simulation is probably required for simulate the electric potential distribution and the derived ion-insertion pathways.

Part Three

Conclusion

8.

Summary and Outlook

In this thesis, the critical requirement for a robust graphene characterisation protocol is addressed. The term ‘graphene’ is often misused in many research fields and because of the difficulties in large-scale production of true two-dimensional graphene, further graphene application is thus limited. Although graphene can be positively identified using modern high-resolution electron microscopy techniques, the approach is time-consuming and costly. Using its unique properties to distinguish graphene is another way to characterise the material within a shorter period, but many of the properties of graphene are still too ill-defined to be used to identify the material. Therefore, while synthesis methods like solution-assisted graphite exfoliation are deemed to have the potential to achieve large-scale graphene production, a fast and universally reliable characterisation method is still the main obstacle to monitoring and quantifying the degree of exfoliation, the crystal quality, the sheet thickness and the lateral dimension achieved during the synthesis and refinement process. Thus, by developing a universally reliable characterisation protocol, the inhomogeneity and nanostructural features in a graphene suspension can be quantified and used for optimising the graphene synthesis processes.

After introducing the motivation for developing such a protocol in Chapter 1 of this thesis, the general background regarding graphene and its characterisation are introduced in Chapter 2. Electron probe-based techniques can provide precise and direct imaging platform to characterise graphene at high resolution due to the short de Broglie wavelength of accelerated electrons, but such techniques are challenging for making statistically relevant quantitative data interpretation over large sample areas. Photon probe-based techniques provide less direct information but are relatively efficient pathway to characterise graphene. However, the precision and accuracy are yet to be validated because the nanostructural features of graphene often being smaller than the wavelength of

incident photons, making the photon scattering event less localised compared to corresponding events in the electron probe-based technique. Therefore, a methodology that can link the observations obtained from the electron probe-based technique to photon probe-based techniques is critical if the properties of graphene are to be determined with both detail and efficiency.

The general sample preparation process, equipment settings and data interpretation methodologies are introduced in Chapter 3. Graphene samples were prepared by several different solution-assisted graphite exfoliation methods, where each sample was washed by deionised water and re-dispersed in isopropyl alcohol (IPA) before characterisation. A commercial SAEG graphene prepared by milling in ionic liquid was used as the reference for other samples, and the commercial SAEG graphene sample was initially characterised by Transmission Electron Microscopy (TEM) prior to the other measurements being carried out. Graphene nanostructural features were quantified from TEM images and statistically analysed and the results are used as a benchmark for the other characterisation techniques.

8.1. Summary of results and conclusions

In Chapter 4, a method to estimate the lateral size distribution for exfoliated graphene in suspension was developed. The graphene lateral dimension distribution was initially derived from TEM images. The result was compared to the lateral size distribution obtained from analysing optical microscopy images. The image analysis technique was developed based on graphene reflection spectrum on SiO₂/Si interferometer substrates and can distinguish thin graphene flakes from its image. The image analysis technique is rapid and detailed lateral dimension distribution of thin graphene can be obtained by analysing multiple optical microscopy images. A very good correlation was found when comparing the image analysis technique to the TEM results, with an error of 0.9% and 0.5% for the mean value of primary flake and aggregated flake size respectively. To develop an in-situ

observation of the graphene lateral size distribution, the Dynamic light scattering technique was used, and approximate optical properties of graphene were used to obtain number particle size distribution (PSDs) from DLS. To avoid heterogeneity in the sample, the sedimentation-based size selection method was used to prepare dispersions of graphene. In all cases, the lateral flake size distributions were firstly measured using OM. The same dispersion was then characterised by DLS. It was found that the number PSDs outputted from DLS fits well with the size distribution measured from OM, especially for flakes smaller than 1000 nm wide (relative deviation <22%). This finding allows us to write an empirical expression that correlates the flake size distribution from OM to the DLS data, providing a fast and simple method to obtain a good estimation of the mean lateral size of graphene dispersed in liquid.

In Chapter 5, a relatively rapid method was intended to be developed to assess the crystalline imperfections within graphene. Initially, the presence of crystal imperfections was visualised using bright-field TEM images. With the help of Electron diffraction (ED), electron energy loss spectroscopy (EELS) and dark-field (DF) imaging techniques, the spatial distribution of crystal imperfection within graphene was quantified. It was found that the topological point defects present a higher concentration on thin graphene regions and tend to cluster or distribute unevenly in a flake. Although the uneven defect distribution can be observed by TEM images, it is difficult for it to be obtained and quantified by conventional Raman spectroscopy. This is not only because of the limitation of spatial resolution in the photon-probe based technique, but also because the existing conventional models that were used to link the spectra to graphene crystal disorder are still ambiguous, especially for the small lateral size graphene flakes. Therefore, a simple method based on linear correlation and random sampling was proposed to indicate the source of disorder in graphene samples. The coherence length (L_a) and the average distance between defects (L_D) were calculated via the Tuinstra–Koenig relation and the local activation model respectively. The result was compared to the TEM study, and the differences were assigned to the uneven distribution of the defects in graphene flakes.

In chapter 6, various methods were used to determine the thickness of SAEG graphene flakes. The most straightforward method involved direct imaging of the edge of the folded

graphene flake, which was correlated to the image Mean Greyscale Value Ratio (MGVR) to develop a rapid characterisation for the thickness of graphene. The MGVR measured on zone axis decreased as the number of graphene layers increased and can be approximated by an inverse linear relationship for graphene thicknesses < 30 layers. The inverse linear relationship decays faster than that found in the experimental work at 7° sample tilt conducted by Rubino et al, but decays slower than the computer simulation at zone axis. This could be due to the different operating voltages and objective aperture sizes that were used. The MGVR values were further compared to the relative thickness determined by the log-ratio method in low-loss EELS. The result shows that the MGVR remains in inversely linear relationship to the relative thickness ($t_R = \frac{t}{IMFP}$). The observation further allows us to compare the material dependent absorption constant (δ) to the inelastic mean free path (IMFP) from the slope of the linear relationship. By comparing the IMFP obtained from MGVR to the IMFP estimated via Mali's equation in GMS 3, the result showed that Mali's equation is more applicable, with regard to thinner flakes, while a difference of $\pm 11.4\%$ was obtained from six selected graphene flakes. This could be explained by the presence of surface plasmon in thin flakes, leading to an over-estimation of relative thickness and affect the accuracy of estimated IMFP from the both methods.

To improve the graphene thickness estimation method, the variation in the EELS low-loss plasmon band as a function of number of graphene layers was obtained. A π plasmon peak shift toward lower energy losses accompanied by a $\pi+\sigma$ plasmon peak broadening was observed as the number of graphene layers decreased, which could be due to the contribution of the surface plasmon mode and was roughly explained by the competition of the out-of-plane and in-plane plasmon excitation modes in graphene and graphite. This potentially indicates an evolution in the electronic band structure from graphene to graphite. Nevertheless, for an even more rapid investigation of graphene thickness, the photon-probe based technique was used. Since the variation of 2D (G') band in Raman spectroscopy was reported to reflect the evolution of graphene band structure, well-established data was taken from Ferrari's previous work based on the variation in peak shape and peak position. Several empirical equations were then derived from the variation of the 2D band shape. These empirical equations were applied to the same SAEG

graphene, showing that whilst the equation based on the variation of peak shape can resolve the number of graphene layers, the equation based on the shift of peak position is the most effective method for the characterisation of number of graphene layers. However, applying these thickness characterisation methods to a SAEG sample resulted in significant deviations in the results: the MGVR method estimated the mean flake thickness of 13.21 nm for primary flakes; estimation via Raman spectroscopy obtained around 7-8 coupled layers are consisted in a flake; the AFM measurement obtained an average thickness of 3.11nm for the same SAEG sample. The uncertainty of the MGVR measurement could be due to the presence of the flake aggregation, folded or overlapping graphene regions; while the presence of buffer layer when depositing graphene onto the substrate could result to inaccurate measurements from AFM. However, from Raman spectroscopy, a mean 7-8 graphene layers was estimated in the 2Dtech aquagraph sample, which was estimated to be 2.38-2.72 nm, not too far from the observation using AFM on the sample (a mean value of 3.11 nm). This could be because of the Raman spectroscopy “sees” flakes with thickness \gg 10 layers as 10 layers, the statistics is therefore biased to thinner flakes. Therefore, though the thick flakes were avoided when performing the AFM measurement, the differences between the number of graphene layers estimated via AFM and Raman is coincidentally small. Nevertheless, although analysing the 2D peak of Raman spectroscopy is deemed to be a comparably rapid and fairly precise method, and accurate thickness characterisation method may not be achievable for rapid large-scale characterisation in this stage. However, despite obtaining the precise number of graphene layers, identifying the level of graphitic character is rather more important and can be used to improve the graphene synthesis process. Therefore, unlike the microscopic methods that utilise probes to measure the physical thickness of graphene layers, Raman spectroscopy directly detects the scattering properties of graphene, which are strongly affected by the band structure and the number of graphene layer coupled ^{21,111,222}. Therefore, despite the limitations and difficulties mentioned earlier, the variation of 2D peak is one of the most practical techniques to be used to determine the level of graphitic character.

In chapter 7, the graphene characterisation protocol was applied to the SAEG samples synthesised using different exfoliation conditions. Initially, the starting material, pressed to different degrees, was investigated by X-Ray diffraction (XRD). It was found that the

(002) peak is being shifted slightly to higher 2θ angles with increasing pressing force, which indicated a smaller interlayer space in the high-force-pressed graphite. The pressed graphite was further examined by SEM, where a smoother surface morphology was obtained after the graphite was pressed. The pressed graphite was used as an electrode for electrochemical exfoliation of itself, and the current density was plotted as a function of applied voltage (I-V curve) to investigate the applied voltage for the electrochemical exfoliation. It was found that electrochemical exfoliation commences when the applied voltage exceeded 4 V and utilising a 10 V bias voltage on 0.5 tons pressed graphite can rapidly electrochemically exfoliate graphite. A relatively large lateral flake size (~ 825 nm) and a low defect density (I(D)/I(G) ratio = 0.115) were obtained via such an exfoliation condition. However, the exfoliation condition does not delaminate graphene completely and the yield of graphene was estimated to be $\sim 65\%$ using Raman spectroscopy. In contrast, although a higher I(D)/I(G) ratio was obtained for electrochemically exfoliated HOPG, using HOPG as the starting material yielded thinner SAEG samples ($> 90\%$ graphene yield) under the same condition.

To study the exfoliation mechanism, the graphite residue following exfoliation was characterised via various techniques. A step-like surface morphology was found in the pressed graphite residue whilst the HOPG residue was found significantly expanded. Both XRD and scanning Raman measurements revealed a minor change in the pressed graphite after it was electrochemically exfoliated, which could indicate a different exfoliation path when a graphite structure with different coherence length was used. Possible ion insertion paths were studied by electric potential simulation, which shows that the ions may insert into the graphite through both the edge and the flake / grain boundaries. However, ions inserted through the graphite edge may provide a more effective exfoliation than through the grain boundaries, due to the longer vanishing depth of the electric field distribution near the graphite edge, which may drift the ions to a position in the interlayer space that allows the following gas evolution to effectively peel the graphene flake from the graphite. Thus, a higher density of grain boundaries/defects presenting in the pressed graphite can be the reason why exfoliating pressed graphite is much faster and presented a step-like morphology in the graphite residue following exfoliation. Since the higher density of grain boundaries/defects in the pressed graphite provides additional insertion

channels, it is possible for the ions to drift deeper/further from the graphite surface resulting in the exfoliation of a larger proportion of thicker graphite rather than of thin graphene flakes. Also, because of the short coherence length of the pressed graphite, the graphene/graphite flakes were peeled off before the graphite expanded, resulting in a step-like morphology in the graphite residue rather than the expanded morphology generated from HOPG.

In conclusion, a graphene characterisation protocol was developed by quantifying the fundamental nanostructural features of graphene. The results obtained from photon probe-based techniques were compared to observations obtained by direct imaging techniques, enabling the limitations and accuracies of the proposed techniques to be evaluated. This allows development of a rapid characterisation routine to quantify the inhomogeneity and nanostructural features on a large-scale and can further be used for optimising graphene synthesis processes.

8.2. Outlook and future perspectives

Throughout this project, several techniques have been developed to characterise graphene. However, further refinements are still needed in order to develop a more profound understanding of the material and the characterisation techniques.

As discussed in Chapter 4, an image analysis technique has been developed based on the graphene reflection spectrum on SiO₂/Si interferometer substrates, which can also be used to distinguish thin graphene flakes in the optical microscope images. The principle of the technique is to design an interferometer for graphene based on its refractive index: using a selected material (suitable refractive index) and thicknesses of each layers, the image contrast of graphene is enhanced by the reflection spectrum of the interferometer substrate, which can visualise graphene as thin as ~1 nm (see section 4.2 and 6.4). Thus, it is possible to adapt the technique to other thin layered materials such as MoS₂. By derive

the refractive index of the thin layered materials, an optimised thicknesses and materials (suitable refractive index) can be selected by calculating the reflection spectrum, an interferometer can be formed by depositing the target thickness of each layers to enhance the contrast of the thin layered materials, so that it can be seen under optical microscopy.

In chapter 5, crystal imperfection in graphene was observed via TEM and Raman spectroscopy. By quantifying the D band enhancement and G peak broadening in Raman spectra, a simple method based on linear correlation and random sampling was proposed to indicate the source of disorder in graphene samples. However, a direct observation on the variation of Raman spectra by the presence of graphene crystal disorder is still unavailable because of the limited spatial resolution of conventional Raman spectroscopy. Thus, the existing model is still ambiguous and unable to reflect the uneven distribution of defects in detail. A more direct observation of the spectrum variation near edges and defects can be obtained by utilising a Tip-Enhanced Raman Spectroscopy (TERS). With an improved probe size giving ~50 nm spatial resolution, an improved model to quantify the spatial distribution of defects in graphene can possibly be derived.

In Chapter 6, several methods of measuring the thickness of graphene were demonstrated. It was found that many of the conventional thickness estimation techniques may not be precise enough when applied to the ultra-thin graphene flakes: AFM measurements can be imprecise due to the presence of substrate roughness; the well-established log-ratio method based on low-loss EELS could also overestimate the thickness of thin graphene as surface plasmons arise. Although an empirical equation was proposed to estimate the thickness of graphene via the variation of the low-loss EELS plasmon peak, the detailed mechanism of the plasmon peak variation as well as its corresponding graphene dielectric properties are not clear yet. However, with deeper understanding of the Kramers-Kronig relation and the performance of the momentum-resolved EELS measurement with band structure simulation, the possibility of linking the observations from EELS experiments to the dielectric properties that evolve with increasing number of graphene layers becomes greater.

In chapter 7, a model that considers the electric potential distribution in the graphite electrode structure under a constant bias voltage was proposed. The model aims at improving understanding of the mechanism of electrochemical exfoliation. However, such a model can only provide an insight as to how the ions are inserted into the graphite electrode; and how the potential and electric field distribution can be imprecise due to the finite number of grid points used for calculation. Also, since the electric potential increased rapidly with decreasing distance from the charge, it is often difficult to simulate the potential distribution at the nanoscale. As the position gets closer to the point charge position an unreal value could result, thus it is difficult to simulate the potential distribution at the nanoscale. Therefore, a more complicated Molecular Dynamics simulation is probably required to precisely simulate the electric potential distribution, as well as the movement of ions on the nanoscale, in order to help us understand the detailed mechanism of electrochemical exfoliation.

Nevertheless, although improvements can always be made, the proposed graphene characterisation protocol offers a viable method to integrate and evaluate different characterisation techniques. In addition, the protocol development method can be used as a reference point, in which the development process can be applied to other materials in order to develop material-specific characterisation protocols. Notwithstanding, it has been shown that such a graphene characterisation protocol can quantify and differentiate between inhomogeneous solution-processed graphene samples and thus it can be used for optimising the synthesis processes of graphene.

Reference

1. Landau, L. Zur theorie der phasenumwandlungen II. *Phys. Z. Sowjetunion* **11**, 26–35
2. Novoselov, K. S. et al. Electric field effect in atomically thin carbon films. *Science* **306**, 666–9 (2004).
3. Novoselov, K. S. et al. Two-dimensional gas of massless Dirac fermions in graphene. *Nature* **438**, 197–200 (2005).
4. Novoselov, K. S. et al. A roadmap for graphene. *Nature* **490**, 192–200 (2012).
5. Wu, J. et al. Organic solar cells with solution-processed graphene transparent electrodes. *Appl. Phys. Lett.* **92**, 4–6 (2008).
6. Hofmann, M. et al. Controlling the properties of graphene produced by electrochemical exfoliation. *Nanotechnology* **26**, 335607 (2015).
7. Parvez, K. et al. Electrochemically exfoliated graphene as solution-processable, highly conductive electrodes for organic electronics. *ACS Nano* **7**, 3598–606 (2013).
8. Jeon, K.-J. et al. Fluorographene: a wide bandgap semiconductor with ultraviolet luminescence. *ACS Nano* **5**, 1042–6 (2011).
9. Geim, A. K. & Novoselov, K. S. *The rise of graphene*. Nature materials **6**, (Nature Publishing Group, 2007).
10. Morozov, S. V. et al. Two-dimensional electron and hole gases at the surface of graphite. *Phys. Rev. B* **72**, 201401 (2005).
11. Partoens, B. & Peeters, F. From graphene to graphite: Electronic structure around the K point. *Phys. Rev. B* **74**, 075404 (2006).
12. Su, C. Y. et al. High-Quality Thin Graphene Films from Fast Electrochemical Exfoliation. *ACS Nano* **5**, 2332–2339 (2011).
13. Khan, U., O’Neill, A., Lotya, M., De, S. & Coleman, J. N. High-concentration solvent exfoliation of graphene. *Small* **6**, 864–871 (2010).
14. Hernandez, Y. et al. High-yield production of graphene by liquid-phase exfoliation of graphite. *Nat. Nanotechnol.* **3**, 563–568 (2008).
15. Li, H. et al. Rapid and reliable thickness identification of two-dimensional nanosheets using optical microscopy. *ACS Nano* **7**, 10344–10353 (2013).
16. Z. H. Ni, † et al. Graphene Thickness Determination Using Reflection and Contrast Spectroscopy. *Nano Lett.* **7**, 2758–63 (2007).
17. Bruna, M. & Borini, S. Optical constants of graphene layers in the visible range. *Appl. Phys. Lett.* **94**, 1–4 (2009).
18. Mak, K. F., Sfeir, M. Y., Misewich, J. A. & Heinz, T. F. The evolution of electronic structure in few-layer graphene revealed by optical spectroscopy. *Proc. Natl. Acad. Sci.* **107**, 14999–15004 (2010).
19. Koshino, M. & Ando, T. Magneto-optical properties of multilayer graphene. *Phys. Rev. B* **77**, 115313 (2008).
20. Blake, P. et al. Making graphene visible. *Appl. Phys. Lett.* **91**, 063124 (2007).
21. Ferrari, A. C. et al. Raman Spectrum of Graphene and Graphene Layers. *Phys. Rev. Lett.* **97**, 187401 (2006).
22. Warner, J. H., Schaffel, F., Rummeli, M. & Bachmatiuk, A. *Graphene : fundamentals and emergent applications*. (Elsevier, 2013).

23. Liu, N. et al. Universal Segregation Growth Approach to Wafer-Size Graphene from Non-Noble Metals. *Nano Lett.* **11**, 297–303 (2011).
24. Li, X. et al. Large-area synthesis of high-quality and uniform graphene films on copper foils. *Science* **324**, 1312–4 (2009).
25. Parvez, K. et al. Exfoliation of graphite into graphene in aqueous solutions of inorganic salts. *J. Am. Chem. Soc.* **136**, 6083–91 (2014).
26. Novoselov, K. S. et al. Two-dimensional atomic crystals. *Proc. Natl. Acad. Sci. U. S. A.* **102**, 10451–3 (2005).
27. Zhao, W. et al. Preparation of graphene by exfoliation of graphite using wet ball milling. *J. Mater. Chem.* **20**, 5817–5819 (2010).
28. Zhao, W., Wu, F., Wu, H. & Chen, G. Preparation of colloidal dispersions of graphene sheets in organic solvents by using ball milling. *J. Nanomater.* **2010**, (2010).
29. Zhu, J. New solutions to a new problem. *Nat. Nanotechnol.* **3**, 528–529 (2008).
30. Eda, G., Fanchini, G. & Chhowalla, M. Large-area ultrathin films of reduced graphene oxide as a transparent and flexible electronic material. *Nat. Nanotechnol.* **3**, 270–4 (2008).
31. Geng, D. & Loh, K. P. Controlled Growth of Graphene Crystals by Chemical Vapor Deposition: From Solid Metals to Liquid Metals. in *2D Materials* (eds. Avouris, P., Heinz, T. F. & Low, T.) 238–256 (Cambridge University Press, 2017). doi: 10.1017/9781316681619.014
32. Kozhemyakina, N. V. et al. Non-Covalent Chemistry of Graphene: Electronic Communication with Dendronized Perylene Bisimides. *Adv. Mater.* **22**, 5483–5487 (2010).
33. Walter, J. et al. Determination of the lateral dimension of graphene oxide nanosheets using analytical ultracentrifugation. *Small* **11**, 814–825 (2015).
34. Rubino, S., Akhtar, S. & Leifer, K. A Simple Transmission Electron Microscopy Method for Fast Thickness Characterization of Suspended Graphene and Graphite Flakes. *Microsc. Microanal.* **22**, 250–256 (2016).
35. Erickson, K. et al. Determination of the local chemical structure of graphene oxide and reduced graphene oxide. *Adv. Mater.* **22**, 4467–4472 (2010).
36. Eigler, S. et al. Statistical-Raman-Microscopy and Atomic-Force-Microscopy on Heterogeneous Graphene Obtained after Reduction of Graphene Oxide. *J. Phys. Chem. C* (2014). doi:10.1021/jp500580g
37. Dresselhaus, M. S., Dresselhaus, G. & Saito, R. Physics of carbon nanotubes. *Carbon* **33**, 883–891 (1995).
38. Nika, D. L. & Balandin, A. A. Two-dimensional phonon transport in graphene. *Journal of Physics Condensed Matter* **24**, 233203 (2012).
39. Kittel. *Introduction to solid state physics.* (John Wiley & Sons, 2007). doi: 10.1007/978-3-540-93804-0
40. Cooper, D. R. et al. Experimental Review of Graphene. *ISRN Condens. Matter Phys.* **2012**, 1–56 (2012).
41. Jorio, A., Saito, R., Dresselhaus, G. & Dresselhaus, M. S. *Raman Spectroscopy in Graphene Related Systems.* (WILEY-VCH Verlag GmbH, 2011).
42. Ariel, V. & Natan, A. Electron effective mass in graphene. *Proc. 2013 Int. Conf. Electromagn. Adv. Appl. ICEAA 2013* 696–698 (2013). doi:10.1109/ICEAA.2013.6632334

43. Jeong, B. W., Ihm, J. & Lee, G.-D. Stability of dislocation defect with two pentagon-heptagon pairs in graphene. *Phys. Rev. B* **78**, 165403 (2008).
44. Dettori, R., Cadelano, E. & Colombo, L. Elastic fields and moduli in defected graphene. *J. Phys. Condens. Matter* **24**, 104020 (2012).
45. Meyer, J. C. et al. Direct imaging of lattice atoms and topological defects in graphene membranes. *Nano Lett.* **8**, 3582–3586 (2008).
46. Yazyev, O. V. & Chen, Y. P. Polycrystalline graphene and other two-dimensional materials. *Nat. Nanotechnol.* **9**, 755–767 (2014).
47. Yazyev, O. V. & Louie, S. G. Topological defects in graphene: Dislocations and grain boundaries. *Phys. Rev. B - Condens. Matter Mater. Phys.* **81**, 195420 (2010).
48. Huang, P. Y. et al. Grains and grain boundaries in single-layer graphene atomic patchwork quilts. *Nature* **469**, 389–392 (2011).
49. Lahiri, J., Lin, Y., Bozkurt, P., Oleynik, I. I. & Batzill, M. An extended defect in graphene as a metallic wire. *Nat. Nanotechnol.* **5**, 326–329 (2010).
50. Cockayne, E. et al. Grain boundary loops in graphene. *Phys. Rev. B - Condens. Matter Mater. Phys.* **83**, 195425 (2011).
51. Robertson, A. W. et al. Atomic Structure of Interconnected Few-Layer Graphene Domains. *ACS Nano* **5**, 6610–6618 (2011).
52. Jia, X., Campos-Delgado, J., Terrones, M., Meunier, V. & Dresselhaus, M. S. Graphene edges: a review of their fabrication and characterization. *Nanoscale* **3**, 86–95 (2011).
53. Chuvilin, A. From graphene constrictions to single carbon chains. *New J. Phys* **11**, (2009).
54. Warner, J. H., Lin, Y.-C., He, K., Koshino, M. & Suenaga, K. Atomic Level Spatial Variations of Energy States along Graphene Edges. *Nano Lett.* **14**, 6155–6159 (2014).
55. Enoki, T., Kobayashi, Y. & Fukui, K.-I. Electronic structures of graphene edges and nanographene. *Int. Rev. Phys. Chem.* **26**, 609–645 (2007).
56. Guisinger, N. P., Rutter, G. M., Crain, J. N., First, P. N. & Stroscio, J. A. Exposure of Epitaxial Graphene on SiC(0001) to Atomic Hydrogen. *Nano Lett.* **9**, 1462–1466 (2009).
57. Kobayashi, Y., Fukui, K., Enoki, T. & Kusakabe, K. Edge state on hydrogen-terminated graphite edges investigated by scanning tunneling microscopy. *Phys. Rev. B* **73**, 125415 (2006).
58. Lee, J.-K. et al. The Nature of Metastable AA' Graphite: Low Dimensional Nano- and Single-Crystalline Forms. *Sci. Rep.* **6**, 39624 (2016).
59. Singh, M. K. et al. Atomic-scale observation of rotational misorientation in suspended few-layer graphene sheets. *Nanoscale* **2**, 700 (2010).
60. Bottari, G. et al. Chemical functionalization and characterization of graphene-based materials. *Chem. Soc. Rev.* **46**, 4464–4500 (2017).
61. Wang, Y. et al. Twisted Bilayer Graphene Superlattices. *Nano Res.* **6**, 269–274 (2013).
62. Schmidt, H., Rode, J. C., Smirnov, D. & Haug, R. J. Superlattice structures in twisted bilayers of folded graphene. *Nat. Commun.* **5**, (2014).
63. Partoens, B. & Peeters, F. M. From graphene to graphite: Electronic structure around the K point. *Phys. Rev. B - Condens. Matter Mater. Phys.* **74**, 075404 (2006).
64. Bistritzer, R. & Macdonald, A. H. Moiré bands in twisted double-layer graphene. *PNAS* **108**, 12233–12237 (2011).

65. Zhong, X., Pandey, R. & Karna, S. P. Stacking dependent electronic structure and transport in bilayer graphene nanoribbons. *Carbon* **50**, 784–790 (2012).
66. L. Reimer H. Kohl, Reimer, L. & Kohl, H. *Transmission Electron Microscopy :Physics of Image Formation*. (Springer Verlag, 2008).
67. Egerton, R. F. TEM Applications of EELS. in *Electron Energy-Loss Spectroscopy in the Electron Microscope* 293–397 (Springer US, 2011). doi: 10.1007/978-1-4419-9583-4
68. Williams, David B., Carter, C. B. *Transmission Electron Microscopy - A Textbook for Materials Science* | Springer. (Springer; 2nd ed. 2009 edition (27 Aug. 2009)).
69. Meyer, J. C. et al. On the roughness of single- and bi-layer graphene membranes. *Solid State Commun.* **143**, 101–109 (2007).
70. Meyer, J. C. et al. The structure of suspended graphene sheets. *Nature* **446**, 60 (2007).
71. Horiuchi, S. et al. Carbon nanofilm with a new structure and property. *Japanese Journal of Applied Physics, Part 2: Letters* **42**, L1073–L1076 (2003).
72. Akhtar, S., Rubino, S. & Leifer, K. A simple TEM method for fast thickness characterization of suspended graphene flakes. *12* (2012).
73. Reimer, L. & Kohl, H. *Transmission Electron Microscopy - Physics of Image Formation*. (Springer Verlag, 2007).
74. Bachmatiuk, A. et al. Low voltage transmission electron microscopy of graphene. *Small* **11**, 515–42 (2015).
75. Meyer, J. C., Girit, C. O., Crommie, M. F. & Zettl, A. Imaging and dynamics of light atoms and molecules on graphene. *Nature* **454**, 319–322 (2008).
76. Na, M. Y., Lee, S., Kim, D. H. & Chang, H. J. Dark-field Transmission Electron Microscopy Imaging Technique to Visualize the Local Structure of Two-dimensional Material ; Graphene. **45**, 23–31 (2015).
77. Kim, K. et al. Grain Boundary Mapping in. *ACS Nano* **5**, 2142–2146 (2011).
78. Liu, Y. & Yakobson, B. I. Cones, pringles, and grain boundary landscapes in graphene topology. *Nano Lett.* **10**, 2178–2183 (2010).
79. Lehtinen, O. et al. Non-invasive transmission electron microscopy of vacancy defects in graphene produced by ion irradiation. *Nanoscale* **6**, 6569–6576 (2014).
80. Hinrichs, R. et al. Amorphization of Graphite Flakes in Gray Cast Iron Under Tribological Load. *Mater. Res.* **21**, (2018).
81. Schimpf, C., Motylenko, M. & Rafaja, D. Quantitative description of microstructure defects in hexagonal boron nitrides using X-ray diffraction analysis. *Mater. Charact.* **86**, 190–199 (2013).
82. Huang, J., Varlamov, S., Dore, J., Yun, J. S. & Green, M. A. Micro-structural defects in polycrystalline silicon thin-film solar cells on glass by solid-phase crystallisation and laser-induced liquid-phase crystallisation. *Sol. Energy Mater. Sol. Cells* **132**, 282–288 (2015).
83. Wachsmuth, P., Hambach, R., Benner, G. & Kaiser, U. Plasmon bands in multilayer graphene. *Phys. Rev. B - Condens. Matter Mater. Phys.* **90**, 235434 (2014).
84. Lu, J., Loh, K. P., Huang, H., Chen, W. & Wee, A. T. S. Plasmon dispersion on epitaxial graphene studied using high-resolution electron energy-loss spectroscopy. *Phys. Rev. B* **80**, 113410 (2009).

85. Liou, S. C. et al. Π -Plasmon Dispersion in Free-Standing Monolayer Graphene Investigated By Momentum-Resolved Electron Energy-Loss Spectroscopy. *Microsc. Microanal.* **20**, 1788–1789 (2014).
86. Zhang, X., Schneider, R., Müller, E. & Gerthsen, D. Practical aspects of the quantification of sp^2 -hybridized carbon atoms in diamond-like carbon by electron energy loss spectroscopy. *Carbon* **102**, 198–207 (2016).
87. Zhang, Z. et al. Investigating the structure of non-graphitising carbons using electron energy loss spectroscopy in the transmission electron microscope. *Carbon* **49**, 5049–5063 (2011).
88. Mironov, B. E. et al. Electron irradiation of nuclear graphite studied by transmission electron microscopy and electron energy loss spectroscopy. *Carbon* **83**, 106–117 (2015).
89. Griffiths, D. J. *Introduction to Electrodynamics*. (Cambridge University Press, 2005). doi:10.1119/1.4766311
90. Skulason, H. S., Gaskell, P. E. & Szkopek, T. Optical reflection and transmission properties of exfoliated graphite from a graphene monolayer to several hundred graphene layers. *Nanotechnology* **21**, (2010).
91. Saito, R., Dresselhaus, G. & Dresselhaus, M. S. *Physical Properties of Carbon Nanotubes*. (Imperial College Press, 1998).
92. Childres, I., Jauregui, L. & Park, W. Raman spectroscopy of graphene and related materials. ... *Phot. Mater.* ...
93. Stauber, T., Peres, N. M. R. & Geim, A. K. The optical conductivity of graphene in the visible region of the spectrum. 1–8 (2008). doi:10.1103/PhysRevB.78.085432
94. Nair, R. R. et al. Fine structure constant defines visual transparency of graphene. *Science* **320**, 1308 (2008).
95. Zhu, S. E., Yuan, S. & Janssen, G. C. A. M. Optical transmittance of multilayer graphene. *Epl* **108**, 1–4 (2014).
96. Mak, K. F. et al. Measurement of the optical conductivity of graphene. *Phys. Rev. Lett.* **101**, 2–5 (2008).
97. Kuzmenko, A. B., Van Heumen, E., Carbone, F. & Van Der Marel, D. Universal optical conductance of graphite. *Phys. Rev. Lett.* **100**, 2–5 (2008).
98. Ni, Z. H. et al. Graphene thickness determination using reflection and contrast spectroscopy. *Nano Lett.* **7**, 2758–63 (2007).
99. Nelson, F. J. et al. Optical properties of large-area polycrystalline chemical vapor deposited graphene by spectroscopic ellipsometry. *Appl. Phys. Lett.* **97**, 253110 (2010).
100. Mak, K. F., Sfeir, M. Y., Misewich, J. A. & Heinz, T. F. The evolution of electronic structure in few-layer graphene revealed by optical spectroscopy. *Proc. Natl. Acad. Sci. U. S. A.* **107**, 14999–5004 (2010).
101. Koshino, M. & Ando, T. Magneto-optical properties of multilayer graphene. *Phys. Rev. B* **77**, 115313 (2008).
102. Gammelgaard, L. et al. Graphene transport properties upon exposure to PMMA processing and heat treatments. *2D Mater.* **1**, 035005 (2014).
103. Jorio, A., Dresselhaus, M. S., Saito, R. & Dresselhaus, G. *Raman Spectroscopy in Graphene Related Systems*. (Wiley, 2011).

104. Huang, M. et al. Phonon softening and crystallographic orientation of strained graphene studied by Raman spectroscopy. *Proc. Natl. Acad. Sci. U. S. A.* **106**, 7304–8 (2009).
105. Mohiuddin, T. M. G. et al. Uniaxial strain in graphene by Raman spectroscopy: G peak splitting, Grüneisen parameters, and sample orientation. *Phys. Rev. B* **79**, 205433 (2009).
106. Ferrari, A. C., Rodil, S. E. & Robertson, J. Resonant Raman spectra of amorphous carbon nitrides: The G peak dispersion. *Diam. Relat. Mater.* **12**, 905–910 (2003).
107. Beams, R., Canç Ado, L. G., Novotny, L., Gustavo Cançado, L. & Novotny, L. Raman characterization of defects and dopants in graphene. *J. Phys. Condens. Matter* **27**, 83002–26 (2015).
108. Dresselhaus, M. S., Jorio, A., Souza Filho, A. G. & Saito, R. Defect characterization in graphene and carbon nanotubes using Raman spectroscopy. *Philos. Trans. R. Soc. A Math. Phys. Eng. Sci.* **368**, 5355–5377 (2010).
109. Casiraghi, C. et al. Raman spectroscopy of graphene edges. *Nano Lett.* **9**, 1433–1441 (2009).
110. Malard, L. M., Pimenta, M. A., Dresselhaus, G. & Dresselhaus, M. S. M. Raman spectroscopy in graphene. *Phys. Rep.* **473**, 51–87 (2009).
111. Cançado, L. G., Reina, A., Kong, J. & Dresselhaus, M. S. Geometrical approach for the study of G' band in the Raman spectrum of monolayer graphene, bilayer graphene, and bulk graphite. *Phys. Rev. B - Condens. Matter Mater. Phys.* **77**, 245408 (2008).
112. Malard, L. M., Guimarães, M. H. D., Mafra, D. L., Mazzoni, M. S. C. & Jorio, A. Group-theory analysis of electrons and phonons in N-layer graphene systems. *Phys. Rev. B - Condens. Matter Mater. Phys.* **79**, (2009).
113. Malard, L. M. et al. Probing the electronic structure of bilayer graphene by Raman scattering. *Phys. Rev. B - Condens. Matter Mater. Phys.* **76**, (2007).
114. Tuinstra, F., Koenig, J. L. & Koenig, L. Raman Spectrum of Graphite. *J. Chem. Phys.* **53**, 1126–1130 (1970).
115. Lucchese, M. M. et al. Quantifying ion-induced defects and Raman relaxation length in graphene. *Carbon* **48**, 1592–1597 (2010).
116. Cançado, L. G. et al. Quantifying defects in graphene via Raman spectroscopy at different excitation energies. *Nano Lett.* **11**, 3190–3196 (2011).
117. Cong, C., Yu, T. & Wang, H. Raman study on the G mode of graphene for determination of edge orientation. *ACS Nano* **4**, 3175–3180 (2010).
118. Basko, D. M. Boundary problems for Dirac electrons and edge-assisted Raman scattering in graphene. *Phys. Rev. B - Condens. Matter Mater. Phys.* **79**, (2009).
119. Beams, R., Cançado, L. G. & Novotny, L. Low Temperature Raman Study of the Electron Coherence Length near Graphene Edges. *Nano Lett.* **11**, 1177–1181 (2011).
120. Krauss, B. et al. Raman scattering at pure graphene zigzag edges. *Nano Lett.* **10**, 4544–4548 (2010).
121. Mignuzzi, S. et al. Probing individual point defects in graphene via near-field Raman scattering. *Nanoscale* **7**, 19413–19418 (2015).
122. Lotya, M., King, P. J., Khan, U., De, S. & Coleman, J. N. High-concentration, surfactant-stabilized graphene dispersions. *ACS Nano* **4**, 3155–3162 (2010).
123. Sun, C. et al. Solvothermally exfoliated fluorographene for high-performance lithium primary batteries. *Nanoscale* **6**, 2634–2641 (2014)

124. Lee, D. S. et al. Raman Spectra of Epitaxial Graphene on SiC and of Epitaxial Graphene Transferred to SiO₂. *Nano Lett.* **8**, 4320–4325 (2008).
125. Kaniyoor, A. & Ramaprabhu, S. A Raman spectroscopic investigation of graphite oxide derived graphene. *AIP Adv.* **2**, 032183 (2012).
126. Cançado, L. G. et al. Stokes and anti-Stokes double resonance Raman scattering in two-dimensional graphite. *Phys. Rev. B* **66**, 035415 (2002).
127. León, V. et al. Few-layer graphenes from ball-milling of graphite with melamine. *Chem. Commun.* **47**, 10936 (2011).
128. Ravula, S., Baker, S. N., Kamath, G. & Baker, G. A. Ionic liquid-assisted exfoliation and dispersion: stripping graphene and its two-dimensional layered inorganic counterparts of their inhibitions. *Nanoscale* **7**, 4338–4353 (2015).
129. Georgakilas, V. et al. Organic functionalisation of graphenes. *Chem. Commun.* **46**, 1766–1768 (2010).
130. Green, A. A. & Hersam, M. C. Solution Phase Production of Graphene with Controlled Thickness via Density Differentiation. *Nano Lett.* **9**, 4031–4036 (2009).
131. Restolho, J., Mata, J. L. & Saramago, B. On the interfacial behavior of ionic liquids: Surface tensions and contact angles. *J. Colloid Interface Sci.* **340**, 82–86 (2009).
132. Harnisch, J. A. & Porter, M. D. Electrochemically modulated liquid chromatography: An electrochemical strategy for manipulating chromatographic retention. in *Analyst* **126**, 1841–1849 (The Royal Society of Chemistry, 2001).
133. Reed, S. K., Lanning, O. J. & Madden, P. A. Electrochemical interface between an ionic liquid and a model metallic electrode. *J. Chem. Phys.* **126**, 084704 (2007).
134. Koch, C. C., Ovidko, I. A., Seal, S. & Veprek, S. *Structural Nanocrystalline Materials: Fundamental and Applications.* (Cambridge University Press, 2007).
135. De Graef, M. & McHenry, M. E. *Structure of materials : an introduction to crystallography, diffraction, and symmetry.*
136. Speakman, S. A. *Fundamentals of Rietveld Refinement.* Massachusetts Inst. Technol. (2010).
137. Reich, S. & Thomsen, C. Raman spectroscopy of graphite. *Philos. Trans. A. Math. Phys. Eng. Sci.* **362**, 2271–88 (2004).
138. Mantell, C. Nuclear Graphite. in *Handbook of Carbon and Graphite* 391–425 (Academic Press, 1968).
139. Shearer, C. J., Slattery, A. D., Stapleton, A. J., Shapter, J. G. & Gibson, C. T. Accurate thickness measurement of graphene. *Nanotechnology* **27**, 125704 (2016).
140. Lotya, M. et al. Liquid phase production of graphene by exfoliation of graphite in surfactant/water solutions. *J. Am. Chem. Soc.* **131**, 3611–3620 (2009).
141. Bischoff, D. et al. Raman spectroscopy on etched graphene nanoribbons. *J. Appl. Phys.* **109**, 073710 (2011).
142. Enoki, T., Fujii, S. & Takai, K. Zigzag and armchair edges in graphene. *Carbon* **50**, 3141–3145 (2012).
143. Banhart, F. & F. Banhart. Irradiation effects in carbon nanostructures. *Rep. Prog. Phys.* **62**, 1181 (1999).
144. Daniels, H. et al. Experimental and theoretical evidence for the magic angle in transmission electron energy loss spectroscopy. *Ultramicroscopy* **96**, 523–534 (2003).
145. Egerton, R. *Electron Energy-loss Spectroscopy in the Electron Microscope.* (Springer, 2014).

146. Daniels, H., Brydson, R., Rand, B. & Brown, A. Investigating carbonization and graphitization using electron energy loss spectroscopy (EELS) in the transmission electron microscope (TEM). *Philos. Mag.* **87**, 4073–4092 (2007).
147. ImageJ.
148. Stéfan van der Walt, Johannes L. Schönberger, Juan Nunez-Iglesias, François Boulogne, Joshua D. Warner, Neil Yager, Emmanuelle Gouillart, T. Y. and the scikit-image contributors. *scikit-image: Image processing in Python.* (2014).
149. Cervera Gontard, L., Ozkaya, D. & Dunin-Borkowski, R. E. A simple algorithm for measuring particle size distributions on an uneven background from TEM images. *Ultramicroscopy* **111**, 101–106 (2011).
150. Terrés, B. et al. Size quantization of Dirac fermions in graphene constrictions. *Nat. Commun.* **7**, 11528 (2016).
151. Zhu, S., Tang, S., Zhang, J. & Yang, B. Control the size and surface chemistry of graphene for the rising fluorescent materials. *Chem. Commun.* **48**, 4527 (2012).
152. Porwal, H. et al. Effect of lateral size of graphene nano-sheets on the mechanical properties and machinability of alumina nano-composites. *Ceram. Int.* **42**, 7533–7542 (2016).
153. Ma, J. et al. Crucial Role of Lateral Size for Graphene Oxide in Activating Macrophages and Stimulating Pro-inflammatory Responses in Cells and Animals. *ACS Nano* **9**, 10498–10515 (2015).
154. Maragó, O. M. et al. Brownian Motion of Graphene. *ACS Nano* **4**, 7515–7523 (2010).
155. Wu, L. et al. Aggregation Kinetics of Graphene Oxides in Aqueous Solutions: Experiments, Mechanisms, and Modeling. *Langmuir* **29**, 15174–15181 (2013).
156. Kobayashi, Y., Fukui, K., Enoki, T., Kusakabe, K. & Kaburagi, Y. Observation of zigzag and armchair edges of graphite using scanning tunneling microscopy and spectroscopy. *Phys. Rev. B* **71**, 193406 (2005).
157. Brey, L. & Fertig, H. A. Electronic states of graphene nanoribbons studied with the Dirac equation. *Phys. Rev. B - Condens. Matter Mater. Phys.* **73**, 235411 (2006).
158. Wassmann, T., Seitsonen, A. P., Saitta, A. M., Lazzeri, M. & Mauri, F. Structure, Stability, Edge States, and Aromaticity of Graphene Ribbons. *Phys. Rev. Lett.* **101**, 096402 (2008).
159. Zhou, M. et al. Production of graphene by liquid-phase exfoliation of intercalated graphite. *Int. J. Electrochem. Sci.* **9**, 810–820 (2014).
160. Wu, Z.-S. et al. Field Emission of Single-Layer Graphene Films Prepared by Electrophoretic Deposition. *Adv. Mater.* **21**, 1756–1760 (2013).
161. Babick, F. *Suspensions of Colloidal Particles and Aggregates.* (2016). doi: 10.1007/978-3-319-30663-6
162. Elimelech, M., Gregory, J., Jia, X. & Williams, R. *Particle deposition and aggregation, 1995.* Butterworth-Heinemann, Oxford (1995).
163. Warner, J. H. et al. *Graphene : fundamentals and emergent applications.* Elsevier **17**, (Elsevier, 2013).
164. Koskinen, P., Malola, S. & Häkkinen, H. Evidence for graphene edges beyond zigzag and armchair. *Phys. Rev. B* **80**, 073401 (2009).
165. Zhang, T., Li, X. & Gao, H. Fracture of graphene: a review. *Int. J. Fract.* **196**, 1–31 (2015).

166. LUO, Z. P. & KOO, J. H. Quantifying the dispersion of mixture microstructures. *J. Microsc.* **225**, 118–125 (2007).
167. Budarapu, P. R. et al. Crack propagation in graphene. *J. Appl. Phys.* **118**, 064307 (2015).
168. Zhang, J., Ragab, T. & Basaran, C. The effects of vacancy defect on the fracture behaviors of zigzag graphene nanoribbons. *Int. J. Damage Mech.* (2016). doi: 10.1177/1056789516671795
169. Terdalkar, S. S. et al. Nanoscale fracture in graphene. *Chem. Phys. Lett.* **494**, 218–222 (2010).
170. Novotny, L. *Principles of nano-optics.* (Cambridge University Press, 2012).
171. Gaskell, P. E., Skulason, H. S., Rodenchuk, C. & Szkopek, T. Counting graphene layers on glass via optical reflection microscopy. *Appl. Phys. Lett.* **94**, 143101 (2009).
172. Wang, Y. Y. et al. Thickness identification of two-dimensional materials by optical imaging. *Nanotechnology* **23**, 495713 (2012).
173. Chen, Y. F. et al. Rapid determination of the thickness of graphene using the ratio of color difference. *J. Phys. Chem. C* **115**, 6690–6693 (2011).
174. Lotya, M., Rakovich, A., Donegan, J. F. & Coleman, J. N. Measuring the lateral size of liquid-exfoliated nanosheets with dynamic light scattering. *Nanotechnology* **24**, 265703 (2013).
175. Van Der Kooij, F. M. et al. Sedimentation and diffusion in suspensions of sterically stabilized colloidal platelets. *Langmuir* **16**, 5317–5323 (2000).
176. Silvera Batista, C. A., Zheng, M., Khripin, C. Y., Tu, X. & Fagan, J. A. Rod hydrodynamics and length distributions of single-wall carbon nanotubes using analytical ultracentrifugation. *Langmuir* **30**, 4895–904 (2014).
177. Malvern instruments. *Zetasizer Nano Series User Manual.* Department of Biochemistry Biophysics Facility, University of Chambridge (2004). doi:10.1016/S0294-3506(99)80105-7
178. Note, T. Introduction to the calculators in the Zetasizer software. 1–6 (2014).
179. Djurišić, A. ~B. & Li, E. ~H. Optical properties of graphite. *J. Appl. Phys.* **85**, 7404–7410 (1999).
180. M. N. Polyanskiy. *Refractive index database.* Available at: <https://refractiveindex.info>. (Accessed: 17th June 2017)
181. Malvern instruments. *Zetasizer HR 3000.* *Biofutur* **1999**, (1999).
182. Telling, R. H., Ewels, C. P., El-Barbary, A. A. & Heggie, M. I. Wigner defects bridge the graphite gap. *Nat. Mater.* **2**, 333–337 (2003).
183. Gass, M. H. et al. Free-standing graphene at atomic resolution. *Nat. Nanotechnol.* **3**, 676–81 (2008).
184. Liu, X., Balla, I., Bergeron, H. & Hersam, M. C. Point Defects and Grain Boundaries in Rotationally Commensurate MoS₂ on Epitaxial Graphene. *J. Phys. Chem. C* **120**, 20798–20805 (2016).
185. Maclel, I. O. et al. Electron and phonon renormalization near charged defects in carbon nanotubes. *Nat. Mater.* **7**, 878–883 (2008).
186. Cancado, L. G., Beams, R. & Novotny, L. Optical Measurement of the Phase-Breaking Length in Graphene. *Laser Sci.* **24–28**, 5 (2008).
187. Ribeiro-Soares, J. et al. Structural analysis of polycrystalline graphene systems by Raman spectroscopy. *Carbon* **95**, 646–652 (2015).

188. Pimenta, M. A. et al. Studying disorder in graphite-based systems by Raman spectroscopy. *Phys. Chem. Chem. Phys.* **9**, 1276–1290 (2007).
189. Boothroyd, C. B. Quantification of high-resolution electron microscope images of amorphous carbon. *Ultramicroscopy* **83**, 159–168 (2000).
190. Piasecki, R. Entropic measure of spatial disorder for systems of finite-sized objects. *Phys. A Stat. Mech. its Appl.* **277**, 157–173 (2000).
191. Kotakoski, J. et al. Stone-Wales-type transformations in carbon nanostructures driven by electron irradiation. *Phys. Rev. B - Condens. Matter Mater. Phys.* **83**, (2011).
192. Warner, J. H. The influence of the number of graphene layers on the atomic resolution images obtained from aberration-corrected high resolution transmission electron microscopy. *Nanotechnology* **21**, 255707 (2010).
193. Grantab, R., Shenoy, V. B. & Ruoff, R. S. Anomalous Strength Characteristics of Tilt Grain Boundaries in Graphene. *Science (80-.)*. **330**, 946–948 (2010).
194. Brown, L. et al. Twinning and twisting of tri- and bilayer graphene. *Nano Lett.* **12**, 1609–1615 (2012).
195. Fang, W. et al. Rapid identification of stacking orientation in isotopically labeled chemical-vapor grown bilayer graphene by Raman spectroscopy. *Nano Lett.* **13**, 1541–1548 (2013).
196. Jeong, H. K. et al. Evidence of graphitic AB stacking order of graphite oxides. *J. Am. Chem. Soc.* **130**, 1362–1366 (2008).
197. Iwasaki, T. et al. Formation and structural analysis of twisted bilayer graphene on Ni(111) thin films. *Surf. Sci.* **625**, 44–49 (2014).
198. Santos, J. M. B. L. dos et al. Graphene bilayer with a twist: Electronic structure. *Phys. Rev. Lett.* **99**, 0–3 (2007).
199. Lu, C.-C. et al. Twisting Bilayer Graphene. *ACS Nano* **7**, 2587–94 (2013).
200. Lin, Y. C. et al. Structural and Chemical Dynamics of Pyridinic-Nitrogen Defects in Graphene. *Nano Lett.* **15**, 7408–7413 (2015).
201. Eigler, S., Dotzer, C. & Hirsch, A. Visualization of defect densities in reduced graphene oxide. *Carbon* **50**, 3666–3673 (2012).
202. Kelly, R. A., Holmes, J. D. & Petkov, N. Visualising discrete structural transformations in germanium nanowires during ion beam irradiation and subsequent annealing. *Nanoscale* **6**, 12890–12897 (2014).
203. Andrey, P. et al. Statistical analysis of 3D images detects regular spatial distributions of centromeres and chromocenters in animal and plant nuclei. *PLoS Comput. Biol.* **6**, 27 (2010).
204. Ollion, J., Cochenec, J., Loll, F., Escudé, C. & Boudier, T. TANGO: a generic tool for high-throughput 3D image analysis for studying nuclear organization. *Bioinformatics* **29**, 1840–1 (2013).
205. Ferrari, A. C. & Robertson, J. Raman Spectroscopy of Amorphous, Nanostructured, Diamond-like Carbon, and Nanodiamond. *Philosophical Transactions: Mathematical, Physical and Engineering Sciences* **362**, 2477–2512
206. Cançado, L. G., Pimenta, M. A., Neves, B. R. A., Dantas, M. S. S. & Jorio, A. Influence of the atomic structure on the Raman spectra of graphite edges. *Phys. Rev. Lett.* **93**, 5–8 (2004).
207. Wallace, P. The Band Theory of Graphite. *Phys. Rev.* **71**, 622–634 (1947).

208. Bonaccorso, F., Sun, Z., Hasan, T. & Ferrari, A. C. Graphene photonics and optoelectronics. *Nat. Photonics* **4**, 611–622 (2010).
209. Zhang, J. et al. Reduction of graphene oxide via ascorbic acid. *Chem. Commun.* **46**, 1112–1114 (2010).
210. Shen, Z., Li, J., Yi, M., Zhang, X. & Ma, S. Preparation of graphene by jet cavitation. *Nanotechnology* **22**, 365306 (2011).
211. Ferrari, A. & Basko, D. Raman spectroscopy as a versatile tool for studying the properties of graphene. *Nat. Nanotechnol.* **8**, 235–46 (2013).
212. Basko, D. M. Theory of resonant multiphonon Raman scattering in graphene. *Phys. Rev. B - Condens. Matter Mater. Phys.* **78**, (2008).
213. Malis, T., Cheng, S. C. & Egerton, R. F. EELS log-ratio technique for specimen-thickness measurement in the TEM. *J. Electron Microsc. Tech.* **8**, 193–200 (1988).
214. Gatan. Assess sample thickness | EELS.info. Gatan (2017). Available at: <http://www.eels.info/how/quantification/assess-sample-thickness>. (Accessed: 26th March 2018)
215. Zhang, H. R., Egerton, R. F. & Malac, M. Local thickness measurement through scattering contrast and electron energy-loss spectroscopy. *Micron* **43**, 8–15 (2012).
216. Alexander, D. Chapter 3 and 4 TEM Crystallography and Diffraction. (2014).
217. Eberlein, T. et al. Plasmon spectroscopy of free-standing graphene films. *Phys. Rev. B - Condens. Matter Mater. Phys.* **77**, 233406 (2008).
218. Wachsmuth, P., Hambach, R., Benner, G. & Kaiser, U. Plasmon bands in multilayer graphene. *Phys. Rev. B - Condens. Matter Mater. Phys.* **90**, 1–5 (2014).
219. Stéphan, O. et al. Dielectric response of isolated carbon nanotubes investigated by spatially resolved electron energy-loss spectroscopy: From multiwalled to single-walled nanotubes. *Phys. Rev. B - Condens. Matter Mater. Phys.* **66**, 1–6 (2002).
220. Potapov, P. L., Engelmann, H. J., Zschech, E. & Stöger-Pollach, M. Measuring the dielectric constant of materials from valence EELS. *Micron* **40**, 262–268 (2009).
221. Ferrari, A. C. Raman spectroscopy of graphene and graphite: Disorder, electron-phonon coupling, doping and nonadiabatic effects. *Solid State Commun.* **143**, 47–57 (2007).
222. Hao, Y. et al. Probing layer number and stacking order of few-layer graphene by Raman Spectroscopy. *Small* **6**, 195–200 (2010).
223. Aizawa, T., Souda, R., Otani, S., Ishizawa, Y. & Oshima, C. Bond softening in monolayer graphite formed on transition-metal carbide surfaces. *Phys. Rev. B* **42**, 11469–11478 (1990).
224. Kim, J. S. et al. Between scylla and charybdis: Hydrophobic graphene-guided water diffusion on hydrophilic substrates. *Sci. Rep.* **3**, 2309 (2013).
225. SPI HOPG GRADE 2 | SPI Supplies. Available at: <https://www.2spi.com/category/hopg-grade-2/hopg-spi-supplies/>. (Accessed: 30th May 2018)
226. Liu, J. et al. Improved synthesis of graphene flakes from the multiple electrochemical exfoliation of graphite rod. *Nano Energy* **2**, 377–386 (2013).
227. University of Cambridge. DoITPoMS - TLP Library Kinetics of Aqueous Corrosion - Kinetics of Corrosion - the Tafel Equation. Available at: https://www.doitpoms.ac.uk/tlplib/aqueous_corrosion/tafel.php. (Accessed: 30th May 2018)
228. Hori, Y. *Modern Aspects of Electrochemistry Vol.42.* (2008). doi: 10.1007/978-0-387-49489-0

229. Beck, F., Junge, H. & Krohn, H. Graphite intercalation compounds as positive electrodes in galvanic cells. *Electrochim. Acta* **26**, 799–809 (1981).
230. Beck, F., Jiang, J. & Krohn, H. Potential oscillations during galvanostatic overoxidation of graphite in aqueous sulphuric acids. *J. Electroanal. Chem.* **389**, 161–165 (1995).
231. Speakman, S. *Estimating crystallite size using xrd*. Centre for Materials Science and Engineering (2011).
232. Singh, D. A. K. *Advanced X-ray Techniques in Research and Industry*. (IOS Press, 2005). doi:1586035371
233. Praveen Ranganath. *Electric Field distribution using 2D Poisson Equation*.
234. Peiro, J. & Sherwin, S. *Finite Difference, Finite Element and Finite Volume Methods for Partial Differential Equations*. *Handb. Mater. Model.* **M**, 2415–2446 (2005)
235. Jawaid, A. et al. Mechanism for Liquid Phase Exfoliation of MoS₂. *Chem. Mater.* **28**, 337–348 (2016)
236. Coleman, J. N. Liquid Exfoliation of Defect-Free Graphene. *Acc. Chem. Res.* **46**, 14–22 (2013)
237. Cunningham, G. et al. Solvent Exfoliation of Transition Metal Dichalcogenides: Dispersibility of Exfoliated Nanosheets Varies Only Weakly between Compounds. *ACS Nano* **6**, 3468–3480 (2012)
238. Hughes, J. M., Aherne, D. & Coleman, J. N. Generalizing solubility parameter theory to apply to one- and two-dimensional solutes and to incorporate dipolar interactions. *J. Appl. Polym. Sci.* **127**, 4483–4491 (2013)
239. Hernandez, Y., Lotya, M., Rickard, D., Bergin, S. D. & Coleman, J. N. Measurement of multicomponent solubility parameters for graphene facilitates solvent discovery. *Langmuir* **26**, 3208–3213 (2010).
240. Coleman, J. N. Liquid-Phase Exfoliation of Nanotubes and Graphene. *Adv. Funct. Mater.* **19**, 3680–3695 (2009).
241. Hansen, C. M. *Hansen solubility parameters : a user's handbook*. (CRC Press, 2007)
242. O'Neill, A., Khan, U., Nirmalraj, P. N., Boland, J. & Coleman, J. N. Graphene dispersion and exfoliation in low boiling point solvents. *J. Phys. Chem. C* **115**, 5422–5428 (2011)
243. Lu, J. et al. One-Pot Synthesis of Fluorescent Carbon Graphene by the Exfoliation of Graphite in Ionic Liquids. *ACS Nano* **3**, 2367–2375 (2009).
244. Liu, N. et al. One-step ionic-liquid-assisted electrochemical synthesis of ionic-liquid-functionalized graphene sheets directly from graphite. *Adv. Funct. Mater.* **18**, 1518–1525 (2008)
245. Su, C. Y. et al. High-Quality Thin Graphene Films from Fast Electrochemical Exfoliation. *ACS Nano* **5**, 2332–2339 (2011).
246. Abdelkader, a. M., Cooper, a. J., Dryfe, R. a. W. & Kinloch, I. a. How to get between the sheets: a review of recent works on the electrochemical exfoliation of graphene materials from bulk graphite. *Nanoscale* **7**, 6944–6956 (2015).